PROCEEDINGS OF THE SPACE OPTICAL TECHNOLOGY CONFERENCE

VOL. II

APRIL 1966

U. S. Government Contractors Only.

NASA —— MARSHALL SPACE FLIGHT CENTER

HUNTSVILLE, ALA.
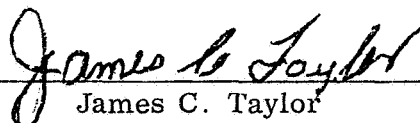
NASA-GEORGE C. MARSHALL SPACE FLIGHT CENTER

SPACE OPTICAL TECHNOLOGY CONFERENCE
HELD NOVEMBER 2-4, 1965, AT
GEORGE C. MARSHALL SPACE FLIGHT CENTER
VOLUME II

George C. Marshall Space Flight Center
Huntsville, Alabama

APPROVED: _James C. Taylor_
James C. Taylor
Chief, Applied Research Branch

TABLE OF CONTENTS

Page

TABLE OF CONTENTS (Concluded)

Page

iv

A SYSTEMS STUDY OF A
MANNED ORBITAL TELESCOPE

D. Bogdanoff*
The Boeing Company

Previous NASA studies have made it apparent that one of the principal reasons for developing a manned orbital space station is the opportunity to perform astronomical observations of a scope far beyond anything possible from the ground or with unmanned systems such as the OAO. The capabilities of such an orbital observatory, as compared with ground-based telescopes, form an important part of the background of such a study. These capabilities are illustrated in Figure 1. It should be noted that to justify a project of this magnitude, the observatory should be capable of performing a variety of observations. The main limitation for the spectrographic, photoelectric, and thermoelectric work of earth-based observatories is the presence of the atmosphere, which acts as a filter for all but some narrow bands (in the visible and IR ranges) in the frequency spectrum to be covered by the MOT. This range has been assumed to be from the Lyman limit (912 $\overset{o}{A}$) to approximately one millimeter. Astrometric work and planetary photography in ground-based telescopes are restricted by the phenomenon of "seeing," which limits the average resolution to one second of arc or slightly better. In the case of the MOT, a performance very nearly approaching the full diffraction limit of 0.05 second of arc should be attainable.

NASA has instituted a broad program of investigation into the various problems associated with the performance of such observations. To explore experiments possible with such an observatory and to define its general design characteristics, a study was performed by Dr. L. W. Fredrick of the University of Virginia. In addition, a study was undertaken by the J. W. Fecker Division of the American Optical Company to establish, in a preliminary sense, the design feasibility of the telescope and a possible design configuration. These studies provided baselines in their respective areas for the present study.

The broad objective of the overall NASA program of investigation is to establish the feasibility of designing, fabricating, launching, and operating a manned astronomical observatory. Within this framework the specific objectives of the Systems Study of a Manned Orbital Telescope were to:

---

* Boeing Study Program Manager

1.   Investigate the possible operational modes of such an observatory with special emphasis on the way in which man will be used to support the observatory;

2.   Accomplish the necessary engineering studies, analyses, design, and planning required to select the best operational mode and observatory design;

3.   Indicate areas of technology where state-of-the-art advances are necessary.

The study constraints and scope of the work were defined as follows:

1.   The telescope aperture is to be 304. 8 cm (120 in.), and diffraction-limited performance for the basic optics at the midpoint of the visible light spectrum is required.

2.   The telescope is to be launched unmanned on the Saturn IB and is to rendezvous and operate in conjunction with the NASA MORL space station as defined by the Douglas MORL studies.   A circular orbit of 463 km (250 n. mi.) and 28. 7° inclination is used.

3.   The scientific studies defined by Dr. Fredrick, with certain noted exceptions, are to form a basis for the scientific objectives of the MOT.

4.   Three basic modes of operation of the telescope that were considered are: telescope docked and permanently coupled to the MORL; telescope coupled to the MORL for experiment setup but decoupled for operation; and telescope and laboratory completely decoupled.

5.   Special attention is to be given to selecting the best mode of operation, the role of man, structural configuration, attitude control and stabilization, and the thermal/optical problem.

6.   Indication is to be made of the areas where state-of-the-art advancement may be necessary.

7.   Sufficient design and operational analysis is to be accomplished to select the best mode of operation and to verify the design feasibility of the observatory.

The approach taken in establishing the basic optics of the telescope was to develop in some detail the requirements for the astronomical observations shown in Figure 1. This involved defining the equipment requirements, the form of the data, the duration of the exposure, the effective focal ratio, etc., for each of the observations. With these requirements defined, it was possible to specify the primary optics, their quality, and instrumentation for each type observation. Operational and performance criteria were established, and total system performance was analyzed. This process was iterated several times in the course of the study to match up the performance of the basic optics with that of the instrumentation, insofar as possible. As a result of these iterations, the Cassegrainian-type optical configuration of Figure 2 was recommended. This consists of a 304. 8-cm (120-in.) primary mirror with two alternate secondary mirrors and two flat folding mirrors. The two secondary mirrors permit the telescope to be used at two equivalent focal ratios, ef/15 and ef/30.

There are a number of modifications that can be made to this system to correct for coma and astigmatism. During the course of the study, the Wynne-Cassegrain, the Ritchey-Chretien, the Dall-Kirkham, and the Herzberger-Hoadley designs were examined. The modification selected for the MOT was the Ritchey-Chretien design.

Various modes of operation were studied during the program to select the best mode of operation for the observatory. The approach used in examining the modes of operation and the associated design problems was to generate a-baseline configuration that included all the optical and experiment subsystems and the structural support. Modifications were then incorporated as required to satisfy the varying functions associated with the modes of operation being considered.

Figure 3 shows the final baseline design developed during the study.

The telescope has a double shell construction with 2. 54 cm (1 in.) of vacuum thermal insulation on the outside of the inner shell. The inner shell is the main structure that supports all the elements of the optical systems. The complete inner shell, mirrors, mirror supports, and scientific instrumentation mounting platen are attached to the cabin as an integral unit by a six-bar determinant truss. With this structural design, the telescope optical system is decoupled from the outer shell and the cabin to minimize thermally and mechanically induced distortions. A flexible bellows is shown between the platen tubular support and the cabin bulkhead. This permits the cabin bulkhead to be deflected without producing strains on the optical system structure.

The primary mirror is mounted on a three-point tangent bar support, designed to minimize heat shorts and structural distortions. During boost, the mirror is structurally decoupled from the tangent bars and floated on pneumatic bladders to preserve the mirror figure. Doors on the front side of the mirror protect the optical surface and provide structural support for the pneumatic bladders. Star trackers are mounted directly to the primary mirror support structure to minimize bore-sighting problems.

The secondary mirrors are mounted in a control cell that is capable of automatic adjustment in five degrees of freedom to maintain proper alignment and focus. The figure also shows a mechanism for removing and stowing the f/15 secondary mirror.

An earth shade is shown in the retracted position. This shade, in the extended position, reduces the thermal gradients on the secondary mirrors and the telescope doors. Reduction of thermal gradients on the doors makes thermal control of the primary mirror feasible.

The baseline design was integrated into the final recommended mode of operation shown in Figure 4. In the final selection of the mode of operation some nine variants of the basic three modes of operation were examined and evaluated against technical risk, operational capability, and operational constraints on the MORL.

The observatory is shown in the orbital configuration, attached to the end of the MORL opposite to that used for docking and storing the logistic vehicles. The MOT is docked to the MORL in essentially the same manner as an Apollo logistic vehicle, except the MOT is unmanned and must be remotely controlled by the MORL crew. The design concept utilizes a structural attachment consisting of an open frame type support, manually attached to the MORL, and a soft spring-type suspension of the pitch and yaw gimbal axes of the telescope. The very soft gimbal suspension transmits the small, almost steady-state forces associated with station keeping while attenuating the high level, high frequency forces associated with MORL internal disturbances. The soft gimbal suspension is rigidized for operations that require man to enter the telescope cabin or during the time the MORL-MOT combination is slewed to acquire a new target but would be released for telescope observations.

The illustration shows a man in a spacesuit making the attachment of the MOT to the MORL. Special attention was given in the operational analysis of the various modes of operation to identify the various tasks that man would perform in conjunction with the telescope operation. These analyses indicated that

4

the presence of man would be essential, especially in the areas of setup, checkout and alignment, retrieval of photographic plates, and for unscheduled maintenance.

There were several technological areas that were common to all modes of operation and that received special attention from the standpoint of feasibility. Two of these areas, namely, attitude control and the control of the mirror figure, will be discussed in this paper.

The basic requirement of the MOT attitude control system is to provide a stable platform that can be oriented precisely to any point of the celestial sphere. The top row of Figure 5 indicates the absolute pointing accuracy required for the listed experiments. This pointing accuracy is defined as the average precision of the optical axis with respect to the experiment star. The value of 0.01 arc second for high dispersion stellar spectroscopy is set by the entrance slit of the instrument. Because the star positions are not known to this accuracy, this can only be accomplished by guiding on the experiment star itself. The fine pointing sensor uses some of the experiment light for generating the control error signal, but this still minimizes the experiment time when the loss of light due to off-axis guidance inaccuracies are considered. The remainder of the absolute pointing requirements can be met with off-axis pointing. In off-axis pointing, a star, angularly separated from the experiment star, is selected as the guide star and the fine pointing sensor offset from the optical axis the proper off-axis angle such that when the sensor locks on the guide star, the experiment is on-axis. Off-axis pointing can achieve an absolute accuracy of 0.2 arc second. The required value of 0.05 arc second for planetary spectroscopy requires assistance from the crew in recognizing and acquiring the area of the planet to be observed.

The next row, pointing stability, is the pointing deviation allowed once the observation has been started. The most severe requirement is the 0.01 second of arc for stellar photography to minimize image smear.

Time duration for pointing during observation varies from less than 1 orbit to 10 orbits. This requires the capability of reacquiring the experiment star each orbit during the observation.

Guide stars vary from the brightest available down to a star of +13 visual magnitude. For those experiments using off-axis pointing, the capability to track stars this dim allows complete coverage of the sky with reasonable offset angles, approximately 10 arc minutes.

5

General Electric, the subcontractor to Boeing for the attitude control subsystem, proposed the following control system concept for the telescope.

From booster separation to MORL rendezvous, the MOT attitude is automatically controlled by a gyro reference system and reaction jets. After rendezvous and upon activation of the telescope, a stellar reference is established utilizing a sun sensor and star trackers for initial acquisition and coarse pointing. During the initial phases of these operations, control torques are furnished by a reaction jet system; during later phases by control moment gyros. Accuracy in the coarse pointing mode is limited to 3 arc minutes. Error sensing is then switched to an intermediate star tracker system. The intermediate pitch and yaw star tracker is bore sighted to the MOT line of sight, and the roll axis intermediate tracker is mounted perpendicular to the line of sight. The accuracy expected in all axes is approximately 4 arc seconds. This accuracy is sufficient for the roll axis but does not approach that required for pitch and yaw axes. Control is then switched to the pitch and yaw fine pointing mode. A null type photomultiplier sensor or an image orthicon tube or a combination of both provides the error signal for the fine pointing mode. During occultation of the guide star, the control reference is switched to the three-axis gyro reference system which is updated during the observation period. During the coarse, intermediate, and fine pointing modes, control torques are furnished by single degree of freedom, twin rotor, control moment gyros, one for each axis. A dual level reaction jet system is provided in order to desaturate the control moment gyros as well as perform the initial stabilization and orbit maneuvering.

A detailed study was made to evaluate the single axis performance of the fine pointing loop by means of an analog simulation that included the effects of sensor noise, control moment gyro gimbal friction, disturbance torques, and structural bending. The major source of error was found to be the gimbal friction in the control moment gyro, which causes an oscillation in the system. This oscillation, however, takes place within required accuracy range of 0.01 second of arc. The amplitude of this oscillation can be reduced by a slight amount of noise from the sensor or external disturbances. Both tend to reduce the effective control moment gyro threshold by inducing continuous gimbal motion. This effect is illustrated in Figure 6 for sensor noise. If the noise is below approximately 0.01 arc second the effect is beneficial; beyond this point the error increases.

The most important thermal/optical problem in the MOT program involved the thermal distortions of the primary mirror. An ultimate goal of $\lambda/53$ rms surface deviation at 5000 Å and a minimum acceptable level of $\lambda/30$ at 5000 Å for diffraction-limited performance were set for the figure of the primary mirror. The bulk of the thermal investigation centered around the problem of achieving these goals.

6

The first step in this task involved the evaluation of the thermal gradients in the beryllium primary mirror. This involved an orbital thermal analysis of the temperature distributions in the entire telescope. The two cases shown in Figure 7 were analyzed. The first was a case where the telescope axis is perpendicular to the solar vector and views deep space continuously, and the second was a case where the telescope intermittently views the earth and deep space. In addition, a transient case where the telescope swings from the intermittent to the continuous viewing case was analyzed. These cases were selected as representing the most critical cases for the thermal distortions of the primary mirror.

The thermal model was complex and involved some 88 nodes and 385 radiant heat transfer paths. The thermal balance of the telescope was solved using the Boeing Thermal Analyzer (BETA) digital computer program with inputs from subprograms that defined the radiant heat loads based on orbital parameters and internal radiant view factors between elements of the telescope structure.

The results of the analysis indicated that the most favorable case from the standpoint of thermal gradients in the primary mirror was the "continuous" viewing case with circumferential gradients of about 0.004° F and axial gradients of 0.008° F occurring. Further analysis indicated that the intermittent viewing case and the transient case could be improved as far as gradients are concerned to a condition as favorable as the continuous viewing case by closing the front telescope doors when viewing the earth. However, it was necessary to maintain the doors at uniform temperature when they were open, which led to the concept of an earth shade that extended beyond the doors. The earth shade contributed an additional benefit in that it will maintain the secondary mirror cell in a uniform temperature field.

The mirror distortions caused by the thermal gradients discussed above were computed through the use of the Boeing COSMOS program. This employs a "stiffness method" analysis that is capable of computing thermal distortions in complex structures.

The carpet plot shown in Figure 8 shows the results of this investigation. The surface deflections are plotted as a function of circumferential and radial location on the mirror. For this investigation the mirror was assumed to have a parabolic shape.

To evaluate the consequences of these distortions in terms of optical performance, a least-squares paraboloid was fitted to the data and the rms deviation evaluated. Although the axial deflections are rather large [20.32 x 10^{-6} to 25.4 x 10^{-6} cm (8 x 10^{-6} to 10 x 10^{-6} in.)] they do not present a significant problem because they arise from dish bending of the mirror, which tends to distort it into a new shape that is very nearly parabolic. The circumferential distortions are more serious since they force entire angular zones of the mirror out of contour. When the least-squares fit was made, it was found that the new paraboloid represented an increase in focal length of 0.0240284 cm (0.00946 in.), which poses no problem since continuous monitoring and adjustment of focus is provided in the basic telescope design. The resulting rms deviation from the new paraboloid is 1.37668 x 10^{-6} cm (0.542 x 10^{-6} in.), which represents a mirror quality of $\lambda/36.3$ at 5000 Å. This indicated that the mirror quality could be controlled within the diffraction limits by a semi-active system involving the use of the telescope doors.

There still remain questions involving the mirror manufacture, the isentropy of its characteristics, and its long term stability, which require investigation beyond the bounds of the contract.

A third technological investigation, which is not reported in detail in this paper, indicated that special precautions must be taken to protect the more sensitive types of films used in the MOT from the effects of geomagnetically trapped radiation.

In summary, the conclusions of the study indicated that the MOT is a feasible system in the time period contemplated, which is the early 1980s. The soft gimbal operational concept is preferred, and the following problem areas require further investigation: manufacture of primary mirror and the investigation of its long term stability, attitude stability and control, and radiation protection of the more sensitive films.

The following actions were recommended: An investigation into the problems associated with the design and fabrication of a large primary mirror; bread board fabrication of the fine pointing sensors and the control moment gyros; a study of the MOT in synchronous orbit; a more thorough investigation and definition of the soft gimbal concept; and the institution of an intermediate sized telescope program to check out the feasibility of the technological solutions and to establish the role of man.

BIBLIOGRAPHY

1. Fredrick, L. W., ed.: Final Report for Applications in Astronomy Suitable for Study by Means of Manned Orbiting Observatories and Related Instrumentation and Operational Requirements. vol. I and II, supported by NASA Grant NsG-480.

2. Final Report, Feasibility Study of a 120-Inch Orbiting Astronomical Telescope. American Optical Co., Fecker Div., AE-1148, prep. under NASA-Langley Contract NAS 1-1305-18.

3. Final Report, Systems Study of a Manned Orbital Telescope. The Boeing Co., D2-84042-1, prep. under NASA-Langley Contract NAS 1-3968.

COMPARISON OBSERVATION	GROUND BASED TELESCOPES	MOT
HIGH DISPERSION SPECTRA VISIBLE & UV	VISIBLE SPECTRUM RANGE	LIMITED BY CUMULATIVE EXPOSURE TIME
LOW DISPERSION SPECTRA	VISIBLE SPECTRUM RANGE	LIMITED BY CUMULATIVE EXPOSURE TIME
PHOTOELECTRIC PHOTOMETRY	VISIBLE SPECTRUM RANGE	• GREATER RESOLUTION • FAINTER SOURCES
PHOTOGRAPHIC ASTROMETRIC & ASTROPHYSICAL	LIMITED BY SEEING CONDITIONS (1 ARC SEC) AND ABSORPTION OF IR & UV	• ASTROMETRIC - 0.06 ARC SEC RESOLUTION • COMPLETE SPECTRUM
HIGH DISPERSION IR SPECTRA	ONLY THROUGH NARROW WINDOWS (8 - 13 μ)	LIMITED ONLY BY EXPOSURE TIME
THERMOELECTRIC MEASUREMENTS	ONLY THROUGH NARROW WINDOWS (8 - 13 μ)	LIMITED ONLY BY SOURCE INTENSITY
PHOTOGRAPHIC (PLANETARY)	LIMITED BY SEEING CONDITIONS (1 ARC SEC OR SLIGHTLY BETTER)	0.06 ARC SEC RESOLUTION

FIGURE 1. SCIENTIFIC CAPABILITY COMPARISONS

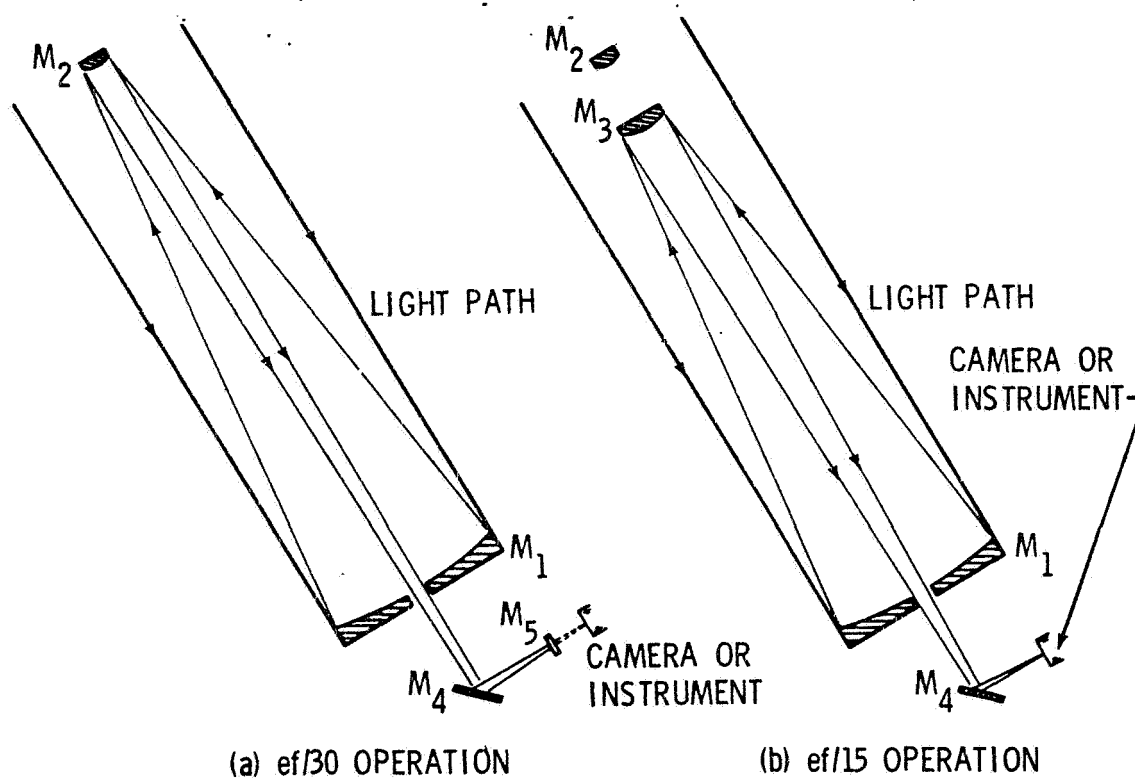(a) ef/30 OPERATION   (b) ef/15 OPERATION

FIGURE 2. OPTICAL SCHEMATIC

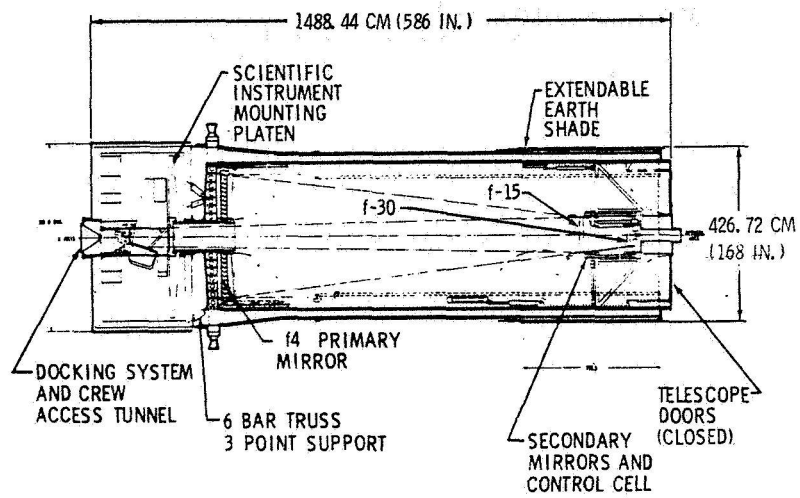FIGURE 3. BASELINE CONFIGURATION, 304.8-CM (120-IN.) MANNED
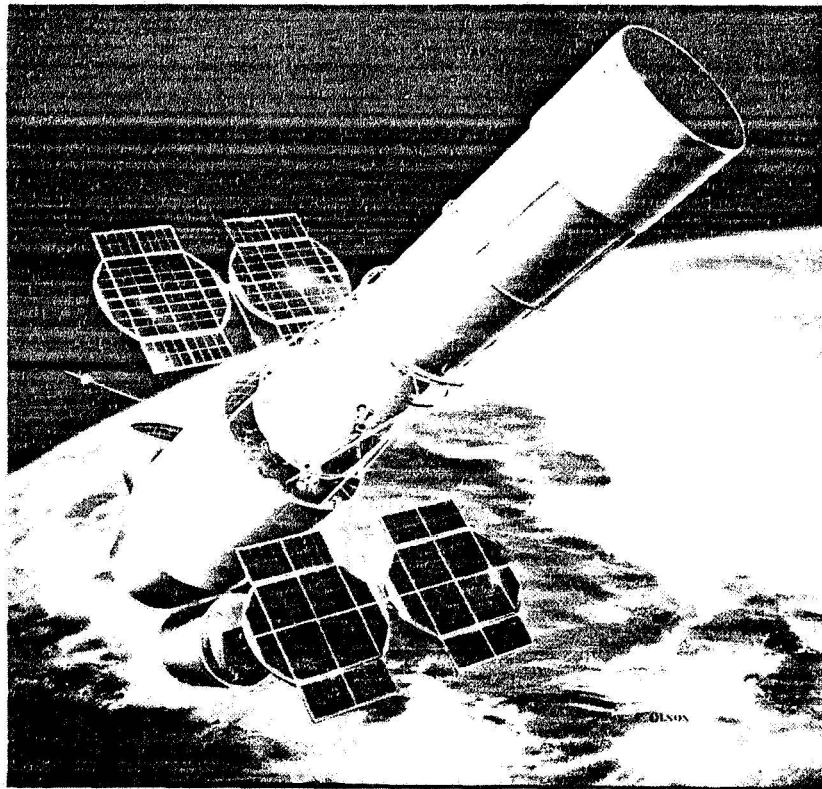ORBITAL TELESCOPE

FIGURE 4. SELECTED OPERATIONAL CONCEPT, MANNED
ORBITAL TELESCOPE

|	HIGH DISPERSION STELLAR SPECTROSCOPY	LOW DISPERSION STELLAR SPECTROSCOPY	PHOTOTOMETRY	STELLAR PHOTOGRAPHY	PLANETARY PHOTOGRAPHY	PLANETARY SPECTROSCOPY
POINTING ACCURACY	± .01 SEC	± .2 SEC	± .2 SEC	± 10 SEC	± 10 SEC	± .05 SEC
POINTING* STABILITY	± .03 SEC	± 0.3 SEC	± 0.3 SEC	± .01 SEC	± .01 SEC	± .05 SEC
MAXIMUM TIME DURATION	TO 10 ORBITS	TO 10 ORBITS	TO 10 ORBITS	TO 10 ORBITS	ONE ORBIT	ONE ORBIT
GUIDE STAR MAGNITUDE	+ 10	+ 13	+ 13	+ 11	+ 11	+ 12

* 95% OF TIME

FIGURE 5. OBSERVATIONAL REQUIREMENTS
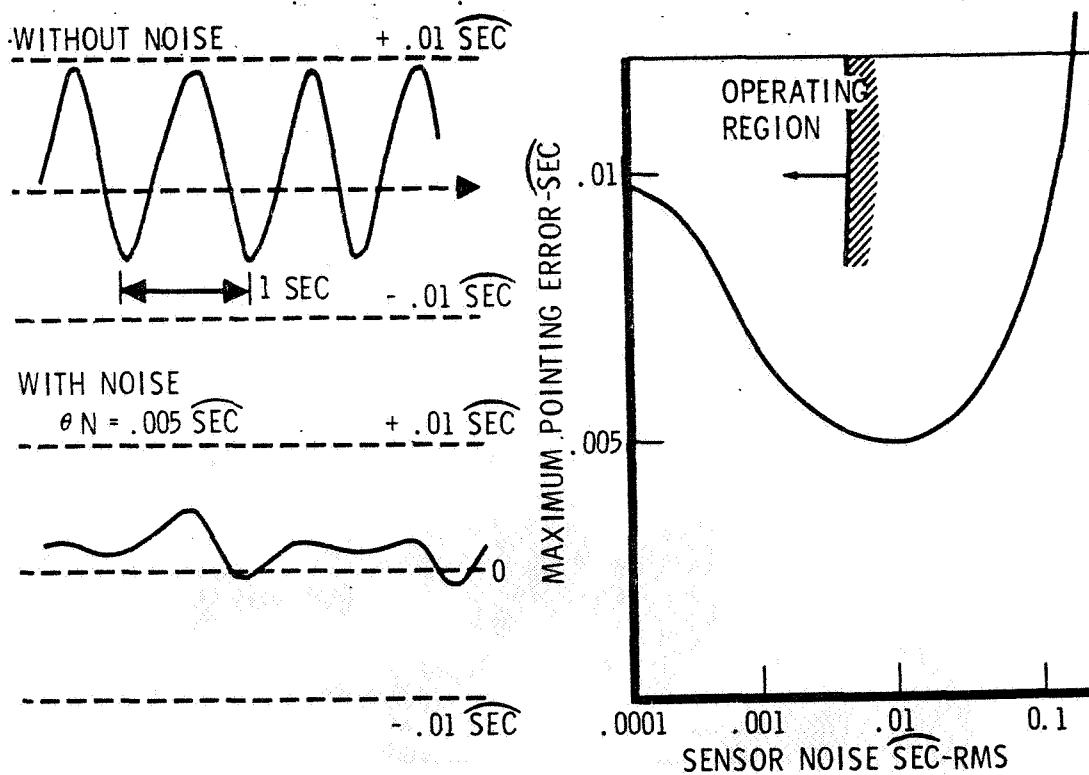
FIGURE 6. SENSOR NOISE
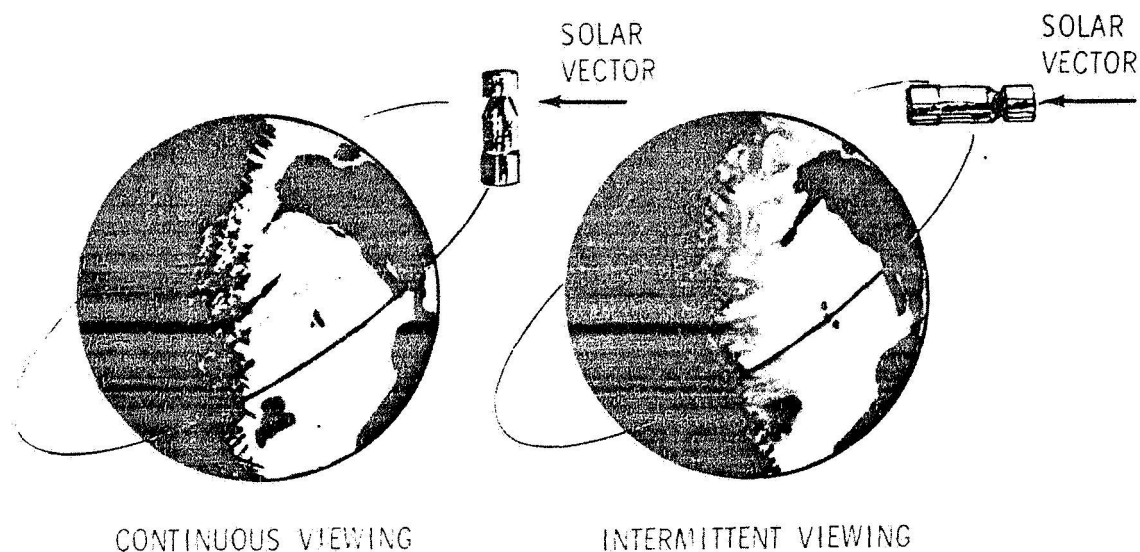
FIGURE 7. THERMAL ANALYSIS ORBIT DEFINITION; 463-KM (250-N. MI.)
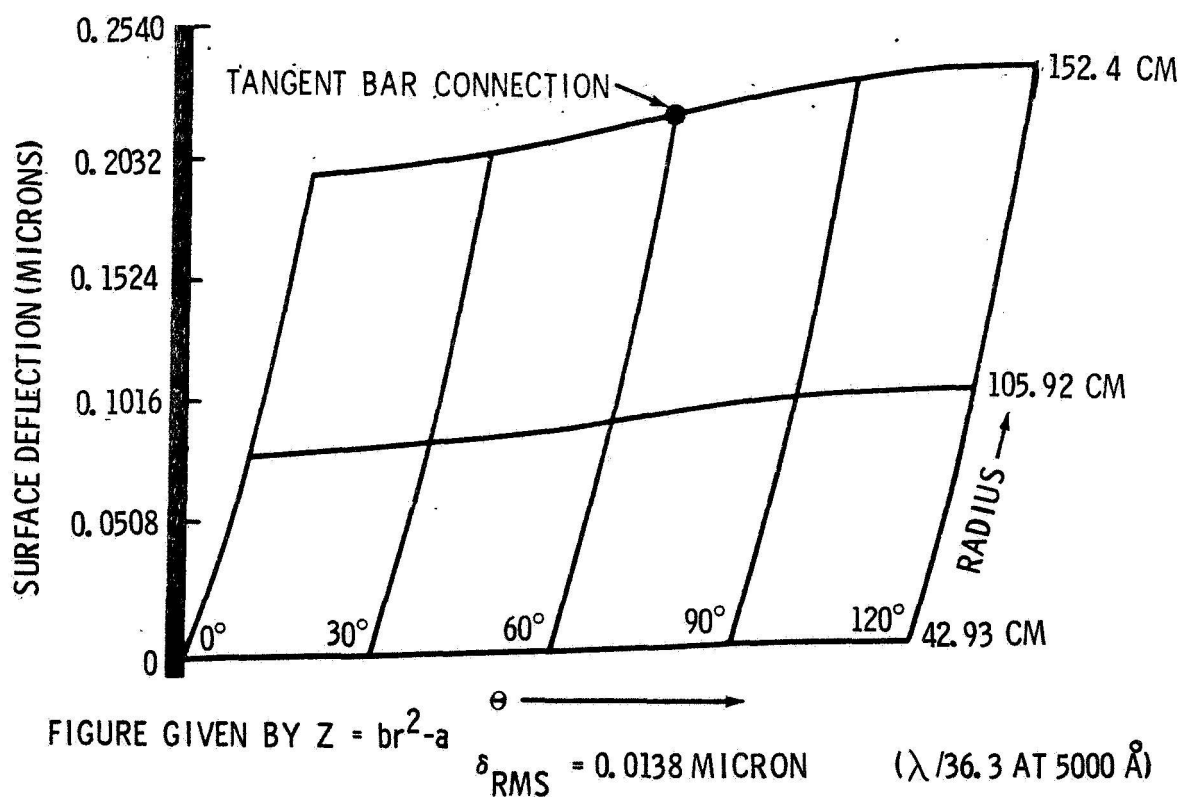CIRCULAR ORBIT, 28.7° ORBITAL INCLINATION

FIGURE GIVEN BY $Z = br^2 - a$

δ_{RMS} = 0.0138 MICRON   (λ/36.3 AT 5000 Å)

FIGURE 8. PRIMARY MIRROR THERMAL DEFLECTIONS,
CONTINUOUS VIEWING CONDITION

NASA-AMES LASER FIELD PROGRAMS*

R. Condon
D. Erway
G. White
Electro-Optical Systems, Inc.

The paper discusses current laser propagation and laser communication efforts supported by the NASA Ames Research Center. The laser propagation experiments will involve transmission and attenuation measurements on laser beams from a ground tracking station to corner reflectors on the Explorer 22 satellite. The laser communication experiments will involve acquisition and tracking of a ground station 5145-$\overset{\circ}{A}$ argon laser beacon by Gemini 7 astronauts, with ground reception of laser communication from the spacecraft.

Recognizing the need to obtain more experimental data on the propagation of laser radiation through the total earth atmosphere, the NASA Ames Research Center selected Electro-Optical Systems to conduct field experiments in laser propagation. The Explorer 22 satellite will be used as an orbiting reflector of laser signals from the earth. The tracking pedestals, laser transmitter, and optical receiver will also be used as a ground station on the Gemini 7 optical communication experiment. These efforts are closely integrated since so much equipment is common to both.

The prime objective of the laser propagation research effort is to study the transmission characteristics of the total atmosphere from earth to space and return. An additional objective is to perform optical experiments relating to navigation and tracking. The experiments to be performed are shown in Tables I and II. These experiments will give information on aerosol back-scatter versus altitude, aerosol particle size, water-vapor distribution, corner reflector array scintillations, and laser-aided acquisition and tracking of satellites.

Because the equipment for the Laser Propagation Research Studies could economically be modified to serve as a ground station for the Gemini 7 (MSC-4) Optical Communications Experiment, and because additional propagation experiments seem possible using signals from the spacecraft transmitter, scope of Laser Propagation Research Studies was expanded to include this additional

---

effort. The principal experiments to be conducted on Gemini 7 are the basic demonstration of voice communication from a hand-held laser transmitter to a ground station and the measurement of audio frequency fluctuations in signal strength caused by atmospheric effects and pointing errors.

The accomplishment of these objectives by the NASA Ames Research Center program will have demonstrated the utility of the Explorer 22 satellite as an atmospheric research aid, will have aided the demonstration of the first laser space communication, and will have utilized the first field operation of the visible argon gas laser. Thus, in addition to direct experimental results, important advances in technology applicable to communications, tracking, guidance, and control will have occurred.

The Explorer 22 and 27 satellites were placed in orbit primarily to determine the overall profile of the earth's atmosphere. These satellites are, however, equipped with an array of quartz cube corners as retro-reflectors for propagation and tracking experiments using laser beams from earth.

The Explorer 22 is in a near-polar orbit with an inclination to the equator of 79.7°. The satellite has an apogee of 1100 km and a perigee of 939 km and is magnetically stabilized so that the corner reflectors point toward the earth when the satellite is in the northern hemisphere.

The Explorer 22 is in a high orbit, nearly circular, with relatively constant orbital parameters. The Explorer 22 satellite, equipped with a 136-MHz Minitrack beacon, is continually tracked by the NASA-Goddard Minitrack Network. The orbital track is determined by the NASA-Goddard computer. Predicted look angles for any point on earth at any time are readily available to an accuracy of several milliradians.

Because the Explorer 22 satellite is in a polar orbit, the geographic locale of a tracking site is relatively unimportant. The constancy and long life of the orbit permit reasonably accurate prediction of look angles. Thus, satellite tracking is possible independent of range facilities if the site coordinates and time are well known.

The basic ground station consists of two modified Nike-Ajax pedestals with control van. Since no major range facilities are needed, the site will be near Moffett Field, California. Some thirty sites in the mountains to the east and west of San Francisco Bay were evaluated by criteria of cloud cover, atmospheric turbulence, accessibility, logistics, sky illuminance, and available facilities. Several adequate sites were selected from this list. Since none of

16

these are currently government facilities, site acquisition may be an important factor. Final site arrangements await completion of the Gemini 7 program.

Look angles versus time are available from NASA-Goddard for about one week in the future. These data are accurate within several milliradians. Azimuth, elevation, and range in microseconds are encoded on the tape at one-second intervals.

In the field acquisition aid, a tape reader transfers the azimuth, elevation, range, and time data from serial to parallel form. Binary coded decimal format (BCD) is transferred to pure binary format. A digital clock advances digital angle data once per second. To drive the Nike system with these data, digital angle information is converted to synchro form by a solid-state control transformer together with 400-Hz synchro pedestal positional signals. The output of the solid-state control transformer is a 400-Hz error signal proportional to the difference in the digital angle command and the Nike pedestal angle. Range predictions may be processed by the system to generate a delayed range gate for laser ranging operations. The digital clock is driven by a precise time base generator synchronized to WWV. Figure 1 shows details of the acquisition aid system.

It is not plausible to provide tape data more often than once per second. During one second, the satellite travels approximately 3 mrad. The receiver and transmitter beamwidths are thus required to be 3 mrad or greater. If more accurate tracking is desired, to the approximate limit of the Nike system (≈ 0.1 mrad), improved means of pedestal pointing are required.

During twilight, when the satellite is illuminated by the sun against a dark sky background, the Explorer 22 has the brightness of a 6th to 8th magnitude star. An automatic optical tracker may lock on this reflected solar energy from the satellite and provide pointing error signals to drive the Nike system. For sufficient sensitivity to track a 9th magnitude star, the optical tracker has a small instantaneous field of view (≈ 1.2 mrad). With this small field, the tracker must be initially oriented in the vicinity of the satellite by the acquisition aid. The tracker scans its instantaneous field of view over the 3-mrad uncertainty of the acquisition aid 400 times a second. When the tracker senses the satellite and generates error signals, the tracking system operator can transfer control of the Nike system from the acquisition aid to the optical tracker.

The optical tracker utilizes an ITT-FW130 deflectable photomultiplier detector boresighted with the 40.64-cm (16-in.)-dia optical receiver. A beam splitter sends 6943-Å laser radiation to the laser detector while permitting

17

shorter wavelengths to reach the optical tracker detector. The tracking resolution of the electrically scanned optical tracker is better than one percent of the instantaneous field of view or < 0.01 mrad. Thus, tracking accuracy will be limited by the Nike pedestals to approximately 0.1 to 0.2 mrad. Both satellite acquisition and tracking are automated functions requiring no operator at the Nike pedestal. All tracking functions are controlled from the control van. Figure 2 shows details of the optical tracker.

Explorer 22 atmospheric experiments will define atmospheric effects on laser propagation and will probe atmospheric composition. Explorer 22 tracking experiments will involve satellite ranging, laser-aided acquisition, and laser-aided tracking.

With the Ionized Argon Laser on one Nike pedestal and a laser receiver on the other, precise aerosol backscatter as a function of altitude will be determined by parallax; that is, by "walking up" the argon laser beam with the laser receiver. From a knowledge of the angle scattering function of aerosols, the concentration with altitude can be determined. Reflection from the satellite plus a knowledge of the satellite range and reflection characteristic allow total atmosphere attenuation of 0.4880μ to be determined.

With a Q-switched ruby laser and KDP generation of second harmonic, aerosol size distribution will be indicated by observing backscatter from the laser beam as a function wavelength. Reflection from the satellite will characterize total atmospheric transmission at 6943 Å and 3472 Å.

A sophisticated experiment involves the determination of absolute humidity versus altitude techniques. The beam from a nitrogen temperature Q-switched ruby laser is directed into a Raman cell containing $C^{12}S_2^{32}$ and $C^{12}S_2^{34}$, isotopes of carbon disulfide. Raman shifted outputs from the cell lie at 7256.3 Å and 7241.8 Å. One Raman line is in a water vapor absorption line and the second outside of the line. The selective extinction by the water vapor line as determined by aerosol scattered return signals will characterize the altitude distribution of water vapor. Selective extinction in returns from the satellite indicates total water vapor content in the atmosphere.

The variations of cw laser reflection from the Explorer 22 satellite will depend upon the interference pattern due to the corner cube array, upon velocity aberration effects, and upon atmospheric turbulence. Clearly, to evaluate this fluctuating intensity function is complex, but use of a cw laser plus geometrical separation of transmitter and receiver offer potential for unraveling these effects.

18

Laser-aided acquisition will utilize the same scanning of a 1.2-mrad field-of-view optical tracker over the 3-mrad tape coordinate uncertainty as sunlit twilit acquisition utilizes. However, the argon laser will be radiating a 3-mrad beam into the uncertainty interval, so sunlight is not required. Narrowing the laser beam after acquisition would permit more accurate error signals. Success of this method will allow experimental use of nontwilight Explorer 22 passes.

Laser-aided tracking will direct the argon laser beam at a sunlit satellite already being followed by the optical tracker. Increased received signal strength should result. The optical receiver will then be filtered to pass only argon laser radiation. Success of this method should permit tighter error signals and tighter tracking.

Experiments with pulsed laser satellite ranging will also be attempted. It is not expected that ranging results will be significantly different from those already obtained by other groups.

The Explorer 22 program provides the basic equipment for both the atmospheric and Gemini 7 experiments; namely, the dual pedestal Nike system with independent and slaved pedestal capability, the 40.64-cm (16-in.) optical receivers (Fig. 3) with provisions for various filters and detectors, and the argon laser. Equipment used for the Explorer 22 work alone includes the punched tape acquisition system and the automatic optical tracker.

The additional piece of equipment required for atmospheric and navigational experiments is the pulsed laser system. Figure 4 shows details of the laser head design that provides for 1.524 by 15.24-cm (0.6 by 6-in.) ruby or neodymium glass laser rods in a closed coupled cavity. The laser rod temperature may be controlled over the range from 273° K to 357° K to an accuracy of ± 1°. The laser will have a capability of more than 1 joule per Q-switched pulse at 10 pulses per minute.

The laser power supply and closed cycle cooling system will be located adjacent to the Nike pedestal with the laser remotely controlled from the tracking station. The Q-spoiled laser is collimated by a 30.48-cm (12-in.) Newtonian reflector, with beam divergency adjustable over the range of 0.5 to 10 mrad. Provisions have been made for a continuous pulse output sampling by means of a high-speed photodiode. Between the laser head and the collimating telescope, provision is made for either a Raman cell or a frequency doubling KDP crystal.

A system used only with the pulsed laser is the satellite ranging system, shown in Figure 5. As indicated, a high-speed photodiode pulse activates a

10-nsec range counter and is also displayed on a dual beam oscilloscope. A range prediction derived from the pulsed tape acquisition aid system is presented as delayed sweep trigger for the second scope trace, the delay being the range prediction minus an adjustment based on confidence in the prediction. When the scope is triggered, it sweeps typically at a rate of 10 nsec/cm. This displays the interval of time expected for the return pulse in high linear resolution. When the pulse is received, it displaces the time base and is recorded by a scope camera. The pulse also stops the range counter at the measured range value.

Following the Gemini 7 mission, the modified Nike system will be retrofitted with the pulsed laser, the optical tracker, and the acquisition aid. The equipment will be established at a site near Ames Research Center at Moffett Field, California. Explorer 22 tracking and atmospheric propagation experiments will commence at that time. The experimental program is flexible, and modifications to the plans of this paper are possible as the field program proceeds.

The Gemini 7 Optical Communications Program is significantly influenced by the Gemini spacecraft orbital characteristics. The Manned Spaceflight ground stations have the long range acquisition and tracking capability necessary for narrow beamwidth optical communications. It follows that stations of the Manned Spaceflight Network are the most desirable sites for conducting this experiment. The best orbital coverage readily available is thus from the Manned Spaceflight Network station in Hawaii (22° N). The crux of the NASA-Ames Research Center efforts on Gemini 7 Optical Communications is thus the adaptation of the Explorer 22 equipment for such use, and its installation at Kauai Island, Hawaii.

Stations of the Manned Spaceflight Network are logical choices as sites for the Laser Communication experiment. The optical ground station operated by MSC is located at White Sands, New Mexico. After evaluating a number of site selection criteria, the optical ground station operated by ARC was located on Kauai, Hawaii, consideration having been given to Guaymas, Mexico; Carnarvon, Australia; and Western Test Range, California. The criteria used in the selection were cloud cover, atmospheric turbulence, latitude, viewing angles, accessibility, acquisition aids, logistics, sky illumination, and available facilities.

Minimum probability of cloud cover is obviously important. Meteorological data from all sites were examined for the year preceding the mission schedule. One must note that data collected from weather stations several miles distant from the proposed site may have no relation to the weather at the site. For instance, the proposed site at Western Test Range lay directly on the coast and was subject to periodic heavy coastal fog, while the inland weather station at

20

WTR would report clear skies. The reverse situation was true of Kauai, Hawaii, where the weather on the northeast coast is intensely rainy, while the southwestern coast at the tracking station is much drier.

Atmospheric turbulence causes fluctuations and beam direction changes that can degrade optical communications to and from space. Atmospheric turbulence effects decrease with altitude. Thus, a high-altitude Manned Spaceflight Network station becomes a desirable site. Hawaii [1154 m (3787 ft)] and White Sands [1234 m (4048 ft)] are the highest Manned Spaceflight Network stations in this hemisphere.

The latitude of the optical ground station determines the number and angular altitude of satellite passes. The number of passes with angular altitude above 40° for the various sites studied were:

Carnarvon, Australia	19
Hawaii	15
Western Test Range	11

for originally planned 72° Gemini 7 launch. Current plans for zero-orbital inclination favor a mid-latitude site such as Hawaii over sites at extreme latitudes such as Carnarvon and Western Test Range, California.

All Manned Spaceflight Network stations have suitable viewing angles with no major local obstructions. Accessibility of all these stations is guaranteed to be adequate. All stations have acquisition aids. However, the stations do not all have the FPS-16 radars necessary for optimum tracking of the spacecraft and pointing of the laser beam. Hawaii, Western Test Range, and White Sands have such radars, but Carnarvon and Guaymas do not.

Logistics was the final major difference between network stations, with sky illuminance and available support facilities adequate at all stations. Essentially, the final decision became that the FPS-16 radar availability at low latitude in Hawaii overcame the moderate to poor logistics situation.

Location of the Laser Communication ground station at a major spacecraft tracking station permits full use to be made of the acquisition and tracking capabilities of the station. As the spacecraft comes over the local horizon, TELTRACK or AGAVE telemetry tracking antennas acquire the spacecraft 225-to-260-MHz telemetry transmission. These antennas are pre-positioned by

computer from NASA-Goddard. Once acquisition has been accomplished, the C-band FPS-16 antennas are slaved to the telemetry tracking antennas and acquire the spacecraft, aided by the on-board C-band radar beacon transponder. The FPS-16 tracks the spacecraft from a few degrees above the horizon with an accuracy of tenths of a milliradian.

The laser communication receiving equipment, which is mounted on modified Nike-Ajax tracking pedestals, is slaved to the FPS-16 with an overall tracking accuracy of 0.2 to 0.4 mrad. Slaving to the FPS-16 is accomplished by taking 1 and 16-speed synchro position information from the FPS-16 and comparing it with synchro position data from the Nike-Ajax system. An error signal proportional to the difference between the angles of the two systems is generated and fed to the Nike pedestals, which then null the pointing error.

Figure 6 is a block diagram of the FPS-16 slaving system. FPS-16 servos operate at 60 Hz while those of the Nike system are 400 Hz. This has necessitated installation of 60-Hz synchros in the Nike-to-FPS-16 slaving loop.

The basic communication experiment involves the experimental transmission of voice intelligence by a hand-held pulsed FM gallium arsenide laser transmitter from the Gemini spacecraft to the ground receiving station. The factors to be evaluated will be the characteristics of the pulse following propagation through the atmosphere, the received signal strength versus time, amplitude fluctuations due to pointing errors or atmospheric effects, and the quality of the demodulated audio voice intelligence.

For this experiment, two optical receivers are being utilized, partially for backup security, and partly for monitoring the magnitude of astronaut pointing errors. Acquisition and recording are illustrated in Figure 7.

As indicated, two channels of received information are being displayed on a dual beam oscilloscope equipped with a high-speed motion picture camera. Correlation of the received signals, their pulse shape and amplitude, is then possible. Both signal channels are then amplitude and frequency-demodulated. The output of the frequency-demodulated channels is the audio intelligence transmitted by the astronauts. The output of the amplitude-demodulated channels will contain amplitude modulation on the signal due to both pointing errors and atmospheric effects. Spectrum analysis of both the amplitude modulation and audio channels will be possible after the mission. Additional data to be recorded include time, capsule communication, azimuth, elevation, and range information. During experimental orbits, the naval base at Barking Sands will probe the atmosphere to 50 km with weather balloons and from 50 to 200 km with Arcas

22

meteorological rockets. Weather prediction for forthcoming orbits will be available from the weather bureau in Honolulu.

The two tracking pedestals of the Nike system are slaved together, and each is equipped with an optical receiver and signal processing electronics. By placing the receivers some 122 m (400 ft) apart, it will be possible by time correlation of the received intensity from the two receivers to obtain quantitative data on the pointing ability of the astronaut. This experiment is limited by the fact that the maximum separation of the pedestals, 152 cm (500 ft), is of a small fraction of the minimum laser spot size of the earth, $\approx$610 cm ($\approx$2000 ft). It is obvious, however, that nothing may be deduced from a single receiver other than that the astronaut is either on or off the target.

The experimental equipment, shown in Figure 8, consists of the two Nike-Ajax tracking pedestals and the tracking van. Each pedestal is equipped with a 40.64-cm (16-in.) Newtonian telescope of 314.4-cm (60-in.) focal length. A 100-Å bandpass filter centered at 9060 Å is located within a collimating lens system.

The optical beacon used by the astronaut to acquire the receiver site is an argon laser of 3-W cw output power. A commercial model of this laser system, consisting of the laser head, power supply, and closed-cycle liquid cooling system, is shown in Figure 9. An identical laser head will be used on the Gemini program. However, the power supply and cooling unit have been integrated into a mobile field cart that has environmental protection. An optical chopper is provided that interrupts the laser beam at 7 Hz or permits cw operation, depending on whether the injection laser radiation is being received or not.

The ARC Laser Communication equipment is currently in final stages of assembly. This equipment will be air-lifted to the NASA-Kokee Park Tracking Station on Kauai, Hawaii. A site is being prepared along the FPS-16 boresight range. This station will participate in the Gemini 7 pre-flight simulation tests of beacon visibility and of receiver operation with a gallium arsenide laser transmitter. In December, the equipment will be used in support of the Gemini 7 (MSC-4) Optical Communications experiment. Following this mission the equipment will be moved to San Francisco Bay area, where the Explorer 22 program of atmospheric propagation and satellite navigation and tracking experiments will be conducted.

It is anticipated that the results of the MSC-4 experiment to be conducted on Gemini 7 will have a profound effect upon the future of space optical communications. The success of this experiment is bound to stir the imagination

of program planners. Future effects in deep-space optical communication will be able to proceed with enhanced definition and surety.

Demonstration of acquisition and tracking of the ground station by the astronauts will exhibit the ability of manned spacecraft systems to meet critical performance requirements without requiring heavy costly automatic tracking techniques in the space communications transmitter.

Examination of the propagation data obtained during the MSC-4 experiments and also the Explorer 22 experiments may result in the development of new modulation/demodulation techniques to circumvent the degrading effects of the atmosphere on optical communications. The experience gained on the programs will aid materially in the selection and development of suitable sites of site selection for future NASA optical ground stations. Further, space techniques will have been developed to obtain valuable atmospheric data:

aerosol backscatter and attenuation versus range

aerosol size distribution versus range

humidity and total water vapor versus range.

In addition, laser-aided acquisition and tracking of satellites will open the door to future high-resolution radar systems for satellite tracking.

The versatility of the available equipment and techniques allows many new experiments relating to optical technology that extend beyond the present efforts to be conducted. Table III lists some possible experiments of this type that could be economically performed with future Gemini/Apollo spacecraft and with modestly improved ground facilities. Such experiments could be very useful in extending space optical technology, soon and simply, before OTAES and deep-space special spacecraft are available.

The earliest returned signals from a satellite were detected by Dr. H. Plotkin and his associates at NASA-GSFC. The present ARC program profits from the experience and advice of Dr. Plotkin and his associates. It is anticipated that the results will provide the scientific laser community with valuable atmospheric propagation data, largely as a result of this cooperation.

Success on the MSC-4 Optical Communications experiment depends heavily upon the efforts of Mr. W. L. Thompson and his associates, who have planned and implemented the basic communication experiment at NASA-MSC. By adding

some additional studies to this experiment, this program should serve as an effort of significance to future system designs.

Appendix

An argon laser plus field support service were provided to NASA Manned Spacecraft Center by EOS for the Gemini 5 Laser Beacon Experiment in August 1965. This appendix reports the results obtained during these tests, conducted at the White Sands Missile Range. Included are data on the argon laser used and comments on the operational problems encountered.

Scope of Effort. The argon laser was mounted on a platform oriented by a modified Nike-Ajax tracking system. The Nike-Ajax system was, in turn, slaved to an FPS-16 instrumentation radar, capable of both beacon track and skin track of the Gemini spacecraft.*

The major design requirements of the argon gas laser were as follows:

    power output - 1 W

    beamwidth - 1 to 2 mrad

    modulation frequency - 3 to 10 pulses/s   (adjustable).

The laser was capable of being boresighted to the Nike-Ajax platform to an accuracy of the order of 0.3 mrad. The laser beacon included all power supplies, cooling systems, and instrumentation necessary for operation.

Results. The argon laser beacon was fabricated, tested, and installed on the Nike-Ajax platform prior to the GT-5 launch. The laser beacon met or exceeded all operating specifications and was operational throughout the GT-5 experiment.

The astronauts were unable to acquire the beacon on three separate orbits. Several adverse factors contributed to this inability. An understanding of these

---

* The FPS-16 can track the Gemini 5 C-band beacon within ±0.1 mrad. Static tests with the Nike-Ajax system indicated that it could be slaved to the FPS-16 radar to within ±0.3 mrad.

factors can improve the likelihood of success on forthcoming experiments involving an argon laser beacon.

Laser Operational Data. A silicon photovoltaic cell was mounted on the rear of the laser and calibrated so as to indicate the output from the beacon. During the orbits when the experiment was attempted, the laser was operated between 0.9 and 1.1 W. The laser output was chopped at approximately 5 to 6 pulses per second during the experimental operation. The output was approximately a square wave. Signals corresponding to the chopper frequency and the laser output power were fed to a recorder in the NASA van for future reference.

The laser's angular beamwidth was measured by observing the diameter of the illuminated area on the boresight target 442 m (1450 ft) from the laser. The beamwidth was found to be 1.5 mrad. Boresight of the argon laser with the Nike-Ajax platform was accomplished by setting up a target on the face of a building at the FPS-16 boresight tower, taking into account the parallax resulting from the displacement of the boresight telescope from the laser beacon output. Boresight was accomplished to well within 0.3 mrad. The use of "Scotchlite" for the boresight target permitted checks of the boresight in daylight by observing the illuminated target through the boresight telescope..

Attempted Experiments. The only orbits available at White Sands Missile Range were daylight passes, the earliest being about 6:00 am, 1/2 hour after sunrise. On the average, two good passes would occur per day having elevation angles above 40° and slant ranges of about 161 km (100 mi).

The astronauts were instructed to attempt to see the laser on August 27, 1965, orbit 92, and on August 28, 1965, orbits 105 and 197. They did not succeed in acquiring the laser during any of these tries.

A number of factors reduced the astronauts' ability to acquire the laser:

1. The spacecraft attitude control system had malfunctioned and the astronauts were not allowed to stabilize the spacecraft to look down into the vicinity of the laser site.

2. The astronauts were unfamiliar with the terrain and the location of the site and, because of the way in which instructions were given, were probably looking at the White Sands Dry Lake rather than the site, 129 km (80 mi) to the south.

3. The astronauts did not have any nighttime passes in which acquisition of the laser would have been very easy. [The laser looks like a -7 magnitude star to an observer 161 km (100 mi) distant.]

4. The astronauts did not have optical filters, which would have improved the contrast of the laser with respect to the background. [The irradiance of the laser at 161 km (100 mi) is equivalent to that received from the sunlit earth in a 10^{-7} steradian field of view.]

It was found that RFI, generated during operation of the argon laser, was sufficient to interfere with the acquisition mode of the FPS-16 radar. Because the FPS-16 tracked satisfactorily, once acquisition had taken place, an operating procedure was adopted where the laser would remain off until the FPS-16 operator indicated they were properly tracking.

Summary. Perhaps the most important benefits from the effort described above are those things that will contribute to the success of related programs in the future. The understanding of the factors that contributed to the failure of the astronauts to observe the beacon are most important in this respect. Further, the planning of improved procedures for the Gemini 7 mission, plus the design improvements being incorporated in an advanced laser beacon, will help insure a minimum of difficulties in the future.

TABLE I. ATMOSPHERIC EXPERIMENTS

A. EXPERIMENTS TO BE ACCOMPLISHED

EXPERIMENT	LASER	WAVELENGTH	POWER	AEROSOL RANGE BY	PRINCIPAL DATA
cw Backscatter & Attenuation	cw Argon$^+$	4880 Å	1-2 W cw	Parallax	Precise aerosol backscatter, precise attenuation to and from satellite
Pulsed Backscatter & Attenuation	Q-Switched Ruby + Doubler KDP	6943 Å +3472 Å	100 MW +10 MW	Time Delay	Aerosol size distribution, attenuation vs wavelength, satellite range

B. EXPERIMENTS TO BE ATTEMPTED

EXPERIMENT	LASER	WAVELENGTH	POWER	AEROSOL RANGE BY	PRINCIPAL DATA
Humidity Experiment	Raman-Shifted Ruby: $C^{12}S_2^{32}$ $C^{12}S_2^{34}$	7252.3 Å 7241.8 Å	5-10 MW 5-10 MW	Time Delay	Absolute humidity vs altitude, total water vapor in atmosphere

C. ALTERNATIVE EXPERIMENTS

TABLE I. ATMOSPHERIC EXPERIMENTS (Cont'd)

EXPERIMENT	LASER	WAVELENGTH	PURPOSE
cw Backscatter & Attenuation	cw Argon[+]	5145 Å 5682 Å	Alternatives to 4880 Å for precise aerosol backscatter and attenuation measurements
Pulsed Backscatter & Attenuation	Q-Switched Nd:Class + Doubler KDP	$1.06\ \mu$ $0.53\ \mu$	Alternative to ruby + KDP as PLIDAR for aerosol size distribution and attenuation versus wavelength
Atmospheric Constituent Experiment	Ruby or Nd:Glass + Various Raman Shifters	Assorted	Determination of absorption at wavelengths characteristic of CO_2, O_2, and O_3

TABLE II. NAVIGATION AND TRACKING EXPERIMENTS

A. EXPERIMENTS TO BE ACCOMPLISHED

EXPERIMENT	LASER	WAVELENGTH	POWER	PRINCIPAL DATA	METHOD
cw Laser Reflection Experiment	cw Argon+	4880 Å	1-2 W cw	Velocity aberration, lobe pattern from cube corner array, amplitude scintillation vs rf and optical Doppler frequency shift	Calculated curves will be compared with experimental values for differing spacings between transmitter and receiver

B. EXPERIMENTS TO BE ATTEMPTED

EXPERIMENT	LASER	PRINCIPAL DATA	METHOD
Laser Aided Acquisition	cw Argon+	Difficulty of automatic acquisition (probability of acquiring vs system parameters)	Use both manual and programmed pointing; use scan or beam divergence mode; try both visual and automatic star tracker acquisition.
Laser Aided Tracking	cw Argon+	Satellite azimuth and elevation angles vs time; laser pointing error vs time	Measure the platform position vs time; correct with star tracker error signal vs time.

TABLE II. NAVIGATION AND TRACKING EXPERIMENTS (Cont'd)

C. ALTERNATIVE EXPERIMENTS

EXPERIMENT	LASER	PRINCIPAL DATA	METHOD
Laser Range Determination	Q-Switched Ruby	Range vs time	Measure two-way transit time.

TABLE III. POSSIBLE ADDITIONAL EXPERIMENTS

REQUIRED FACILITIES

EXPERIMENT	STATION 1 (GROUND)	STATION 2	NOTES
0.1 arc-second tracking of a ground beacon	Present ground station	Balloon-borne optical tracker	High-altitude aircraft could also be used. Low-orbit satellites possible although tracking rates are excessive.
Tracking in presence of spacecraft motion	As above	As above using shake fixtures to induce additional disturbances	As above
Space-to-ground-to-space loop closure	As above	Balloon-borne optical station	High-altitude aircraft could also be used.
Point ahead experiment	As above	Laser transmitter with point ahead capability located at remote [161-km (100-mi)] ground station	Airborne or spaceborne stations could be employed although unnecessary.
Transfer tracking from one ground station to another	Present ground station plus additional receiver	Laser transmitter with tracking transfer capability located at remote [161-km (100-mile)] ground station	----

32

TABLE III. POSSIBLE ADDITIONAL EXPERIMENTS (Cont'd)

REQUIRED FACILITIES

EXPERIMENT	STATION 1 (GROUND)	STATION 2	NOTES
Optical heterodyne detection on earth	Present ground station with receiver modified for heterodyne detection	Modulated transmitter balloon-borne	Initial experiments might be carried out between remote ground stations.
Communication with 10-MHz bandwidth	As above	As above	Ordinary receiver could be used for comparison to optical heterodyning.
Atmospheric effects	Present ground station	Wide-beam laser transmitter carried on board low-altitude satellite	Scintillation and polarization effects can be evaluated.
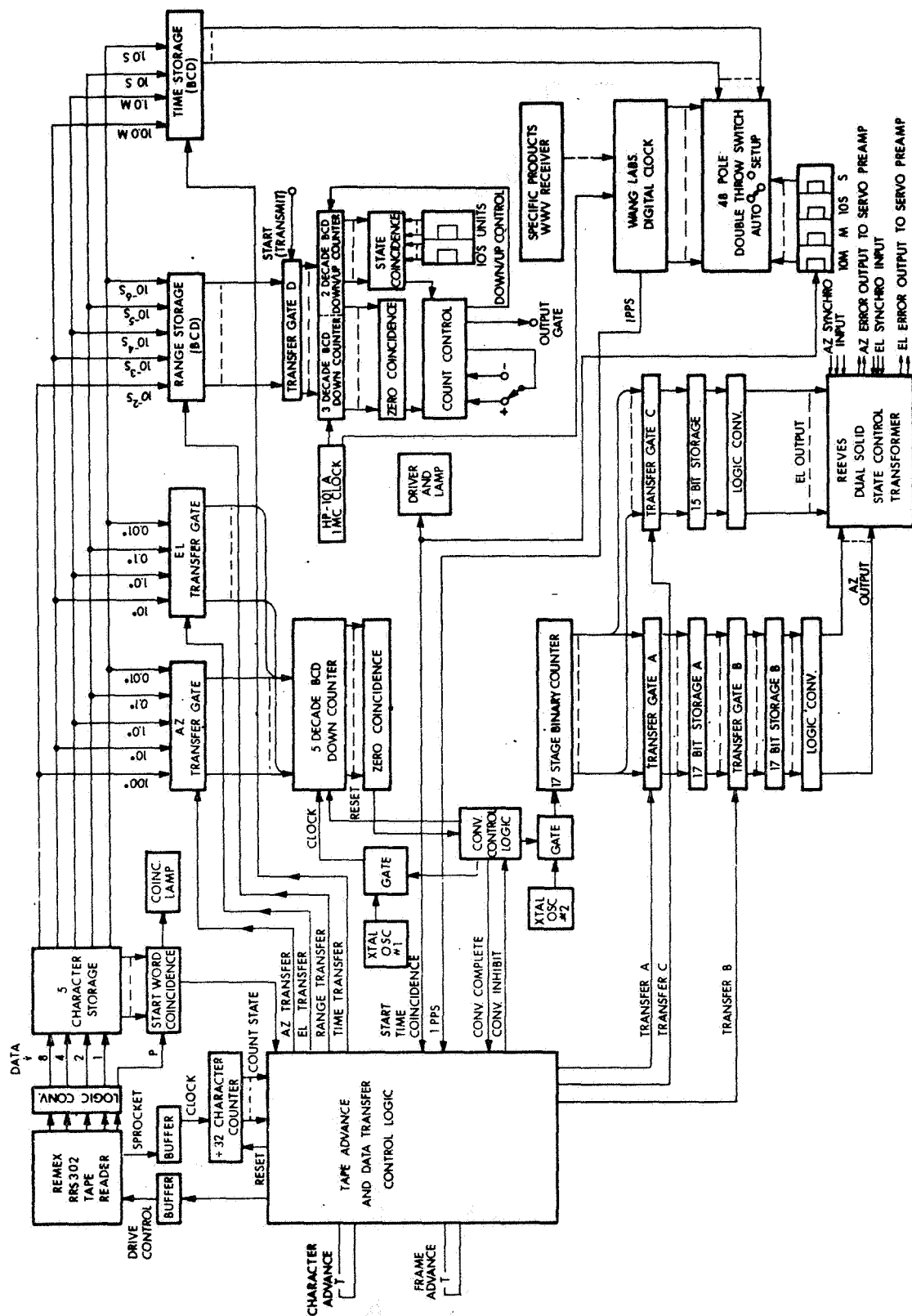
FIGURE 1. ACQUISITION AID SYSTEM
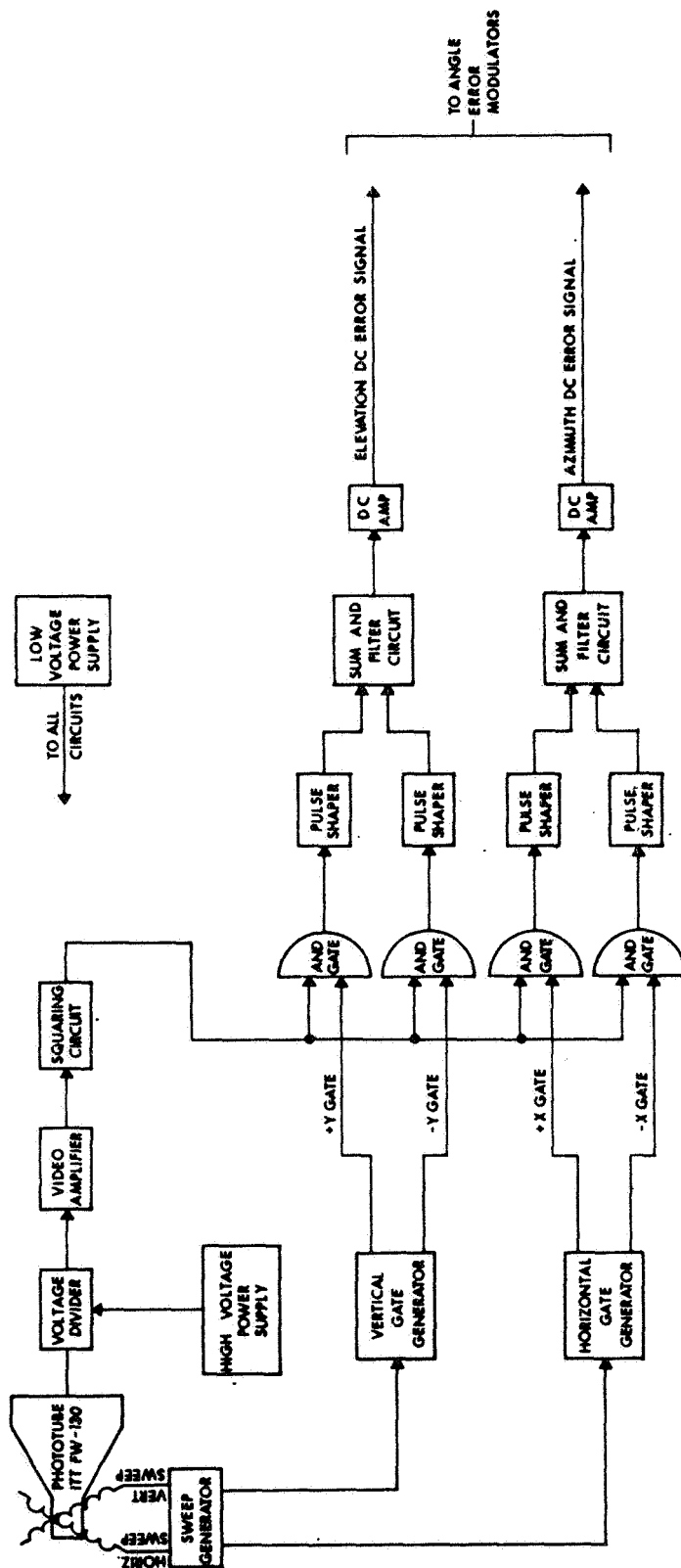
FIGURE 2. . OPTICAL TRACKER
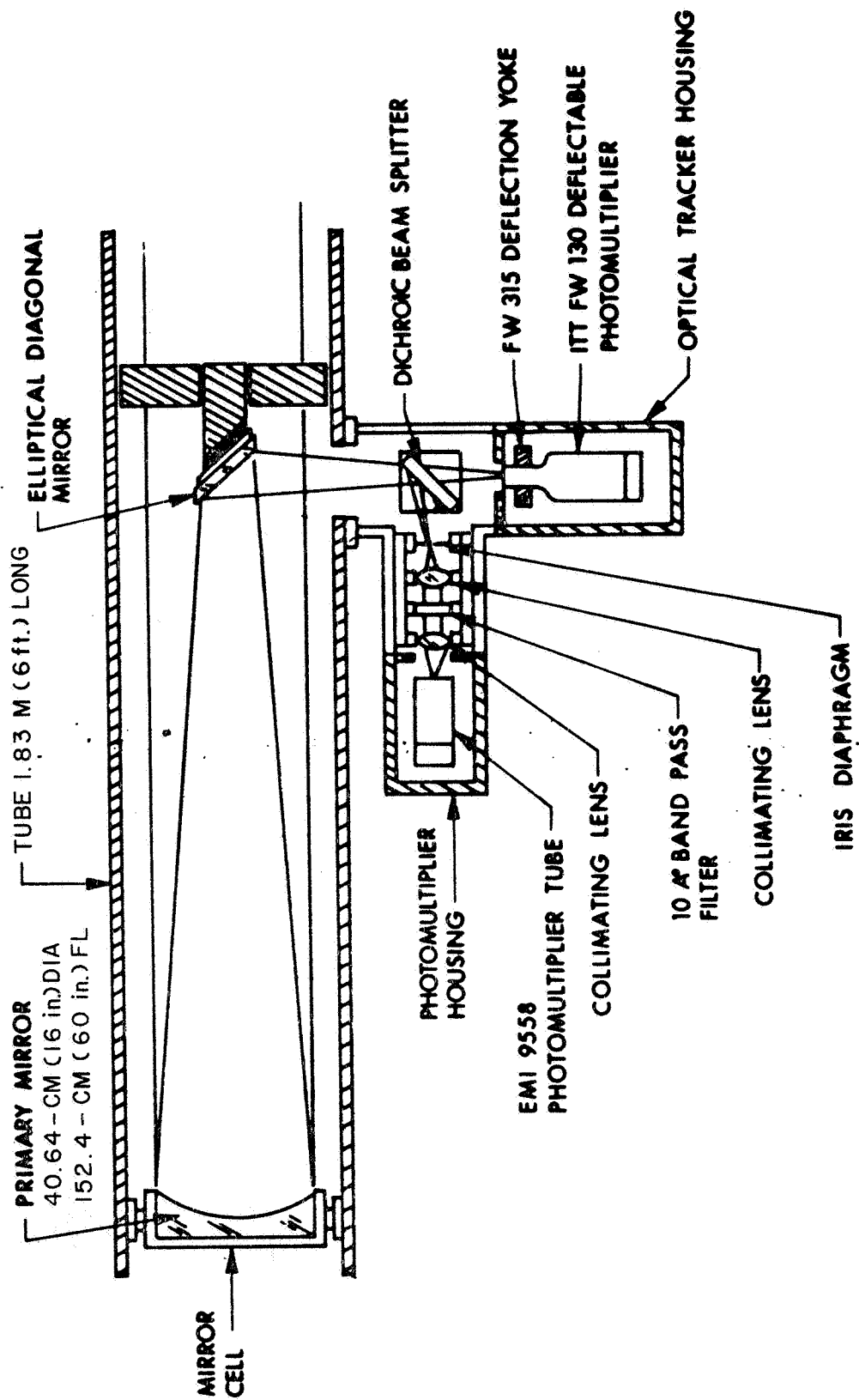
FIGURE 3. 40.64-CM (16-in.) OPTICAL RECEIVER
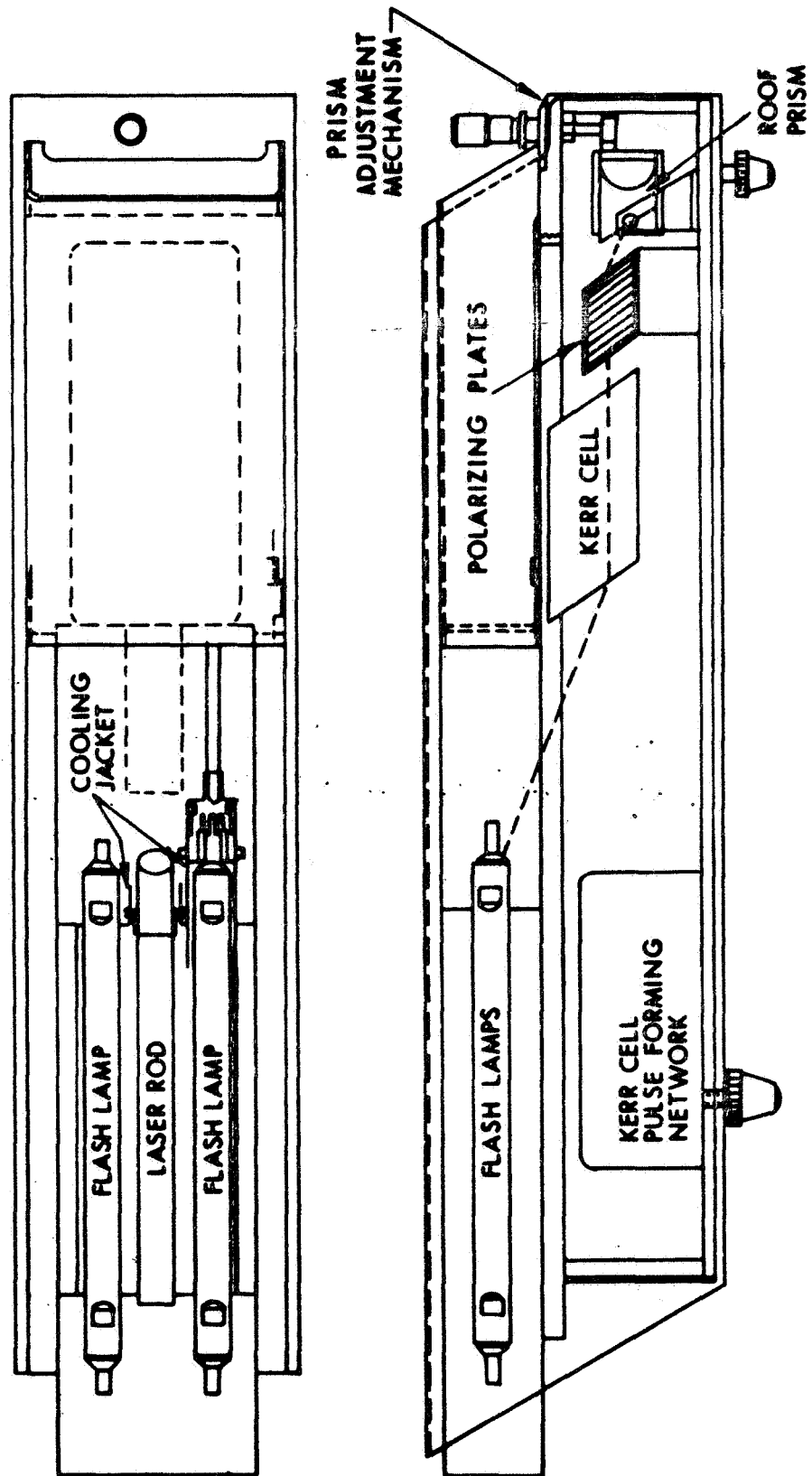
FIGURE 4. Q-SWITCHED LASER

COOLING JACKET

FLASH LAMP

LASER ROD

FLASH LAMP

PRISM ADJUSTMENT MECHANISM

ROOF PRISM

POLARIZING PLATES

KERR CELL

FLASH LAMPS

KERR CELL PULSE FORMING NETWORK

37
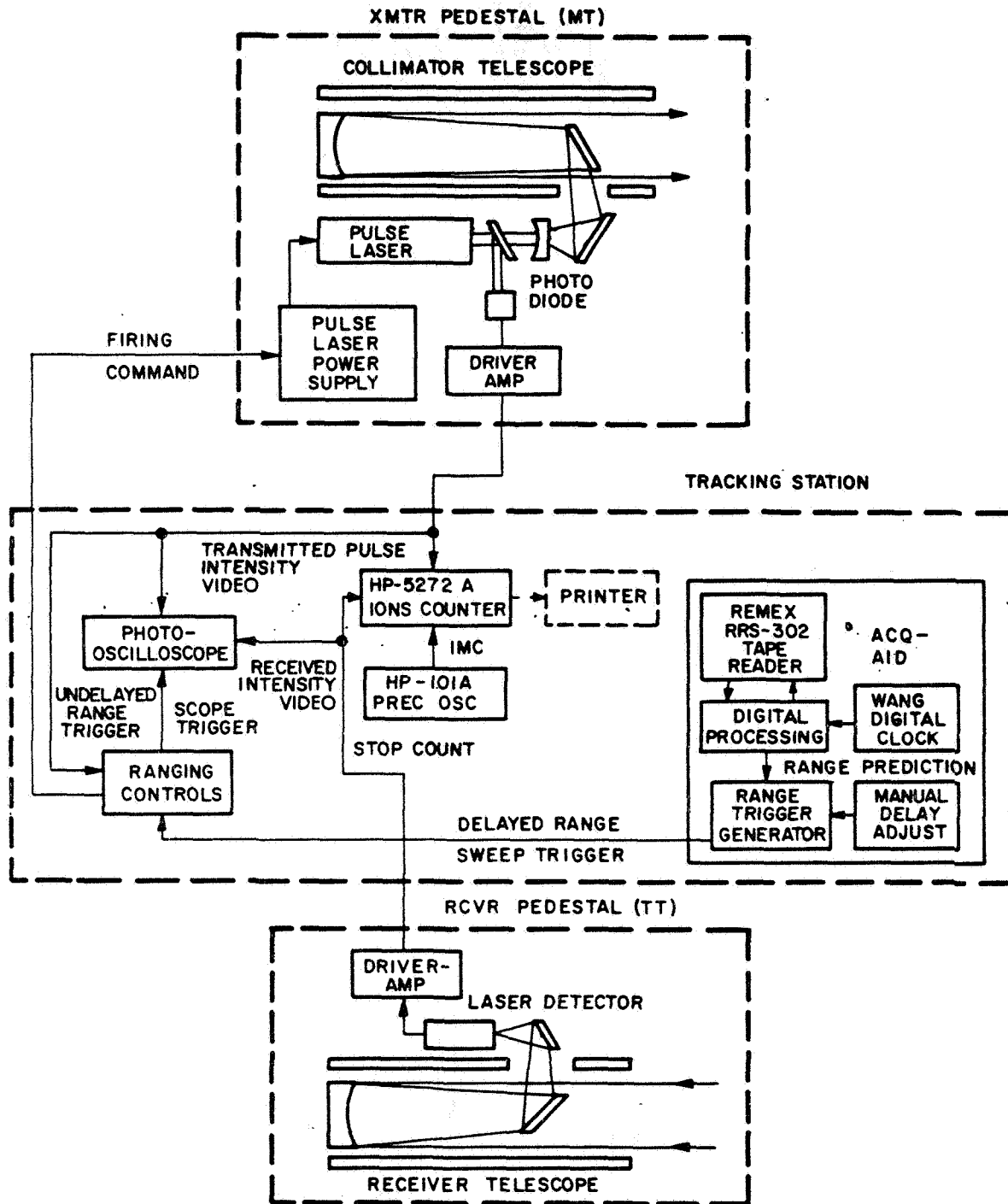
FIGURE 5. SATELLITE RANGING SYSTEM
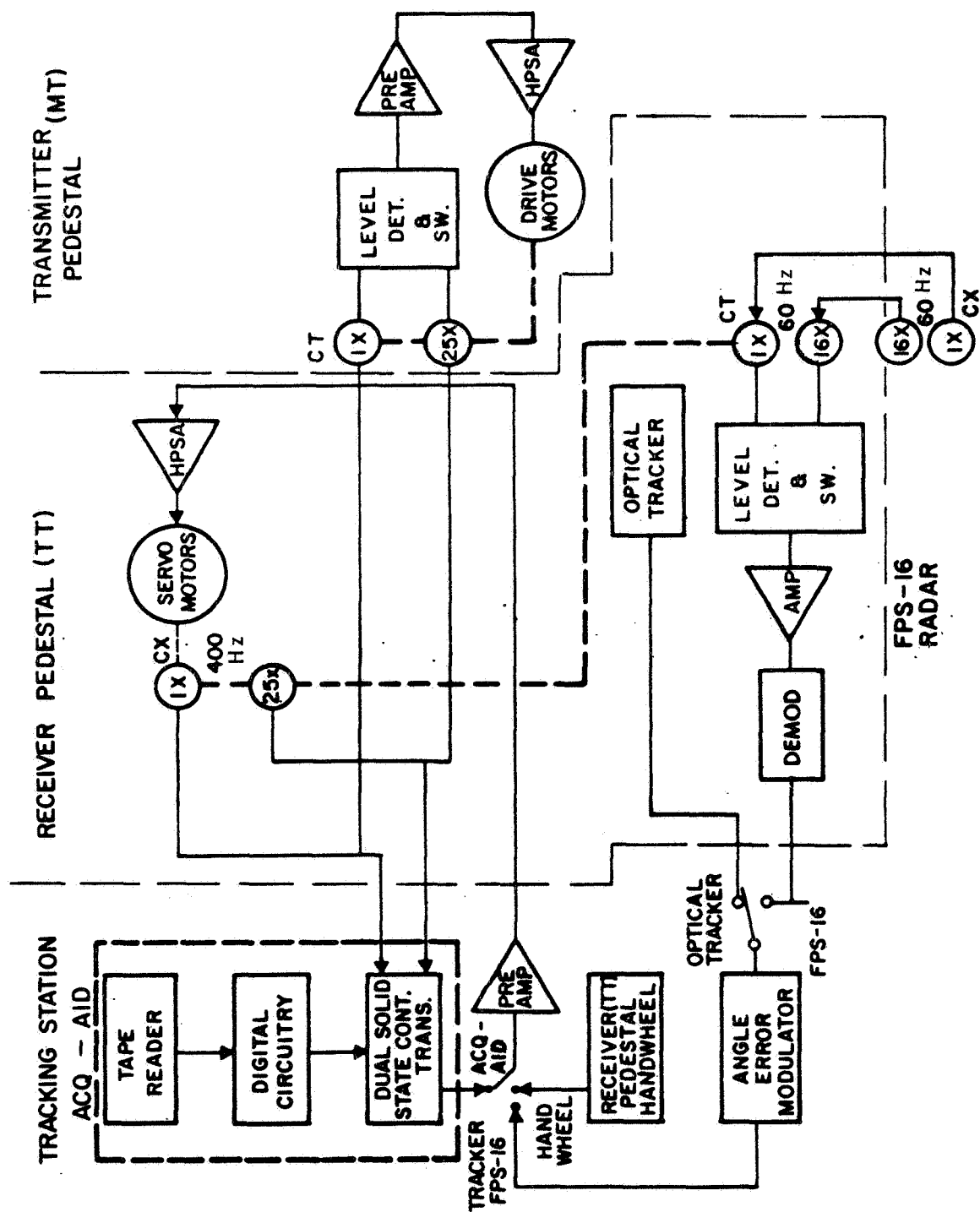
FIGURE 6. FPS-16 SLAVING SYSTEM

39
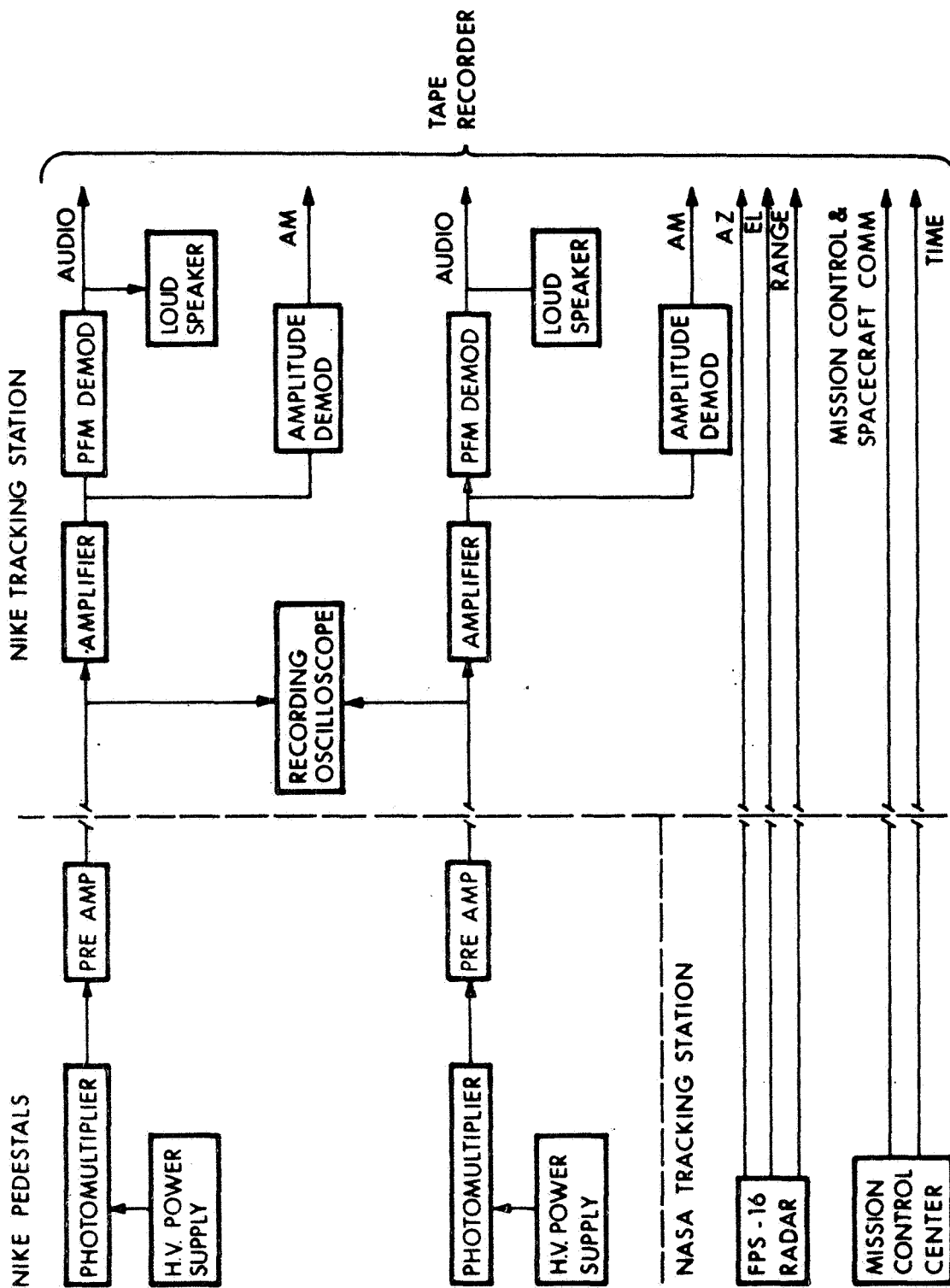
FIGURE 7. DATA SYSTEM

40
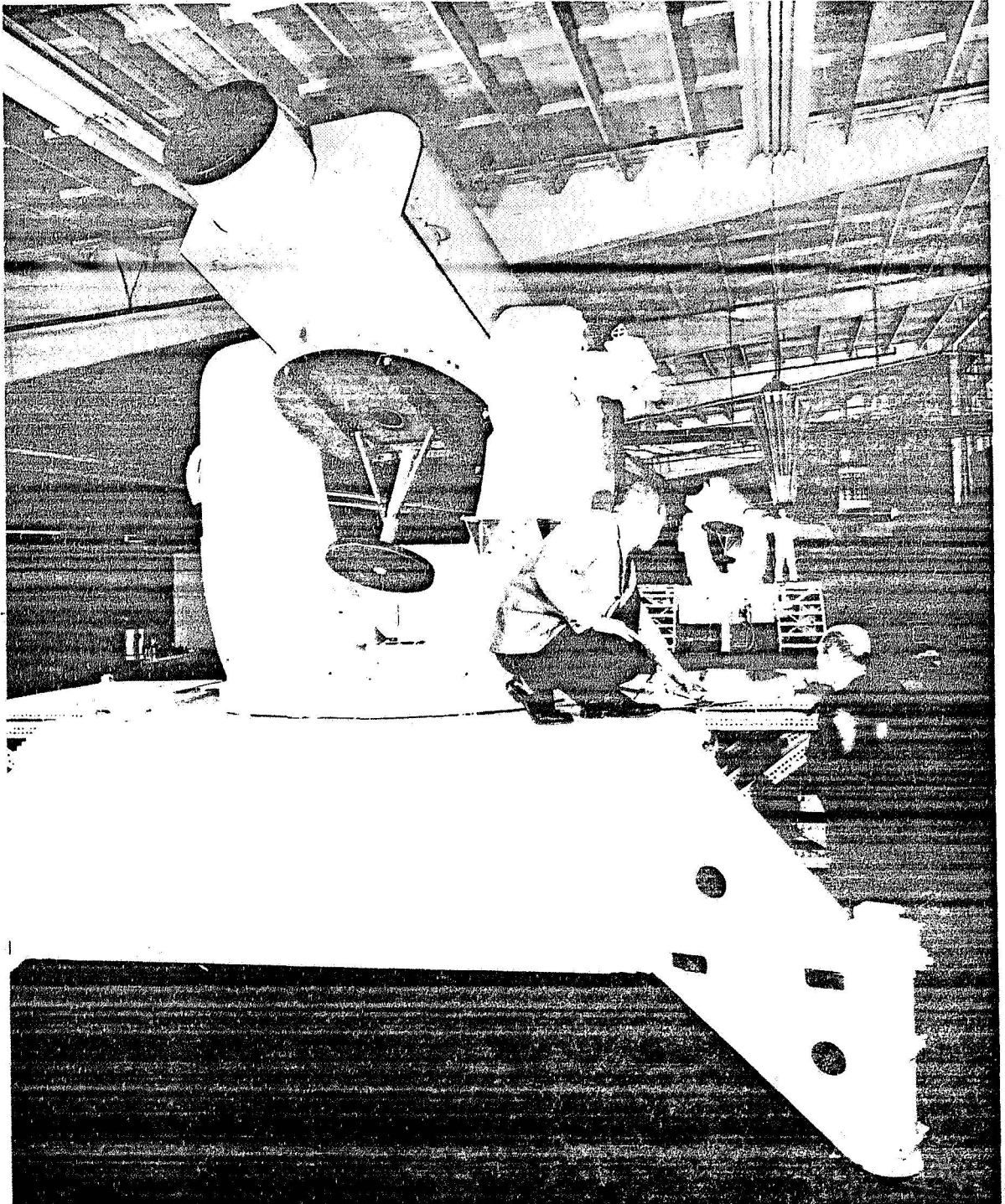
FIGURE 8. EXPERIMENTAL EQUIPMENT
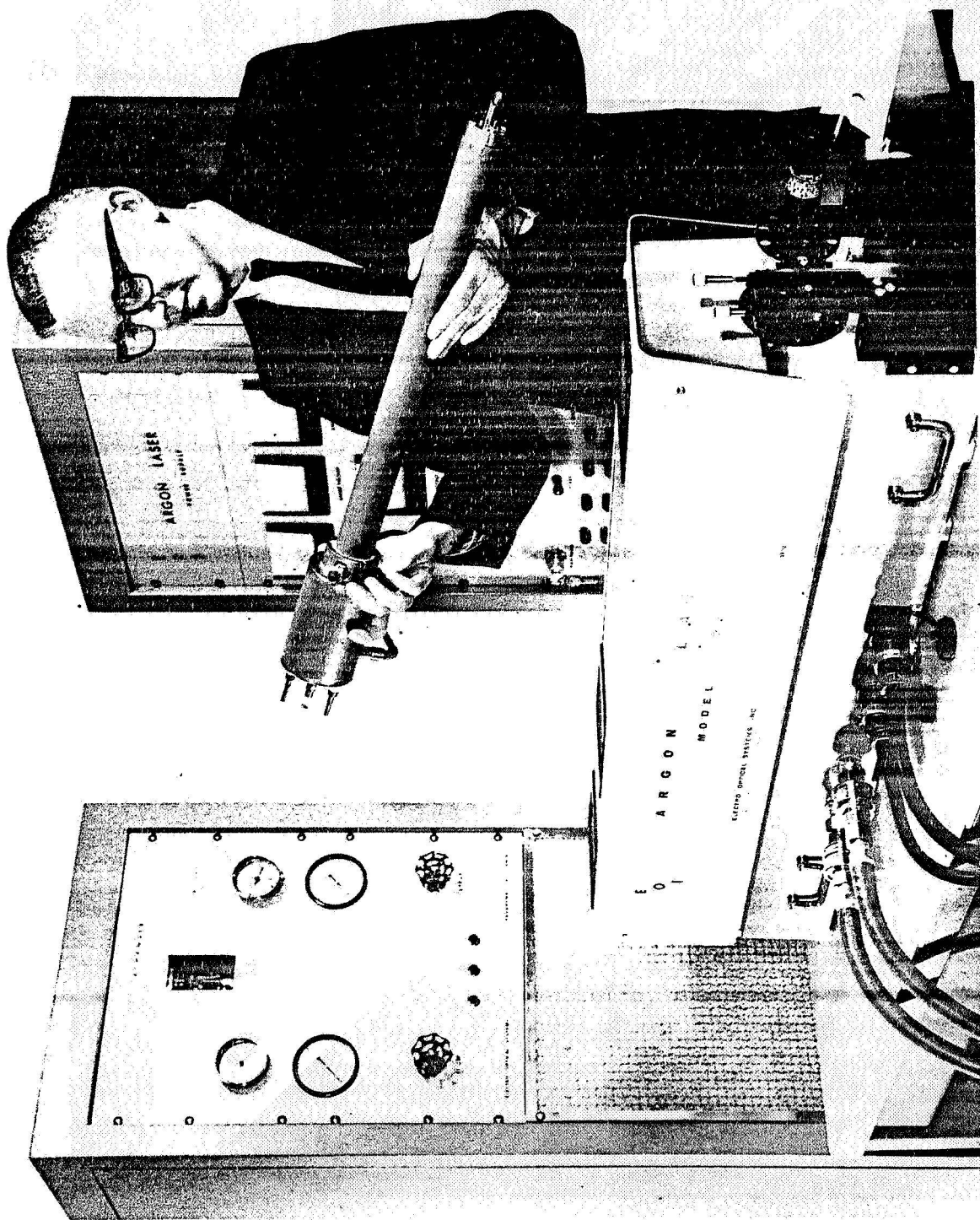
FIGURE 9. ARGON LASER.

EQUIPMENT FOR DEMONSTRATING PCM/PL
LASER COMMUNICATION

N 69 - 71 818

Charles V. Smith
Hughes Aircraft Company

Since April 1965 the Hughes Aircraft Company has been developing
an experimental high-data-rate laser communication system for NASA's
Manned Spacecraft Center. This work, which is being carried out under con-
tract NAS9-4266, represents, in effect, an experimental verification of a key
result of the Deep Space Communications Study conducted by Hughes for MSC
previously. The pulse code modulation/polarization modulation (PCM/PL)
concept developed by that study is the basis of the present system. In this mod-
ulation technique the information to be transmitted is encoded in a PCM format,
and then ones and zeros are transmitted over the laser beam as right and left
circular (or elliptical) polarization, respectively. For further details the
reader is referred to NASA Report CR-73. The requirements of the present
effort are outlined in Figure 1.

The principles of the experimental system are described briefly, followed
by a pictorial review of the equipment status at the present time. Fabrication
and checkout of individual components of the system is well along, with system
integration to begin in three weeks. The tests planned for the first quarter of
1966 are discussed later.

Because the principal signal to be transmitted by the demonstration system
is commerical television, the technique for multiplexing the sound and telemetry
channels with the video is based upon the FCC monochrome composite video
waveform, as shown in Figure 2. In the time division multiplexing scheme used
in this system, horizontal and vertical synchronization signals, and voice and
telemetry samples, are transmitted during the time usually used for the hori-
zontal sync pulse. The balance of the 9.1 μsec blanked period is used to transmit
a chain of alternate ones and zeros, which is used to maintain bit synchronization
in the PCM system.

The PCM portion of this system, while incidental to the advancement of
laser technology, is a major development in its own right. The television

transmission requirements dictate a rate of 30 million bits per second, with 10 million analog-to-digital conversions per second.

Television horizontal sync pulse triggers the transmission of a 13-bit Barker code word, which may also be considered to be the PCM frame sync. Next, 6 bits allocated to vertical sync are transmitted in one pattern during the TV field and its complement during vertical retrace.

The entire demonstration system is shown in block diagram form in Figure 3. An argon ion laser of 2 W nominal output and a wideband electro-optical modulator are critical development items, in addition to the advanced PCM encoder and decoder. The television camera and monitor are standard commerical items.

Key parameters of the system are noted in Figure 4. During daylight operation an optical filter in the receiver will reject all but the 4880-Å line. The curve showing signal-to-noise ratio in the receiver video amplifier as a function of range is based on 100 percent modulation of the laser beam, and in this case sunlight reflected from surroundings of the transmitter station will be the limiting noise. The experimental system will provide on the order of 50 percent modulation, and shot-noise associated with the unmodulated portion of the laser beam will restrict signal-to-noise ratios to somewhat lower values.

Moving on to the equipment description, we look first at the receiver telescope in Figure 5. It is a commercial 20.32-cm (8-in.) Newtonian design, mounted on a heavy tooling stand. The precision adjustable head will allow pointing to about 10 μrad. The optical path is folded back along the telescope tube by the auxiliary Newtonian corner on the left in Figure 6. The optical components shown here are used to detect the polarization modulation and will be mounted in a tube mounted on the telescope. The cutaway tube shown is being used as an alignment jig. To the right of the mirror is a large iris used as a baffle, and on this same ring there is a slot in which neutral density filters can be inserted to simulate long distances. In the center of Figure 6 the adjustable field stop can be seen. On the back of its mount a rotatable prism is mounted, which allows looking through the field stop for final pointing of the receiver. The eyepiece is not shown.

Further to the right are the spectral filter holder, a cell holding a quarter wave plate and Wollaston prism, and a holder for the photomultipliers. These components can be seen better in Figure 7. The quarter wave plate and prism, in the center, are used to convert the incoming PL signal to spatially

44

separated components that are directed to the two photomultipliers in the holder at the upper right. Moving clockwise we see the fine field stop and sighting optics holder, the slide for neutral density filters, one of the spectral filters in its holder, the auxiliary Newtonian corner, and, at the top, the large baffle iris.

The photomultipliers feed video amplifiers, one of which is shown at the bottom of Figure 8. The large unit on the right is the tapped delay line used in detection of the horizontal sync signal. To its left is a small unit that detects horizontal sync and performs gating and timing functions. In the top center is the phase locked loop that provides bit synchronization, and on the far left is a matched filter and threshold unit that synchronously detects the signal plus noise from the video amplifiers to provide clean PCM video. In Figure 9 the units have been closed.

PCM video and the 30-MHz clock signal are the major inputs to the digital decoder, which occupies the two panels on the right of Figure 10. The outputs of the decoder are television video and horizontal and vertical sync pulses, which are fed directly to the monitor, and the sound and telemetry signals. Both the decoder and the encoder on the left make extensive use of Motorola MECL microcircuits.

The encoder accepts television signals from the camera, and, with reference to the horizontal sync pulse, multiplexes in the Barker code word, voice, and telemetry samples, etc. It is built around a high-speed analog-to-digital converter. The 30-MHz clock oscillator is in the upper left corner.

The digital bit stream from the encoder is fed to the modulator driver, shown in Figure 11. It is entirely solid state, using 2N3375 transistors in a push-pull switching type circuit to optimize efficiency. The electro-optical modulator is shown in Figure 12. It contains ten pieces of KDP, each 5.08 cm (2 in.) long. It is a transverse mode modulator. The unit is oil filled to minimize thermal and optical matching problems.

The heart of the transmitter station is the high-power argon ion laser. The Hughes Research Laboratories have been developing this type of laser for a military application for almost a year. Figure 13 illustrates a late model laser using a quartz tube. Several lasers of this configuration have been built and are producing on the order of 2 W. Because of life problems associated with high-power operation of quartz tubes, a great deal of attention has been devoted to perfection of metal ceramic construction techniques. Figure 14 shows a laser of this type. It is our intention to deliver this type of laser with this system.

The laser, modulator, and driver are being mounted on a honeycomb panel, as indicated in Figure 15. The transmitting telescope will allow adjustment of beam divergence. It also includes a provision for sighting along the transmitted beam for system set-up. When looking through the eyepiece one sees the receiving station with the transmitted beam superimposed. The transmitter station is being mounted on a tooling stand identical with the receive end, but because of the weight of this equipment we have had to design a special precision pointing mount for this end, as indicated in Figure 16. The laser alone, in its militarized housing, weighs almost 45 kg (100 lbm).

The laser power supply and control units are shown in Figure 17. These units include starting provisions as well as filament, solenoid, and anode supplies for the laser. Prime power is three phase 400 cycle, since these designs are also spin-offs from military programs.

All of the equipment shown is in the final stages of assembly, or being checked out. At the end of November system integration is scheduled to begin, and, barring unforeseen difficulties, the experimental system should be operating shortly after the first of the year. It is planned to operate the system in the laboratory initially. As soon as reliable system operation is achieved, the system will be set up to transmit from the Hughes Culver City plant to our Baldwin Hills facility, a distance of some 8 km (5 mi). System performance as a function of atmospheric conditions and signal-to-noise ratio will be measured.

Ultimately the system will be delivered to the Manned Spacecraft Center, where operation over a 11.3-km (7-mi) path is planned.

DELIVER A WORKING MODEL OF AN EXPERIMENTAL PCM/PL LASER COMMUNICATION SYSTEM

SIMULTANEOUSLY TRANSMIT

- 5 MHz TV VIDEO
- 4 kHz VOICE
- 1 kHz TELEMETRY

TELEVISION REQUIREMENTS

- AT LEAST 8 SHADES OF GREY
- AT LEAST 28 db SIGNAL-TO-NOISE RATIO
- AT LEAST 360-LINE HORIZONTAL RESOLUTION

PRIOR TO DELIVERY THE SYSTEM SHALL BE TESTED OVER FIELD DISTANCES

FIGURE 1. KEY CONTRACT OBJECTIVES
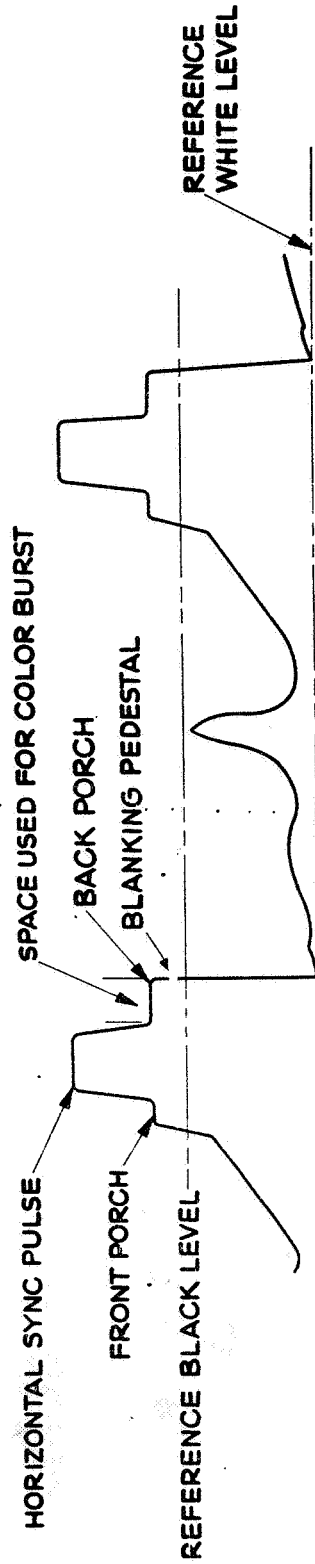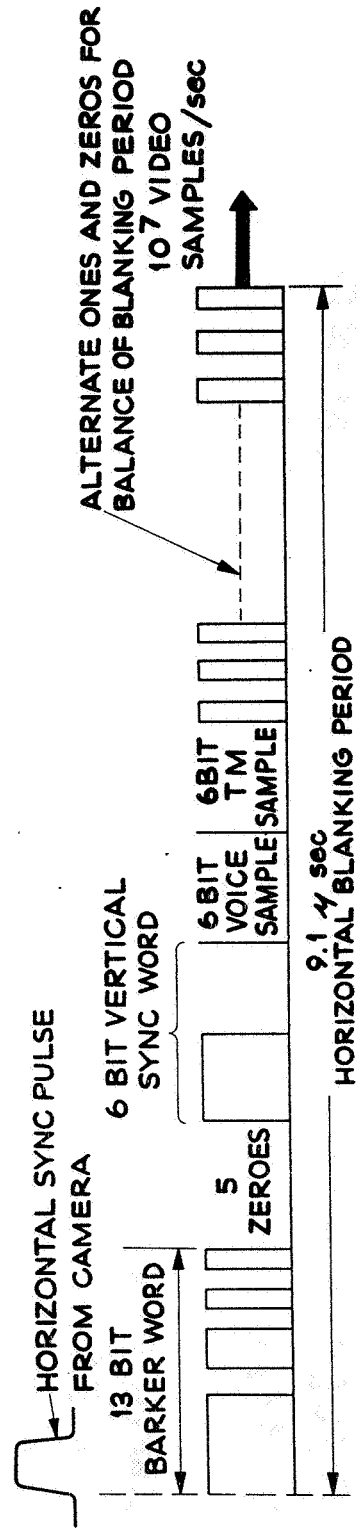
COMPOSITE TELEVISION VIDEO WAVEFORM

REFERENCE WHITE LEVEL

SPACE USED FOR COLOR BURST

BACK PORCH

BLANKING PEDESTAL

HORIZONTAL SYNC PULSE

FRONT PORCH

REFERENCE BLACK LEVEL

ALTERNATE ONES AND ZEROS FOR BALANCE OF BLANKING PERIOD
10⁷ VIDEO SAMPLES/sec

HORIZONTAL SYNC PULSE FROM CAMERA

6 BIT VERTICAL SYNC WORD

13 BIT BARKER WORD

5 ZEROES

6 BIT VOICE SAMPLE

6 BIT TM SAMPLE

9.1 μ sec
HORIZONTAL BLANKING PERIOD

FIGURE 2. PCM/PL SYSTEM MULTIPLEXING SCHEME
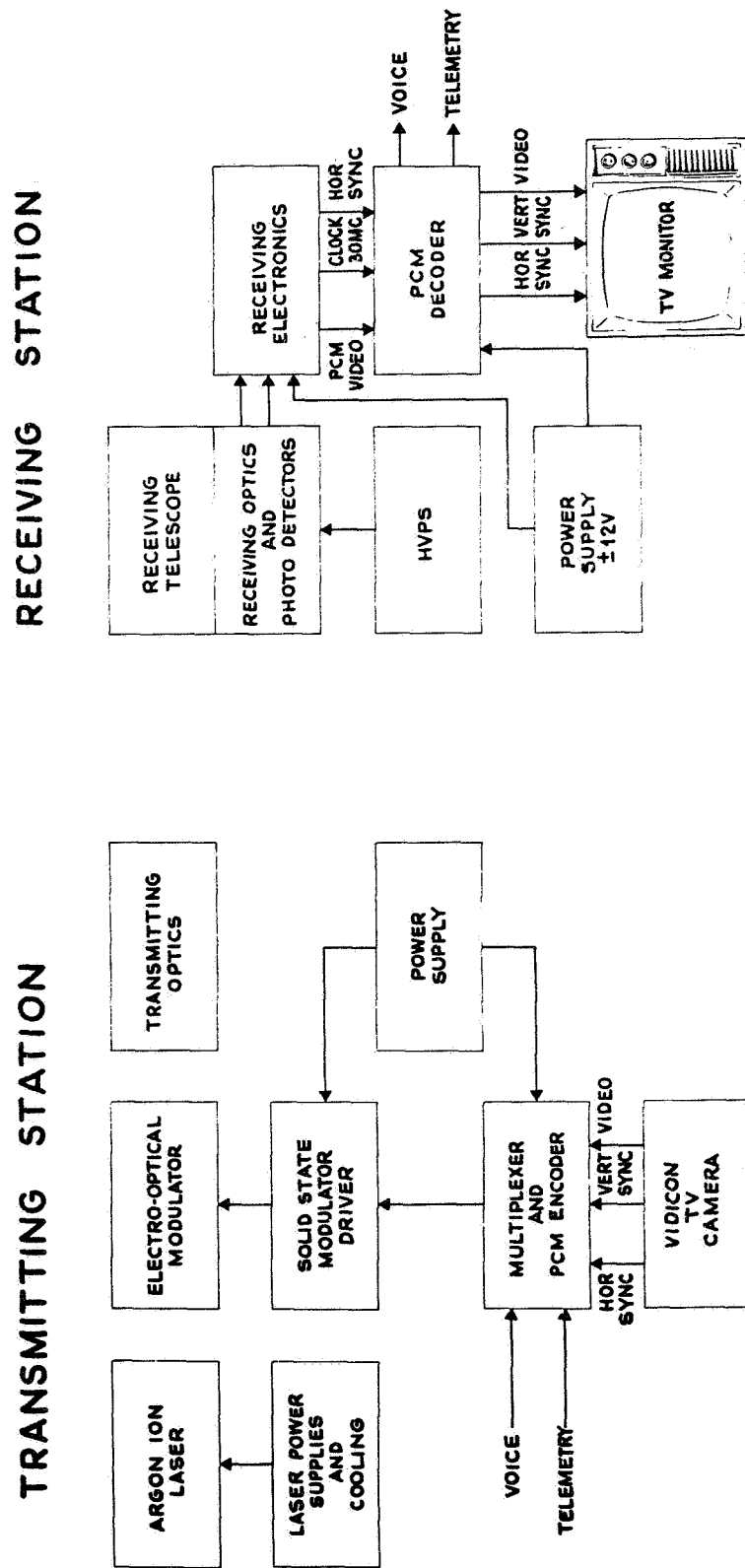
FIGURE 3. PCM/PL COMMUNICATION SYSTEM BLOCK DIAGRAM

49

LASER POWER
- 1 WATT IN THE 4880 Å LINE

OPTICAL EFFICIENCIES
- TRANSMIT 0.5
- RECEIVE   0.2

LASER BEAM DIVERGENCE
- 100 MICRORADIANS (ADJUSTABLE)

RECEIVER FIELD OF VIEW
- 1 MILLIRADIAN (ADJUSTABLE)

RECEIVER OBJECTIVE DIAMETER -
2.32 CM (8 inches)

OPTICAL FILTER WIDTH - 20 Å

PHOTO TUBE QUANTUM EFFICIENCY
- 12.5% (S-20 @ 4880 Å)
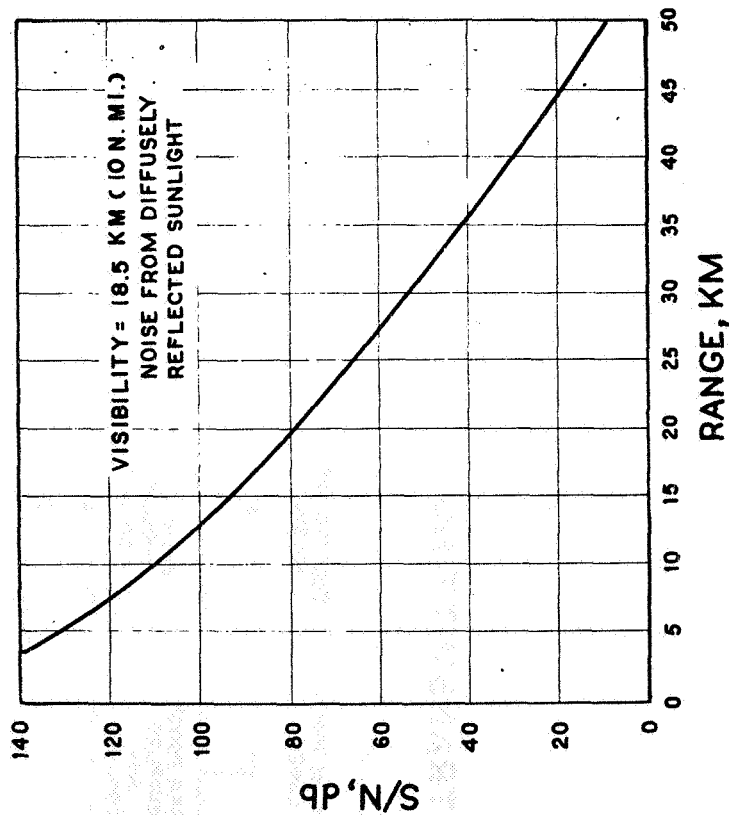
FIGURE 4. PCM/PL COMMUNICATION SYSTEM PARAMETERS
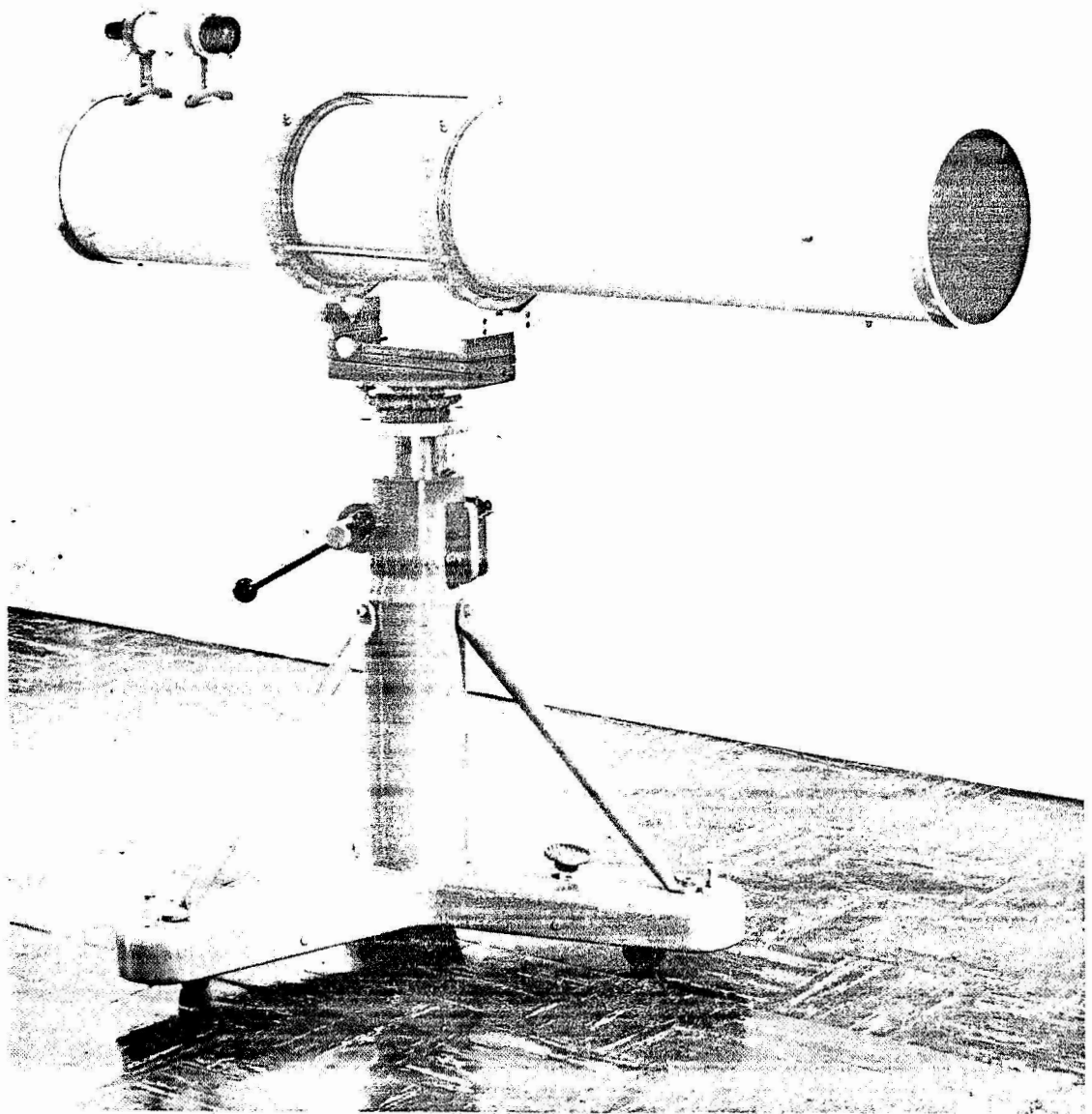
FIGURE 5. RECEIVER TELESCOPE AND MOUNTING
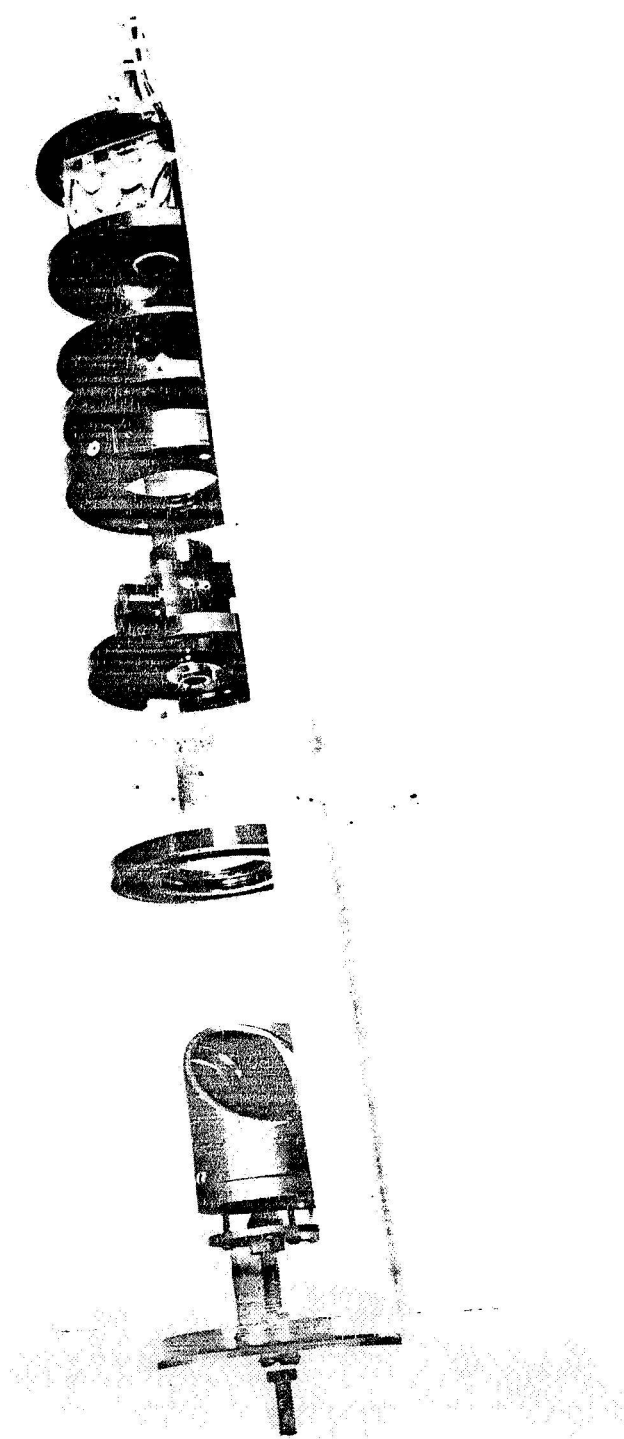
FIGURE 6. PCM/PL RECEIVER OPTICAL CHAIN
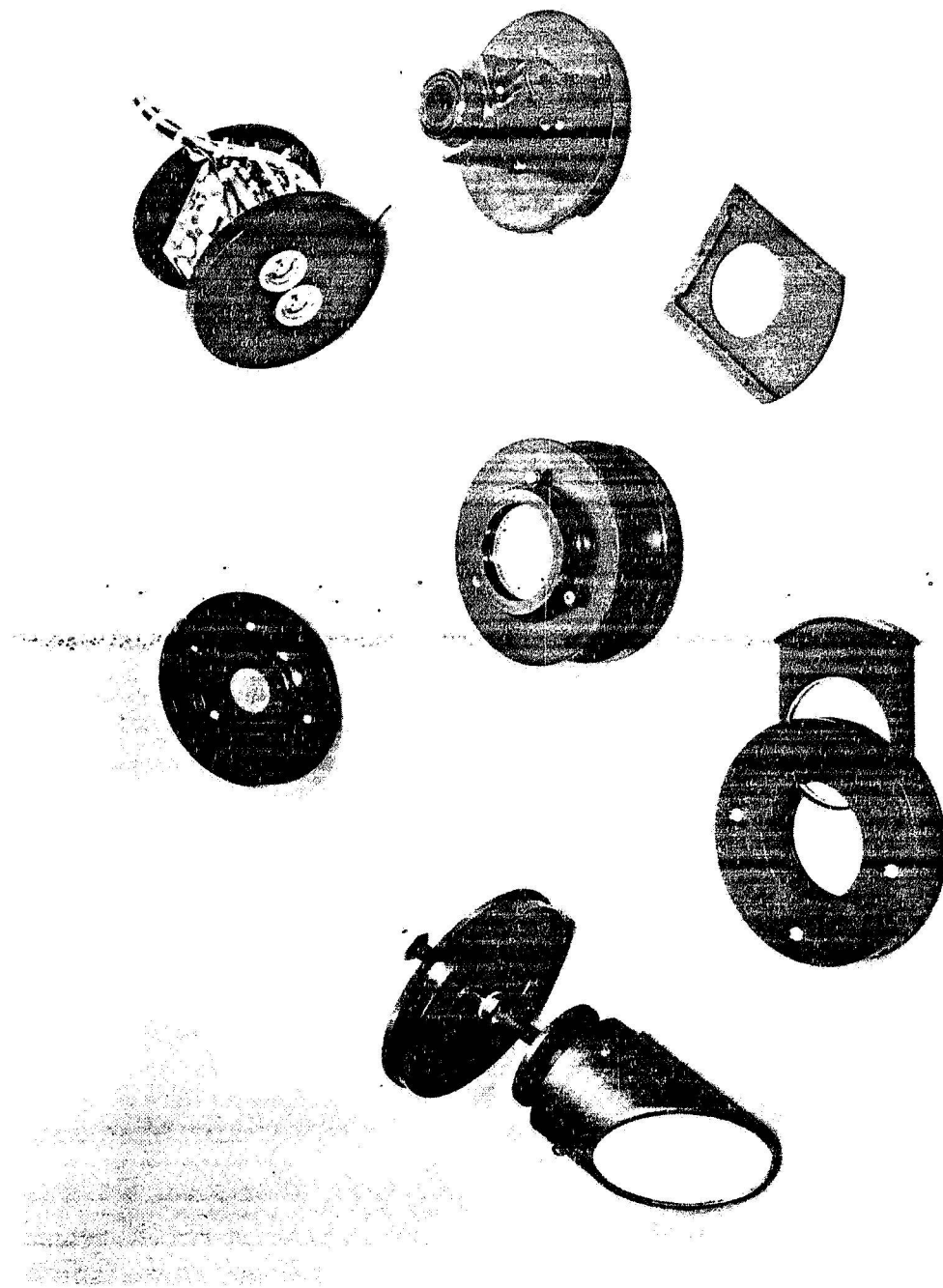
FIGURE 7. RECEIVER OPTICAL COMPONENTS

53
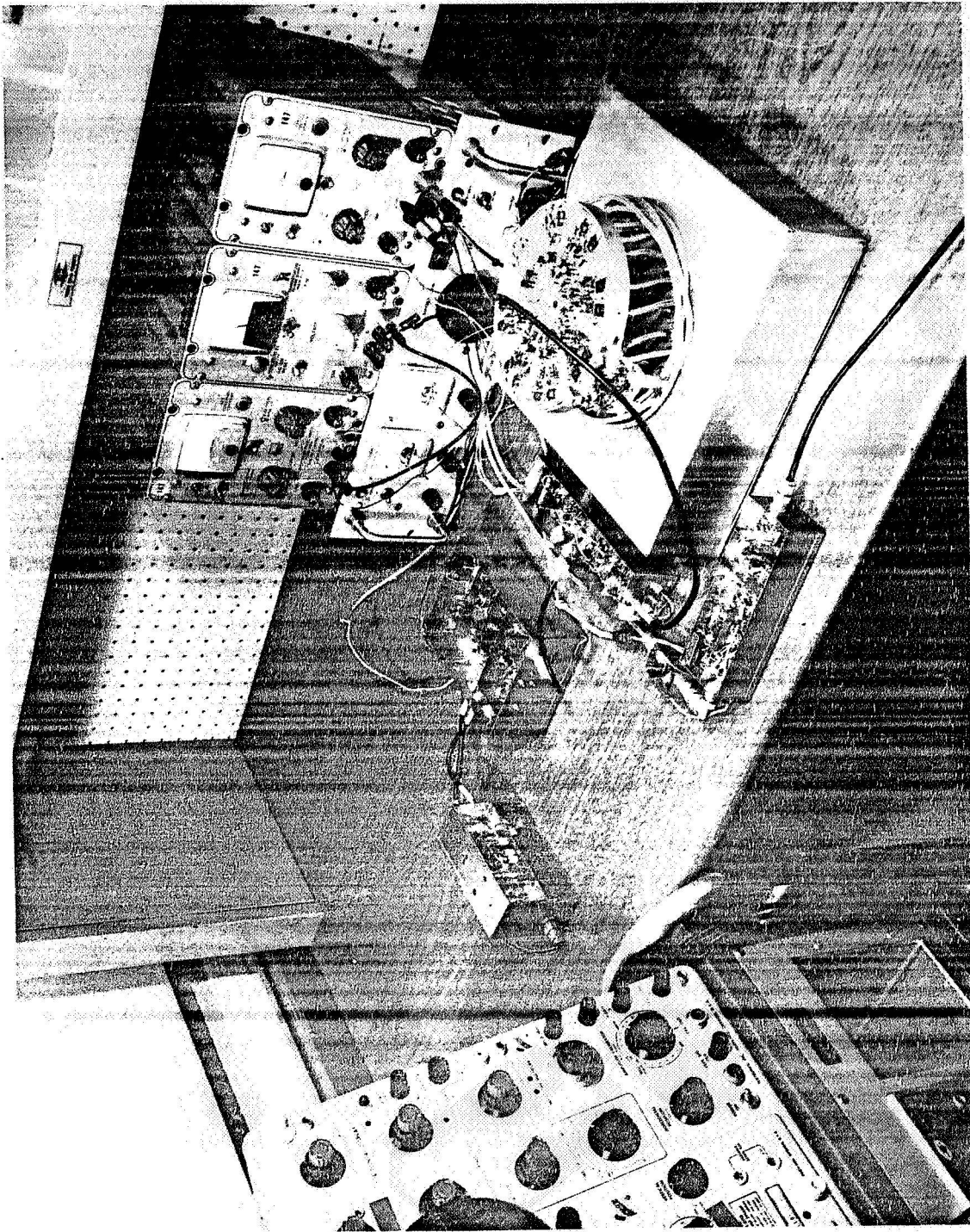
FIGURE 8. RECEIVER ELECTRONICS
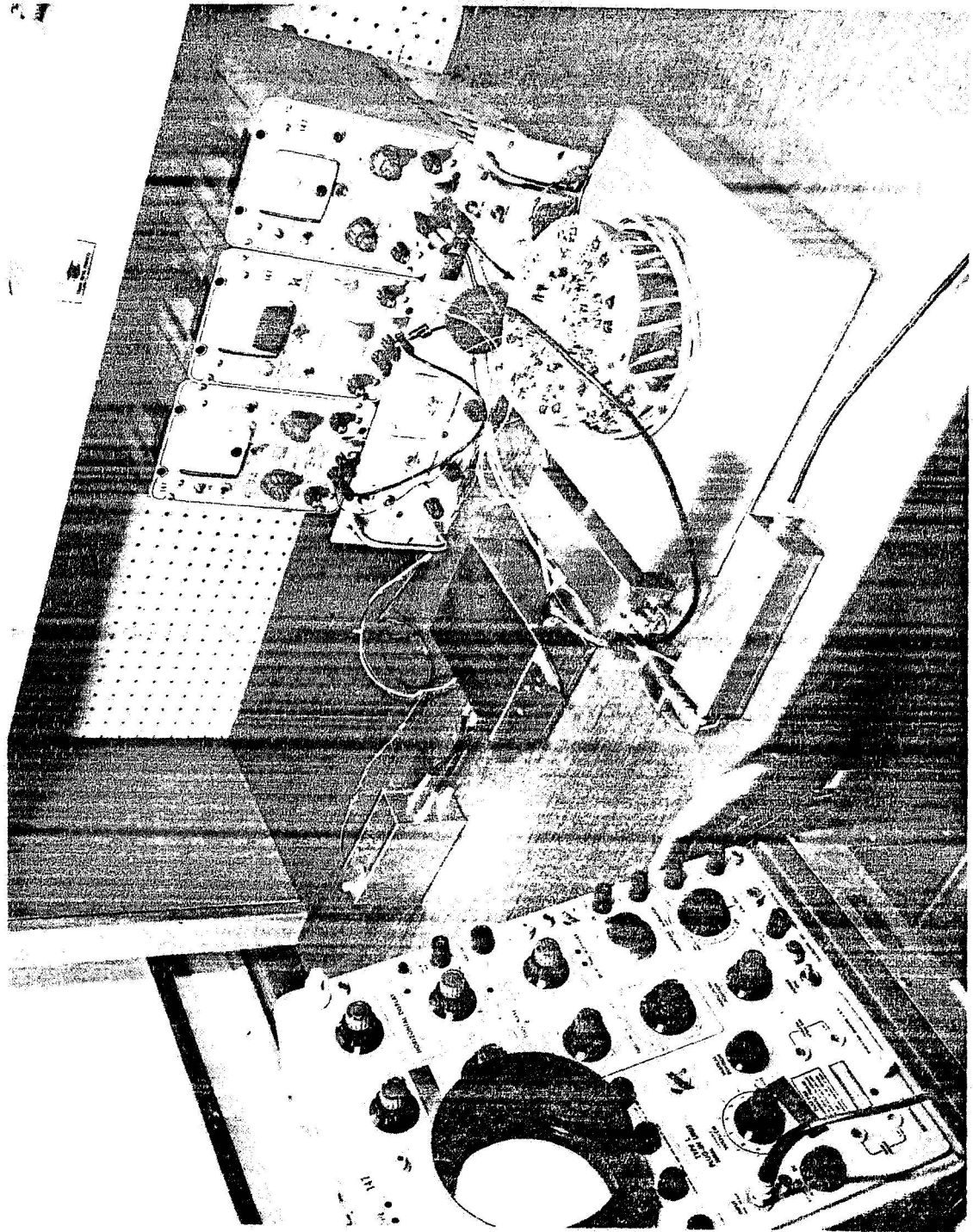
FIGURE 9. RECEIVER ELECTRONICS
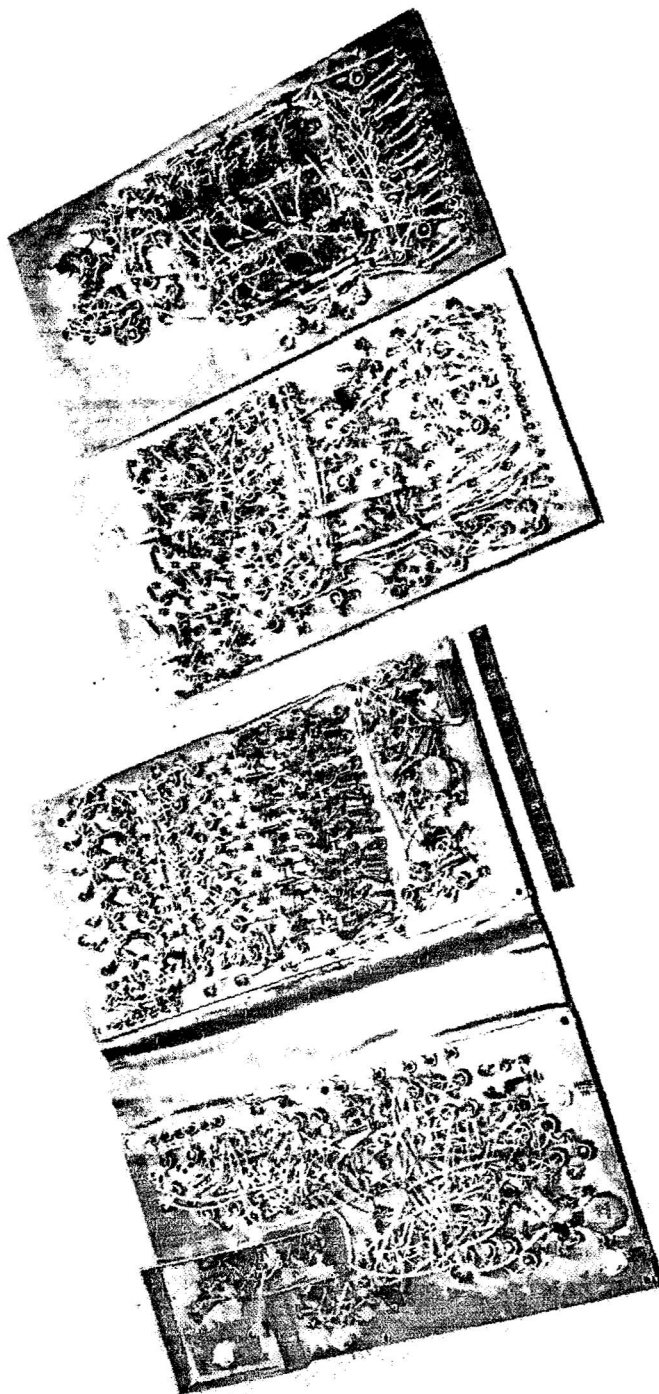
FIGURE 10. PCM ENCODER AND DECODER
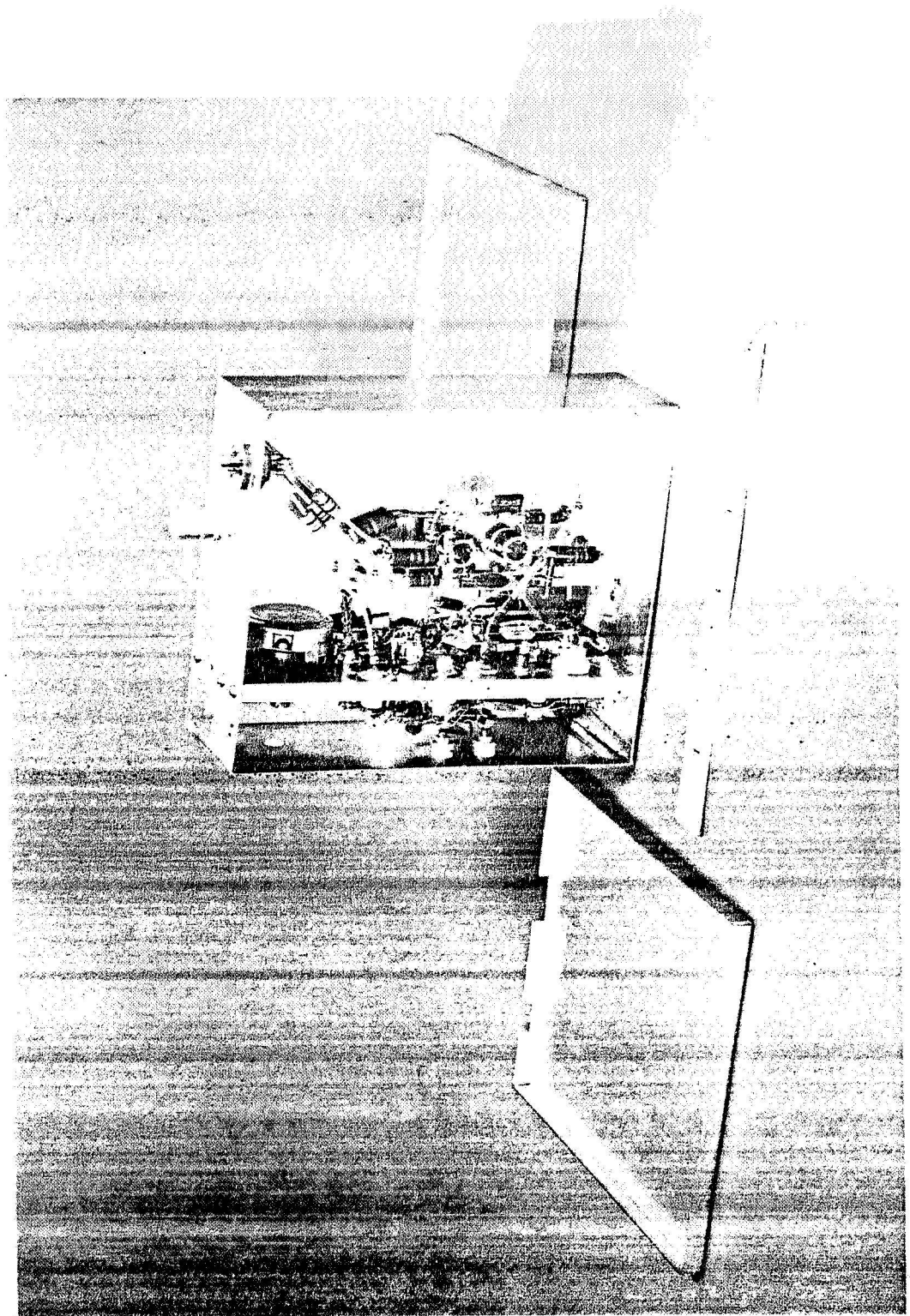
FIGURE 11. SOLID STATE MODULATOR DRIVER
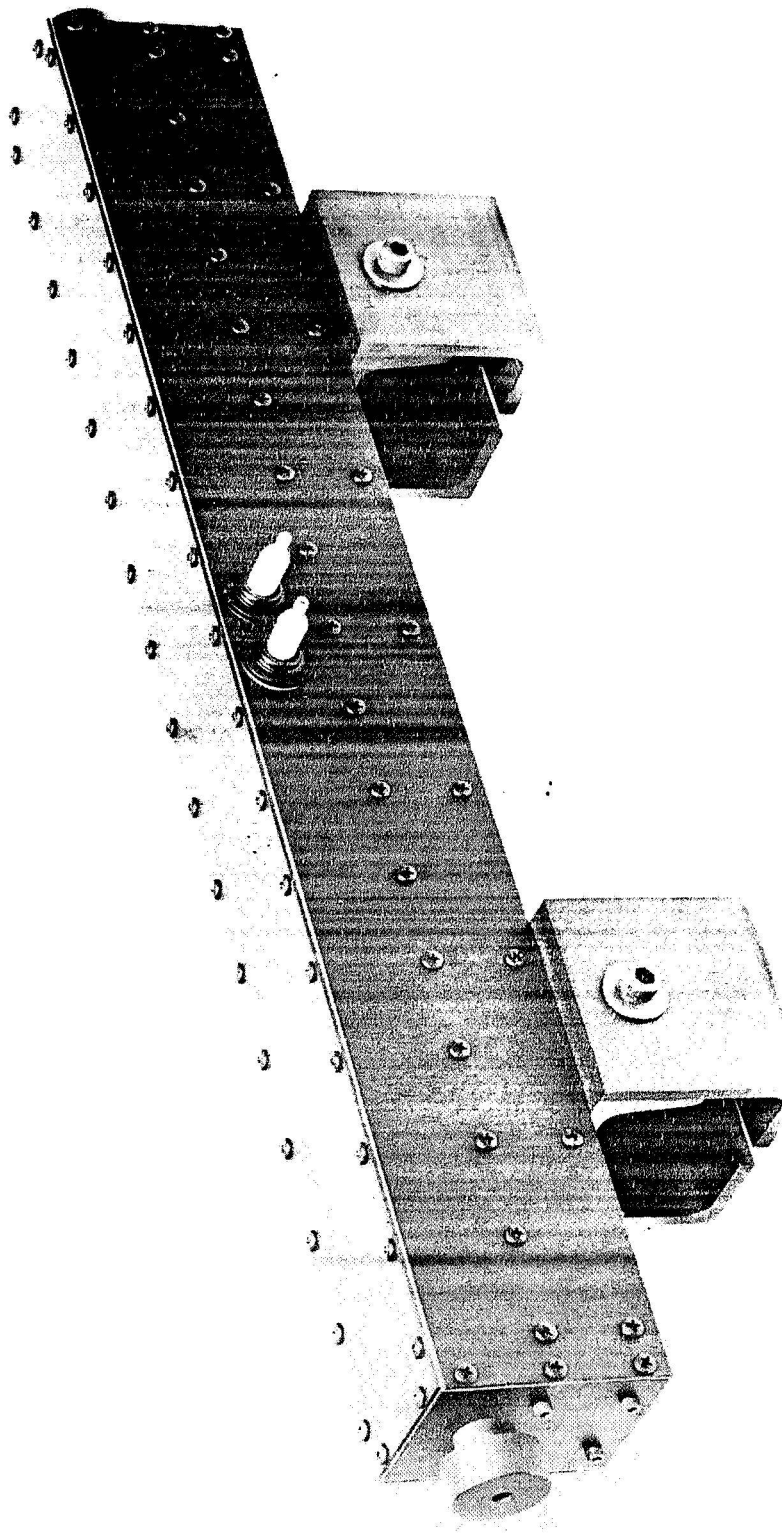
FIGURE 12. ELECTRO-OPTICAL MODULATOR
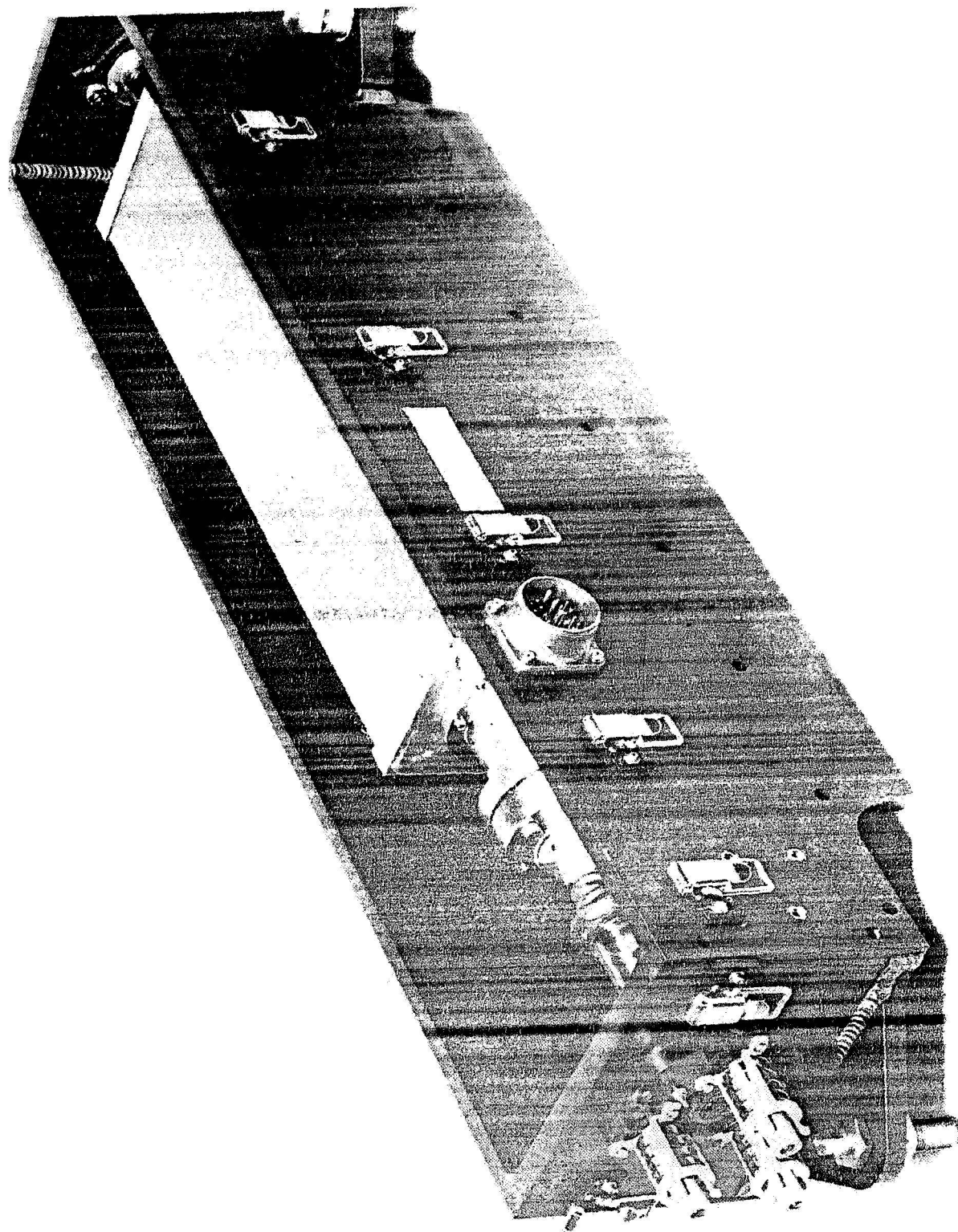
58
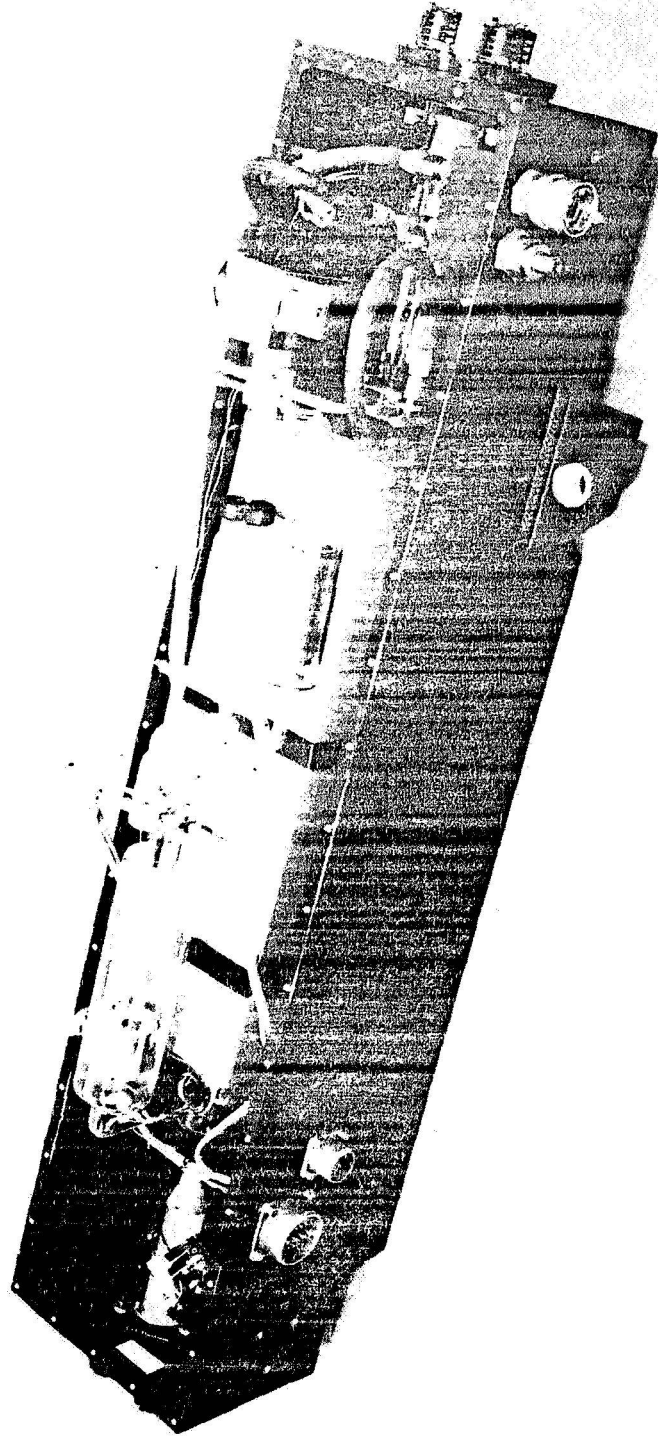
FIGURE 13. QUARTZ TUBE ARGON LASER
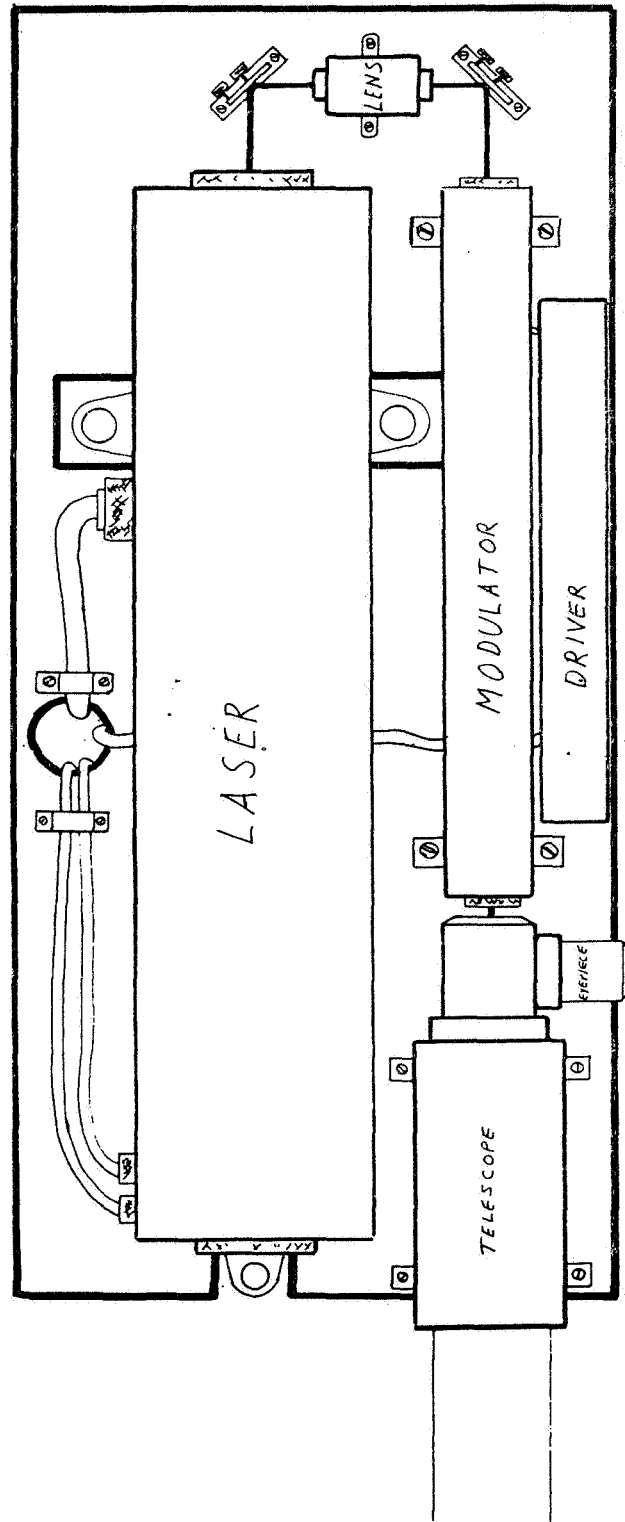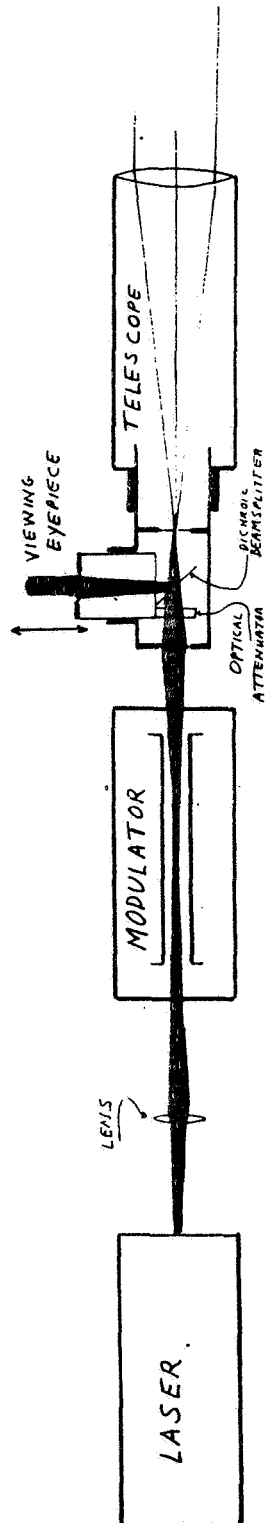
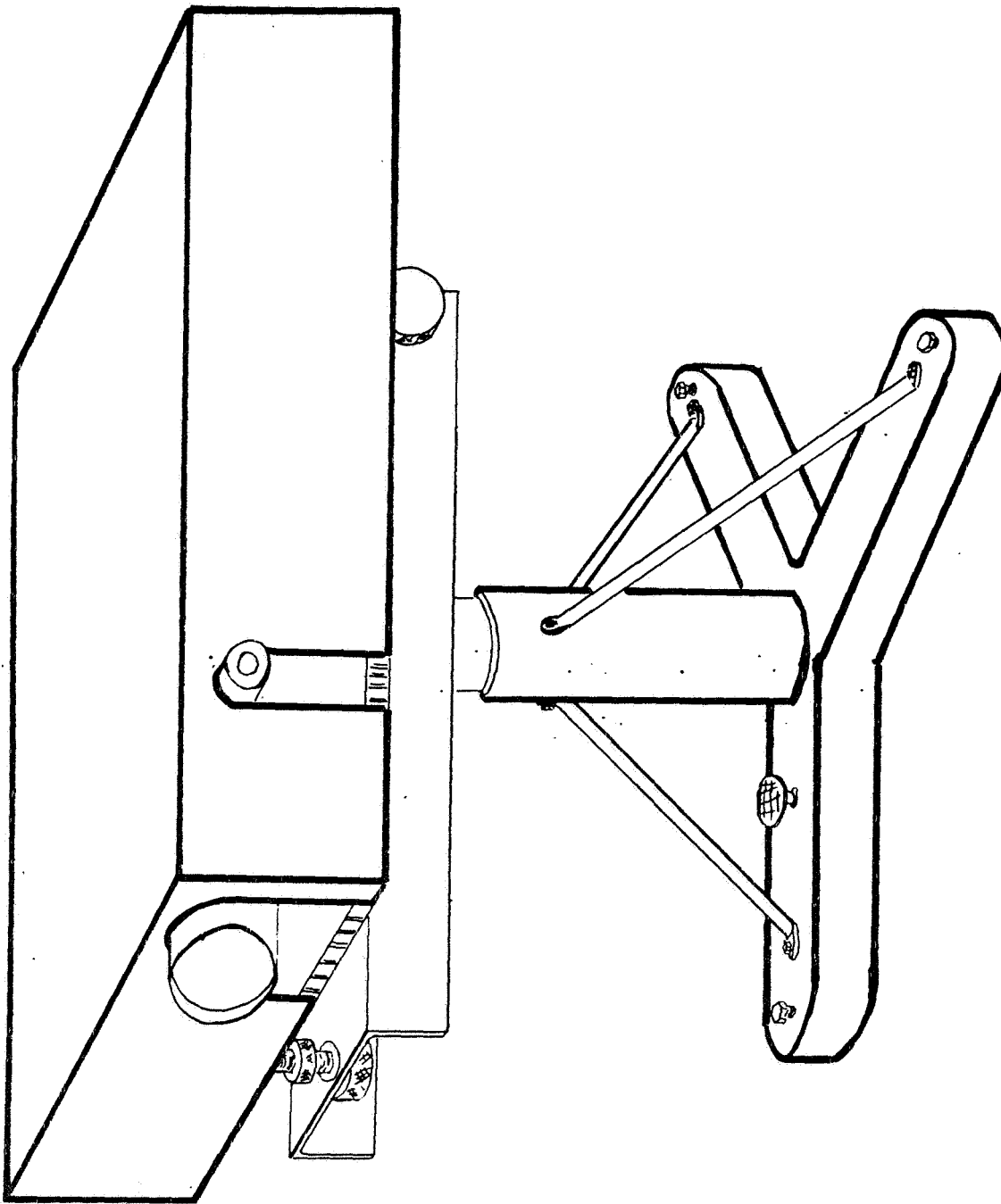FIGURE 14. METAL–CERAMIC ARGON LASER

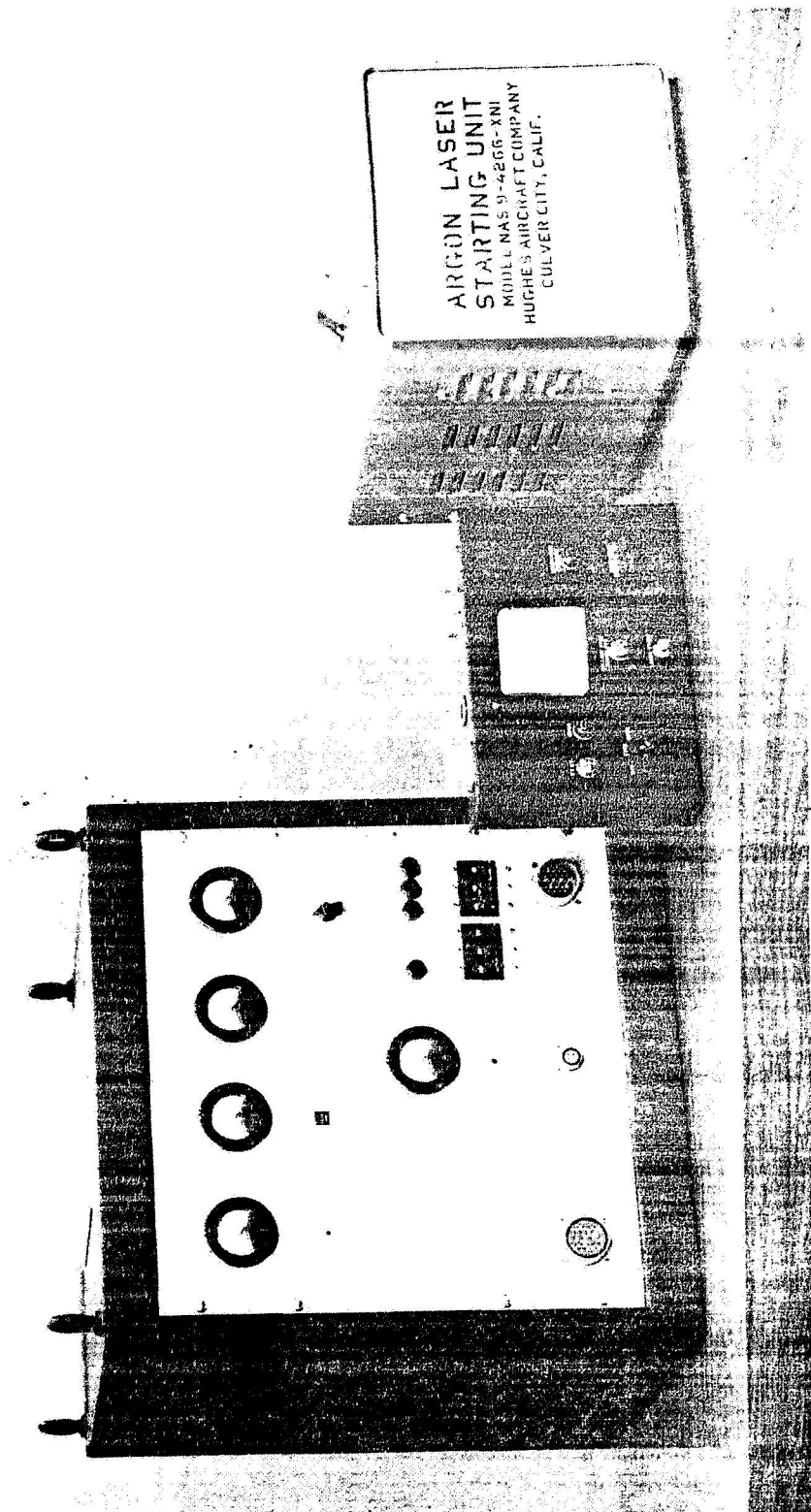FIGURE 15. PCM/PL TRANSMITTER LAYOUT

FIGURE 16. TRANSMITTER MOUNT

ARGON LASER
STARTING UNIT
MODEL NAS 9-4266-XNI
HUGHES AIRCRAFT COMPANY
CULVER CITY, CALIF.

FIGURE 17. ARGON LASER POWER SUPPLY AND CONTROL BOX

PARAMETRIC ANALYSIS OF MICROWAVE AND LASER SYSTEMS FOR COMMUNICATIONS AND TRACKING

Lyle S. Stokes

Hughes Aircraft Company

The Goddard Space Flight Center entered into a study contract on August 6, 1965, with Hughes Aircraft Company to analyze microwave and laser systems for communication and tracking. The purpose of this paper is to introduce the objectives and tasks of this contract. The paper is divided into three sections: first, an introduction to the problems of deep-space communications; second, an indication of the ultimate goal of this study; and third, an illustration of how this goal will be used in solving a typical space telecommunications problem.

A number of telecommunications choices are now available for space communications. These choices include a variety of spacecraft and ground-based hardware using frequencies from the vhf range through s-band. Future planning will undoubtedly include new frequencies and different designs. It is necessary, therefore, that a coherent and logical plan be developed enabling a space communications designer to pick the proper design configuration for an anticipated spacecraft telecommunication system. Not only is the large number of possible choices for communications design a problem for the space designer, but the continuing desire for wider and wider data bandwidth demands that the designer make his choice wisely. In those cases where a high data rate is not generated by spacecraft sensors, time competition for receiving sites will pressure the telecommunications design toward a higher data rate. That is, if a space vehicle is transmitting data at a slow rate, a rate adequate for the data being detected, it may utilize a deep-space tracking station for many hours. If, however, the data were transmitted at a much faster rate, time allotted to such a space vehicle might be arbitrarily short.

The advent of lasers as a possible communications means further compounds the nature of the communications problem. In some areas people are highly in favor of lasers and feel that this is the ultimate answer to the communications problem. In other areas people are very negative toward these new technological methods in terms of deep-space communications. The object of this study is to determine what is the net worth of lasers and then to match that net worth with the particular application for which they are best suited.

There are two major ultimate goals of this study contract. The first goal involves the ground system design. The study requires that the existing ground systems be carefully critiqued. This critiquing will document, in a convenient form, the various key parameters of ground systems. In addition, it will provide a basis for determining what additions or what changes should be made in these systems to provide suitable capability for future deep-space communications requirements. A second part of ground systems review will be the inclusion of proposed improvements or changes to the ground system, allowing both additional radio frequency capabilities and additional capability using laser frequencies. In the latter case, the ground network may be a hybrid system in the sense that the primary receiving site may be a satellite located above the earth's atmosphere working in conjunction with ground stations.

A second major goal of the study contract is to formulate a handbook for space communication design. This handbook will enable a communications designer to determine what is the best communication system based on the requirements given. The handbook will contain three major sections that deal with the solution of the problem. Interwoven with these three major sections will be a fourth, which is the communication choice available to the designer. The three major sections of this space communications handbook are: methodology, parametric studies, and state of the art. The methodology is the method of solving the space communications problem. It will include the interrelationships among the various parameters involved in the space communications problem. In addition, the methodology will contain logical methods of arriving at optimum system for a given set of space communications requirements.

The parametric studies to be documented in the space communication handbook will illustrate the parametric interrelationships of the various parameters of the space communications problem. These parametric studies will be calculated over wide ranges of parameter values and will enable the designer to realize the trade-off of his design.

The state-of-the-art portion of the space design handbook will provide limits to the parametric studies and will document the state of the art at present and will project state of the art for each parameter value for some years into the future.

This section offers a sample solution to a space communication problem in a very simplified way. The objective of this example is to show the general concepts that will be evolved through this study. It is not expected that this

example will be definitive in terms of any particular application presently being envisioned. However, such an example will serve to show the method being used in the subject study.

First, consider the various space communication concepts that might be available for a given space mission. There are the direct spacecraft-to-earth links that might use either a laser or more conventional rf transmission. Second, there is a probe-to-satellite-to-earth transmission link that again might use laser or radio or a combination of these two transmission methods. Third, instead of an intermediate satellite, the moon might be used as an intermediate station with a deep-space probe-to-moon-to-earth link using light and/or radio. Figure 1 illustrates a synchronous satellite above the earth receiving data from a deep-space vehicle. The satellite will be in view by the space vehicle continuously for large portions of the year; thus continuous communication to the synchronous satellite may be achieved with no switchover from receiving station to receiving station such as would be required if the space vehicle were transmitting directly to earth. It might be noted that the satellite shown here as a synchronous satellite may well be a lower altitude satellite, as low as 6436 km (4000 mi), and may still be continuous in view of a space vehicle over a considerable portion of a year. Comparisons of three types of bases, ground bases, moon bases, or satellite bases, are given in Figure 2.

The next step in the designer's consideration of the proper space communication concept to use is that of determining the interrelationships of various parameter values. Figures 3, 4, and 5 illustrate typical parameter values that might be considered by a space designer. In Figure 3, antenna gain versus normalized diameter is given showing the limitations for two different tolerances, one part in two thousand and one part in four thousand. A second typical parametric trade-off that a designer may consider is illustrated in Figure 4. Here the watts per pound available as a function of frequency is given for rf generators. Because of the importance of weight on spacecraft design, this type of curve is extremely important in communications analysis. Figure 5 illustrates another type of parametric consideration that will be required for each spacecraft design, the efficiency of the power supply versus the pounds required for each transmitted watt. If the power supply is very efficient, only a small amount of weight is required for the transmitted watts which corresponds to the power supply conversion equipment. As the power supply conversion equipment becomes less efficient, a larger weight is required, reflecting the increase in weight caused by heat radiators which must be carried by the spacecraft.

The designer, having reviewed spacecraft concepts and parametric interrelationships, would then apply state-of-the-art limitations on the parameter

values to come to a conclusion of the type of design choices available to him. As an illustration, Figure 6 shows state of the art for system noise temperatures using various types of detectors. As a second illustration of typical state-of-the-art limitations, Figure 7 presents available cw output power as a function of frequency. Plotted here is the power available from transmitter tubes as a function of frequency. The 1960 state of the art and the current state of the art are illustrated.

Having reviewed space communications concepts, parametric value variations, and typical state-of-the-art limitations, the designer will then refer to a methodology of how to solve his particular problem. Figure 8 illustrates a very rudimentary flow chart for such a methodology. It includes four major sections: one of operation and system analysis; a second, communication theory; and third, components technology. These three sections supply inputs to the fourth major section, which is frequency trade-offs. By manipulating various functional interrelationships of the key parameter values, it is possible to obtain channel capacity for an optimized wavelength per pound of communications equipment. The calculations indicated in this flow diagram have been completed for four different transmitting frequencies: 5 GHz, 94 GHz, 3.5 μ, and 0.5 μ. These calculations are simplified by not taking account of losses due to atmospheric absorption. They have assumed a very low background noise, the case of a black sky background, and no account has been taken for the acquisition and tracking weight. A tabulation of these four calculations appears in Figure 9. The key parameters are listed in Figure 10 as is the channel capability for each system weight. This calculation is of such a rudimentary nature that the values of 5 GHz, 94 GHz, and 0.5 μ are essentially the same. The calculation for 3.5 μ shows a considerable reduction in the selected figure of merit, bits per second per pound. This low value is caused largely by the low quantum efficiency of detectors at 3.5 μ.

This paper has presented the type of study to be carried out during the contract period. It is expected that by the end of Phase I, to be completed in early February, that a definitive methodology will have been formulated. During the subsequent Phase II, definitive values of parametric studies and state-of-the-art documentation will join the methodology in formulating a space design handbook enabling the space designer to plan an optimum system configuration for a given set of space communications requirements.
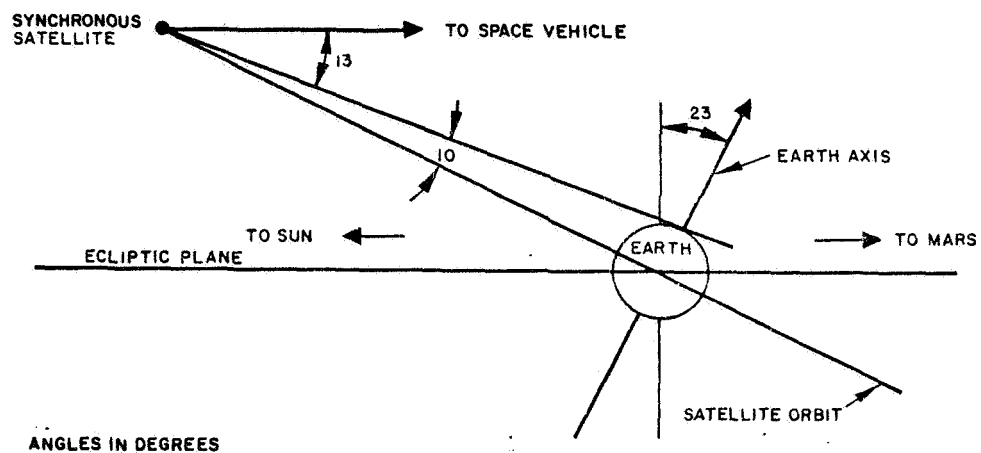
FIGURE 1. FIELD OF VIEW OF EQUATORIAL
SYNCHRONOUS SATELLITE

Base	Advantages	Disadvantages
Ground	Power limited only by laser state of art Antenna size limited only by variable flexure of structure Logistics and maintenance Sophisticated data processing and trajectory prediction equipment available	Pointing accuracy limited by image motion, beam spread Power reduced by absorption and scattering High background noise during daytime operation Possibility of operation depends on meteorological condition Several ground stations required for continuous coverage Switchover and reacquisition problems difficult Long and frequent switchover time
Moon	No atmospheric effects Low background noise Large antenna size possible Possibility of continuous coverage	Pointing accuracy limited by lunar thermal environment Additional ground station required Inter-lunar communication difficulties Sophistication of base(s) dependent on earth-moon transportation and development of manned lunar colonies Most expensive
Satellite	No atmospheric effects Low background noise Continuous coverage probable from single base Reacquisition problems eliminated Cost less than moon link Excellent pointing accuracy	Power and antenna size limited in near future by payload requirements Monitoring and control ground station required Complex equipment Poor maintenance facilities Switchover and reacquisition difficult if occultations occur

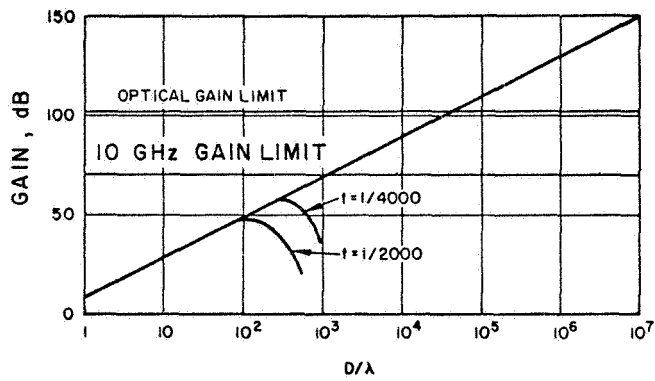FIGURE 2.   COMPARISON BETWEEN OPTICAL LINKS
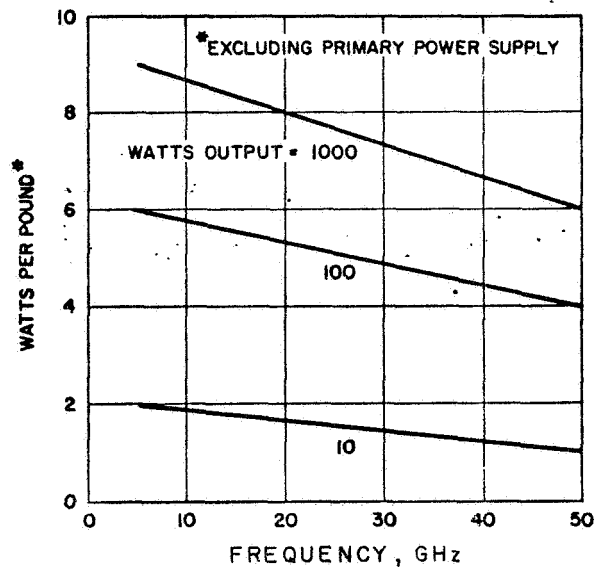
FIGURE 3. PARABOLIC ANTENNA
GAIN VERSUS SIZE

FIGURE 4. ESTIMATED TRANSMITTER WEIGHTS IN
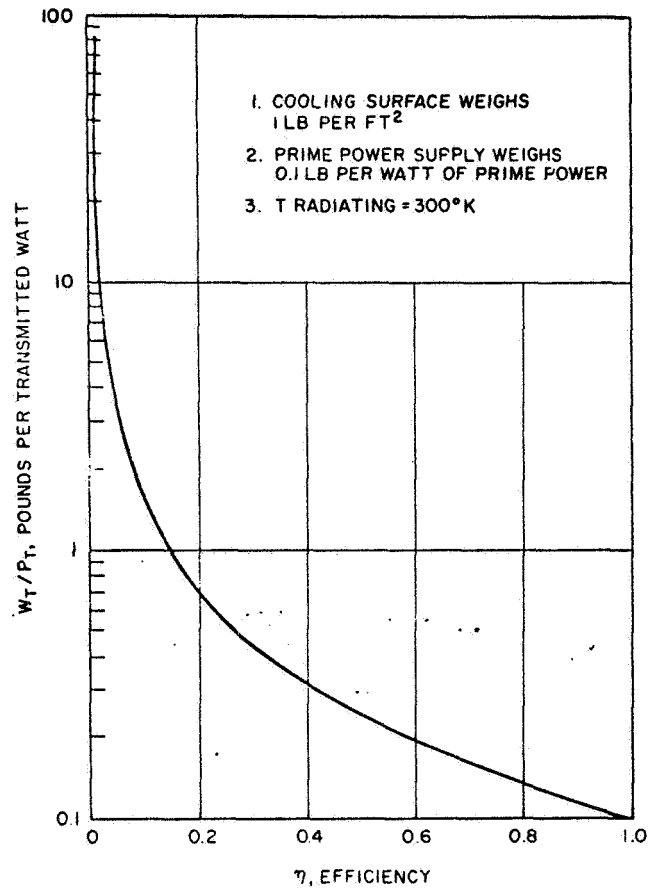SPACE SYSTEM APPLICATIONS

FIGURE 5. WEIGHT OF TRANSMITTER PRIME POWER AND
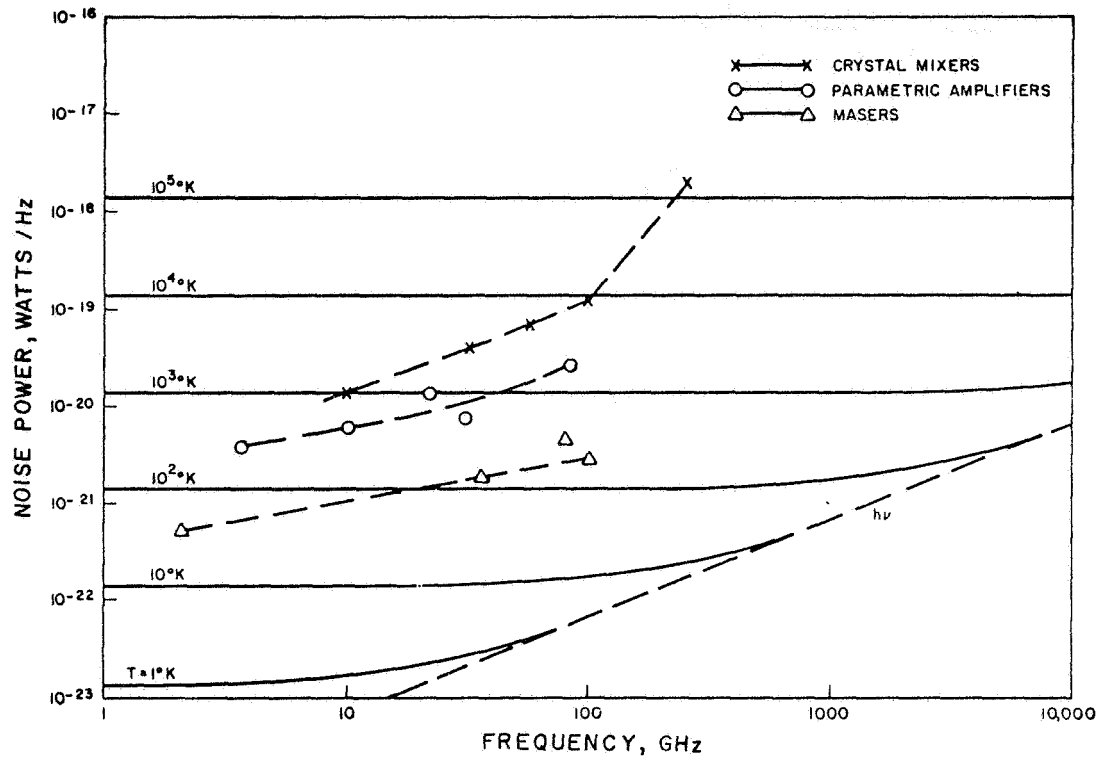COOLING SURFACE VERSUS EFFICIENCY

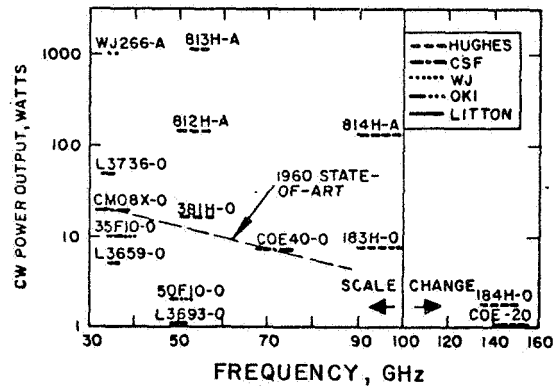FIGURE 6. SYSTEM NOISE TEMPERATURE

FIGURE 7. POWER CHARACTERISTICS OF AVAILABLE HIGH POWER
CW SOURCES. MOST SIGNIFICANT IS 35 PERCENT EFFICIENCY
ACHIEVED IN THE 813H AND MARKED INCREASE IN
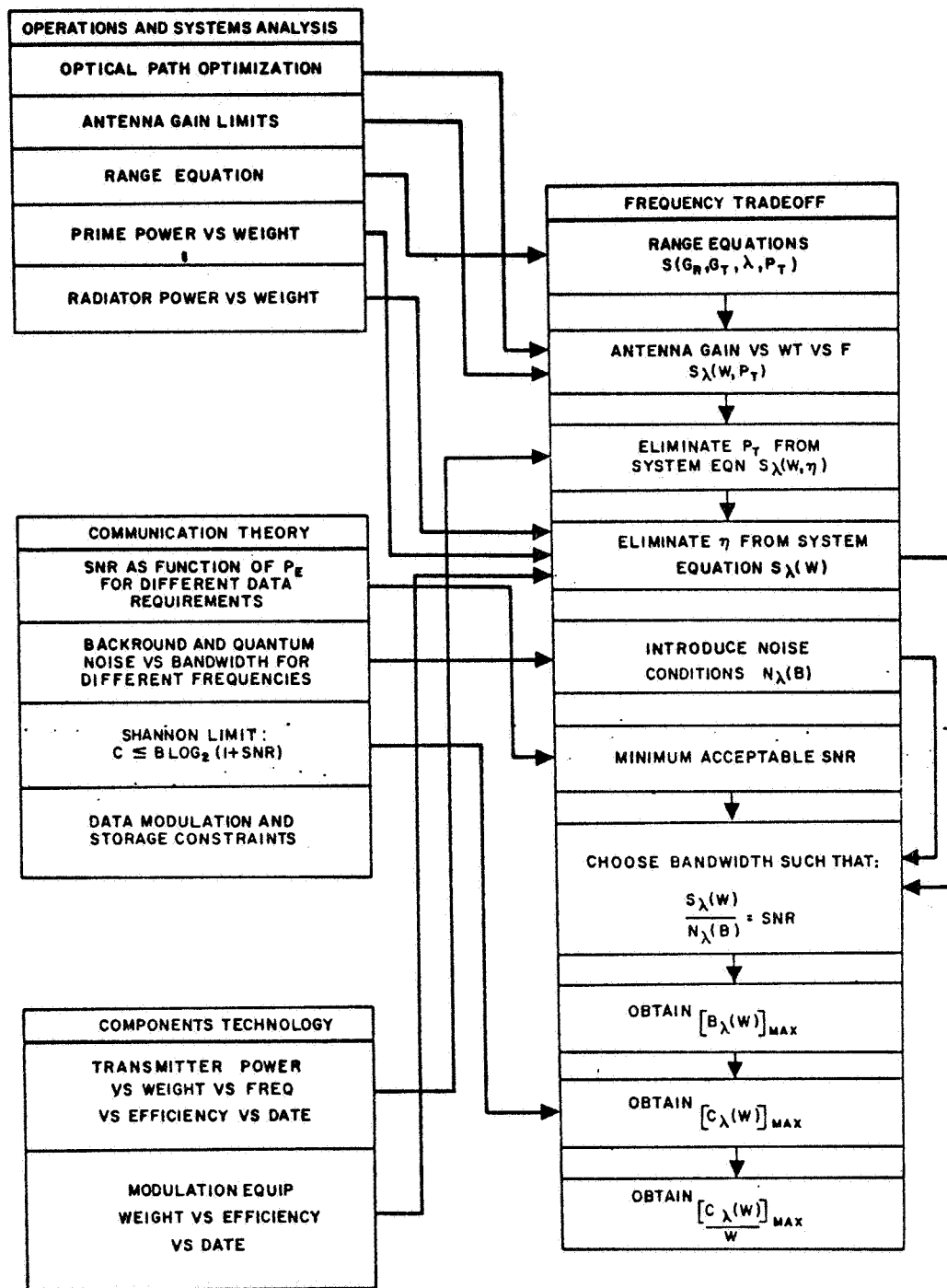AVAILABLE POWER WHICH HAS OCCURRED
SINCE 1960

73

FIGURE 8. FREQUENCY TRADEOFF FLOW CHART

74

E. M. Wave	5 GHz	94 GHz	3.5 μ	0.5 μ
Transmitter Power (watts)	100	100	1	1
Efficiency	0.2	0.2	0.002	0.002
W_T/P_T^*	0.68	0.68	74	74
Prime Power and Heat Radiator Weight (kg)	30.84	30.84	33.57	33.57
Transmitter Weight (kg)	7.71	22.68	4.54	4.54
Antenna Weight (kg)	45.36	27.22	45.36	45.36
Total System Weight (kg)	83.92	80.74	83.46	83.46

FIGURE 9. TYPICAL TRANSMITTER SYSTEM WEIGHT COMPARISON

E. M. Wave	5 GHz	94 GHz	3.5 μ	0.5 μ
Transmitter Power (watts)	100	100	1	1
Range (meters)	10^{11}	10^{11}	10^{11}	10^{11}
Transmitter Antenna Size (meters)	4	3	.1	1
Receiver Antenna Size (meters)	40	20	10	10
Maximum Bandwidth (MHz)	26	258	0.06	520
Transmitter Prime Power (Watts)	500	500	500	500
Total Transmitter Weight* (kg)	83.92	80.74	83.46	83.46
Channel Capacity (bits/sec)	9×10^7	8.9×10^8	2.1×10^5	1.8×10^9
Figure of Merit (bps/kg)	2.18×10^5	2.26×10^6	0.5×10^3	4.4×10^6

*Includes prime power, radiator, and antenna weight.

FIGURE 10. MICROWAVE-OPTICAL COMMUNICATION
SYSTEM COMPARISON

MODULATION-INDUCING RETRODIRECTIVE OPTICAL SYSTEM

R. M. Fleming
I. H. Swift
North American Aviation, Inc.

N 69-71820

The Modulation-Inducing Retrodirective Optical System (MIROS) is a NASA concept for imposing information-carrying modulation onto a light beam by varying the optical properties of a retrodirective reflector. A receiving station directs an unmodulated beam of light at the MIROS transmitter and receives the retroreflected light. By detecting the modulation applied by the MIROS retroreflector, the receiving station acquires the transmitted information.

The MIROS contract requirements included the design of a package incorporating an optical receiver as well as the retromodulator. The optical receiver design is straightforward; therefore, only the retromodulator will be discussed in this paper.

Several approaches are possible for implementing the retromodulator. One approach currently under investigation at Goddard Space Flight Center is based on the use of concentric telescope optics with a mirror at the focus. The telescope optics can be made into a retromodulator by incorporating a means to modulate the light reflected from the curved focal surface, either through interference phenomena or by defocusing the optics by mechanical movement of the mirror surface. The approach studied at North American Aviation (NAA) is to incorporate a means of modulation into an optical corner reflector.

The performance goals for this study were a frequency bandwidth of 20 kHz, ±10-arc seconds return beamwidth, a 50-percent depth of modulation, power requirement of the order of 1 W, and an effective aperture area of 100 cm^2 when used 20° off axis.

In a Phase I program the optical, mechanical, and electrical properties of a corner reflector that incorporated an array of optical modulating elements on one of its three surfaces were investigated (Fig. 1). The corner reflector design was optimized, and the resulting configuration is as shown in the figure. The principal problem studied, however, was the technology of fabricating the modulating elements. The modulating element was a stretched, aluminized Mylar membrane supported by an etched, fused-silica disc (Fig. 2). The area

of the supporting disc behind the membrane was aluminized, thus forming one plate of a capacitor--the aluminized membrane being the other plate. When these plates are electrically driven, the electrostatic forces deflect the membrane from its normal, optically flat position, resulting in modulation of the intensity of the retrodirected beam in the far field.

It was discovered during the study that by allowing a small amount of air to remain in the test chamber enclosing the modulator element rather than evacuating the chamber, the bandwidth of the modulating element could be significantly extended above its vacuum resonant frequency (Fig. 3).

The Phase II program, which was conducted to extend the developments initiated in Phase I, also included new areas of study and experimentation.

The techniques devised during Phase II for the fabrication of the precision optical components of the modulator elements proved to be satisfactory (Fig. 6). Pilot production quantities produced in the NAA optical shop are uniform in height to within 500 Å (1/10 wave). Their membrane mounting surfaces are parallel to their bases to within 0.5 arc seconds, and the mounting surface of each element is flat to within 1/10 wavelength of visible light. The ability to hold these tolerances is significant because, assuming the required optical tolerances of the corner reflector are maintained, the complete MIROS retroreflector should have a return beamwidth less than that corresponding to the individual modulator element dimension (i.e., less than ±10 arc seconds).

The theory of the effect of pressurization on bandwidth and driving power was developed and experimentally verified to frequencies of about 20 kHz. Theoretical extrapolation of these data (Fig. 7) showed that a 90-kHz information bandwidth should be obtained at one atmosphere of pressure. The required drive power increases with the square of the bandwidth, however, as would be expected on fundamental grounds for any modulation technique.

During the second phase, several new membrane materials and fabrication techniques were evaluated relative to the performance goals for a MIROS retromodulator (Fig. 8). Organic pellicle membranes were found to have acceptable flatness and optical quality, but their vacuum resonant frequency was much lower than that of metallic membranes. Several different metallic membranes of 1/10 mil thickness were tested; and it was determined that a low-iron-content stainless steel known as "Havar" had the highest yield strength-to-specific gravity ratio, which results in its having the highest potential vacuum resonant frequency (18.3 kHz). The measured specular reflectivity of Havar membranes was only 7 percent of that of a quality optical flat, however. An attempt to mechanically polish the surface produced an inadequate improvement of 2 percent.

78

A replication process involving vacuum deposition on an optical flat was used to produce several nickel membranes having gold reflecting surfaces (Fig. 9). Test results showed that these membranes had nearly ideal optical properties over their 2-cm aperture. The measured specular reflectivity was 80 percent of that of a quality optical flat. The vacuum resonance frequencies obtainable with a nickel film are, of course, lower than that of Havar.

For linear operation, the membrane must be biased to such a curvature that the far-field intensity is reduced to approximately one-half that obtained with the undeflected, flat membrane. This bias is obtained by applying a dc voltage to the modulator. Applied ac modulating signals then cause greater or less deflection of the membrane relative to this biased position. As the membrane becomes more concave or more nearly flat as a function of the modulating signal, there is a respective decrease or increase of the light intensity in the far field. It may be noted that if this dc bias is not applied, then frequency doubling (i.e., severe distortion) will result.

A fundamental problem with the electrostatic drive approach that has been described is that if the bandwidth is extended significantly by pressurization, the restoring force acting on the membrane at signal frequencies will be predominantly due to compression of the confined gas; but the restoring force at zero frequency, or dc, is due only to membrane tension (Fig. 10). This is caused by the fact that the orifice connecting the volumes on either side of the membrane is designed to have a low impedance at low frequencies and a high impedance at high frequencies. There is, therefore, a large difference in the effective spring constant at dc compared with signal frequencies. A relatively small dc voltage will provide the required membrane bias deflection; but, to avoid distortion, the ac modulating signal must be less than the dc bias voltage. Consequently, when the bandwidth is significantly increased by pressurization, only small depth of modulation can be obtained without severe distortion.

The net conclusion from this study is that, assuming further work would yield membranes with the mechanical properties of Havar combined with the optical properties of replicated nickel, the resulting overall performance would approximately meet the stated MIROS goals (return beamwidth of ±10 arc seconds, approximately 20 kHz bandwidth). A modulation index of 42 percent would be obtained with 18-percent distortion; higher distortion would result with a higher modulation index. In view of the inherent difficulties, however, further work along this direction for achieving the projected performance is not recommended.

Subsequent to the completion of the Phase II program, a new approach that obviates these problems was conceived for driving the MIROS modulators.

This new approach employs a drive method similar to that used in electrostatic speakers, to which we can apply the name "push-pull." With this approach, pressurization can be used to obtain the desired bandwidth, and the relationship between membrane driving force and applied modulating voltage is linear. Because high membrane tension is not necessary, replicated metal membranes, such as have been made with high optical quality can be used; pellicle membranes probably can be used also.

The configuration envisioned for the MIROS pressurized modulator element using push-pull drive is as shown in Figure 11. The lower portion of the element is similar to the original design, but a flat quartz disc attached by a thin spacer ring covers the modulator membrane. A transparent conductive coating applied to the inner side of the cover plate forms a third electrode. The gas required for achieving the desired bandwidth by pressurization is permanently sealed within the modulator element. An orifice provides low-frequency pressure equalization on either side of the membrane.

In contrast to the single-ended drive, it is possible with this configuration to deflect the membrane in either direction from its flat position, i.e., both convex and concave deflection are possible. Because membrane deflection in either direction from the normally flat position causes a decrease in the light intensity in the far field, a steady-state bias still is necessary to provide linear operation and prevent frequency doubling. This could be accomplished by applying a dc voltage to the modulator as described previously. It can be accomplished more easily and reliably in this case, however, by an optical rather than electrical bias. The optical bias can be provided by a weak "lens" formed by convex spherical curvature of the top surface of the cover plate. The saggita required is $\frac{1/8\lambda}{n-1}$, where λ is the light wavelength and n is the index of refraction of the cover plate. For n = 1.5, a saggita of $\lambda/4$ will provide the correct bias.

The membrane is located between two electrodes in the MIROS pressurized push-pull configuration (Fig. 12). A voltage is applied between the top electrode and the membrane and between the bottom electrode and the membrane. The difference in the square of the two voltages produces a spherical deformation of the membrane. The pressure restoring forces at high frequencies so far exceed the tension restoring force that the resonant frequency and the required modulation voltage are essentially determined by the gas pressure and the pressure chamber volumes.

The critical parameters are the dimensions of the cell--its diameter D, the depth of the pressure chambers (d) which establish the gaps between electrodes, the thickness of the membrane t, the gas pressure P in the pressure

chambers, and the area density of the membrane material ρ. (All dimensions and units will be in MKS units, unless otherwide indicated.) To produce modulation at an angular frequency, ω, the voltage between the bottom electrode and the membrane will be $E_1 + V \sin \omega t$ and between the top electrode and the membrane it will be $E_2 - V \sin \omega t$.

It can be shown that for the pressurized push-pull configuration the resonant frequency f_r, which is assumed approximately to define the modulation bandwidth, is

$$f_r \simeq 0.141 \sqrt{\frac{P}{\rho d}} \tag{1}$$

Attention will be restricted to a nickel membrane one micron thick, although, presumably, organic pellicle membranes could also be used. Results are presented with pressure measured in units of atmospheres, denoted by a, and the gap size measured in units of thousandths of an inch, denoted by b. Making suitable substitutions*, it can be shown that

$$f_r \simeq 0.95 \times 10^5 \quad \sqrt{a/b} \quad (Hz) \; . \tag{2}$$

This dependence is shown in Figure 13.

Assuming that $E_1 = E_2 = V_0$, it can be shown that the sagitta, Δ, of the spherical deformation of the membrane due to the applied voltages will be

$$\Delta = \frac{\epsilon_0}{55 \, f_r^2 \rho} \left\{ \left(\frac{V_0 + V \sin \omega t}{d} \right)^2 - \left(\frac{V_0 - V \sin \omega t}{d} \right)^2 \right\} + \Delta_0 \; . \tag{3}$$

Δ_0 is an effective or apparent saggita resulting from the weak "lens" used for biasing the modulator as described previously. Simplification of equation (3) leads to

$$\Delta = \Delta_0 + \frac{\epsilon_0}{55 \, f_r^2 \rho} \quad \frac{4V_0 V}{d^2} \quad \sin \omega t \; . \tag{4}$$

The on-axis far-field intensity of light of wavelength λ, reflected from a spherically deformed surface with sagitta Δ, has been shown to vary as

---

* The bulk density of nickel is 8.9×10^3 kg/m^3 so the area density for a one-micron thick membrane is 8.9×10^{-3} kg/m^2. One atmosphere of pressure is approximately 10^5 N/m^2, so $P = 105a$. A thousandth of an inch is approximately 25.4×10^{-6} m, so $d = 2.5 \times 10^{-5}$ b.

$$[\sin (2\pi\Delta/\lambda)/(2\pi\Delta/\lambda)]^2 \quad,$$

so that modulating the deformation symmetrically about an optimum bias* of $\Delta_0 = \lambda/4$ through a minimum sagitta of $\Delta_{min} = \lambda/8$ and to a maximum of $\Delta_{max} = 3\lambda/8$ achieves an intensity swing from 90 percent of maximum to about 30 percent of maximum, giving a 60 percent depth of modulation. Thus, to obtain a 60 percent depth of modulation, the sagitta will have to be modulated over a distance $\lambda/4$. The modulating term of equation (4) will then have to be

$$\frac{8\epsilon_0}{55\, f_r^2 \rho} \left(\frac{V_0}{d}\right)\left(\frac{V}{d}\right) = \frac{\lambda}{4} \quad. \tag{5}$$

Because of the possibility of high-voltage breakdown across the electrode gap, it is necessary to minimize the peak voltage across the gap while satisfying equation (5). This is accomplished by setting V_0 equal to V. (Larger values of V_0 will decrease the required value of V and hence the power dissipation, but the minimization of the peak voltage will be selected as the primary consideration.) With $V_0 = V$, the modulation electric field amplitude E_s (equal to V/d) is

$$E_s^2 = \frac{55}{8\epsilon_0}\, \rho\, f_r^2\, \frac{\lambda}{4} \quad. \tag{6}$$

For 6328-Å light:

$$E_s \simeq 3.14 \times 10^6\, \frac{a}{b} \quad \text{(volts/meter)} \tag{7}$$

$$V = 78.6a \quad \text{(volts)} \quad . \tag{8}$$

Equation (7) is plotted in Figure 13 and equation (8) in Figure 14.

Now the driving power requirements will be considered, the MIROS modulator unit may be considered as two capacitors in parallel, each with a diameter D equal to 0.02 m. The capacitance is thus

$$C = (2\epsilon_0\pi/4)\ (D^2/d)**$$
$$= 2.23 \times 10^{-10}\, \frac{1}{b} \quad . \tag{9}$$

---

* As indicated previously, Δ_0 is obtained by means of spherical curvature of the upper surface of the modulator cover plate rather than by an applied dc voltage.

** For the pressures of interest here we will assume the dielectric constant in vacuo (ϵ_0) to be close enough to the actual dielectric constant.

Strictly speaking, there need be virtually no power dissipation in the modulator. In practice, the product of the rms oscillating voltage times the rms current, which we will call the "volt-ampere power," P_{VA}, will be a measure of the power dissipation associated with the driving circuitry. The rms oscillating voltage is 0.707 V. The current that will flow when the voltage is oscillating at frequency f_m (= $\omega/2\pi$) has an amplitude

$$I_s = 2\pi \, f_m \, C \, V \quad , \tag{10}$$

and the rms current is 0.707 I_s. It is assumed that the power spectrum of the driving signal will be spread uniformly over the frequency range from almost zero to f_r, the resonant frequency. The volt-ampere product is proportional to f_m and therefore the average volt-ampere product or average power is proportional to the average f_m, which will be about 0.5 f_r. Thus the average power dissipation should be

$$P_{VA} = (0.707)^2 \, 2\pi \, (0.5 \, f_r) \, C(V)^2$$

$$P_{VA} = 2.39 \times 10^{-16} \, f_r^{\,3} \, a \quad . \tag{11}$$

This dependence is plotted in Figure 15.

Let us consider a specific design example for which we choose a gap size d equal to two-thousandths of an inch, with a pressurization equal to one-tenth of an atmosphere. From Figure 13, the resonant frequency is seen to be 21 kHz and the modulation field strength will be $E_s = 1.57 \times 10^5$ V/m. The peak electric field across the electrode gap (bias plus modulation) will be 2 E_s = 3.14 x 10^5 V/m. The safe (i.e., no arc-over or breakdown) electric field across a gap is proportional to pressure (in the range of interest); 3 x 10^6 V/m is safe at one atmosphere. Because experience has shown that this limit can be exceeded by a large factor with no detectable problem, we conclude that 3.14 x 10^5 V/m at one-tenth atmosphere is a more than safe peak field strength. From Figure 14, we see that the required modulation voltage will have a zero-to-peak swing V = 7.8 volts. From Figure 15, we see that the power dissipation will be 0.22 mW per modulator unit.

An example of another configuration that could be selected if power requirements were of critical importance is one that operates at one atmosphere pressure with a gap dimension of twenty-thousandths of an inch. The resonant

frequency would again be 21 kHz. Keeping the peak electrical field across the gap less than the conservatively estimated safe value of 3×10^6 V/m, the same depth of modulation could be maintained by increasing the dc voltage to about 1600 V and decreasing the zero-to-peak ac voltage to 4 V. The power dissipation (volt-ampere product) will then be down to 5.5 μW per modulator element. Other combinations of parameters, of course, are possible including configurations having bandwidths considerably greater than 20 kHz. Limiting beamwidths less than ±10 seconds also presumably could be attained through the use of larger diameter modulator elements.

The MIROS concept offers a number of unique advantages for space communications. Based on the studies that have been made, it appears that MIROS retroreflectors fundamentally are capable of being developed into practical, lightweight, rugged, radiation-resistant, and long-lived devices that have very small power requirements. Based on the parameters shown (Fig. 16), the range performance of a satellite-to-ground MIROS system is as shown in Figure 17.

With such performance, it is possible to conceive a number of practical applications of MIROS systems, including the following (Fig. 18):

1. earth-orbiting communications satellite

2. lunar-orbiting communications satellite

3. excursion module/individual astronaut for spacecraft communication link

4. lunar surface-to-spacecraft telemetry

5. spacecraft-to-ground link during rf communications "blackout"

MODULATION INDUCING RETRODIRECTIVE OPTICAL SYSTEM

FIGURE 1. MIROS

BANDWIDTH	20,000 Hz
BEAMWIDTH	± 10 SEC
DEPTH OF MODULATION	50%
POWER REQUIREMENT	ORDER OF ONE WATT
EFFECTIVE AREA	100 CM^2 WHEN OPERATING 20 DEGREES OFF-AXIS

FIGURE 2. MIROS RETROMODULATOR PERFORMANCE GOALS

OPTICALLY CONTACTED,
FUSED-SILICA
REFLECTOR ASSEMBLY

TRIHEDRAL REFLECTOR
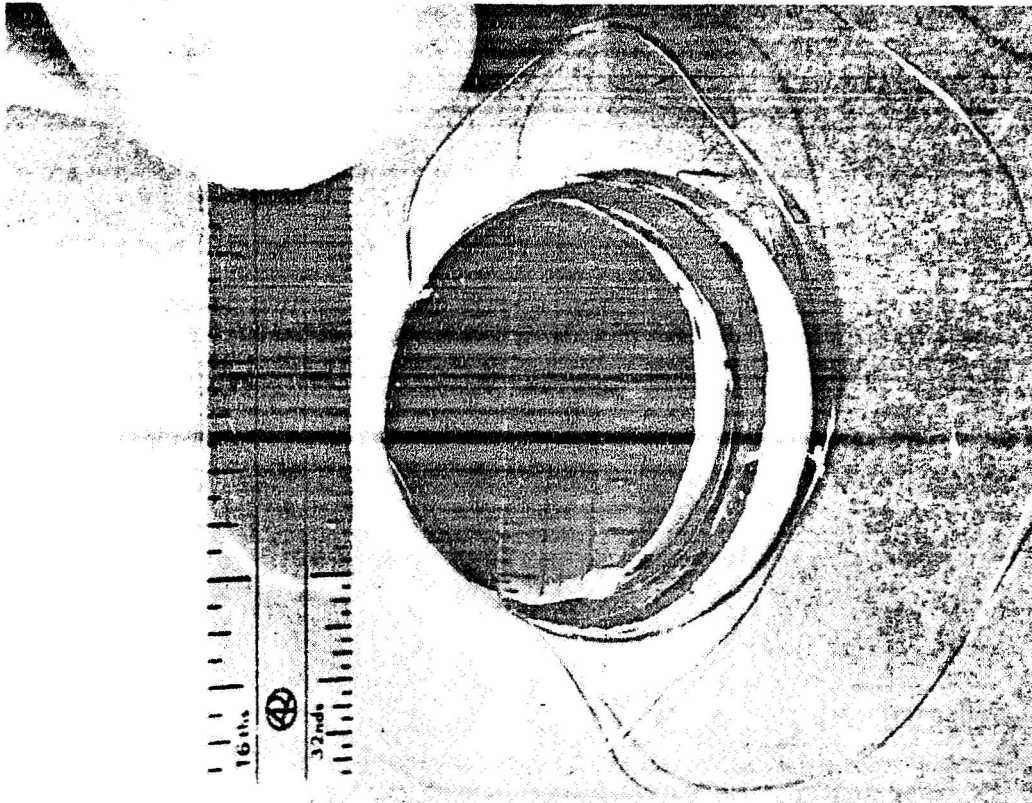CONFIGURATION
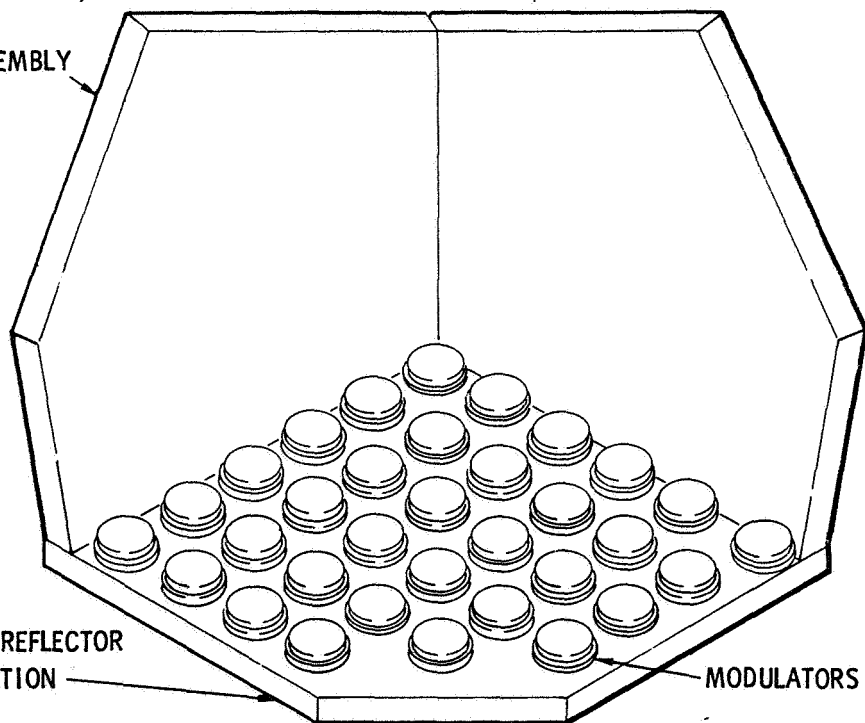
MODULATORS

FIGURE 3. MIROS RETROMODULATOR UNIT

FIGURE 4. MIROS MODULATOR SUBASSEMBLY
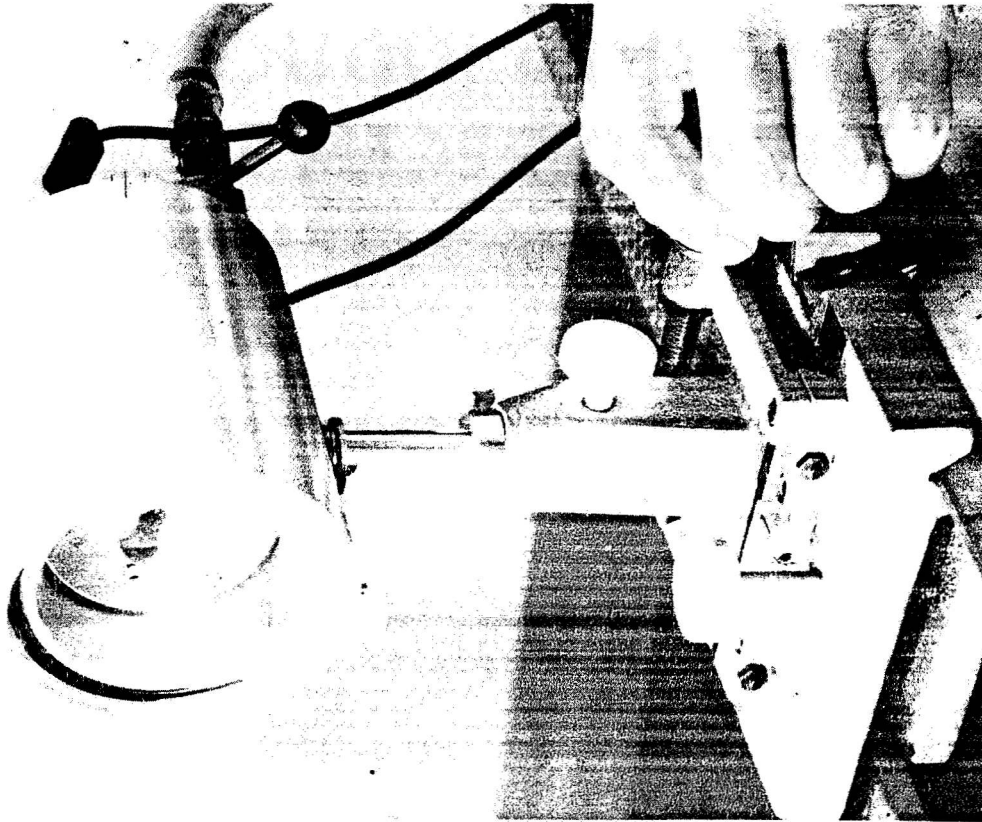
FIGURE 5. VACUUM TEST CHAMBER CONTAINING
MODULATOR SUBASSEMBLY

86
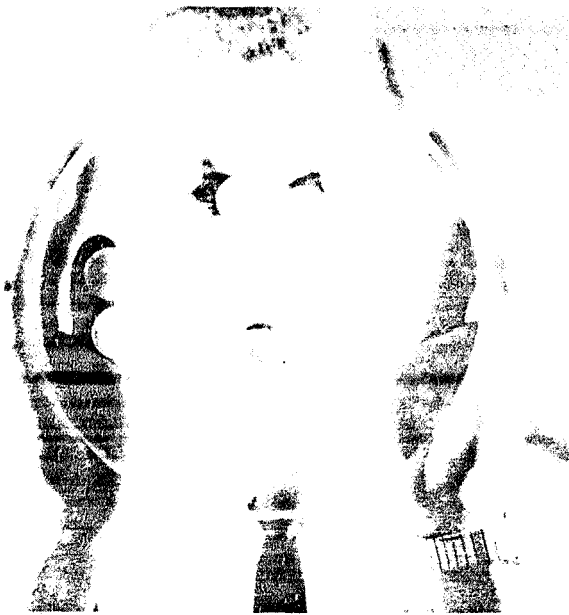
FIGURE 6. OPTICALLY CONTACTED MIROS CENTER DISCS
WITH SUPPORT RINGS
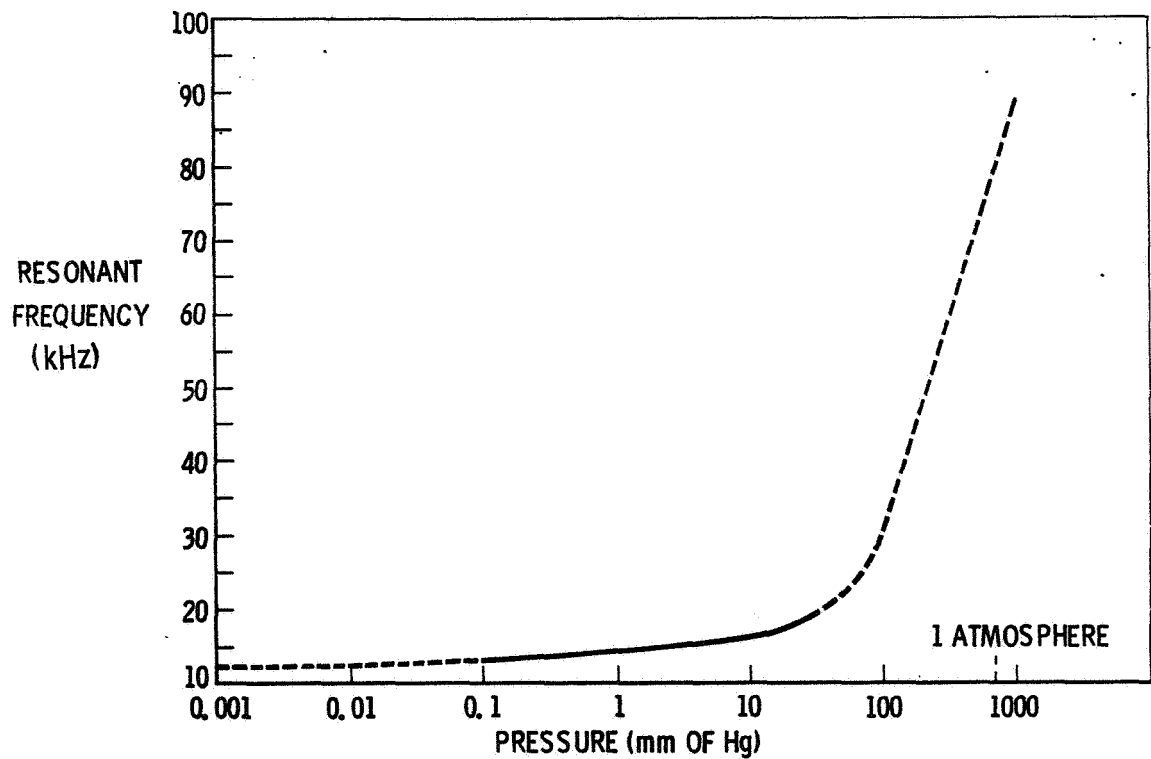
FIGURE 7. RESONANT FREQUENCY VERSUS PRESSURE (EXTRAPOLATED)

87

0. 00254-CM GAP
0. 000254-CM
METAL
MEMBRANE

EVAPORATED GOLD SURFACE

ACTUAL CONTACT
OF GOLD & SILVER

TAB

PYREX RING
FUSED SILICA
MODULATOR DISC
FUSED SILICA MODULATOR BASE

GOLD WIRE

DISC & RING GROOVE
FILLED WITH SILVER PAINT
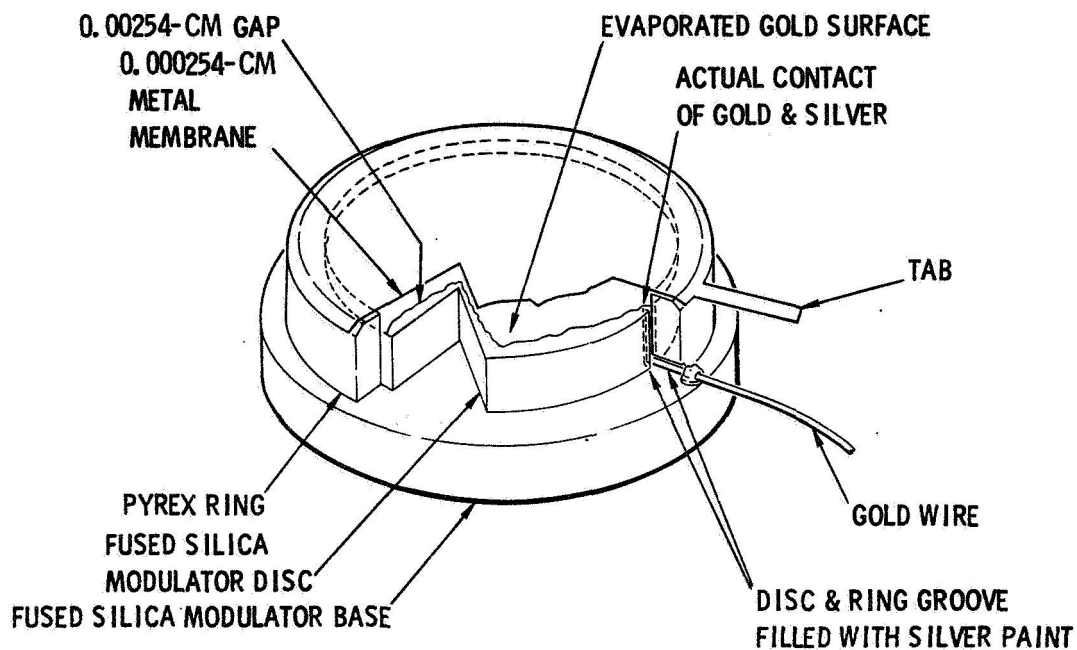
FIGURE 8-A. MIROS MODULATOR SUBASSEMBLY
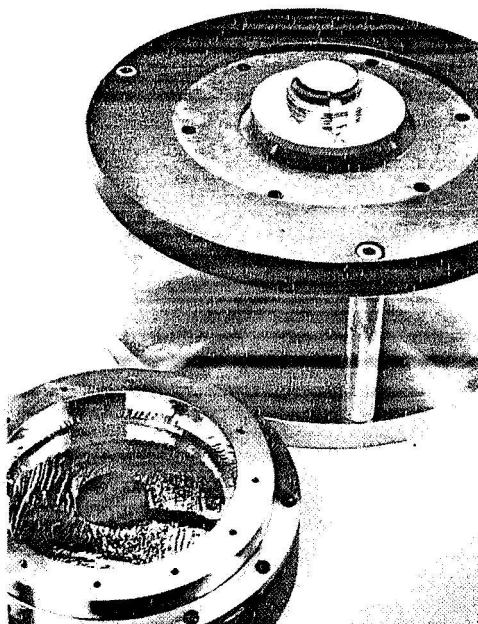
FIGURE 8-B. MIROS SUBASSEMBLY REMOVED FROM ASSEMBLY FIXTURE
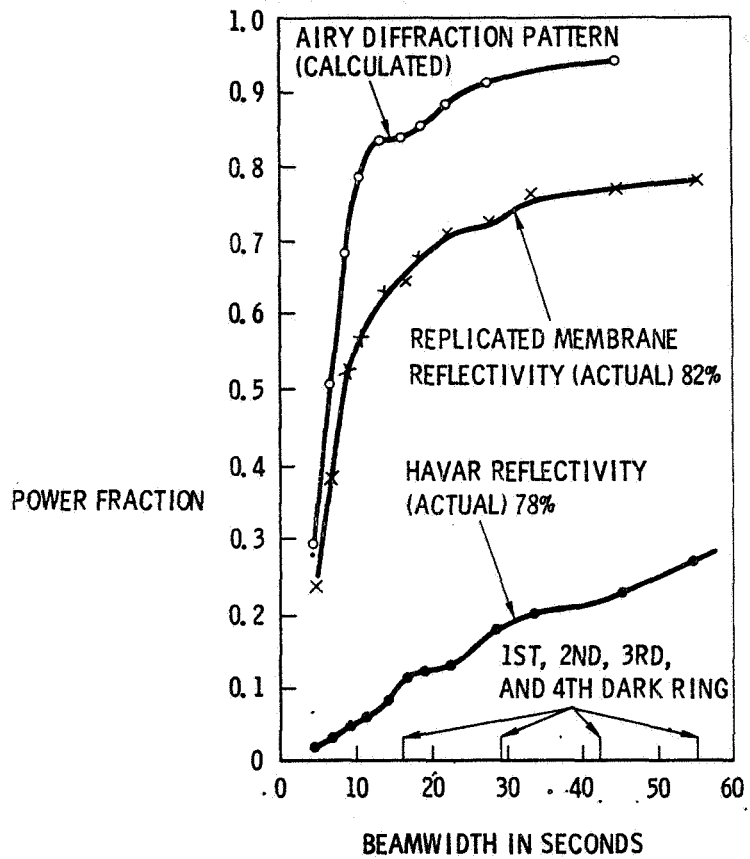
FIGURE 9. BEAM ENERGY VERSUS BEAMWIDTH
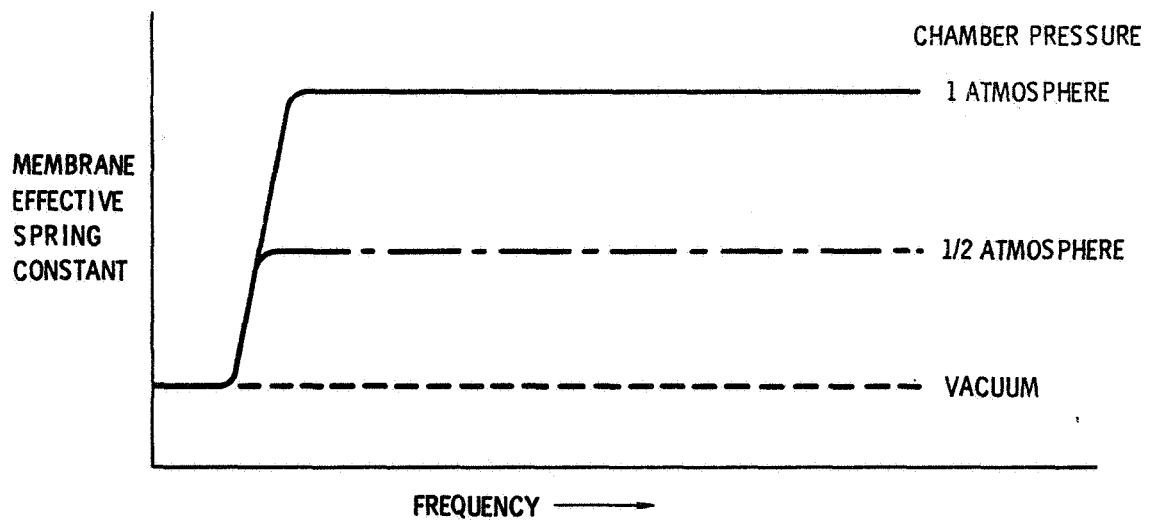
FIGURE 10. MEMBRANE EFFECTIVE SPRING CONSTANT
VERSUS FREQUENCY
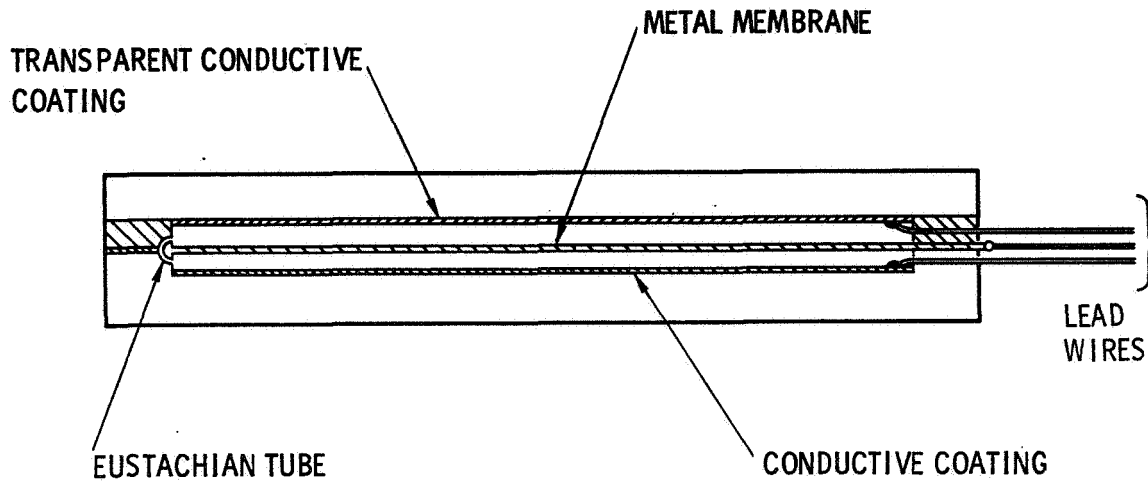
FIGURE 11. CROSS SECTION OF MIROS MODULATOR
(SCHEMATIC - NOT TO SCALE)
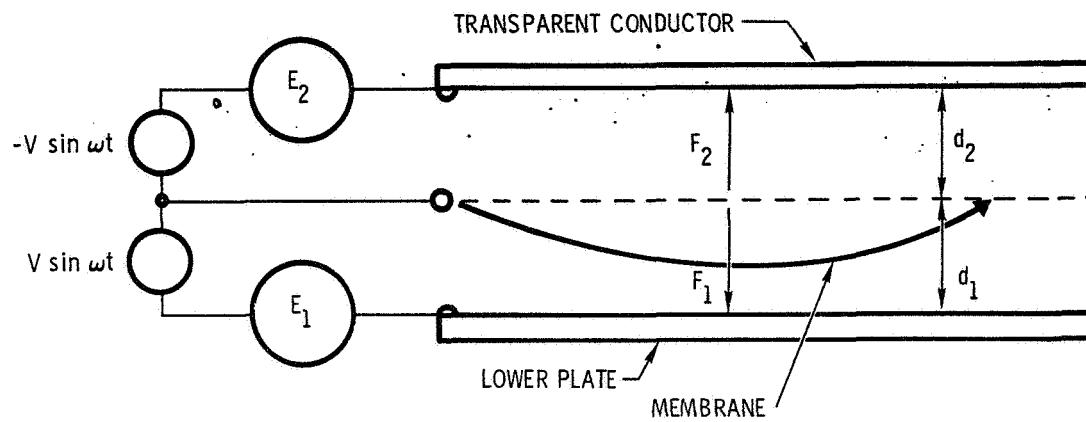
$$\text{NET FORCE} = F_1 - F_2 = K \left[\frac{(E_1 + V \sin \omega t)^2}{d_1^2} - \frac{(E_2 - V \sin \omega t)^2}{d_2^2} \right]$$

WHEN $d_1 = d_2 = d$:

$$\text{NET FORCE} = \frac{K}{d} \left[E_1^2 - E_2^2 + 2V(E_1 + E_2) \sin \omega t \right]$$
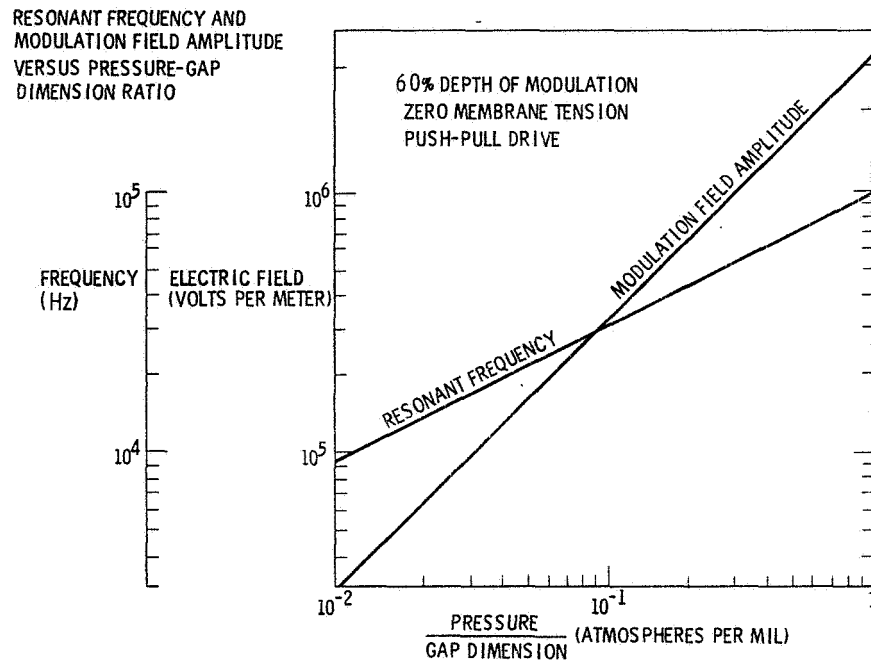
FIGURE 12. PUSH-PULL

90

FIGURE 13. RESONANT FREQUENCY AND MODULATION FIELD
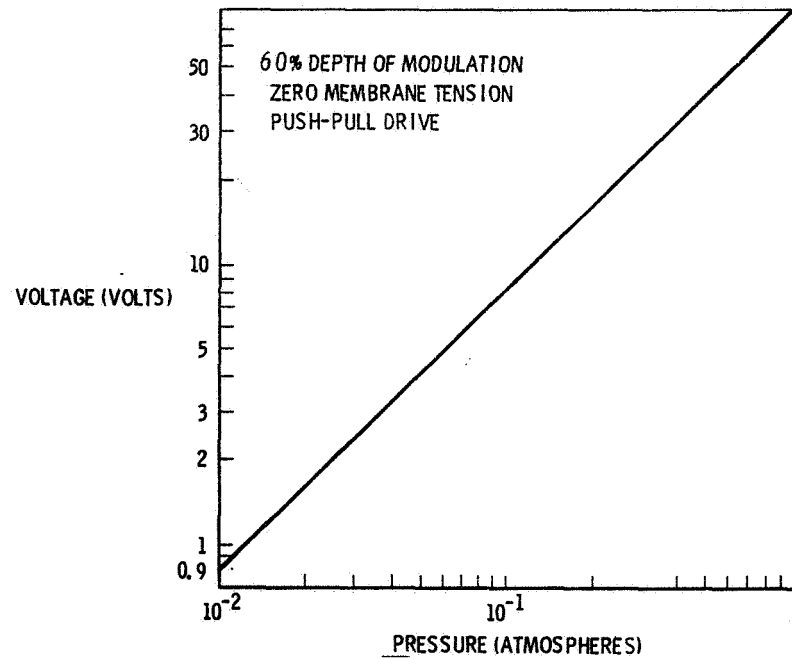AMPLITUDE VERSUS PRESSURE-GAP DIMENSION RATIO

FIGURE 14. MODULATION VOLTAGE VERSUS PRESSURE

VOLT-AMPERE PRODUCT

*ESTIMATED BY VOLT-
AMPERE PRODUCT ASSUMING
MODULATION BANDWIDTH
USED IS EQUAL TO
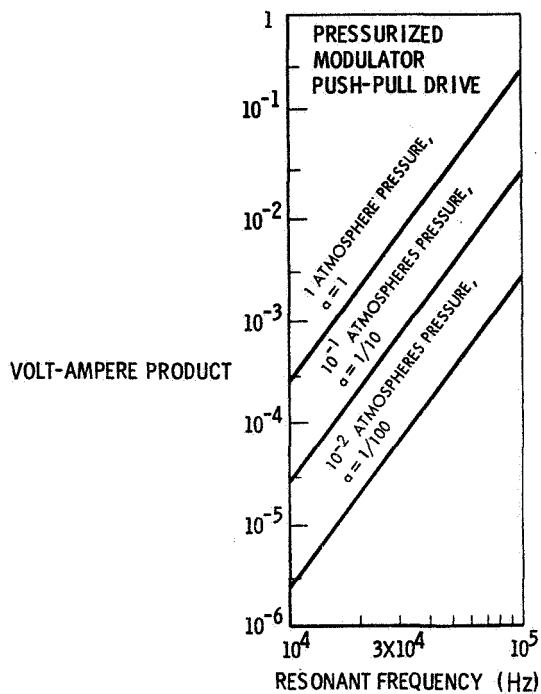RESONANT FREQUENCY AND
60% DEPTH
OF MODULATION

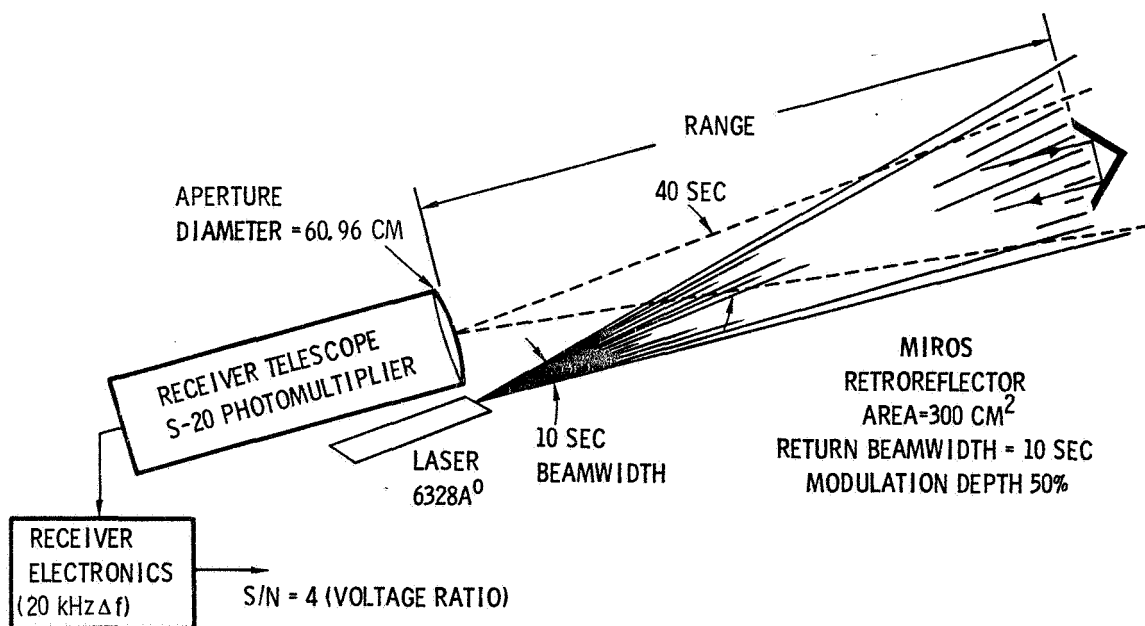FIGURE 15. POWER DISSIPATION* VERSUS RESONANT FREQUENCY
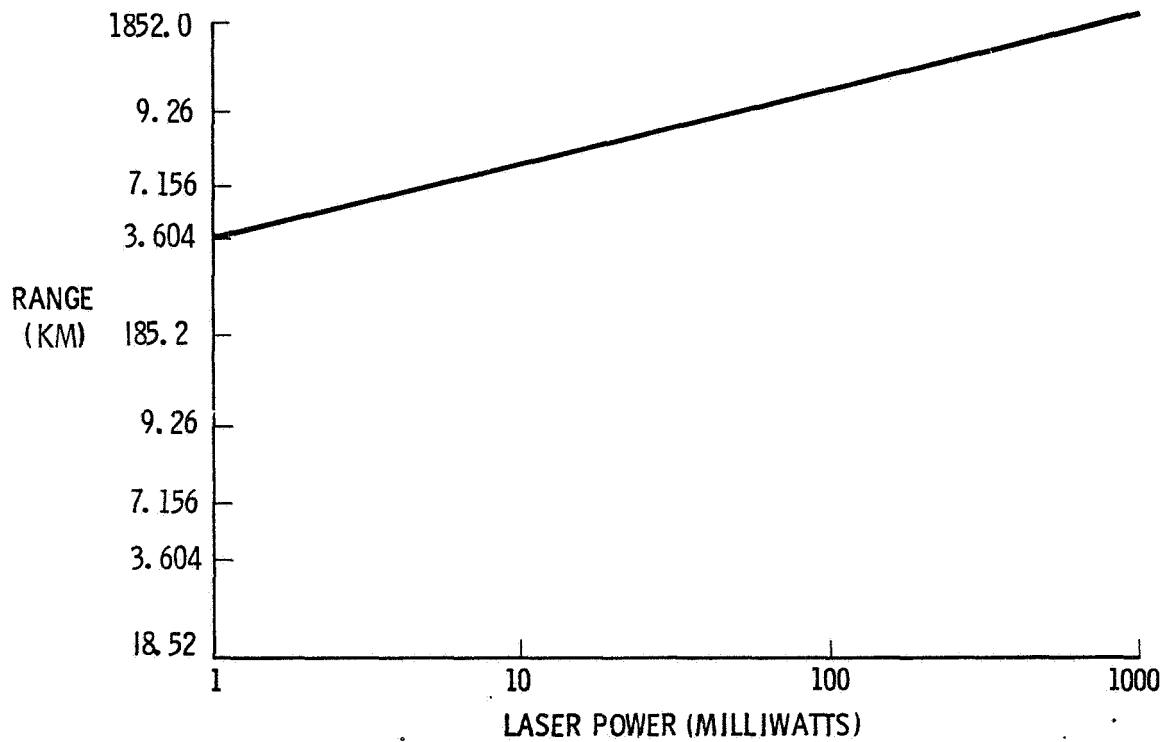

FIGURE 16. MIROS SYSTEM PARAMETERS

92

FIGURE 17. MIROS SYSTEM PERFORMANCE

- EARTH-ORBITING COMMUNICATIONS
  SATELLITE

- LUNAR-ORBITING COMMUNICATION SATELLITE

- EXCURSION MODULE/INDIVIDUAL
  ASTRONAUT-TO-SPACECRAFT COMMUNI-
  CATION LINK

- TELEMETRY-LUNAR SURFACE TO SPACECRAFT

- SPACECRAFT-TO-GROUND LINK DURING RF
  COMMUNICATIONS "BLACKOUT"

FIGURE 18. POSSIBLE APPLICATIONS OF MIROS

DEEP-SPACE LASER ACQUISITION AND TRACKING*

N69 71821

Martin J. Gould
Northrop Space Laboratories

This paper gives some of the highlights and summarizes the results of a 6-month study performed by Northrop Space Laboratories for NASA Manned Spacecraft Center on Deep-Space Laser Tracking and Acquisition [1]. A complete account of this study is contained in a 300-page final report of the work completed in November 1964. This paper is drawn from this final report, but modified to incorporate technological advances brought to light since then. The objectives of the study were as shown in Figure 1.

Although the study was oriented toward optical space communications, we restricted the investigation to the problem of laser/rf acquisition and tracking for possible future manned space missions. The major preliminary problems were the selection of likely missions and the study of occultations and switchover problems for various possible communication link configurations.

The ultimate goal of the study was to uncover R&D requirements in the spirit of the Optical Technology Satellite Program. For this purpose, a conceptual design for a laser/rf acquisition and tracking system was evolved, making use of both present and projected state of the art in lasers, optics, electro-optics, laser pointing, as well as rf tracking.

The various communications links considered are shown in Figure 2:

1. the direct link from earth to Manned Deep-Space Vehicle,

---

2. the use of a lunar relay stations,

3. the use of an earth satellite relay station.

(The lesser problem of communication between two nearby deep-space vehicles was also considered.)

The first objective of the study was to consider the relative basic merits of these configurations as determined from consideration of hypothetical (but typical) missions to Mars and Venus. Some of the missions considered are shown in Figure 3. Here we have three Mars missions with the trajectories projected into the plane of the ecliptic. The ground rules followed in picking these typical trajectories were as follows:

1. to launch near the Mars opposition, which occurs on February 25, 1980,

2. to observe range safety constraints at Cape Kennedy,

3. to have a 30-day launch window at earth,

4. to have a 10-day launch window at Mars,

5. to stay at Mars at least 10 days.

The 1980 opportunity was chosen because it was estimated to be the time of the first manned orbiting or landing excursion to Mars. To keep the total mission time reasonably short, a high-energy trip was assumed. This produced mission times that ranged from 1 to 1.5 years as shown in Cases 1, 2, and 3.

The launch point for all three cases was assumed to be at the same point and time (JD 244 4180 on the Julian Calendar or November 3, 1979).

Here we see the earth orbit; the Mars orbit; and the various MDSV orbits for Case 1 with a 20-day visit to Mars and returning to earth after 420 days; Case 2, also a 20-day visit and returning to earth after 380 days; and Case 3, returning after a 340-day visit. Note that Cases 1 and 2 will pass within the orbit of Venus on the return trip. This near approach to the sun could have serious effects upon the men in the vehicles, due to both thermal and particle radiation, unless they are adequately protected. Note also the low

angular rates involved in the outward journey, and the somewhat faster angular rates on the return journey.

Case 1, the 420-day mission, was studied in greatest detail, and the occultation and switchover studies that preceded the conceptual system design were based on it.

Figure 4 shows the results for three Venus missions. Here again all launches were from the same point and time (JD 244 4340 April 11, 1980). The total mission times were 420, 300, and 200 days, respectively, for Cases 4, 5, and 6.

I indicated earlier that one of the principal objectives was the selection of the most appropriate communication link configuration between direct earth to MDSV, use of lunar relay, or use of earth satellite relay. The most important criterion in making the selection concerns the matter of how many times the communication link will be obstructed by earth, moon, or clouds during the course of the mission. Each time an occultation occurs, it is necessary to switch over the communications to another terminal. Each such switchover amounts to a reacquisition; and with light transit time of 20 minutes round trip, this can interfere with reliability severely. For example, in a cloudless earth three stations, suitably distributed, are required to maintain a direct link at all times of the Case 1 Mars mission. Three switchovers per day for 420 days amounts to 1260 switchovers during the course of the mission.

Figure 5 shows the great advantage of the earth satellite relay in this respect. It can be seen that an MDSV traveling in the ecliptic plane and communicating with an earth satellite relay can avoid occultations altogether if the altitude of the satellite is high enough and it is in a polar orbit. Successive portions of the line-of-sight are indicated by AA', BB', CC', and DD'.

Early in the mission a satellite at 7408 km (4000 n. mi.) would be occulted by the earth for a part of its orbit as indicated by the dotted line 0, whereas a satellite at 14 816 km (8000 n. mi.) or greater would not be occulted. Later in the mission at BB', the situation could improve to the point that a satellite would not be occulted by the earth for any altitude of the satellite. However, still later in the mission at CC', a 7408-km (4000-n. mi.) satellite would be occulted by the earth, but again the 14 816-km (8000-n. mi.) satellite would be clear. During the final stages of the mission, during the return to earth at DD', this situation would deteriorate even more for the 7408-km (4000-n. mi.) satellite, but the 14 816-km (8000-n. mi.) satellite would be still in the clear.

The Northrop study found from computer studies that for a satellite in a circular, polar orbit at an altitude greater than 14 816 km (8000 n. mi.), zero switchovers would be required.

To lessen the reliability requirement imposed on a single satellite relay to operate throughout the entire mission, consideration also was given to the possibility of sharing the mission support time between two satellites at lower altitudes. It was found that this could be done with two circular polar-orbiting satellites, one at 555.6 km (300 n. mi.) and the second at 6852.4 km (3700 n. mi.), each required to operate reliably for 210 days.

An interesting alternative to sharing the mission time is to have the two satellites share the total change of celestial longitude during the mission. This leads to a requirement for two polar orbiting satellites at 2222.4 km (1200 n. mi.), one required to operate for 313 days and the other for 138 days.

The occultations for a lunar relay are somewhat similar to those for a cloudless earth... since a lunar tracker will experience alternately two weeks of viewing and two weeks of occultation. This suggests that two lunar stations would be required to avoid occultations. However, the librations of the moon would lead to periodic occultation of at least the moon-earth link. Therefore three lunar stations are required. The number of switchovers is 1/30 that of the earth, so the number of switchovers range from 20 (Case 6) to 70 (Cases 1 and 4). Although this is a considerable improvement over the number required for the direct earth-link, the logistics of establishing and maintaining three lunar stations is formidable.

Figure 6 summarizes these and other considerations that led to the selection of the earth satellite relay configuration. We have already covered the switchover requirements for the various configurations indicated in the first row. Because approximately 50 percent of the earth is covered by clouds, it can be shown that four redundant stations are required for each of the three ground optical tracking stations, or a total of 15 stations. The lunar relay and the earth satellite relay would require only existing or planned rf stations on the ground. For stabilization and pointing of the tracker, the earth and the moon have a decided advantage over the relay satellite. However, this is somewhat offset by the adverse effects of the earth's atmosphere.

The logistics cost of the direct link stations are low if we ignore costs other than the optical trackers, but they are objectionably large otherwise. Lunar stations are excessively high in cost compared to an earth satellite relay. From a reliability and maintainability point of view, the earth station

is best; but with expected advances in reliability of earth satellites and their components, this may not be significant in the future. We therefore selected the earth satellite configuration as the basis for our conceptual system design with a limited direct link system as a back-up system. The latter must be weighed against the use of the basic rf system as back-up.

Figure 7 indicates the general features of the conceptual system design.

1. From what has been said before, our choice is clearly for a circular polar orbiting earth satellite at an altitude greater than 14 816 km (8000 n. mi.). Although two satellites at lower altitudes can be used with less individual reliability requirements, the higher altitudes make it possible to avoid earth background problems.

2. The past achievements of the DSIF make it a fundamental baseline to any laser system. The ability to reestablish track lost for any reason, at any point of the mission, is mandatory. Therefore the system must be capable of advancing from rf to vernier laser track at all times.

3. In our original system, the astronaut made the coarse optical acquisition by means of a sighting telescope pointed at the sun-illuminated earth. In view of the improved rf tracking accuracy demonstrated in the Mariner, the system now relies completely on rf for coarse acquisition and restricts the use of the astronaut to monitoring and emergency override of the rf pointing commands.

4. Northrop's star point trackers have been used for many applications requiring stellar reference. However, successful use of the image tube tracker in other tracking applications led us to consider it for the conceptual system design. When used with a pulsed laser system, the image tube is attractive for reacquisition because it can determine direction without the necessity of centering the point image, even at low pulse repetition rates. At high pulse repetition rates, or cw, it has the advantage of integration of signal inherent in its operation. It is also attractive from the point of view of providing multiple star reference. The image tube is ideally capable of 1-arc second tracking or better.

5. Preliminary studies of present and projected state-of-the-art studies led to the selection of a 10-joule un-Q-spoiled, 1-pulse-per-second laser. Final decisions as between pulsed and cw systems remain to be determined by basic communication philosophy; i. e., will information be transmitted

intermittently in bursts or continuously? Bradley and transit time errors require differential pointing between transmitted and received signals at any station.

6. The MDSV would employ a 2-axis gimbal system for pointing and the earth satellite relay would rely on vapor jet stabilization [2] and pointing.

Figure 8 shows a simplified block diagram of the conceptual system. The right side is the MDSV transmitter-receiver, and the left side is the earth satellite transmitter-receiver. They are essentially mirror images of each other--optical transmitter, servo control, servo electronics on the earth satellite and vice versa. The initial pointing command comes from the DSIF here at the MDSV computer and here at the earth satellite computer. The astronaut and his override capability are indicated at the top of the MDSV block diagram. The communications system is shown in dotted lines to indicate that it is a completely separate system in this design.

Now let me indicate the general nature of the acquisition procedure with the help of Figure 9.

1. The earth-based rf tracking (DSIF) will provide the initial pointing commands to an accuracy of ± 5 arc seconds from the MDSV to the relay and with an accuracy of 2 to 20 arc seconds from the relay to the MDSV.

2. The astronaut monitors the entire acquisition process, but can also make emergency acquisition with his sighting telescope pointed at the sun-illuminated earth as a point of reference.

3. The astronaut aboard the MDSV pulses the 10-arc second laser beam that illuminates the relay satellite.

4. The earth satellite receiver, previously pointed by the DSIF, acquires the MDSV within its 40-arc second f.o.v. and tracks to an accuracy of approximately 1 arc second using a 50.8-cm (20-in.) optical system.

5. A quasi-boresighted 3-arc second laser beam illuminates the MDSV.

6. The MDSV tracker now tracks this laser beam within its 10-arc second f.o.v. to accuracy of 1 arc second.

As shown in the final report, corrections for transit time errors of up to 20 arc seconds must be incorporated into these tracking loops. This system, employing only moderately small laser beamwidth, produces adequate energy, and the small f.o.v. in the receivers permits the MDSV tracker to see the earth satellite laser without earth background radiation interference. For the laser above, about 10^5 photons per pulse are collected by a 50.8-cm (20-in.) receiver 1.6 x 10^8 km (10^8 mi) away. The laser communication system can now operate within the tracking accuracy of the system.

If the cw communication system requires 0.1-arc second tracking, the system described would require further advances in the state of the art.

Time does not allow discussion of the state-of-the-art studies performed in lasers, detectors, and other components that form the basis for the conceptual design. However, I would like to point out some of the limitations of the present state of the art.

1. In gimbal pointing, radial play uncertainties in ball bearings can cause angular uncertainties of ± 4 arc seconds. If radial play is reduced, bearing friction becomes a limiting factor. However, both fluid and gas bearings are presently achievable, and, under conditions of weightlessness, the friction and gimbal deflection problems can be overcome.

2. Present angular readout by two-speed synchros are limited to about 3 arc seconds.

3. One year lifetime for 10-joule lasers pulsed 1/sec will require an advance in the state of the art.

4. Advances in available pulse repetition rate will increase the system sensitivity because of integration inherent in the image tube. Higher pulse rates may require smaller energy per pulse and this would require smaller beamwidth, which, in turn, would impose the necessity of better pointing accuracy.

5. The ability of an image tube to generate precise error signals is limited by the nonlinearity of the sweep voltages into the deflection coils. Present state of the art is about 0.1 percent.

Drifts in image tube power supplies can also limit resolution.

Because the various parameters are so interrelated, it is clear that advances in all of them are not necessary to produce a feasible system. Almost any two of them would suffice.

In conclusion, because deep-space manned missions are somewhat in the future, the prospects seem optimistic for attaining the required technological advances within the available time scale.

REFERENCES

1. Deep Space Laser Acquisition and Tracking Study. Final Report, NASA/MSC Contract NAS 9-2769, NSL 64-270, Nov., 1964.

2. Vaeth, James E.: Vapor Jet Control of Space Vehicles. IRE Trans. on Auto. Control, Oct. 1962, pp. 67-74.

- STUDY LASER/RF ACQUISITION & TRACKING REQUIREMENTS OF FUTURE MANNED DEEP SPACE MISSIONS

- STUDY SWITCHOVER, GROUND STATION, ACQUISITION & TRACKING PROBLEMS FOR VARIOUS SPACE MISSIONS & COMMUNICATION LINK CONFIGURATIONS

- EVOLVE CONCEPTUAL DESIGN BASED ON PRESENT & PROJECTED S OF A

- EVALUATE SYSTEM & EVOLVE R & D REQUIREMENTS FOR OPTICAL TECHNOLOGY SATELLITE PROGRAM

FIGURE 1.   OBJECTIVES OF 6-MONTH STUDY

EARTH ————————o MDSV

DIRECT

MOON

MDSV

EARTH

LUNAR RELAY

SATELLITE

MDSV

EARTH SATELLITE RELAY
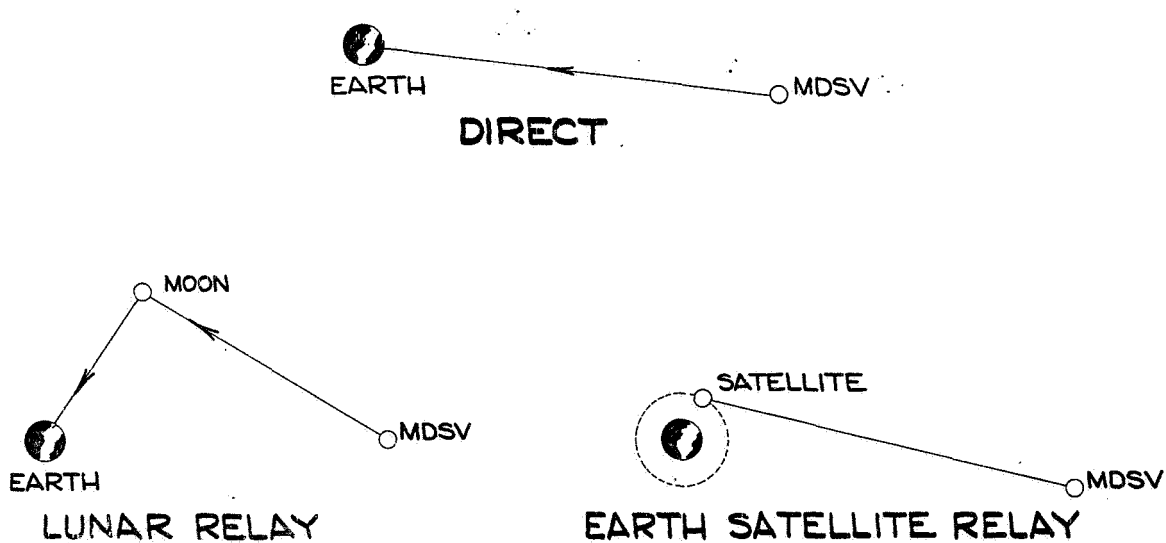
FIGURE 2.   DEEP-SPACE LASER ACQUISITION AND TRACKING

104

PROJECTIONS ON ECLIPTIC PLANE

MDSV

CASE 1 420 DAYS
CASE 2 380 DAYS
CASE 3 340 DAYS

LAUNCH
CALL CASES

VERNAL
EQUINOX

SUN

MARS ORBIT

EARTH ORBIT

VENUS ORBIT

LAUNCH DATE
JD 244 180
(3 NOV 1979)
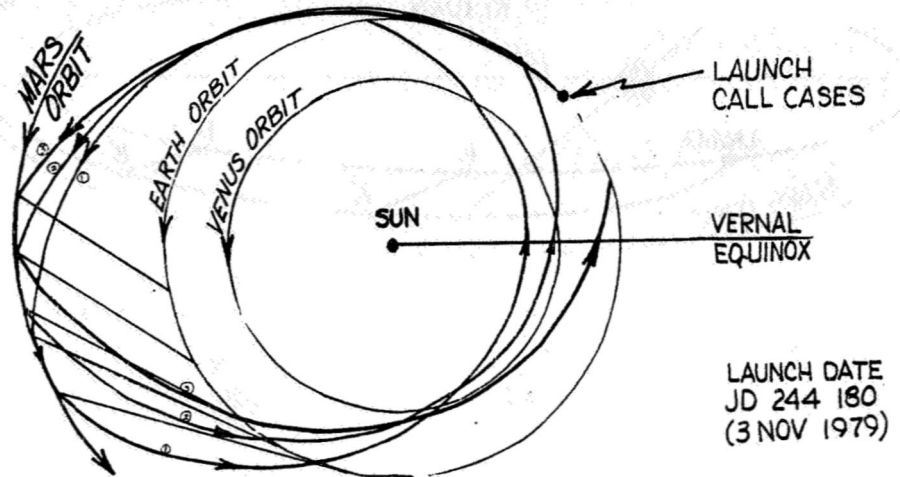
FIGURE 3. TYPICAL MARS TRAJECTORY

PROJECTIONS ON ECLIPTIC PLANE

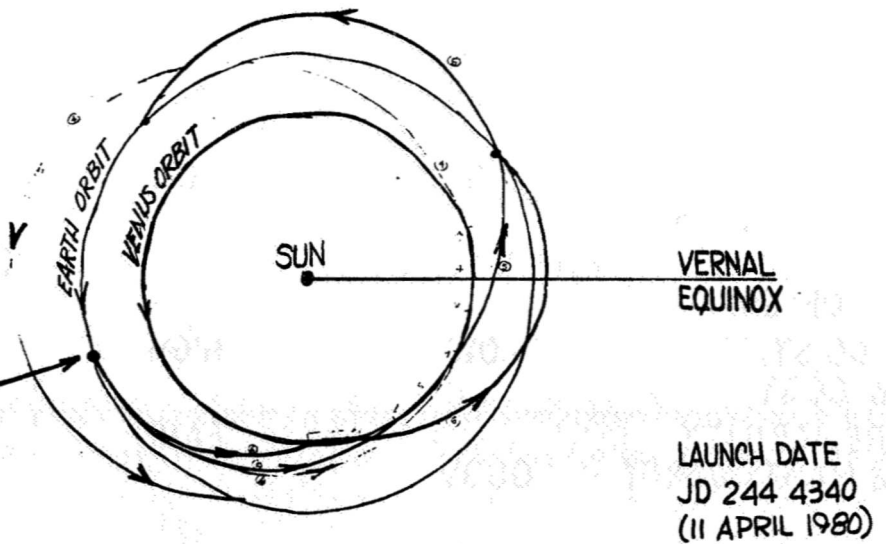MDSV

CASE 4 420 DAYS
CASE 5 300 DAYS
CASE 6 200 DAYS

EARTH ORBIT

VENUS ORBIT

SUN

VERNAL
EQUINOX

LAUNCH
ALL CASES

LAUNCH DATE
JD 244 4340
(11 APRIL 1980)

FIGURE 4. TYPICAL VENUS TRAJECTORY
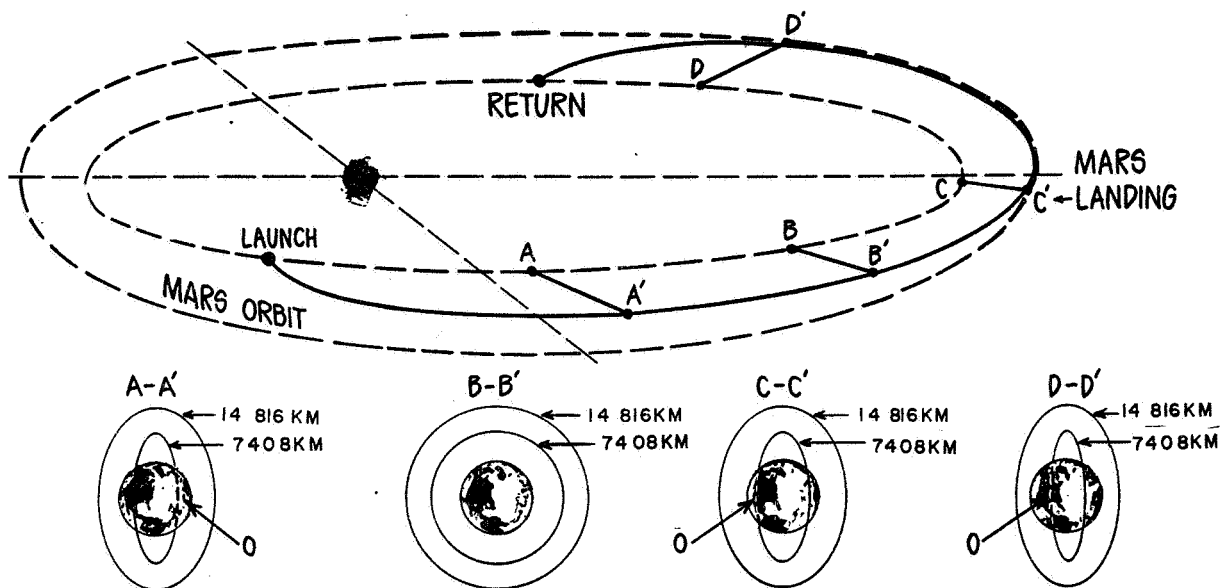
FIGURE 5. OCCULTATION BY EARTH IN TYPICAL MARS MISSION

CONSIDERATION	DIRECT EARTH/MDSV	LUNAR RELAY	EARTH SAT. RELAY
No. OF SWITCHOVER	1263	28	0 1 OR 2
No. OF LASER GRD. STATIONS	15	0	0
POINTING PROBLEM	ATMOSPHERE		STABILIZATION
LOGISTICS & COST	LOW	HIGH	MODERATE
RELIABILITY & MAINTAINABILITY	GOOD	FAIR	FAIR

FIGURE 6. COMPARISON OF VARIOUS COMMUNICATION LINKS

- EARTH SATELLITE RELAY h≥ 8000 NMI

- MAKE USE OF RF (DSIF) FOR COARSE ACQUISITION – ALSO FOR HIGH BANDWIDTH LINK TO EARTH

- USE ASTRONAUT ON MDSV FOR MONITORING AND EMERGENCY ACQUISITION

- USE IMAGE TUBE DETECTOR (50.8 CM OPTICS) FOR LARGE F. O. V. AND 1 SEC TRACKING

- 10 JOULE RUBY PULSES (1/SEC) SEPARATELY POINTED FOR TRANSIT TIME CORRECTION

- VAPOR JET CONTROL OF EARTH SATELLITE POINTING 2 - AXIS GIMBAL CONTROL OF MDSV POINTING
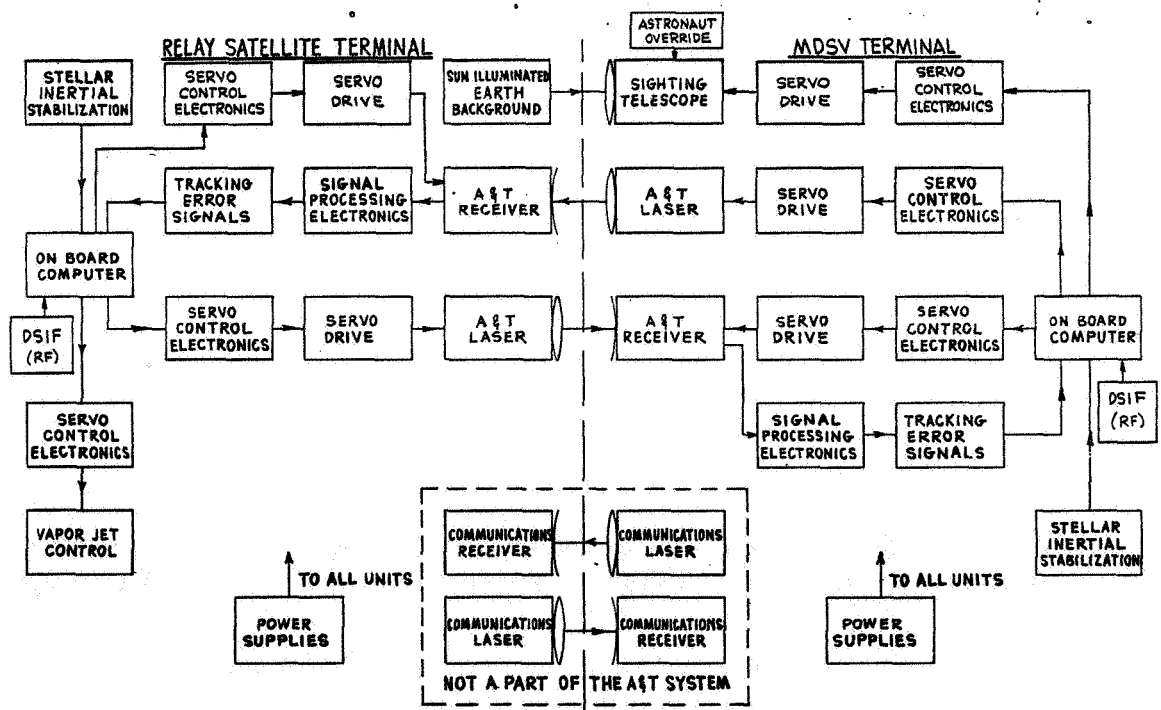
FIGURE 7. CONCEPTUAL SYSTEM DESIGN FEATURES

FIGURE 8. ACQUISITION AND TRACKING SYSTEM BETWEEN MDSV AND RELAY SATELLITE

1 EARTH-BASED RF-TRACKING TO PROVIDE INITIAL
POINTING COMMANDS ± 5 $\widehat{SEC}$ FROM MDSV TO RELAY AND
2 TO 20 $\widehat{SEC}$ RELAY TO MDSV

2 ASTRONAUT MONITORS TRACKING AND CAN MAKE
EMERGENCY ACQUISITION OF SUN-ILLUMINATED EARTH

3 ASTRONAUT ON MDSV PULSES 10 $\widehat{SEC}$ LASER BEAM
WHICH ILLUMINATES RELAY SATELLITE

4 RELAY TRACKER (40 $\widehat{SEC}$ F. O. V.) TRACKS LASER: 1 $\widehat{SEC}$

5 LOCKED 3 $\widehat{SEC}$ LASER (ON RELAY) ILLUMINATES MDSV

6 MDSV TRACKER (10 $\widehat{SEC}$ F. O. V) TRACKS LASER TO 1 $\widehat{SEC}$

FIGURE 9. ACQUISITION PROCEDURE

LASER OPTICS TECHNIQUES

Morley S. Lipsett
Perkin-Elmer Corporation

Steps leading from laser promise to laser practice are under investigation in the Laser/Optics Techniques program Perkin-Elmer is conducting for NASA. Many people have already stressed the promise that lasers hold for high-channel-capacity space communications. The properties of lasers that make for this promise are well known, i. e. , the high degree of spatial coherence that evidently makes practical extraordinarily great antenna gain, and the extremely narrow optical bandwidth that lends itself to narrowband signal detection techniques. The present program is aimed at studying some of the practical factors influencing the design of a future space-worthy optical communication system (O. C. S.). A realistic O. C. S. breadboard is being developed hand-in-hand with experimental studies of the following areas: stability of laser beam intensity distribution in the far field; remote boresight alignment of receiving and transmitting optical channels; isolation of the transmitter channel from the receiver channel; determination of a rotational coordinate reference system about the line of sight; and implementation of fine guidance tracking and pointing offset capabilities.

The system breadboard employs a 40.64-cm (16-in.) aperture diffraction-limited telescope and is based on a one-half scale version of a design outlined in the Phase II OTS report. A Helium-Neon laser functions as the space-borne transmitter, and the guidance optics and detectors are designed for use with a distant argon-laser beam.

A typical layout of the breadboard equipment is shown schematically in Figure 1. An aplanatic Cassegrainian telescope is common to both the transmitting and the receiving optical channels. Channel separation is effected primarily by the dichroic mirror shown in the figure, although the details of obtaining adequate separation are somewhat more complicated and will be discussed in a subsequent section of this paper.

The optical design employs a movable collimating lens for guidance and tracking purposes. By means of the dichroic mirror and two additional lenses, two accurately conjugate f/70 images are formed at the nose of the fine-guidance prism and at the transmit laser field stop respectively. This arrangement insures that the transmitted laser beam is exactly collinear with the incoming beacon

light. The transmitted laser beam can then be offset from boresight as needed for the point-ahead function either by the Risley Prism shown in Figure 1 or by a lateral translation of the lens preceding the laser field stop.

Photographs of the experimental hardware are shown in Figures 2 through 4. The first of these is a photograph of the 40.64-cm (16-in.) aperture telescope structure and shows how it is arranged as a detachable subassembly of the optical bench. Another view of the telescope is shown in Figure 3, which also shows equipment being used to test the transmit-receive isolation properties of specially fabricated dichroic mirrors. The object in the right foreground is a 10-mW Helium-Neon laser, and the black box in the left foreground is a thermoelectrically cooled photomultiplier housing. Figure 4 shows a typical test set up in which the image-transfer optics may be identified as the black cylindrical cells held in the three-axis adjustable mounts. The object in the right foreground is a test autocollimator that was used to try out a method (now superseded) for remote alignment.

A cross-sectional view of the telescope is shown in Figure 5. The secondary mirror is supported at the end of a remote focusing drive assembly, visible in Figure 2, which is electrically driven and imparts an extremely fine control over the telescope focus without otherwise affecting the mirror alignment.

Calculations of signal power received on earth from an optical communications system located in deep space generally assume diffraction-limited concentration of light in the transmitted beam. The practical extent to which this degree of concentration can be stably achieved has been investigated by measuring the beam intensity distribution and fluctuation characteristics in the far field of a typical high-quality gas laser.

An experiment was set up to assess the magnitude of intensity fluctuations in the far field of the Helium-Neon laser shown in Figure 3. By studying the far field, the results relate directly to the beam characteristics of an optical communications system located in deep space. The laser was operated in the lowest order transverse mode (TEM_{oo}) at 6238 Å. As shown in Figure 6, the laser beam was focused to its diffraction-limited spot (its far-field pattern), which was then magnified by a short-focal-length lens and imaged onto a distant screen. This arrangement produced a conveniently large image of the far-field pattern for the subsequent measurements.

110

The principal observations were as follows:

1. The diameter of the far-field pattern was in agreement with diffraction theory. Measurements of the diffraction spread of the laser beam corresponded exactly with the 3-mm bore diameter of the plasma tube.

2. Neither intensity fluctuations within the far-field pattern nor gross lateral motions of the entire far-field pattern were observable visually.

3. Using flexible fiber optic light pipes as probes, the intensity of the light at different points in the far-field pattern was detected by photomultipliers. The photoelectric signals were recorded with a 100-Hz bandwidth, and the fluctuations were measured. The absolute magnitude of the fluctuations was approximately constant across the whole far-field pattern and had an rms value of between 0.5 percent and 1 percent of the maximum intensity in the center of the pattern. This was only slightly more than the relative magnitude of fluctuations appearing in the entire laser output measured in the near field.

4. There was close cross-correlation of the intensity fluctuations at different points of the far-field pattern with respect to each other and with respect to the intensity of the entire laser beam. When the laser output power was reduced (by increasing the mirror spacing of the near-hemispherical resonator, which produces higher diffraction losses) the intensity fluctuations increased considerably.

5. When the output of the photomultipliers was observed with a band-width of 10^4 Hz, the intensity fluctuations in the far field were found to be only slightly increased as compared with the 100-Hz bandwidth observations. The effect of further increasing the bandwidth to 10^5 Hz was merely to raise the level of the shot noise to a comparable magnitude.

From observations 3 and 4 we may infer that the sources of the fluctuations are predominantly smaller than the width of the cavity mode and are statistically independent. The majority of the observed fluctuations probably stem from dust particles floating into the resonant path between the Brewster angle windows and the laser mirror and floating also into the near-field region of the laser beam.

We are therefore able to conclude that, provided the gas laser operates in a fundamental transverse mode, the laser beam does not exhibit spatial fluctuations of sufficient magnitude to be detrimental to a deep-space optical communications system. Intensity fluctuations sampled at various regions in

the far field of the laser beam were found to be typically less than 1 percent, and this amount will not appreciably degrade the S/N of a communications channel.

A synopsis of the present approach to the problem of remote alignment and focus of the optical system is as follows: It can be shown that on account of the large f number of the image transfer optics, the entire optical system can be focused by moving the telescope's secondary mirror and holding the spacing of the rest of the optical elements fixed with respect to the primary mirror. Correct focus can be obtained by monitoring the signals from the fine guidance sensors while the telescope is tracking the earth beacon (effectively a point source). To aid this function, the tracking servo can be dithered slightly. Optimum focus then corresponds to maximum loop gain at the dither frequency, a condition that is easily monitored. It corresponds at the correct focus to minimum dither-induced transfer lens velocity. This is a technique used by Perkin-Elmer in Stratoscope II.

Accurate boresight of the receiver and transmitter channels is not dealt with so easily. Here the best approach is one that uses the least number of additional components. It should also be compatible with the channel isolation requirements and be simple in concept. Figure 7 illustrates one method that meets these criteria. A dichroic mirror is used to pass blue light from an auxiliary source and illuminate the laser field stop. A shutter retracts from in front of two mirrors arranged to reflect light passing through the main dichroic mirror, and an image of the field stop is formed near the nose of the fine-guidance beam dividing prism. This image is in blue light that is passed by the "spike" pre-detection filters. It is detected by the photomultipliers just as incoming beacon light. Boresight alignment is obtained when the laser collimating lens (or a Risley Prism) is adjusted to make the image of the laser stop divide equally among the four fine-guidance photomultipliers. It can be shown that all mechanical tolerances are quite reasonable for this alignment approach.

The key to using common telescope optics for both the receiving (beacon guidance) function and the transmitting function of the spaceborne O. C. S. is effective channel separation. The problem can be stated as follows: how can the guidance photomultipliers be quantum noise or dark current limited at 4880 Å and 5145 Å in the presence of scattered light at 6328 Å from the neighboring high-power HeNe laser transmitter?

By following the optical paths in Figures 1 and 7 it can be seen that the principal source of scattered HeNe light is the main dichroic mirror. If this mirror can be made highly reflective to 6328-Å light and highly transparent to

112

4880-Å and 5145-Å light, and if subsequent optical surfaces leading to the photo-multiplier are given similar coatings, then the isolation problem can be solved in a natural way. To this end we are developing special dielectric dichroic coatings that currently are capable of especially high reflectivity at 6328 Å and 80 percent transmission at the argon lines. In addition, the substrates for these coatings are being fabricated by special techniques that reduce surface scatter to negligible proportions.

Results to date indicate that this approach will not attenuate the sensitivity of the guidance photomultipliers to argon light by more than 50 percent yet it will attenuate their sensitivities to the HeNe light by as much as 140 dB!

If a diffraction-limited laser beam is to intercept a given earth station 16^8 km (10^8 mi) or more away, then it must be biased forward from the apparent line of sight with an earth beacon. The correct aim of the transmitter may be specified by two coordinates; one describing the magnitude of the forward bias angle or point-ahead angle, and the other describing the rotational orientation about the line of sight. An angular reference known to the earth station and available at the spacecraft is needed so that the rotation angle about the line of sight (RLOS) may be determined.

Methods of RLOS determination have been analyzed that rely upon sensing the plane of polarization of the incoming beacon light. Figure 8 shows the results of typical signal-to-noise calculations and is based on fairly optimistic parameters. As may be seen from this figure, the signal-to-noise ratio available as a function of range falls to below unity at about 16×10^6 km (10×10^6 mi).

Another method has been studied and is illustrated in Figures 9 and 10. Two coherent beacons are employed in such a way that the beams are super-imposed at the spaceborne receiver and form parallel interference fringes. The orientation of the fringes may be detected by the scheme shown in Figure 10, thus yielding an RLOS reference. This turns out to be an extremely powerful method at intermediate ranges of less than a few million miles. Its practical limit is about 80.5×10^6 km (50×10^6 mi) and is set mainly by the required base-line separation of the beacons.

Calculations, such as were carried out, all tend to show that at 161×10^6-km (100×10^6-mi) ranges the necessary signal-to-noise ratio for the required RLOS accuracy cannot be met conveniently without resorting to an auxiliary subsystem. It has been shown, however, that if for example a Canopus-seeking star tracker is employed for this purpose these requirements can be met without difficulty.

113

Progress in this area is best summarized by reference to the earlier figures.

Breadboard apparatus is being constructed with precise beam guidance based on equipment and techniques developed in the Stratoscope II project. Instead of steering the line of sight toward a star, the Laser/Optics Techniques approach will steer the line of sight toward a man-made star -- i. e. , an argon beam on earth.

This paper is an interim description of analytical and experimental work in progress on the Laser/Optics Techniques program. This program is clearly demonstrating in the laboratory the suitability of lasers and high-quality optics for deep-space communications. Breadboards of working subsystems are taking shape, and experiments at performance levels suitable for deep-space optical communications are being conducted with the hardware.
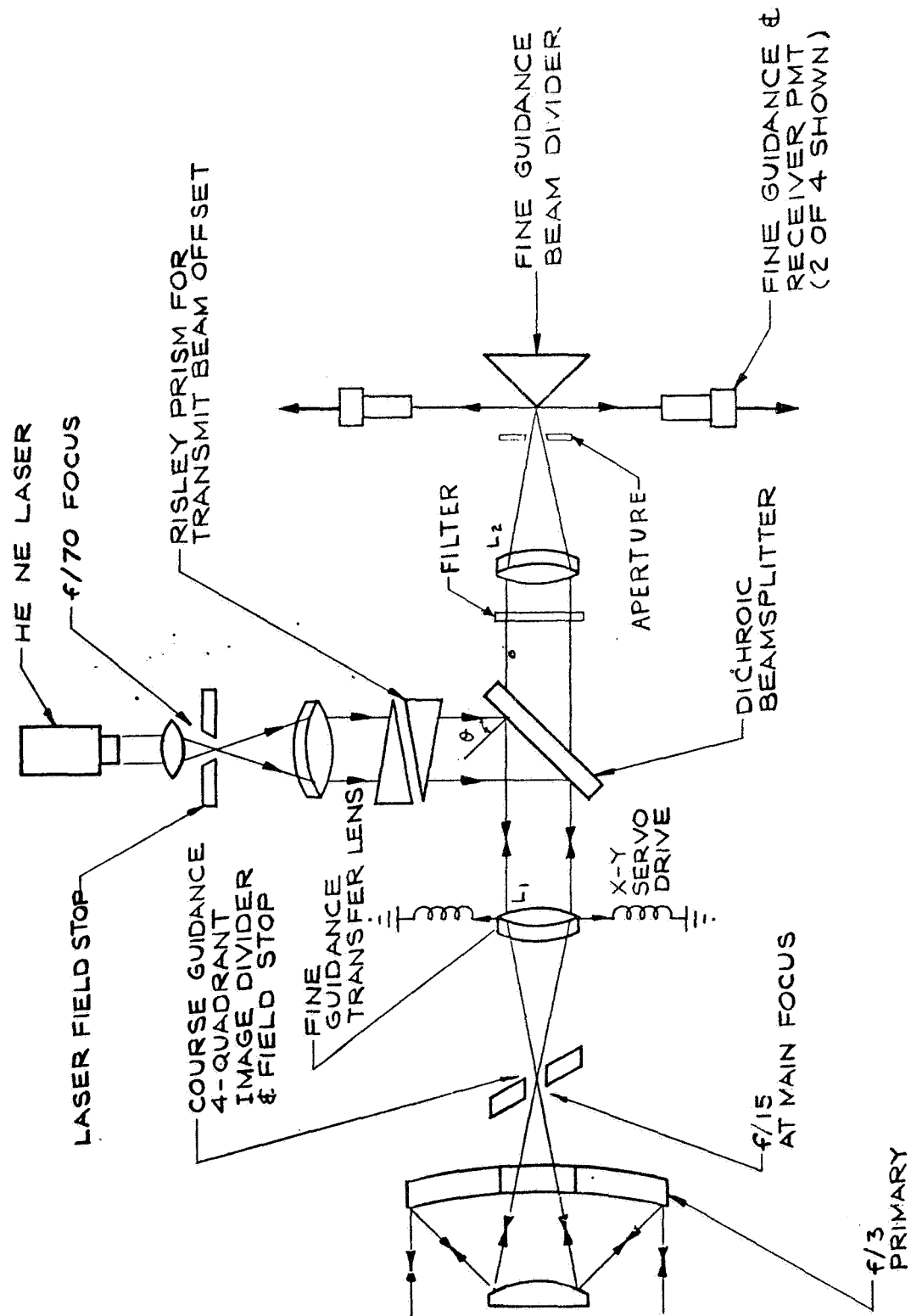
FIGURE 1. LAYOUT OF LASER OPTICS TECHNIQUES BREADBOARD EQUIPMENT

115
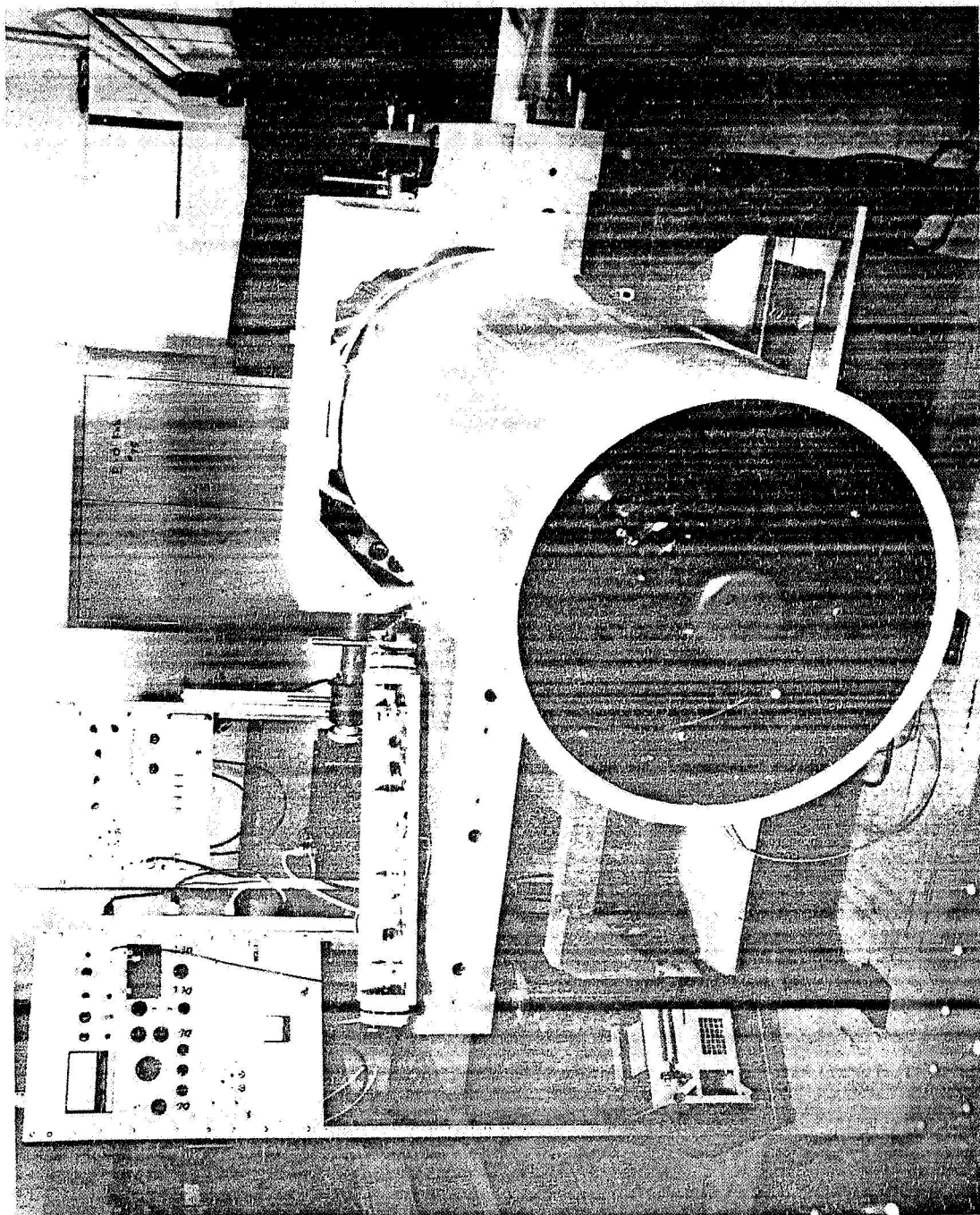
FIGURE 2. PHOTOGRAPH OF OPTICAL BENCH SHOWING TELESCOPE SUBASSEMBLY

116
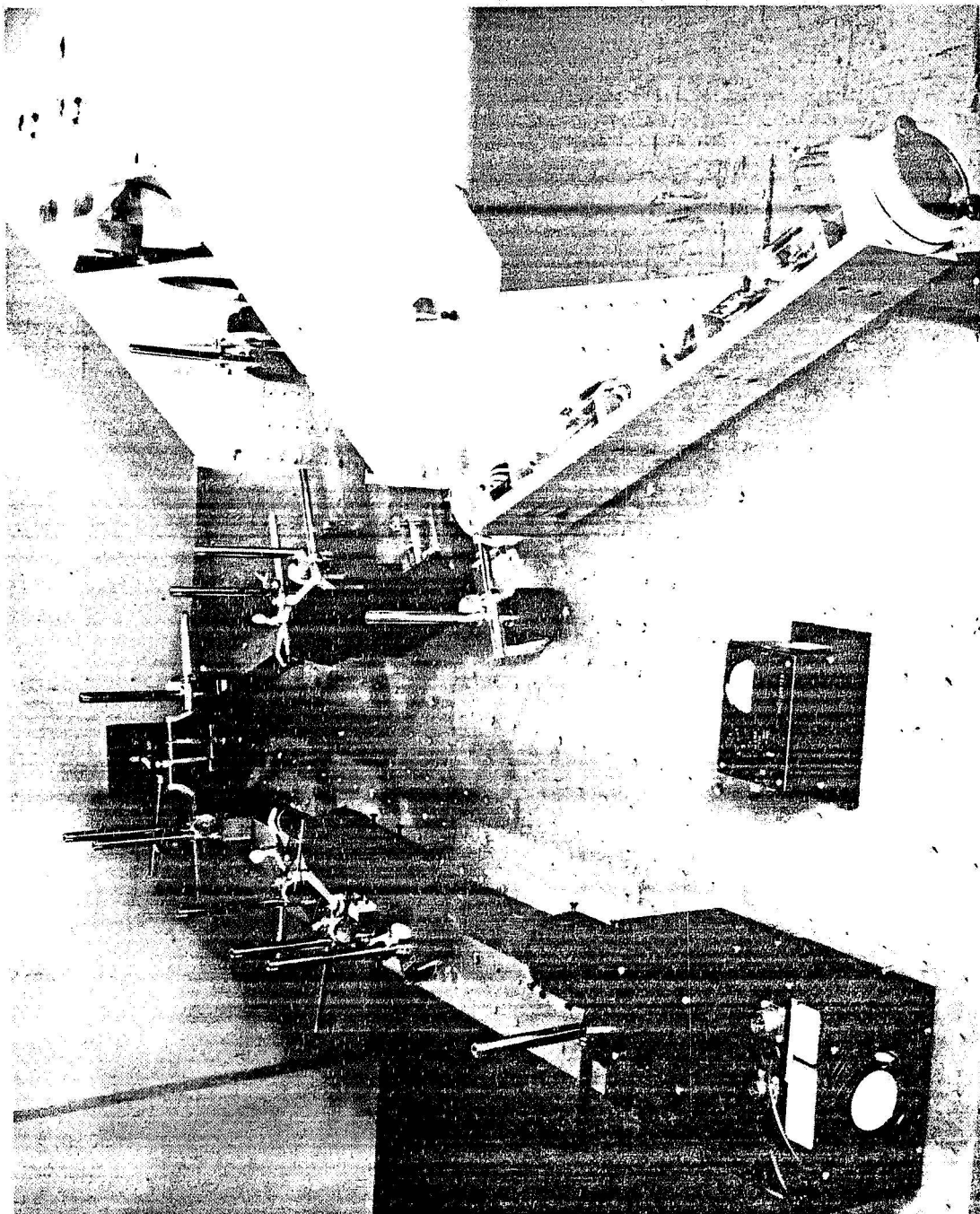
FIGURE 3. VIEW OF OPTICAL BENCH SHOWING EQUIPMENT FOR MEASURING ISOLATION PROPERTIES OF TEST DICHROIC COATINGS

117
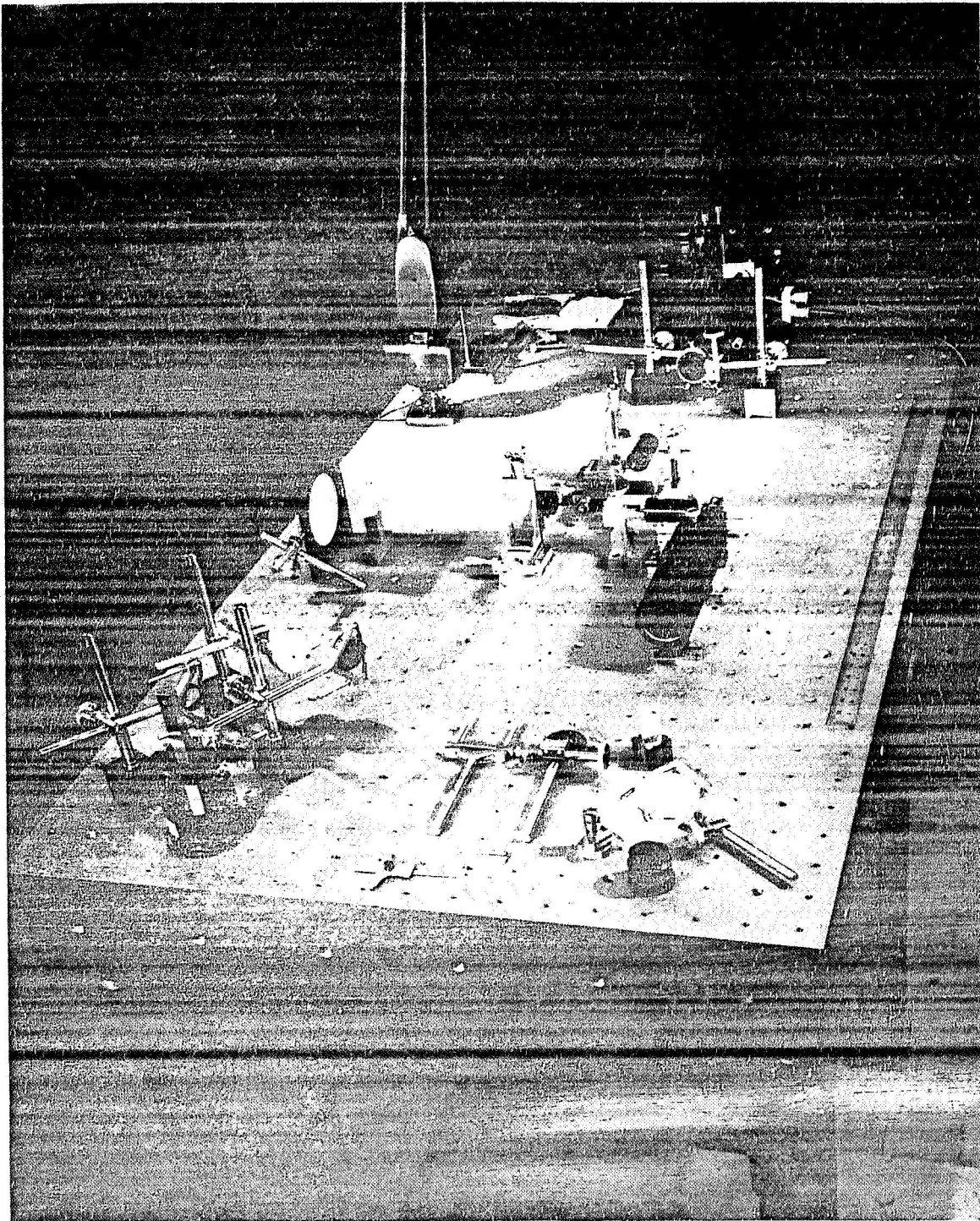
FIGURE 4. VIEW OF LABORATORY EQUIPMENT USED TO
INVESTIGATE ALIGNMENT TECHNIQUES
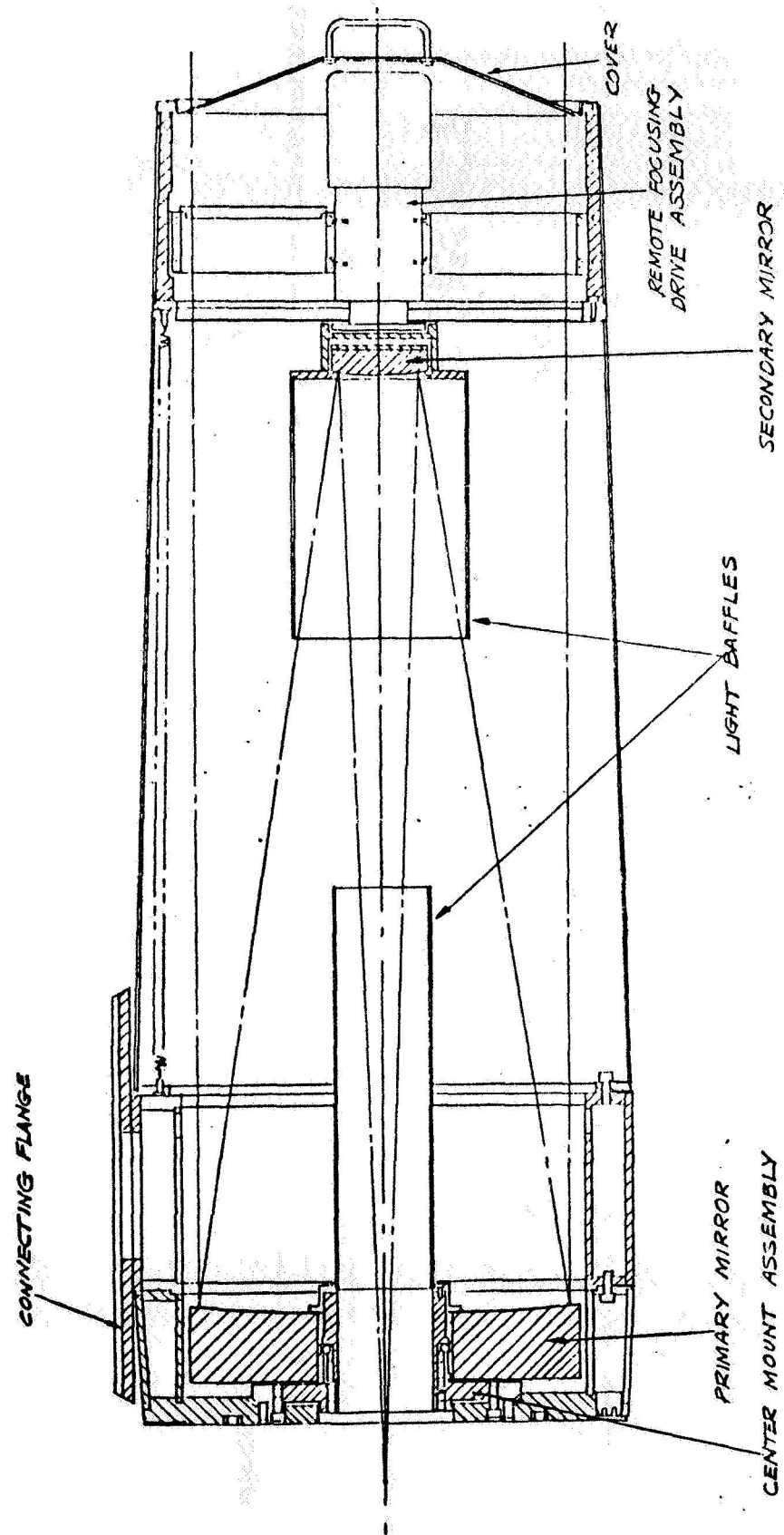
FIGURE 5.   DRAWING OF THE 40.64-cm (16-in.) APERTURE
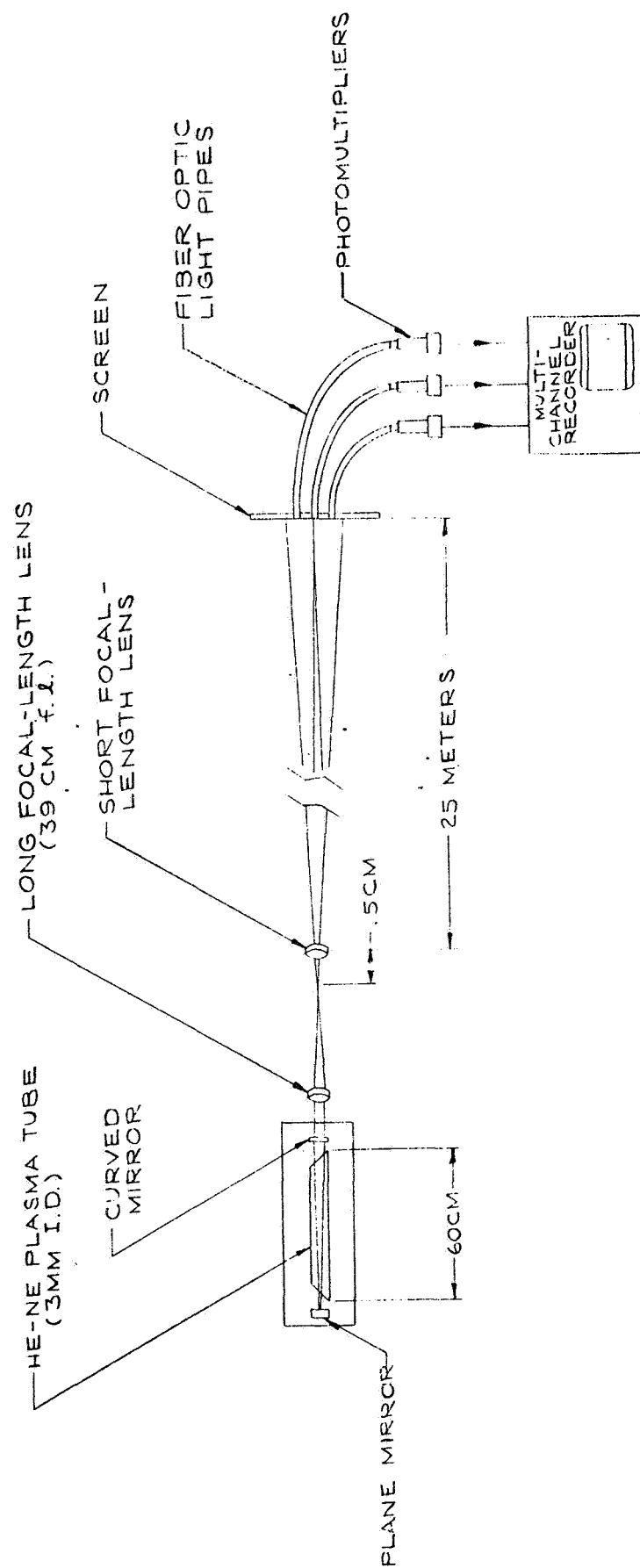LASER/OPTICS TECHNIQUES TELESCOPE STRUCTURE

119

FIGURE 6. EXPERIMENTAL ARRANGEMENT USED FOR MEASURING SPATIAL STABILITY OF LASER BEAMS

120
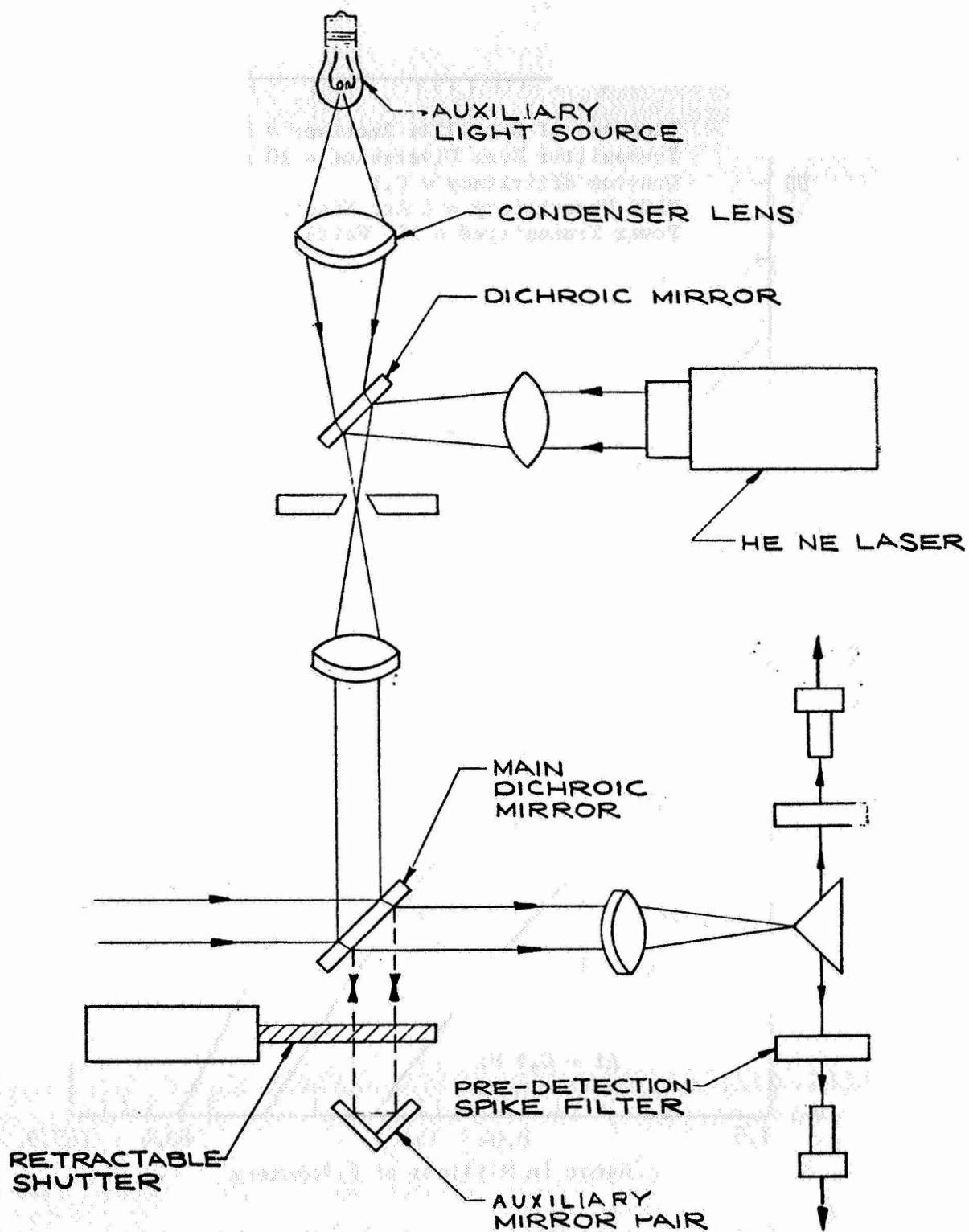
FIGURE 7. EQUIPMENT ARRANGEMENT FOR REMOTE
BORESIGHT ALIGNMENT OF OPTICAL SYSTEM
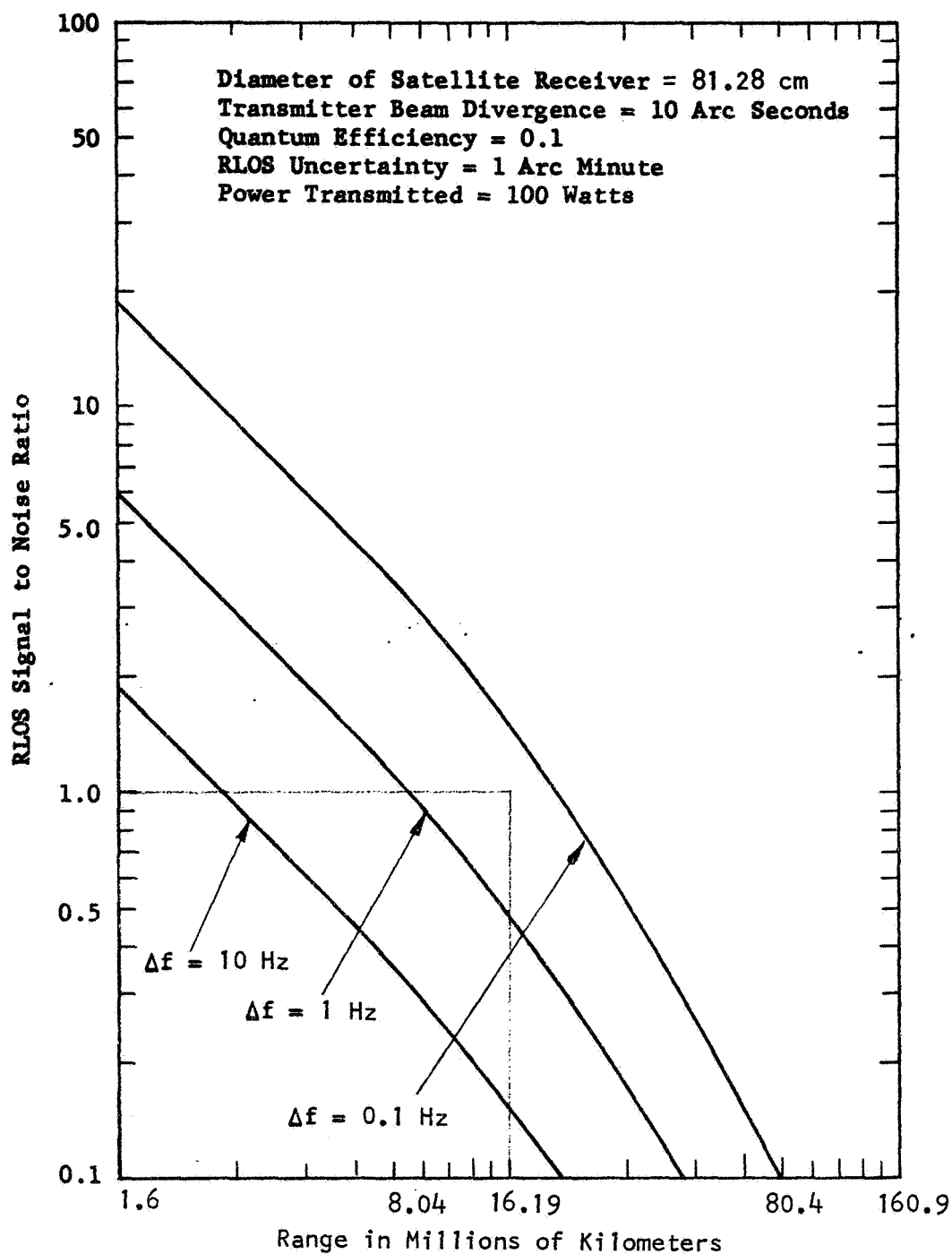
FIGURE 8. RLOS SIGNAL TO NOISE RATIO WITH BEAM
DIVERGENCE OF 10 ARC SECONDS
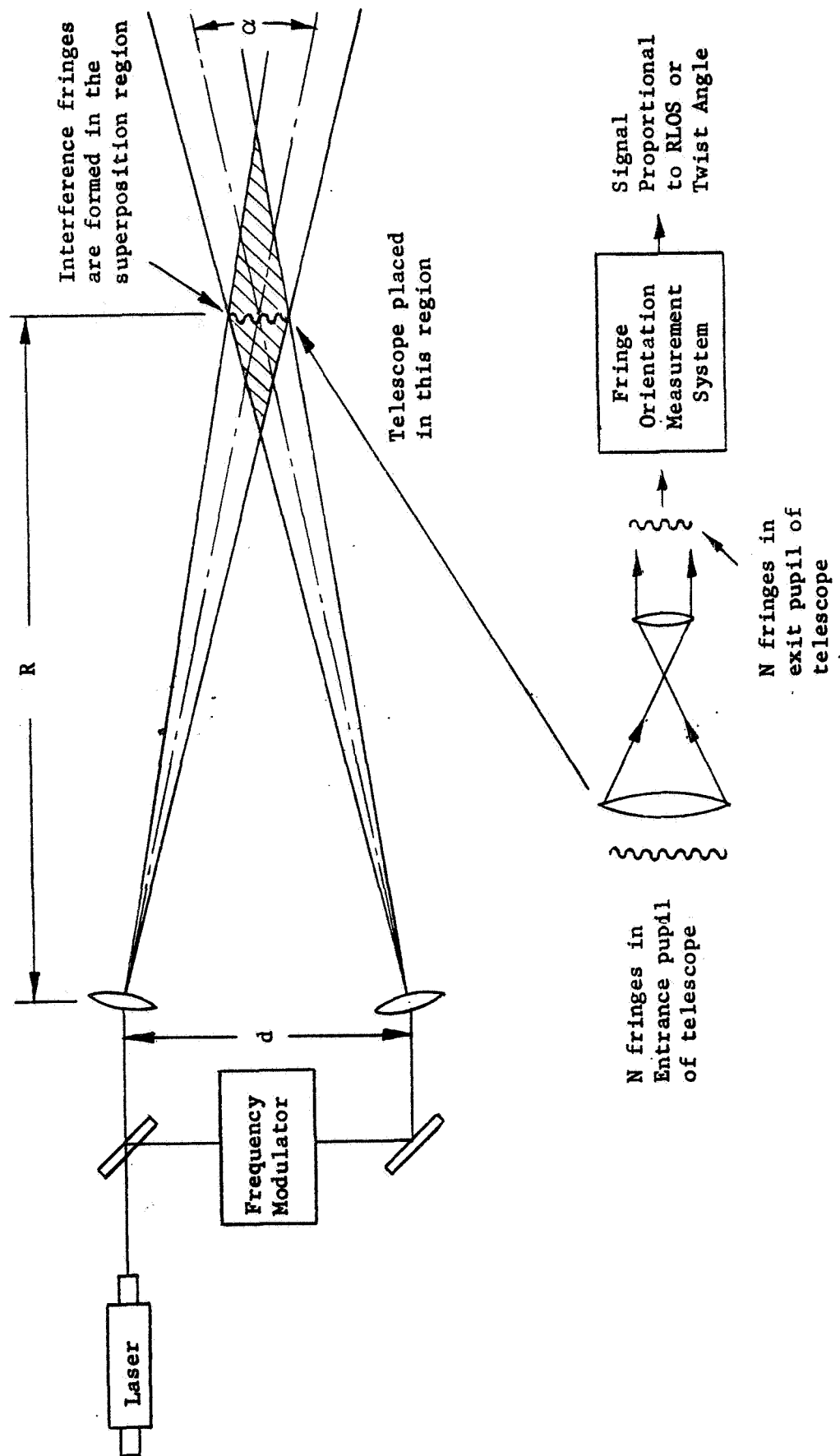
FIGURE 9. DIAGRAM SHOWING PRINCIPLE OF INTERFERENCE FRINGE METHOD FOR
RLOS OR TWIST ANGLE DETERMINATION

123
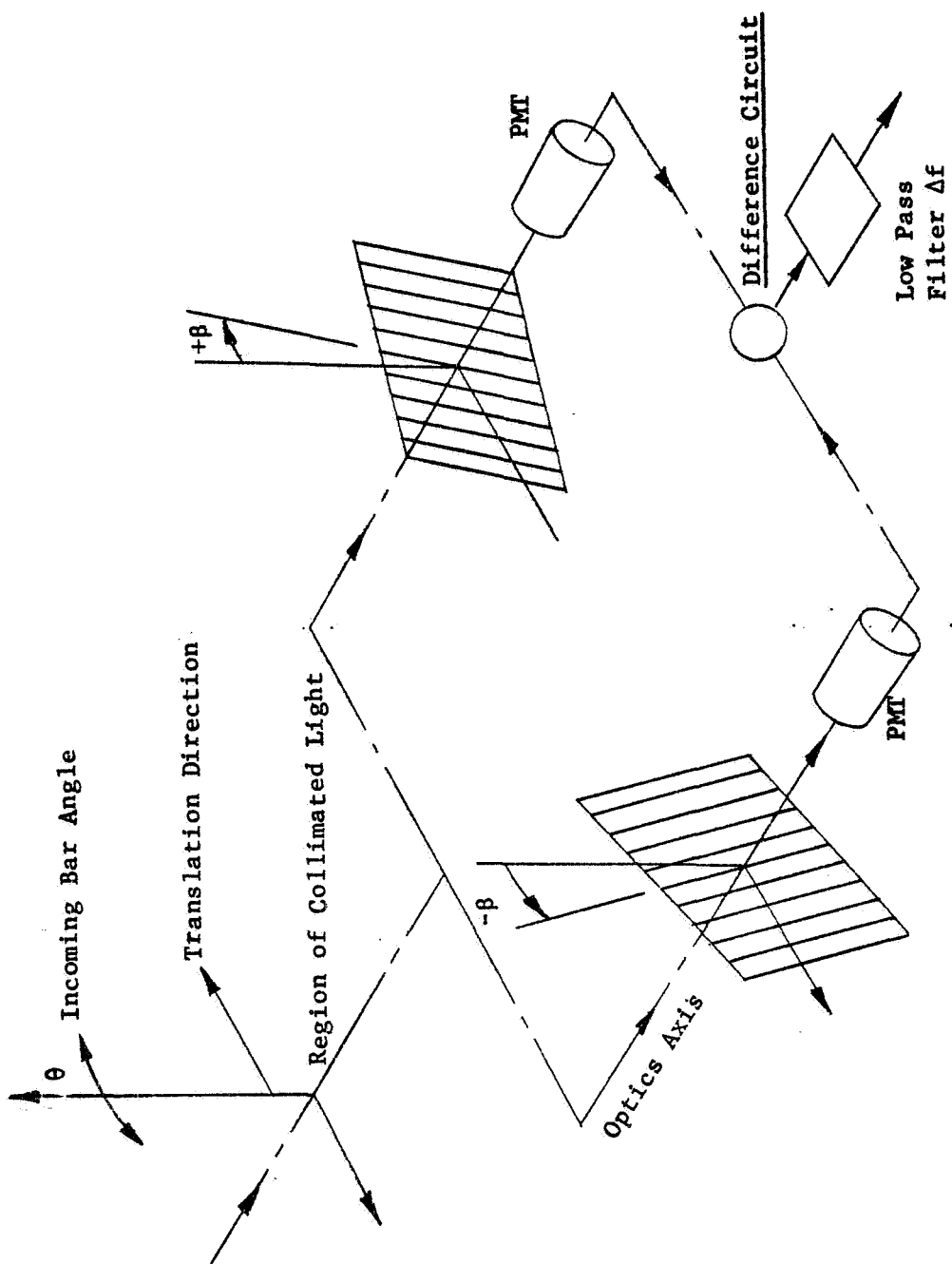
FIGURE 10.   DIAGRAM OF DETECTION SYSTEM

124

ACTIVE OPTICS FOR LARGE ORBITING
ASTRONOMICAL TELESCOPES

Hugh J. Robertson
Perkin-Elmer Corporation

An orbiting diffraction-limited version of the 50.8-cm (200-in.) Hale telescope high above the earth's atmosphere is many an astronomer's dream (Fig. 1). The advantages to be gained by a large-aperture orbiting astronomical telescope over a ground-based telescope are many.

For astronomical research, one advantage is the ability to sense radiation other than visible light and radio waves, which cannot penetrate the atmosphere--the gamma rays, x rays, ultraviolet, infrared, and long radio waves. Another advantage is the possibility of achieving the full diffraction limit of resolution for a large mirror. For ground-based telescopes the resolution of large mirrors has been limited well below the diffraction limit by two major effects. The first of these is atmospheric turbulence, which has limited the resolution obtainable up to now to 0.3 arc seconds. This is the diffraction-limited resolution of a 30.48-cm (12-in.) telescope. The second limiting effect is the strain imposed on a large mirror and its supports by the force of gravity as the telescope is pointed in different directions, strains which distort the mirror figure and limit the size and light gathering capability of earthbound primary mirrors.

The realization of wide spectrum reception and freedom from the effects of atmospheric turbulence are obvious advantages to be gained by simply lifting a telescope above the earth's atmosphere. Orbiting a telescope into a zero-gravity environment however does not automatically solve the problems of obtaining and maintaining a perfect mirror figure, and it is toward the solution of these problems and the problems associated with the launching of a large telescope that the proposed "Active Optics" system is directed.

The difficulties involved in obtaining a large-aperture orbiting telescope are primarily imposed by gravitation and temperature effects. The influence of gravity is felt in two ways. First it sets practical limits on the weight of a mirror that can be launched. This in turn sets limits on the

125

thickness of a mirror of any given diameter that can be orbited. The thickness and diameter of the mirror determine its rigidity and affect the amount of flexure that can be expected when a mirror is figured and tested on the ground and then used in a zero-gravity environment.

Temperature variation in a large mirror can introduce serious problems. A very small difference in temperature from front to back of a large mirror can produce a change in focus that is not too serious if the temperature difference is uniform across the mirror. If a small variation in this temperature difference exists across the mirror, however, the effects on resolution can be considerable.

Let me describe the Active Optical System and how it proposes to meet some of the difficulties just mentioned.

The Active Optical System makes use of a primary mirror composed of individual mirror segments (Fig. 2). These segments are to be positioned and the configuration of the composite surface is to be maintained by precise actuators capable of making displacements of less than a micro-inch. The actuators are to be part of a closed-loop control system that will operate from signals originating from the interference phenomena generated by a sensing system that can continually monitor the surface orientation of the mirror segments. The proposed sensing system will be located near the center of curvature of the primary mirror and will consist of laser and white light sources, interferometers, and a means of converting the information provided by the resulting interference fringes into usable electrical signals. An electronic analyzer will interpret this information and produce signals to control the actuators as necessary for proper orientation of the mirror segments. The actuators for each segment will be located so that the segment can be pivoted around two orthogonal axes and translated in a direction normal to its surface. ·

Let us consider some of the features of an Active Optical Telescope System as described and their application to the problems imposed by gravitational changes and thermal inhomogeneities.

For the same maximum allowable flexure, the individual segments of the Active Optical System could be considerably thinner than a single large conventional mirror, resulting in a significant weight reduction. For instance, a 254-cm (100-in.) primary of fused silica eggcrate construction having the same stiffness characteristics as that used in the Orbiting Astronomical Observatory primary would weigh an estimated 1361 kg (3000 lbm). The weight of a 254-cm (100-in.) segmented primary consisting of seven 81.28-cm

(32-in.)-dia. mirrors would be less than 363 kg (800 lbm). A 10-m primary of fused silica only 25 cm thick would weigh an estimated 49 896 kg (110 000 lbm). A 10-m-dia Active Optical System could weigh less than 9072 kg (20 000 lbm).

Dr. Lyman Spitzer [1] in a paper on space astronomy has estimated that a variation in front to back temperature difference across the mirror surface of only 10^{-2} ° K could produce a serious loss of resolution of a 10-m mirror 25 cm thick. In an Active Optical System, the thermal uniformity requirement would only be that for a mirror the size of one of its segments since each segment is independently controlled and positioned to maintain the mirror figure including corrections for displacement caused by thermal variations.

A further consideration is the ability of small mirror segments compared to that of a large mirror to withstand the shock and vibration of launch, not to mention the ability of a segmented primary to form a more compact payload for assembly in space.

To evaluate the Active Optics concept for use in a spaceborne telescope we have started on an initial program of experimentation using a 50.8-cm (20-in.) spherical mirror (Fig. 3). This mirror will be cut into segments after figuring and used to demonstrate the proposed figure sensing and actuator control techniques. The mirror surface configuration of these segments will produce an interference pattern at the output of the figure sensor interferometer. Figure analyzer circuitry will produce an error signal when the interference pattern shows a displacement of the segments from a spherical surface. This error signal will be applied to the appropriate actuators to reposition the mirror segments and reduce the error.

The investigation is proceeding along several different lines. First we are trying to determine the optimum figure sensing technique. There are several interferometer techniques to choose from, but an interferometer using laser light is proving to be very effective for sensing fractional wavelength displacements by the measurement of differences of interference phase across the image of the primary mirror at the output of the interferometer. A fundamental difficulty appears here, however, since this technique allows one segment to be displaced relative to another along the axis of the system a relatively large number of half wavelengths of the single frequency laser light used without affecting the phase difference at the output of the interferometer (Fig. 4). This phenomena, which we have been calling "integral wavelength ambiguity," does not produce a variation in phase which can be detected by scanning across a segment, until several wavelengths of relative axial displacement exist. To

resolve these ambiguities we are investigating several different schemes involving white light and two wavelength laser interferometers.

Second, we are developing the electronic circuitry required to analyze the figure sensor output and provide the error signal to operate the actuators.

Third, we have been investigating precise fractional wavelength actuators to effect mechanical displacement of the mirrors. Some of the requirements for an ideal actuator for this application are:

1. The ability to make reversible displacements of a small fraction of a micro-inch. A fiftieth of a wavelength, which we would like to better, is approximately 0.4 micro-inches.

2. A large dynamic range. If mirror segment positions require an initial adjustment of as much as 0.0508-cm (±0.020-in.), the ratio of the dynamic range to smallest step required is greater than 100 000 to 1.

3. Zero power requirement when displacements are not being made.

4. The ability to maintain final position in the event of power failure.

5. The ability to operate in a space environment. For example, we would like to avoid metal-to-metal sliding parts requiring hermetic seals.

There are numerous possibilities to satisfy these requirements in various configurations of piezoelectric crystal arrays, magnetostrictive devices, electro-mechanical arrangements, and thermal and chemical actuators.

We have been developing several actuators using magnetostriction for their displacement force. These actuators satisfy most of the requirements listed; however, we have found it difficult to achieve the less than a micro-inch displacement required without supplementing them with a motion reducing lever arm.

The components of the system described are being developed as Phase I of this effort. In Phase II, we will attempt to combine them into an automatic control system with the objective being to align our segmented 5.08-cm (20-in.) mirror to within one twentieth of a wavelength of the desired figure.

We are confident that the Active Optics approach will prove to be an effective one for large-aperture orbiting astronomical telescopes and that it may find application in large ground-based telescopes as well.

REFERENCES

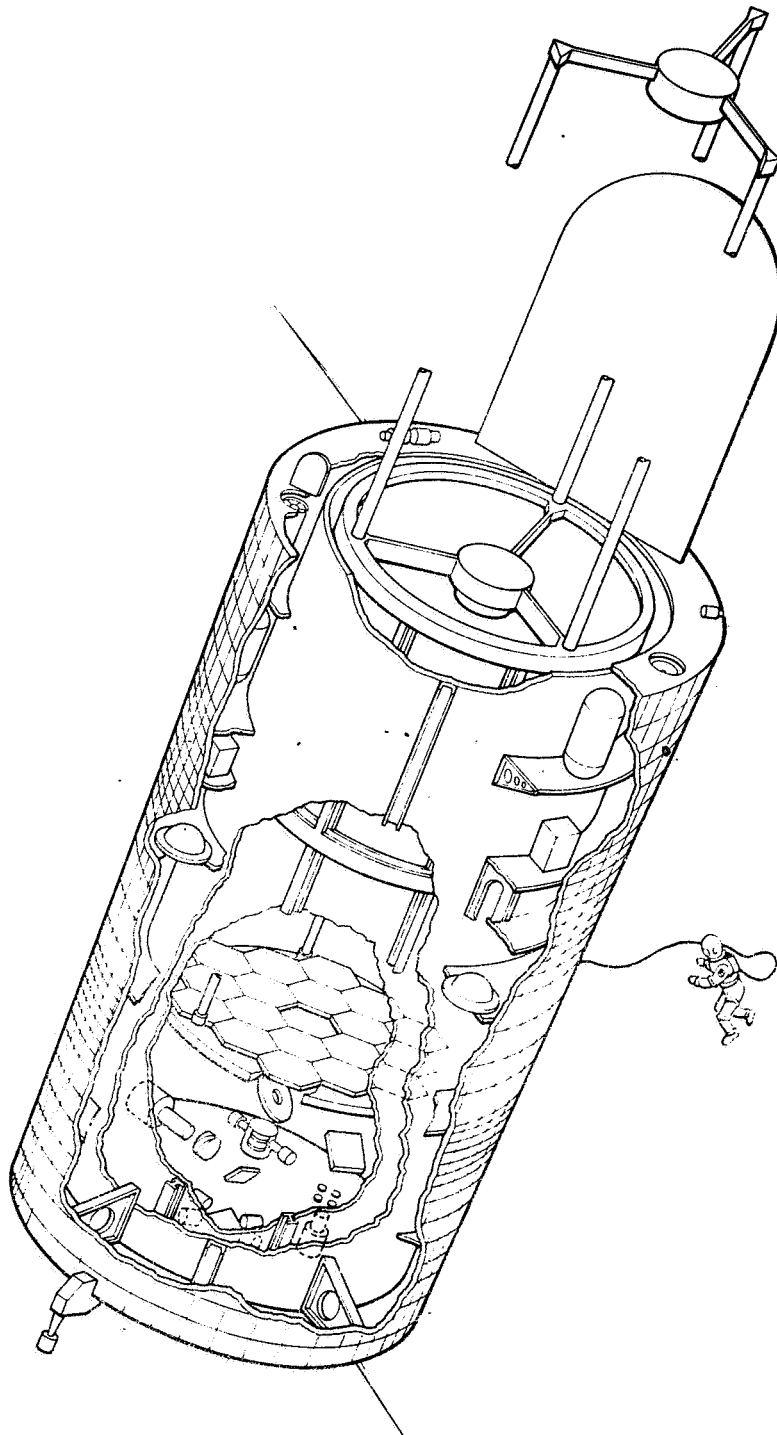1. Lyman Spitzer, Jr.: American Scientist, vol. 50, no. 3, Sept. 1962, pp. 473-484.

FIGURE 1. ACTIVE OPTICS ORBITING ASTRONOMICAL TELESCOPE

MIRROR FIGURE
ERROR SENSOR

TO ACTUATORS
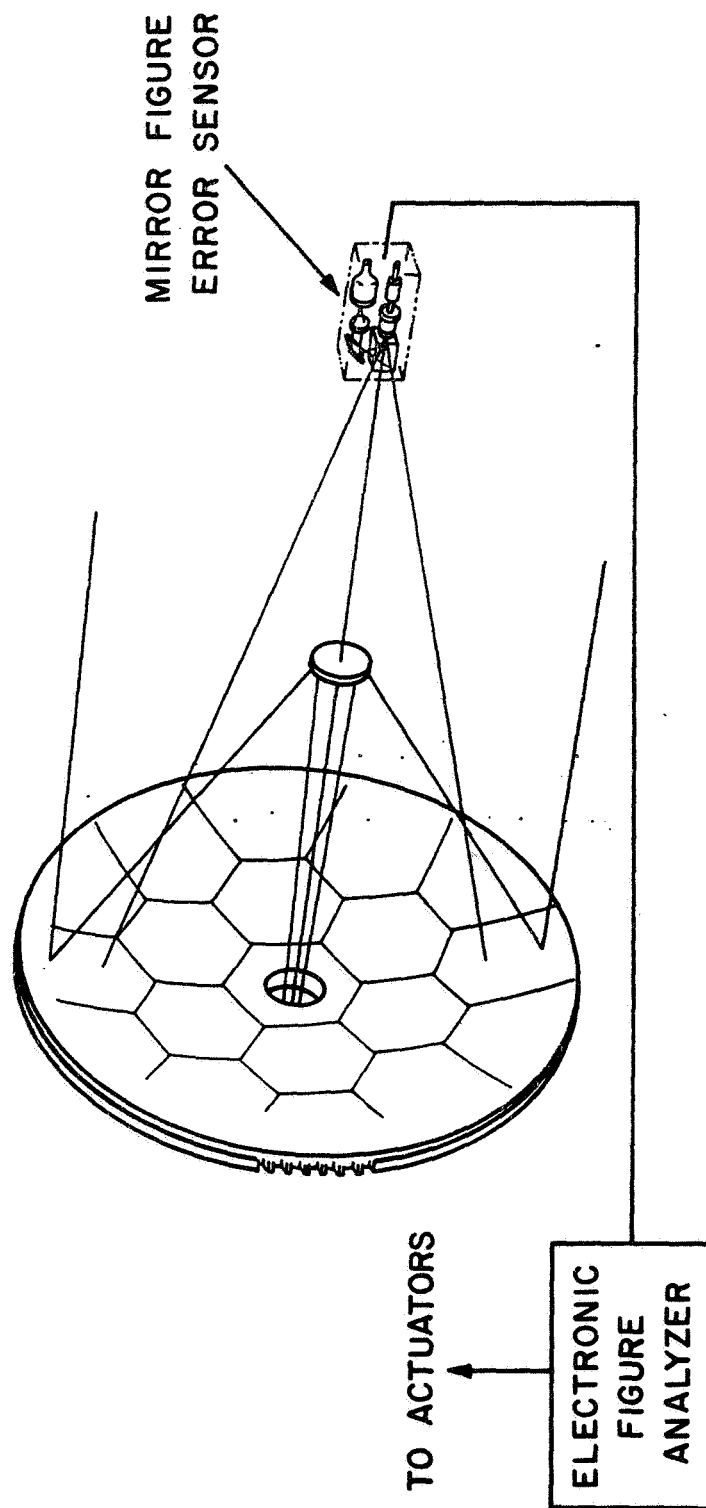
ELECTRONIC
FIGURE
ANALYZER
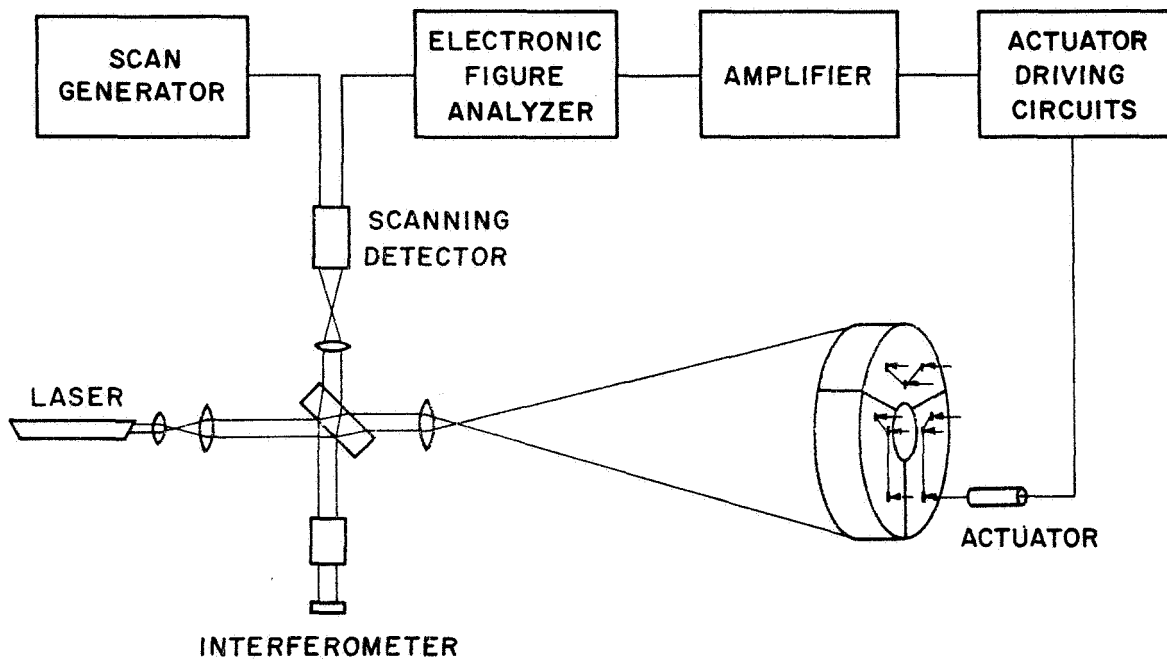
FIGURE 2. ACTIVE OPTICS TELESCOPE SYSTEM
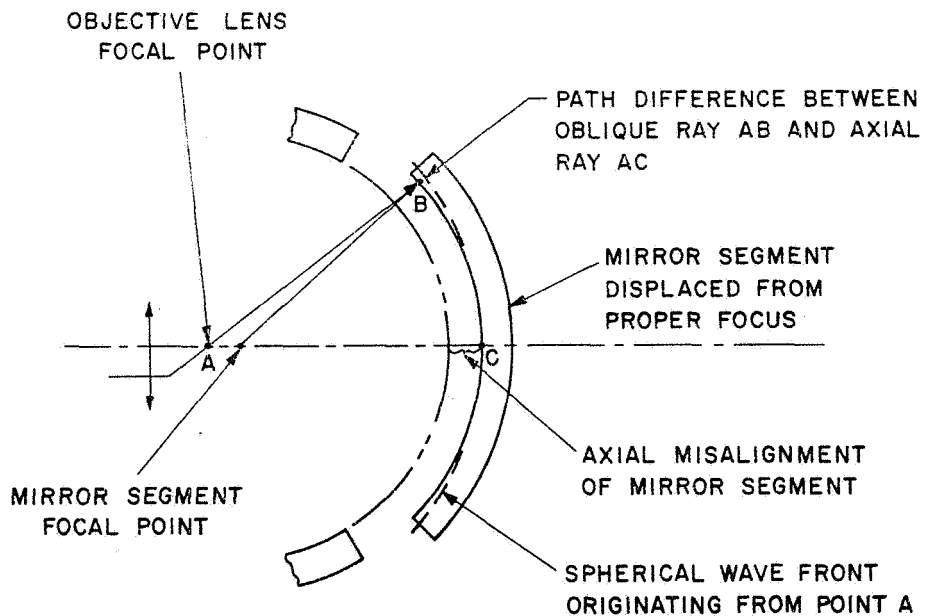
FIGURE 3. EXPERIMENTAL ARRANGEMENT FOR
ACTIVE OPTICS EVALUATION

FIGURE 4. INTEGRAL WAVELENGTH AMBIGUITY IN AXIAL
POSITION OF MIRROR SEGMENT

HIGH FREQUENCY PHOTODIODES

R. B. Emmons
G. Lucovsky
Philco Applied Research Laboratory

Photodiodes of the pn junction type are discussed as detectors of rapidly modulated light. Transit time effects limit the frequency response to about 20 GHz. To prevent RC effects from degrading this frequency response, diode areas in the order of 10^{-4} to 10^{-3} cm^2 are required. At high frequencies the signal and noise power output levels of a photodiode are low. The effect of avalanche multiplication, a suggested remedy, on photodiode frequency response and noise output power is discussed. Design and performance data for high speed, nonavalanching photodiodes are given.

The geometry of pn junction photodiodes is the same as that of solar cells or nuclear particle counters and is shown in Figure 1. Impurity diffusion is commonly used to produce the pn junction. Electron-hole pairs are created by the internal photoelectric effect in the semiconductor to a depth of the order of $1/\alpha$ cm, where α is the absorption coefficient at the wavelength of interest. These pairs must be separated before a photocurrent appears in the external circuit. The separation is accomplished by drift in the field of the pn junction for those pairs created in the junction region. Those pairs created outside the junction must diffuse to the junction before separation can occur. These transport processes, as well as RC effects, limit the frequency response of the diodes. As a result of its RC characteristics, the signal and noise power levels at the photodiode output are low at high frequency. Use of the photodiode in the avalanche breakdown region of its I-V characteristic has been suggested as a remedy for this difficulty. The creation of additional charge carriers in the junction region by avalanche multiplication may, however, increase the time required to separate the charge and may also result in additional current noise.

These limitations on photodiode performance will be discussed briefly, and the results of their application to common semiconductor diode materials will be presented.

The characteristic time required for pairs generated in a p region, whose thickness is W_p, to diffuse to the junction is given by the width of the p region divided by the diffusion velocity [1]

133

$$\tau_{diff} = \frac{W_p^2}{2.43 \, D_n} \leq \frac{W_p}{2.43 \, v} \cdot \qquad (1)$$

This relation is true only if the conditions for good dc response are met, if the resistivity of the layer is uniform, and if the minority carriers are injected in the layer ($\alpha \rightarrow \infty$), but it remains a good approximation for reasonable variations on these initial conditions.

Care must be exercised in applying this relation to high-mobility III-V semiconductor photodiodes, in particular InSb. The diffusion velocity D_n/W_p is limited above by the saturated drift velocity v_s, as indicated in equation (1).

The time required for pairs to be separated by drift in the junction field is given by the width of the junction region, W_I, divided by the saturated drift velocity [2]

$$\tau_{drift} = \frac{W_I}{2.8 \, v_s} \cdot \qquad (2)$$

This expression is strictly true only for a constant junction field and injection of the electrons into the junction, but it remains a good approximation for reasonable variations on these initial conditions.

The lumped constant electrical characteristics of a photodiode also affect its bandwidth and determine the power available from the photodiode (Fig. 2).

The power available from the diode may be characterized by the power available in a conjugate matched load, which is given by [3]

$$P(\omega_m) = \frac{I^2 R_0}{4(1 + R_s/R_0 + R_s R_0 C_0^2 \omega_m^2)}, \qquad (3)$$

where I is the light-generated diode current and ω_m is the frequency at which the diode is conjugate matched. This relation indicates that the diode series resistance limits the magnitude of the power available at high frequencies.

For an arbitrary load, the available power-bandwidth product has an upper limit given by [4]

$$\int_{0}^{\infty} P(\omega) \; d\omega \leq \pi \, I^2/2C_0 \; . \tag{4}$$

This relation indicates how the junction capacity limits the diode performance. Within this limitation, it is possible, in principle, to load the diode in such a way as to obtain any output power and bandwidth characteristic desired. However, a close look at the combination of these two limitations quickly shows that reasonable fractional bandwidths can be obtained at high frequencies only at the expense of available power in the load. Since the detector noise power output varies with frequency in essentially the same manner as the signal power, operation at high frequencies does not reduce the detector signal-to-noise ratios, but the reduction in the absolute values of both the signal-and-noise power at the diode output does make it difficult to obtain a following amplifier that does not degrade the detector performance.

The use of the current multiplication obtained when a diode is back-biased into avalanche breakdown has been suggested as a means of raising the signal and noise power levels at the diode output [5]. The experimental evidence for the usefulness of avalanche multiplication is limited. It is clear, however, from junction transport theory that the effect of multiplication on diode bandwidth and on the diode current noise output power depends critically on whether charge carriers of one sign are responsible for the multiplication or whether both carriers share equally in the multiplication process. If one carrier is responsible for the multiplication, the transit time is insensitivie to the multiplication [6]. Figure 3 shows a typical calculation of frequency response when one carrier only is multiplying. If both carriers share equally in the multiplication, then the transit time is directly proportional to the multiplication [6, 7]. Figure 4 is the calculated frequency response of a simple diode when both carriers multiply equally. Figure 5 is a plot of the 3-dB bandwidths from Figure 4 as a function of multiplication, showing the linear dependence of transit time on multiplication. The transit time is given by

$$\tau_{drift} = \frac{M \, W_I}{3 \, v_s} \; .$$

It was first thought, and measurements indicated [8, 9], that the avalanche process would multiply the signal and noise power levels equally. Theory now indicates that this is true only if one carrier is primarily responsible for the multiplication. If both carriers multiply, the noise power should grow

faster than the signal power [10, 11]. Recent measurements [12] on both Si and Ge diodes indicate that this is the case. Failing the development of a diode material in which one carrier is primarily responsible for avalanche multiplication, this technique appears to have limited value.

The processes that limit the frequency response of a photodiode have been indicated. The design of nonavalanching photodiodes may now be considered in the light of these limitations. Consider first the transit times. In deciding whether diffusion or drift is the more important of the two transport mechanisms, the value of the absorption coefficient is the determining factor. If the absorption constant is greater than 10^4 cm^{-1} in the wavelength region of interest, most of the incident light will be absorbed in the p-type layer. This is the case with direct gap semiconductors, whose absorption constant drops very abruptly from values greater than 10^4 cm^{-1} at the wavelength corresponding to the band gap of the semiconductor. Diffusion of the carriers to the junction then will be the limiting process. Because it is always desirable to have the junction width as large as possible, W_I is made just large enough so that drift of the carriers across the junction does not introduce an additional transit time delay.

If the absorption constant is less than 10^4 cm^{-1} in the wavelength region of interest, the fastest response is obtained by allowing as much of the light as possible to be absorbed in the junction region itself. The p region, therefore, again is made less than 10^{-4} cm thick, and the junction thickness is made $1/\alpha$ cm thick. The limiting transport process in this case is then drift across the junction region. This structure is useful for indirect gap semiconductors, particularly silicon, whose absorption constant is low over an appreciable wavelength range. The necessary wide junction regions can be obtained either by the use of high-resistivity base material, or by epitaxial growth of PIN structures. The PIN structure is best, since it eliminates the spreading resistance associated with a thick wafer of high-resistivity material. The shortest transit times obtainable may be estimated from equations (1) and (2). The thinnest active region from which light-generated carriers can be collected efficiently is of the order of a few tenths of a micron. Saturated drift velocities in semiconductors are of the order of 5×10^6 cm/sec. Transport phenomena will then limit the response times of efficient photodiodes to the order of 10^{-11} sec, or cutoff frequencies to approximately 20 GHz.

Once the structure of the diode has been determined to suit the absorption constant and transport properties of the material, the diode area and contact geometry are chosen so that, if it is practical, the RC response time does not degrade the diode frequency response.

136

Figure 6 contains a summary of the performance data on high-frequency photodiodes fabricated in the authors' laboratory. The wavelength region in which the diodes are sensitive, the diode areas, and typical values of the series resistance R_S and junction capacity C_0 are listed. The frequency response of the diodes as calculated from R_S and C_0 and the transit time frequency response as estimated from the diode geometry are also given. The thickness of the region that determines the limiting transit time is indicated. A comparison of the RC response time and transit time for the diodes given in Figure 6 indicates that a reasonable balance between transit time and RC time has been obtained for most of the diodes.

REFERENCES

1. Sawyer, D. E. and Rediker, R. H.: Proc. IRE <u>46</u>, 1122, 1958.

2. Lucovsky, G.; Schwarz, R. F.; and Emmons, R. B.: JAP <u>35</u>, 622 1964.

3. Johnson, K. M.: Microwave Jour. <u>6</u>, 71, 1963.

4. Emmons, R. B. and Lucovsky, G.: Proc. IEEE <u>52</u>, 865, 1964.

5. Johnson, K. M.: ISCC Digest of Tech. Papers, pp. 64-65, Feb. 1964.

6. Emmons, R. B. and Lucovsky, G.: IEEE Trans. on E. D., to be published.

7. Lee, C. A. and Batdorf, R. L.: Solid State Device Research Conference, Boulder, Colo., 1964.

8. Johnson, K. M.: IEEE Trans. on E. D. <u>12</u>, 55, 1965.

9. Anderson, L. K.; McMullin, P. G.; D'Asaro, L. A.; and Goetzberger, A.: Appl. Phys. Letters <u>6</u>, 62, 1965.

10. Tager, A. S.: Soviet Physics, Solid State <u>6</u>, 1919, Feb. 1965.

11. McIntyre, R. J.: to be published.

12. Melchair, H. and Anderson, L. K.: International Electron Device Meeting, October 21, 1965, Washington, D. C.

138
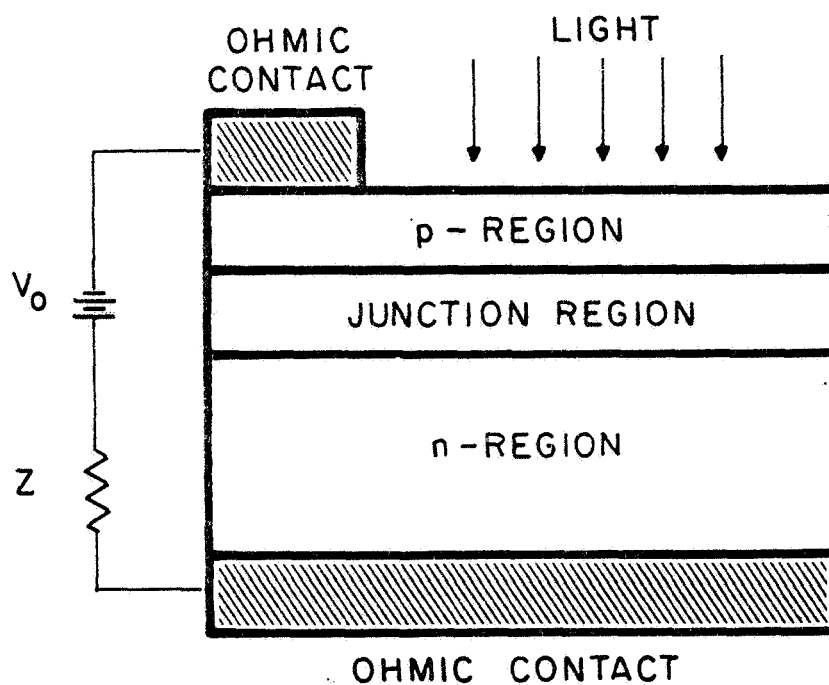
FIGURE 1.   SCHEMATIC REPRESENTATION OF PHOTODIODE GEOMETRY
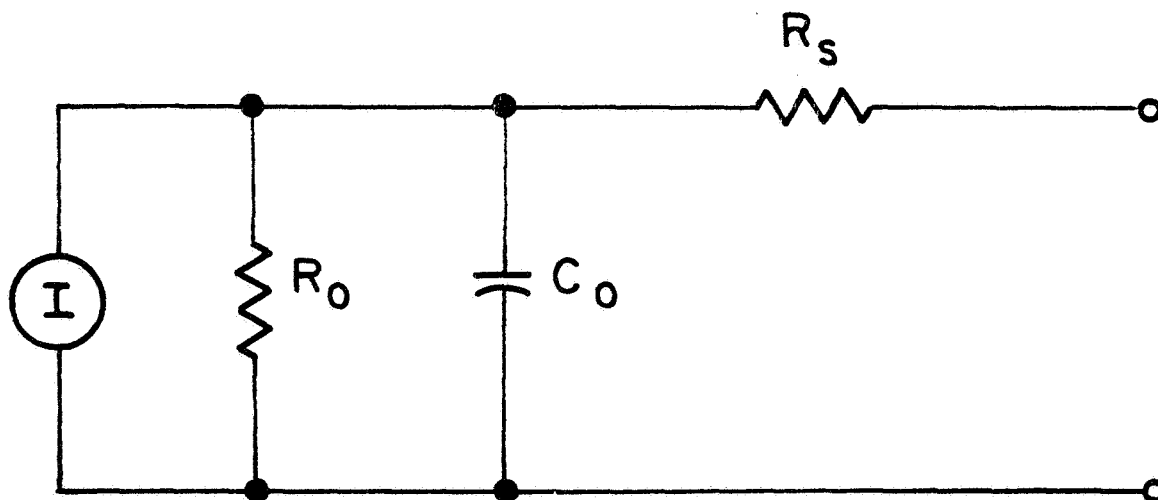
FIGURE 2.   PHOTODIODE EQUIVALENT CIRCUIT. R_O AND C_O ARE THE JUNCTION RESISTANCE AND CAPACITANCE RESPECTIVELY. R_S IS THE SERIES RESISTANCE.   I IS THE EQUIVALENT LIGHT CURRENT GENERATOR.
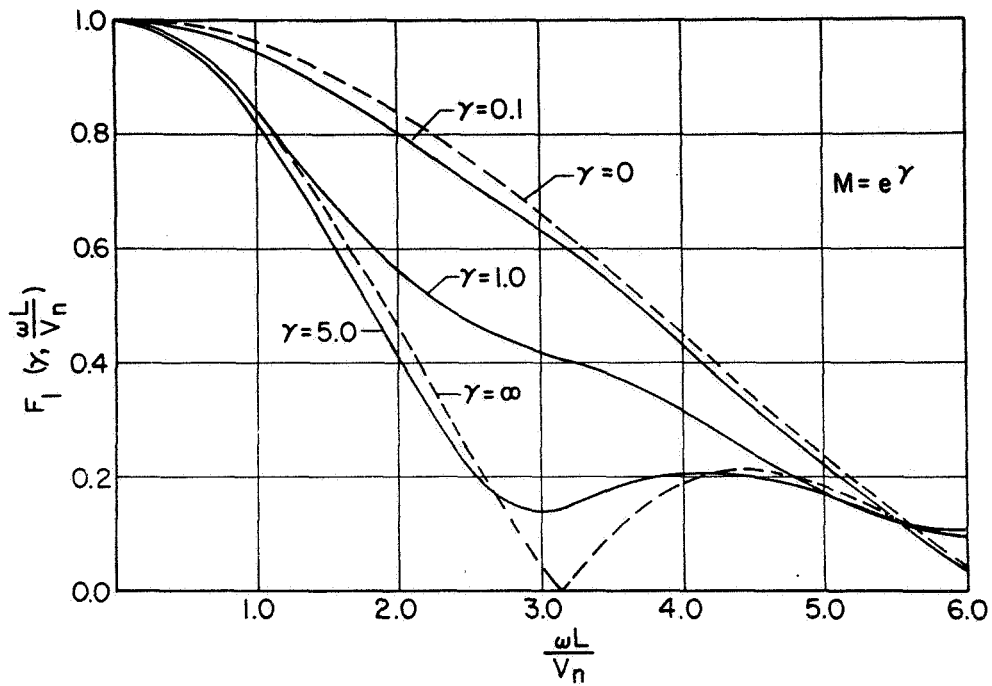
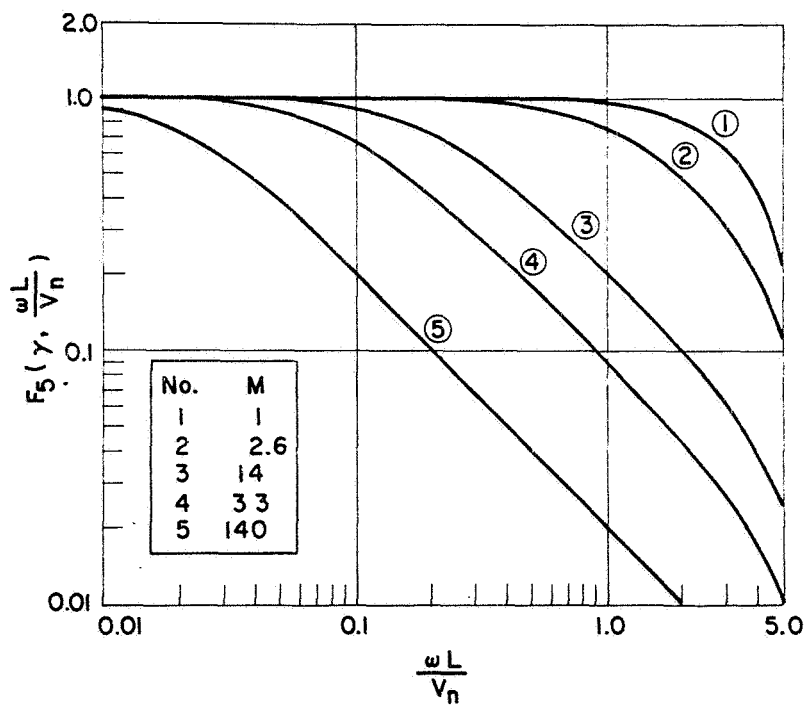FIGURE 3. FREQUENCY RESPONSE OF PIN PHOTODIODE FOR
ONE CARRIER MULTIPLICATION

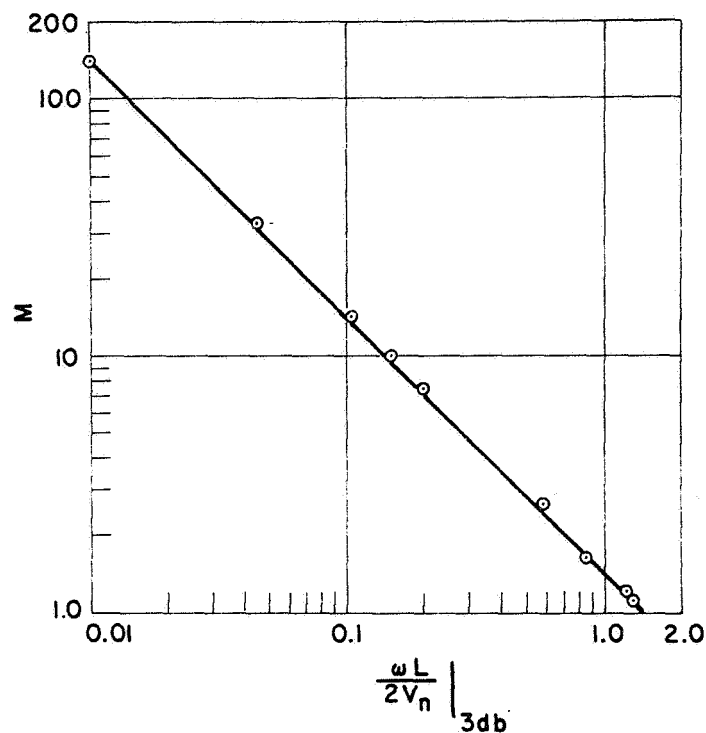FIGURE 4. FREQUENCY RESPONSE OF PIN PHOTODIODE FOR
TWO CARRIER MULTIPLICATION

FIGURE 5. MULTIPLICATION VERSUS BANDWIDTH FOR TWO CARRIER MULTIPLICATION

MATERIAL	WAVELENGTH REGION (μ)	AREA (cm^2)	R_s (ohms)	C_b (pF)	f_{RC} (GHz)	TRANSPORT DISTANCE (μ)	f_{TRANS} (GHz)
Si P-I-N	0.65 - 0.75	6×10^{-5}	5	0.5(-6V)	45	W_I = 2.5	15
	0.65 - 0.75	2×10^{-4}	5	1.5(-10V)	12	W_I = 2.5	15
	0.5 - 0.95	3.5×10^{-2}	65	5.0(-100V)	0.5	W_I = 75.0	0.5
Ge N-P	0.5 - 1.5	4×10^{-4}	6	5.6(-6V)	17	W_N = 0.4	8
GaAs P-N	0.4 - 0.8	1.3×10^{-4}	3.0	7.0(-4.5V)	7.5	W_P = 1.0	8
		7×10^{-4}	2.5	32 (-4.5V)	2	W_P = 1.0	8
InAs P-N	0.5 - 3.5	3.2×10^{-4}	12	3.0(-5V)	4.5	W_P = 2.0	10
		2×10^{-3}	8	30 (-2V)	0.65	W_P = 2.0	10
InSb P-N (77°K)	0.5 - 5.2	5×10^{-4}	18	7.1 (-0.2V)	1.2	W_P = 2.0	10

FIGURE 6. HIGH-SPEED PHOTODIODE CHARACTERISTICS

SOLAR-PUMPED MODULATED LASER

C. W. Reno
Radio Corporation of America

Solar pumping of a laser was first reported by Kiss, Lewis, and Duncan at the RCA Laboratories early in 1963 [1]. As an extension of this work, DEP Applied Research has developed and tested a solar-pumped laser with modulation bandwidths sufficient for TV transmission. Stable operation has been demonstrated with no noticeable degradation in laser performance over several hours of operation.

A comparison of solar pumping and pumping by a broadband source, i.e., a tungsten lamp, reveals that solar pumping is attractive for spacecraft laser systems. For example, to achieve a power output of 1 W, a laser pumped by a broadband source in an "efficient" ellipse will require a lamp input power well in excess of 1 kW. Solar cells providing this amount of input power would require about 9.29 m^2 (100 ft^2) of active collection area. Add to this the disadvantages of weight, cooling requirements, and lamp replacement, and the solar-pumped laser becomes quite attractive. It is expected that a solar-pumped YAG:Nd^{3+} laser using a 78.74-cm (31-in.) parabolic mirror collector with a focal length of 53.34 cm (21 in.) will provide a 1-W power output in use on earth at the present state of the art.

Under NASA contract NAS 9-3671 a solar pumping system was assembled and three laser materials, CaF$_2$:Dy^{2+}, YAG:Nd^{3+}, and YAG:Nd^{3+}:Cr^{3+}, were evaluated. These materials are attractive for solar pumping because of their relatively broad absorption bands [2,3] (Fig. 1).

Most of the excitation for CaF$_2$:Dy^{2+} occurs from pumping in the bands from 5000 to 8000 Å. This is well matched by the solar spectrum. As shown in Figure 2, the laser transition in CaF$_2$:Dy^{2+} takes place between two triply degenerate states, $^1T_1^{(2)}$ ($^5I_7$) → $T_2^{(2)}$ ($^5I_8$). Laser output occurs at 2.36 μm. This transition has a fluorescent linewidth of 0.3 cm^{-1} at 77° K, the highest feasible operating temperature because of thermalization of the lower laser state and broadening of the fluorescent linewidth. For a magnetic field in the [100] direction, the fluorescent line due to the allowed transitions splits with an effective "g" of 9.6, corresponding to 4.5 x 10^{-4} cm^{-1}/gauss. Hence, the fluorescent linewidth can be doubled using a 600-gauss field. In this fashion, magnetic modulation is easily introduced [4].

Pumping in YAG:Nd^{3+} occurs principally in sharp lines at 6000, 7500, and 8000 Å. These lines all lie well within the broad peak in solar energy occurring in the visible and near infrared, making the sun quite a good pump source for this device. The laser transition occurs from the $^4F_{3/2}$ state to the $^4I_{11/2}$ state with a fluorescent linewidth of 2 cm^{-1}. This relatively wide fluorescent linewidth and a low effective "g" make magnetic modulation impractical. The laser wavelength is 1.06 μm.

With YAG:Nd^{3+}:Cr^{3+}, pumping can be accomplished by either of two mechanisms [3]:

1. The same fluorescent lines as for YAG:Nd^{3+}.

2. Cross pumping through the broad Cr^{3+} to the Nd^{3+} absorption bands and the ^3E state of Cr^{3+} to the Nd^{3+} laser state which Kiss [5] has demonstrated to exist. However, there is a long transfer time ($\approx$1 ms) for energy transfer between the ^3E state of Cr^{3+} and the Nd^{3+} laser state.

Based on our tests of these materials the following major advantages were found:

1. CaF$_2$:Dy^{2+}

    a. Magnetic modulation can be used with this material, providing ease in modulation to 300 kHz. No losses are introduced due to external modulators.

    b. Extremely low thresholds are possible due to the narrow laser line of CaF$_2$:Dy^{2+}.

2. YAG:Nd^{3+}

    a. This material can be operated at 300° K (room temperature) as opposed to 77° K for CaF$_2$:Dy^{2+}

    b. The laser output at 1.06 μm allows use of detectors, i.e., multiplier phototubes and silicon photocells, unusable with CaF$_2$:Dy^{2+}.

    c. The output has little spiking compared to CaF$_2$:Dy^{2+} and YAG:Nd^{3+}:Cr^{3+}.

3. YAG:Nd^{3+}:Cr^{3+}

    a. Lasing properties are the same as YAG:Nd^{3+}.

    b. Broad absorption bands add greatly to the effective pumping through efficient energy transfer.

Thus it may be seen that for applications where cryogenic cooling is unavailable or impractical one of the YAG laser systems must be used. Because YAG:Nd^{3+}:Cr^{3+} exhibits a noisy output, YAG:Nd^{3+} must be used for modulation experiments at this time.

The experimental apparatus for solar pumping CaF$_2$:Dy^{2+}, shown in Figure 3, includes a 78.74-cm (31-in.)-dia parabolic dish [53.34-cm (21-in.) focal length] affixed to an equatorial mount and a cylindrical lens which extends the solar image over a large portion of the crystal. The equatorial mount, tracking with a clock drive, allows stable operation over extended periods. Operation in excess of half an hour has been achieved with the principal difficulty being a gusty wind.

The equatorial mount solar power is focused to a 0.47725-cm (3/16-in.) spot at the focus of the mirror. The solar power as measured in tests has been found to be as high as 60 mW/cm^2. Thus the 78.74-cm (31-in.)-dia mirror collects 290 W; of this, 80 percent or 238 W is focused.

As CaF$_2$:Dy^{2+} is not a true 4-level laser system at 68° K, it is necessary to pump as large a portion of the laser as practical to reduce absorptive losses in the unpumped volume. In this experimental set-up, sub-cooled liquid nitrogen was allowed to flow through the dewar that holds the laser at the focus of the parabola. An InAs photodiode was used to detect the lasing output. Continuous operation was achieved with about 30 percent ripple.

Amplitude modulation was achieved by placing the crystal in a varying magnetic field [4]. The desired field was established by two coils (Fig. 4). Coil A was activated using a dc current of about 10 A to split the laser line and bias the laser off. Coil B was energized with 5-A, 5-μsec pulses at the required rate for modulation. Figure 5 shows typical modulation. Voice was transmitted by using this technique and varying the pulse rate.

Because of the very broad pump bands added by the Cr^{3+} cross pumping, YAG:Nd^{3+}:Cr^{3+} was expected to be the most efficient of the lasers tested. Unfortunately, this material had such a large ripple on its dc output that it was unusable for electro-optic modulation.

Continuous operation was easily achieved using the configuration of Figure 6. End pumping was chosen over side pumping because the small size of the image is well matched to the crystal end. The side walls of the flow tube are made reflective. This means that, neglecting the absorption of the crystal, a uniform brightness is achieved throughout the length of the flow tube allowing a long effective path through the crystal volume for the pump light. This allows much greater absorption than for side pumping. As the Nd^{3+} doped lasers are 4-level systems, inhomogeneous pumping does not degrade performance. Threshold was 100 W collected by the mirror, or 25 W coupled to the crystal. (Because of the mismatch between crystal and solar image, only about 25 percent of the light is coupled into the laser crystal.) The laser was pumped using the flow tube shown in Figure 7. This allows water to flow over the crystal sides with complete access to the crystal end for pumping. Laser output is taken from the end opposite the pumping end. An output power of 100 mW was observed for this nonoptimized system.

Excellent continuous operation was achieved with $YAG:Nd^{3+}$ in confocal ended crystals making the output "quiet" enough for modulation experiments, although some spiking was observed. For a crystal 0.23876 x 3.810 cm (0.094 x 1.5 in.), the threshold was 100 W collected by the mirror, or about 25 W into the laser crystal. This crystal was operated using the same physical set-up as the double doped YAG laser. Maximum power output achieved was 100 mW.

Electro-optic modulation was used to transmit the picture shown in Figure 8. About 40 percent modulation was achieved using a GaAs crystal and an applied voltage of 600 V peak-to-peak.

Until recently good optical quality in large cubic crystals having large electro-optic coefficients was unavailable. With the availability of large GaAs crystals from RCA's Semiconductor Materials Research Group in Somerville, N. J., this problem has been eliminated.

Figure 9 shows the major components of the optical communication system. The polarizer permits light polarized in only one plane to reach the crystal. As the plane polarized light passes through the crystal, it becomes elliptically polarized, the amount of ellipticity varying as a function of the voltage applied to the crystal. Since the analyzer transmits light polarized in only one plane, the intensity of the light transmitted through the modulator varies as the rotation of the polarization produced by the crystal, providing amplitude modulation.

One major problem arises: Piezoelectric resonances occur in the modulator material below 1 MHz. Figure 10 shows this effect in the swept response of a GaAs electro-optic modulator system. By using FM subcarrier modulation, the modulation spectrum can be shifted away from these perturbations, avoiding signal distortion. This is the method used to transmit the picture in Figure 8.

It has been shown experimentally that solar-pumped modulated lasers can operate efficiently and that modulation bandwidths in excess of 6 MHz can be realized. Further refinements in the manufacture of laser crystals and optimization of pump power collection systems are expected to make possible practical communication systems employing solar-pumped lasers.

REFERENCES

1. Kiss, Z. J.; Lewis, H. R.; and Duncan, R. C.: Sun Pumped Continuous Optical Maser. Appl. Phys. Lett., vol. II, no. 5, Mar. 1, 1963.

2. Wittke, J.; et al.: Solid State Laser Exploration. TR AFAL-TR-64-334.

3. Pressley, R. J.: Private Communication.

4. Kiss, Z. J.; et al.: Zeeman Tuning and Internal Modulation of the $CaF_2:Dy^{2+}$ Optical Maser. Appl. Phys. Lett., vol. 3, 9, Nov. 1963, pp. 145-148.

5. Kiss, Z. J.; and Duncan, R. C.: Cross Pumped Cr^{3+}-Nd^{3+}:YAG Laser System. Appl. Phys. Lett., vol. 5, 10, Nov. 15, 1964, pp. 200-2.
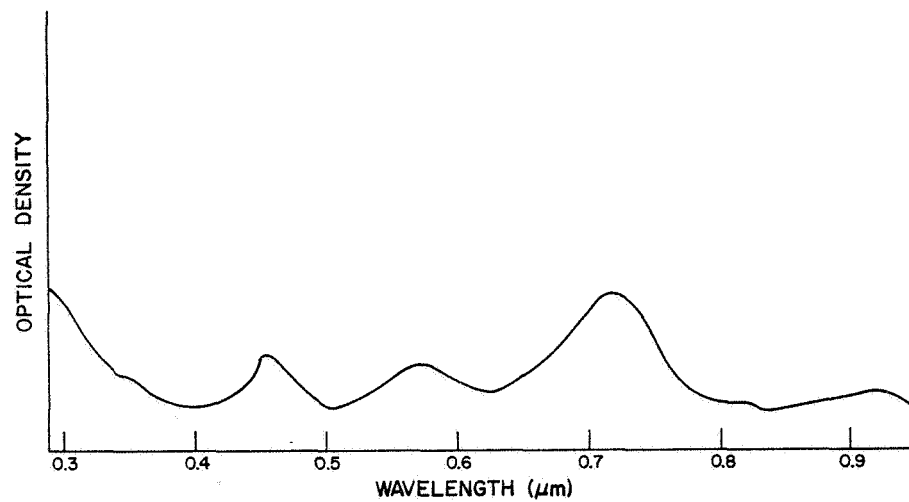
a. $CaF_2:Dy^{2+}$
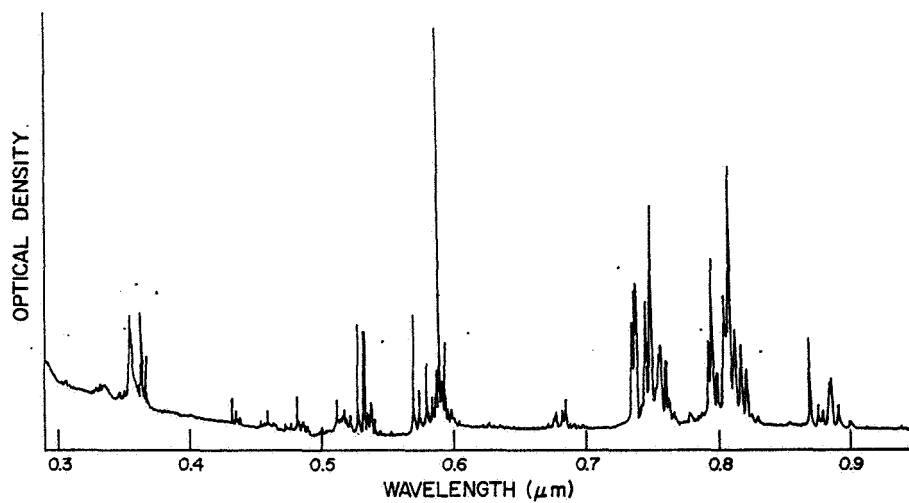
b. $YAG:Nd^{3+}$
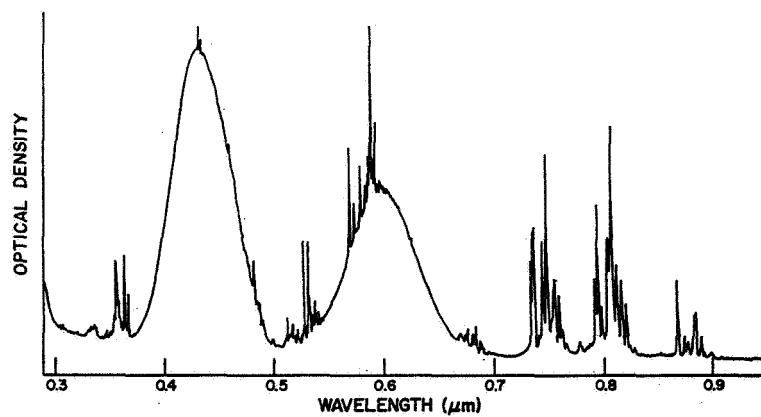
c. $YAG:Nd^{3+}:Cr^{3+}$

FIGURE 1. ABSORPTION SPECTRA OF LASER CRYSTALS
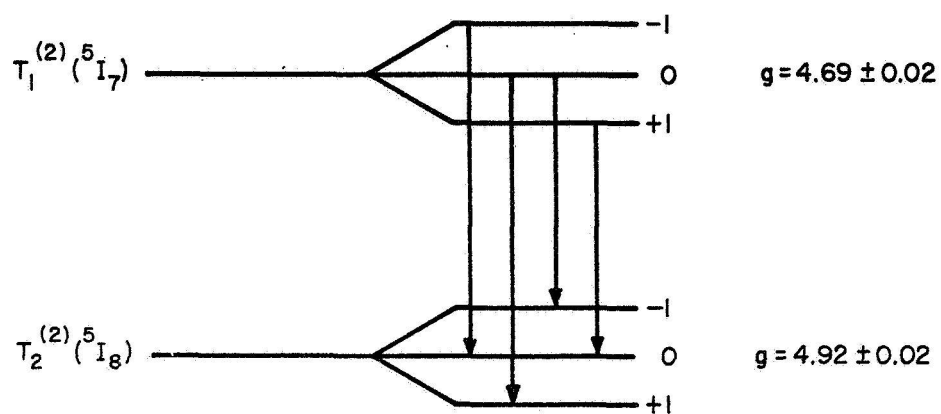
FIGURE 2. ZEEMAN SPLITTING OF LASER LINE IN CaF_2:Dy^{2+}
SHOWING ALLOWED ($\Delta M = \pm 1$) TRANSITIONS FOR [100]
ORIENTATION OF MAGNETIC FIELD
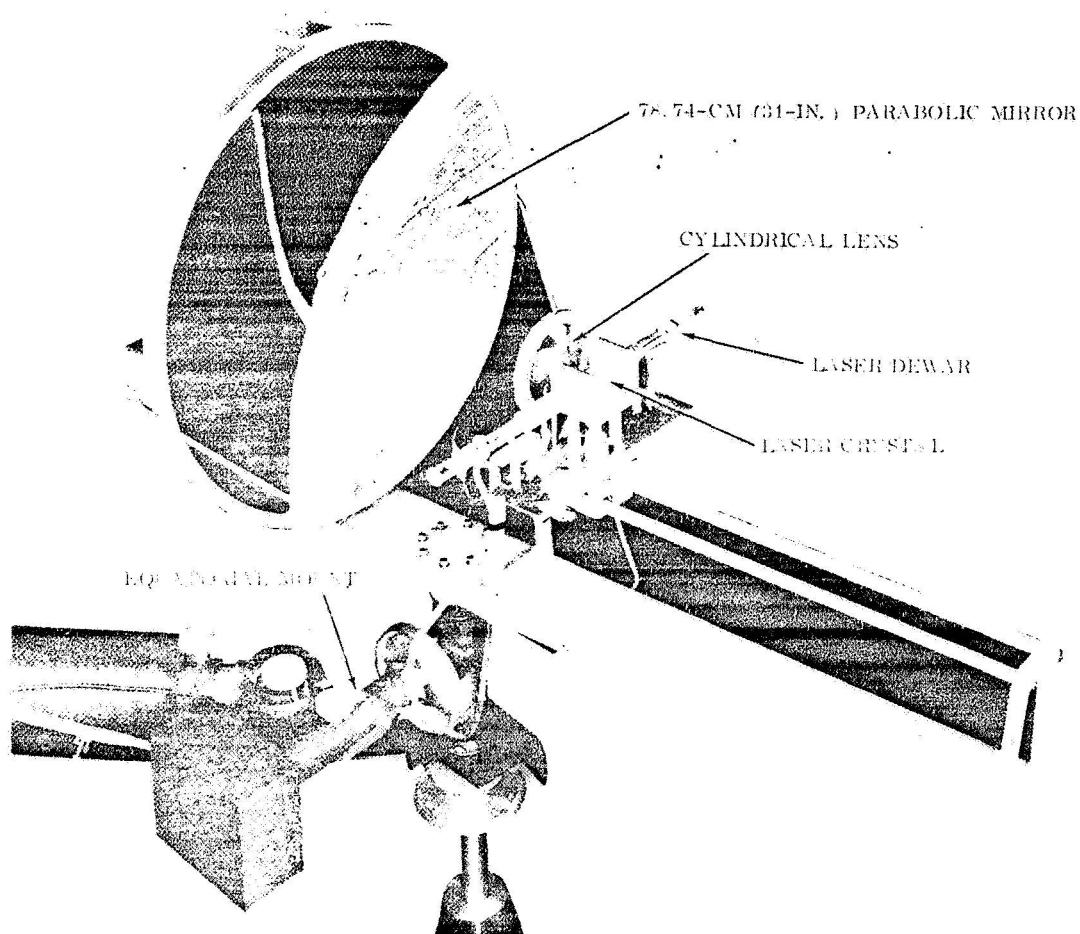
FIGURE 3. EQUATIONAL MOUNT WITH DISH AND DEWAR
MOUNTED FOR SOLAR PUMPING CaF_2:Dy^{2+}

150
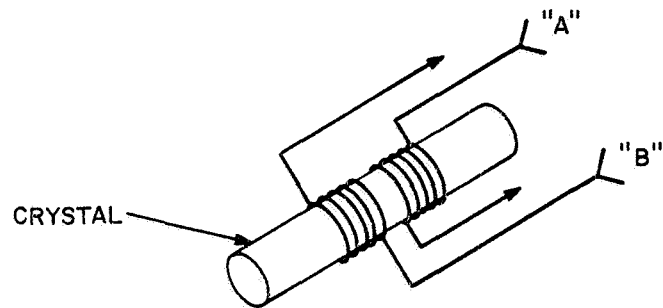
FIGURE 4. PHYSICAL ARRANGEMENT OF COILS AND
CRYSTAL FOR MAGNETIC MODULATION
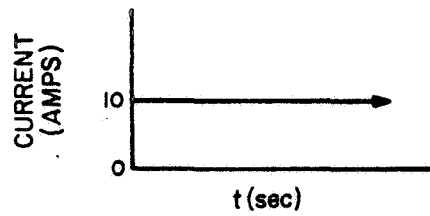
a. CURRENT IN COIL "A"
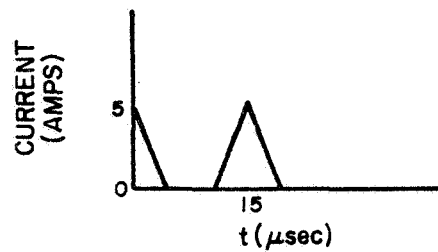
b. CURRENT IN COIL "B"
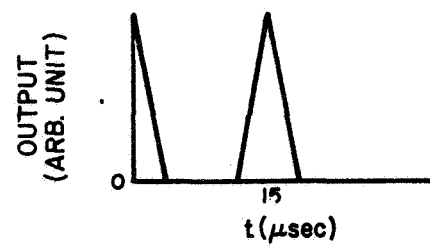
c. LASER OUTPUT

FIGURE 5. MAGNETIC MODULATION
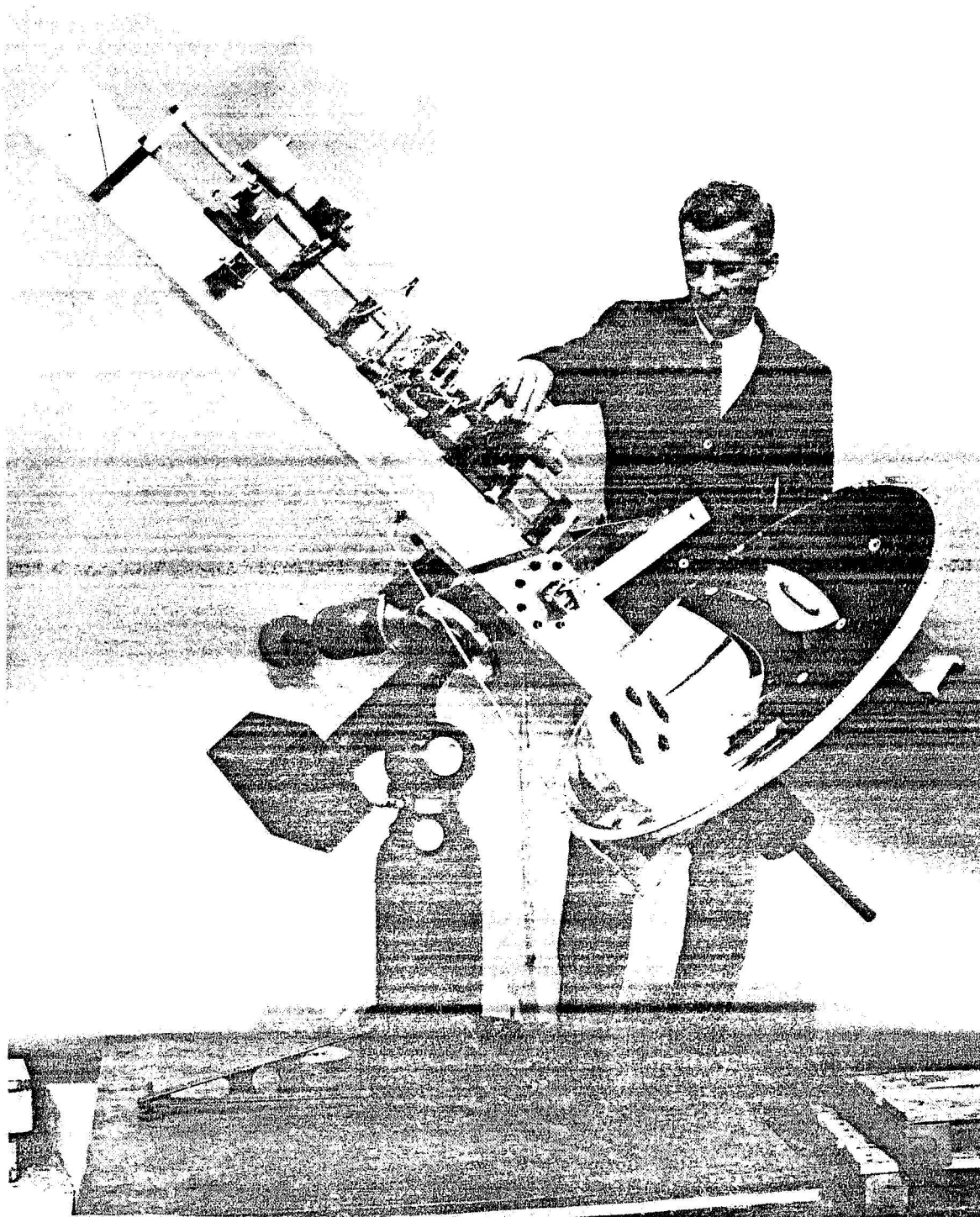
FIGURE 6. SOLAR PUMPING APPARATUS IN CONFIGURATION
USED IN PUMPING YAG CRYSTALS
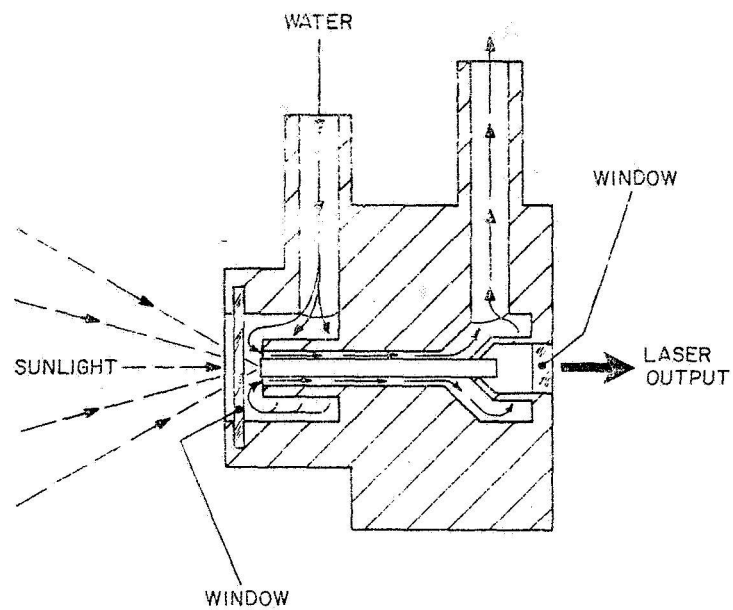
FIGURE 7. FLOW TUBE FOR YAG LASERS
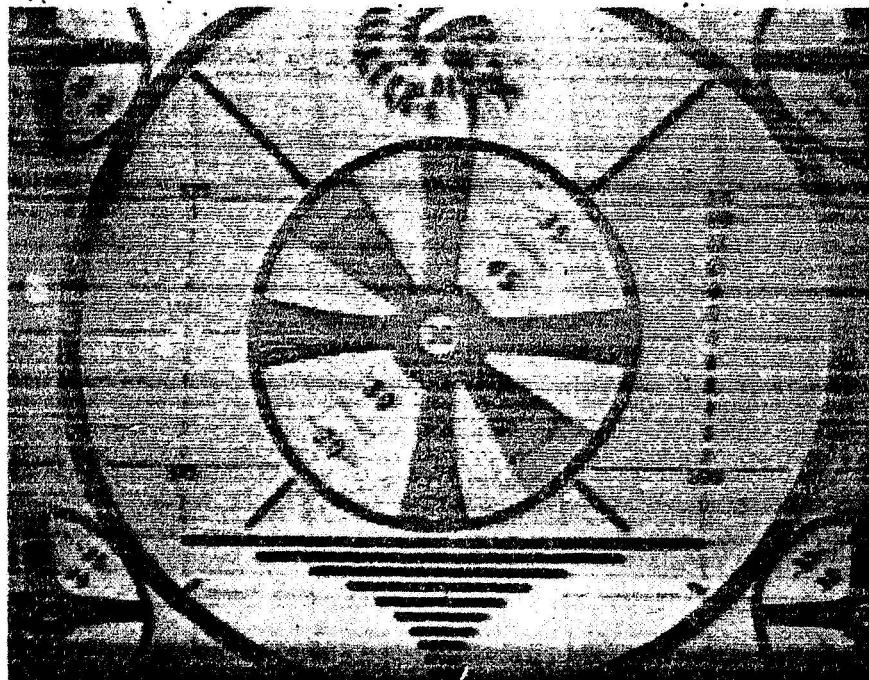
FIGURE 8. TEST PATTERN TRANSMITTED USING ELECTRO-OPTIC
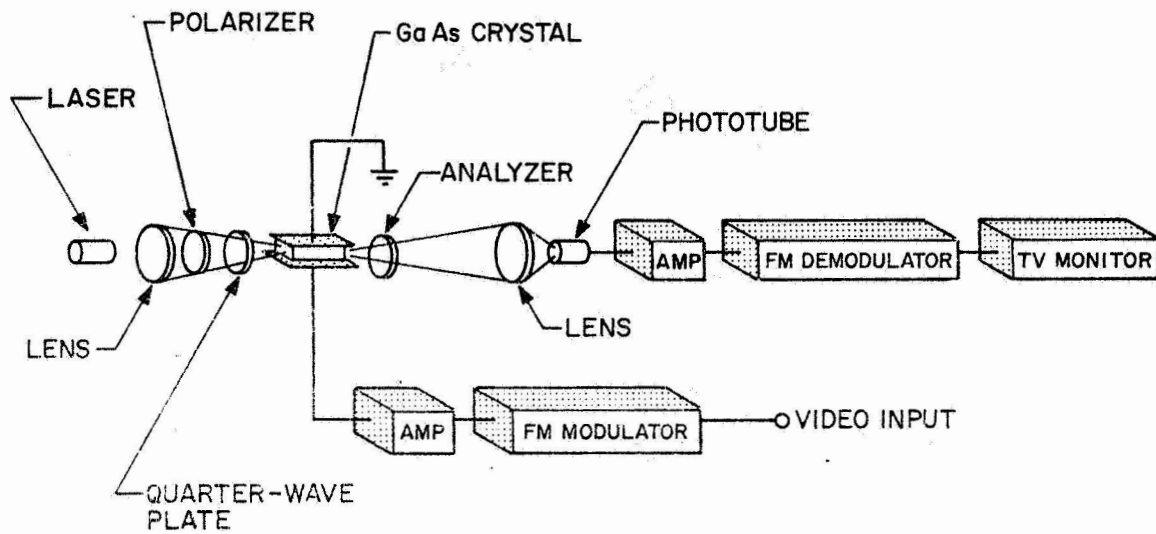MODULATION YAG:Nd^{3+} SOLAR PUMPED LASER

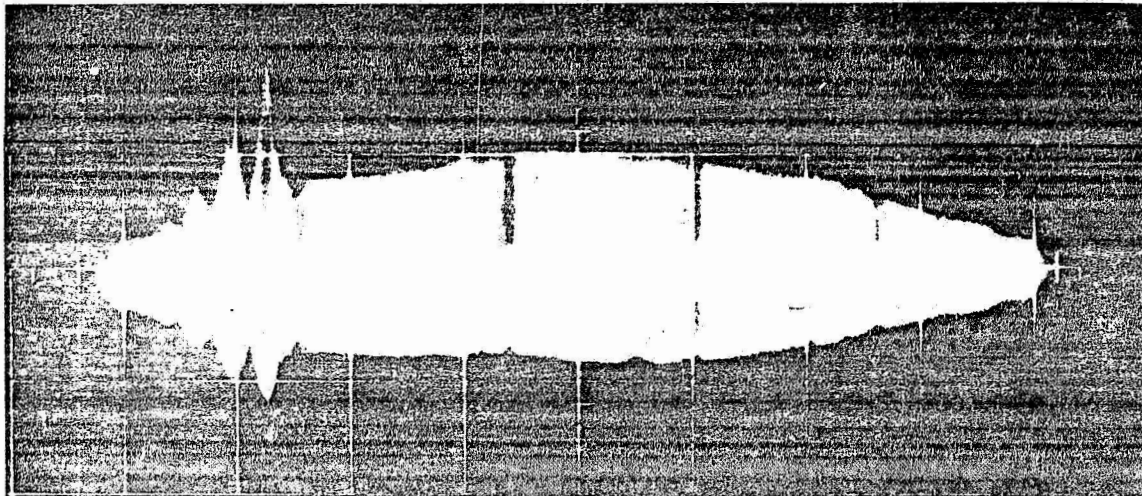FIGURE 9.   OPTICAL TV COMMUNICATION SYSTEM

FIGURE 10.   FREQUENCY RESPONSE OF GaAs CRYSTAL.
(MARKERS ARE AT 1, 3, 5 AND 7 MHz)

OPTICAL SUPERHETERODYNE RECEIVER DEVELOPMENT*

C. J. Peters
R. F. Lucy
Sylvania Electronic Systems

Under this program the feasiblity of operation of an optical superhetero-
dyne receiver with large-diameter optics in the atmosphere has been demon-
strated. Such a receiver has been operated over a 1.6-km (1-mi) atmospheric
path. The results of this experiment indicate that sufficient coherence of the
beam will be retained for both horizontal and vertical paths through the atmos-
phere to make operation of the optical superheterodyne possible and hence make
it possible to realize the advantages of the optical superheterodyne receiver.
As a result of the experiments and design studies a design for a deliverable
model of an optical superheterodyne receiver has been achieved. This unit is
now being constructed.

A major accomplishment of last year's program was the experimental
confirmation of an optical design that preserves coherence of the received op-
tical beam and that also expands the allowable angular tracking error. Assum-
ing that both the received signal and local oscillator are plane waves, the allow-
able tracking error for an optical superheterodyne receiver with an optical
aperture on the order of 20.32 cm (8 in.) would be in the microradians. Our
optical design expanded this allowable tracking error to approximately 200 μrad.
This means that an angular tracking servo of comparatively conventional design
can be used to track the incoming signal. This receiver will be installed in a
mobile van as shown in Figure 1. The van mounting makes it comparatively
easy to perform experiments at various geographical locations and also provides
a much larger field of view than is usually available from a laboratory building.

The block diagram for the optical superheterodyne receiver is shown in Figure 2. Generally speaking, the operation of the diagram is self-explanatory.

The spatial tracking function of the optical superheterodyne receiver is of vital importance to the receiver flexibility. The heterodyne optics and subsequent photomixing operation are extremely sensitive to angular changes of the signal direction. The spatial tracking follows the line of sight direction of transmitted signal and maintains the signal along the optical axis of the system. Tests performed upon the optical superheterodyne receiver have shown that the angular limits of operation are ± 100 μrad. Thus, the angular tracking accuracy of the spatial tracking system must be less than this value. The total error is the sum of the dynamic error arising from the relative motion between the receiver and the transmitter plus the static error produced by frictional torques and tachometer noise.

The servo constructed gives the desired tracking accuracy. The control configuration utilizes an image dissector for noncoherent spatial error detection and dc torque motors as prime movers.

When tracking low-acceleration targets such as satellites and airplanes, this tracker has an accuracy of approximately 25 μrad rms. The accuracy under these conditions is set by the static friction and equivalent noise bandwidth of the tracker and the scintillation of the atmosphere. When tracking high acceleration targets such as rockets, the tracker has a tracking error that is directly proportional to the angular acceleration of 0.6 rad/sec^2; the tracking angular error peaks to 0.6 mrad at launch and settles to 0.1 mrad within 0.1 second thereafter. Thus, the tracking accuracy against low-acceleration targets is comparable to the accuracy of a star tracker.

The controlled member in the tracker is a two-axis gimballed mount on which is carried the flat directing mirror. Both axes of this mount are powered by dc torque motors directly coupled to the unit. Angular rate feedback information is obtained by dc tachometers, which are also fastened directly to their respective axes.

The lowest structural resonance occurs about the azimuth axis at 45 Hz. This resonance limits the azimuth gain crossover frequency but does not significantly affect the elevation loop. The rate loop gain crossover frequencies are 30 Hz in the azimuth and 50 Hz in the elevation channel. The position loop gain crossover frequencies are 10 Hz in azimuth and 17 Hz in elevation. Both

156

axes have integral networks with an upper break frequency at 2 Hz and a lower break frequency of 0.02 Hz. The equivalent noise bandwidth for the tracker is 19 Hz in the azimuth and 30 Hz in the elevation.

High precision bearings of the ABEC class 7 type are used in both axes. Including the contributions from the various potentiometers, tachometers, and motors, the measured static friction on both axes is 9.52×10^{-2} joule (7×10^{-2} ft-lb). The static pointing accuracy on both axes is on the order of 10 μrad.

The trace of signal rays and local oscillator rays through the system is shown in Figure 3. The received rays are reflected from the beam director to the parabolic mirror and thence to the secondary beam forming mirror. The collimated return signal is then mixed with the local signal at the mirror adder and the resultant beat detected by the photomultiplier. The laser local oscillator signal is focused by a beam forming lens to match the return signal in size and divergence angle.

Another signal takeoff at C provides the optical error signal for the angle tracking servo. A spotting telescope is also incorporated in the system for visual data takeoff.

The optics have been experimentally tested, and it was found that heterodyning was not impaired over input angle of arrival variations of up to 10 mrad providing local oscillator and signal alignment were readjusted to accommodate the input angular offset. Without readjustment the allowable offset increments could only be 100 μrad.

The physical design of the optical portion of the receiver is shown in Figure 4. This drawing shows the main signal collecting optics, the various alignment fixtures, and the viewing telescope. The angle tracking servo, which fits on the right end of the optical structure, is not shown.

In an optical superheterodyne receiver using a photoemissive detector the detection of the beat frequency is performed at the photosurface. At low light intensities the resultant currents are small even when large local oscillator power is used. Maximum receiver sensitivity is obtained when the signal-to-noise ratio P_{so}/P_{no} is given by [1]

$$\frac{P_{so}}{P_{no}} = \frac{QP_s}{h\nu\Delta f} \quad , \tag{1}$$

157

where

Q is the quantum efficiency

P_s is the signal power

$h\nu$ is the energy per photon

Δf is the electrical bandwidth.

The sensitivity expressed by equation (1) will be degraded if the amplification following the photosurface detection process introduces a noise power greater than $h\nu\Delta f/Q$. In photomultipliers the secondary emission amplification introduces some noise. This additional noise degrades the value of equation (1) about one dB in well designed and operated tubes. In photomultipliers this "noiseless" amplification is sufficiently large to eliminate further signal-to-noise degradation by the amplifiers following the tube output.

Standard fast rise time tubes have 3-dB cutoff frequencies of about a hundred megahertz. In this system the detector bandwidth must only be greater than the i.f. bandwidth following the detection even for Doppler frequency tracking to 1 GHz.

The laser local oscillator noise and power requirements are discussed in Biernson and Lucy [1]. Ideally sufficient monochromatic power should be available to permit discrimination against random noise-producing sources such as reflected or scattered sunlight. Also the noise produced at the output of the photomixer caused by the local oscillator should not exceed the expected shot noise level for the corresponding local oscillator power. An existing single frequency laser, the Spectra Physics Model 119 laser, has been evaluated for this purpose and found to be satisfactory. The monochromatic power output is approximately 100 μW. Anticipated severe background levels such as a bright cloud should not exceed 0.1 μW. Thus, the local oscillator should be at least 1 μW to provide good background discrimination. Measurements of the noise in a 4-MHz bandwidth for the laser tested showed the noise to be "white." The rms value of the noise exceeded by three times the minimum shot noise level expectations. This level degrades the system performance. Measurements of the short-term rate of change of frequency are 10^8 Hz^2. The design of the rf frequency tracking loop is based on this estimate.

The laser is also tunable over a 1200-MHz range via a voltage controllable cavity length at a rate up to 5 kHz. Thus this laser is used in the frequency tracking loop to cover a Doppler range of 1000 MHz.

The frequency tracking loop provides the automatic tuning to keep the difference frequency constant at the intermediate frequency as the Doppler frequency changes. Eventually the tracking loop should provide search and acquisition capabilities since momentary or prolonged disruption of the optical link could occur.

The laser signal containing the Doppler shift is mixed with the optical local oscillator signal in the photomixer. The output of the photomixer containing the Doppler frequency is fed into the i.f. amplifier.

Because of the closed-loop operation, an error signal is developed at the discriminator that keeps the difference frequency between the two signals at a constant i.f. value. The bandwidth of the AFC loop is chosen at the minimum value consistent with the expected rates of change of frequency. This insures a relatively high signal-to-noise ratio.

The AFC loop bandwidth is determined by the maximum rate-of-change of the input frequency expected. For instance, the maximum frequency deviation rate caused by the drift of a single frequency laser such as the Spectra Physics Model 119 has been found to be 10^8 Hz^2. If the error were required to be half of the AFC loop bandwidth of $\Delta f_c / 2$, then the necessary loop bandwidth (gain-crossover frequency) would be

$$\frac{\dot{f}}{\Delta f_c} = \frac{\Delta f_c}{2} \quad , \tag{2}$$

which for

$$\dot{f} = 10^8 \text{ Hz}^2$$

$$\Delta f_c = 5.7 \times 10^3 \text{ Hz}^2 \quad .$$

In a similar fashion the bandwidth necessary to accommodate the rate-of-change of the received signal frequency due to relative motion between the system end points can be calculated. For a mission such as a missile being launched straight up from a launch pad at a certain distance from the tracker,

the maximum rate-of-change of Doppler occurs at an elevation of $\pi/4$ rad and is proportional to the $\sqrt{2}$ times the missile acceleration. For a missile undergoing an acceleration of 30.5 cm/sec^2 (100 ft/sec^2) the maximum Doppler rate of change is approximately 150 MHz^2. To track this rate-of-change in frequency on the incoming signal the bandwidth must be 6.7 kHz.

The accuracy with which the AFC loop can operate will be a function of the signal-to-noise ratio at the discriminator input. The tracking error δf in the loop bandwidth Δf_c is approximately

$$\delta f = \frac{\Delta f_c}{N} , \qquad (3)$$

where N is the signal-to-noise voltage ratio. In system calculations a minimum value of N has been required to be 10 in a 4-MHz bandwidth. If Δf_c is 6 kHz as calculated above, the maximum tracking error will be approximately $\delta f = 23$ Hz.

Coherent light propagation experiments over 1829-m (6000-ft) atmospheric paths have been performed. They were carried out using the local oscillator as both the transmitter and receiver in a homodyne mode of operation. For convenience a frequency offset for the local oscillator was obtained by using a reciprocating mirror to generate Doppler frequency. The object of the experiments has been to determine the effects of the atmosphere on the heterodyne frequency signal. Amplitude, phase, and angle of arrival fluctuations all produce signal variations.

Data have been taken over the 1829-m (6000-ft) atmospheric path under varying meteorological conditions. The transmitter-receiver has been located at the Sylvania Waltham Laboratories, and the retroreflector is located on Bear Hill, which is 914 m (3000 ft) away. The elevation of the transmitter-receiver and retroreflector installation are approximately the same. Terrain in between is a tree studded valley whose elevation is approximately 31 m (100 ft) less than the propagation path. Typical system performance data are summarized in Table I.

Typical signal returns are shown in the oscillogram, Figure 5. This record was obtained in June 1964 on a fair weather day. The wind velocity was about 9 m=sec (20 mi/hr). A 6.35-cm (2.5-in.)-dia retroreflector was used to reflect the signal back to the receiver. The top trace shows the beats generated by heterodyning the return with the local oscillator. The beats occur in

groups because of the manner in which the local oscillator frequency offset was obtained and should repeat every 1.7 msec. The rounding of the envelope is caused by the amplifier bandwidth. The signal was filtered by a bandpass filter that passed 3 kHz to 10 kHz to remove the low-frequency intensity fluctuations. Frequency translation was performed mechanically. The laser output was shifted in frequency to form the local oscillator signal by reflecting the beam from a moving mirror. Because a reciprocating mirror motion was actually used, the Doppler frequency shift varied with time giving rise to the envelope of the waveform in Figure 5. The lower trace in Figure 5 is the return signal passed through a low-pass filter with a cutoff frequency of 1 kHz. No beats are present because they do not fall within this bandwidth. The trace is a representation of this instantaneous photocurrent. It indicates the signal power fluctuations since the atmospheric turbulence produces only low-frequency variations. Approximately 80 to 90-percent amplitude modulation is represented by intensity signal excursion. In general, one would expect the beat signal to be somewhat smoothed as compared with the optical power fluctuation because the beat signal is proportional to the square root of the received optical power. Preliminary tests indicate this to be true at times, although other effects can be observed.

In preliminary observations, pronounced beat amplitude variations have been noted that cannot be correlated with the amplitude fluctuations. These observations as shown in Figure 5 include increases in beat amplitude with decreasing optical power return and vice versa. Also complete beat signal dropouts without intensity dropouts have been observed. In Figure 5 the largest beat signal occurs at a medium intensity level; smaller beat then occurs at a higher intensity level, and a partial dropout has occurred between these beats. The fourth beat is also missing. Then when the power is low a relatively good beat occurs. The low amplitude fine structure in the beat signal display is laser local oscillator noise.

In an optical superheterodyne receiver, an electrical beat signal is generated by adding the incoming optical signal to the optical local oscillator of a slightly different frequency and detecting the envelope in a square-law detector. The wavefronts of the optical signal must be perfectly matched to the wavefront of the local oscillator to obtain a maximum beat signal. If the wavefronts are inclined to each other the photocurrent signal can be severely degraded. To understand why, recall the Michelson interferometer. Interference fringes are produced as a result of one mirror being at a slight angle with the other. In the Michelson interferometer two waves of the same frequency are

used to produce the interference pattern. In our case the waves are at slightly different frequencies; thus, there is a heterodyne beat between the two wave-fronts. If we observe the area of interferences as in the Michelson interferometer we would see the interference pattern changing with time. The bright and dark bands would move in progression across the observation area at the beat frequency rate. The changing pattern is indicative of the changing phases between the two optical waves.

If a phototube surface were illuminated with this pattern then the cross section of the photocurrent output would be a replica of the time changing interference pattern. The ac component of the photocurrent would be the beat note. The dc component would be proportional to the intensities of the two optical waves. The anode of the phototube sums the instantaneous values of all the signals. If there are many fringes in the pattern then alternate plus and minus signal components cancel each other. The net photocurrent would be the residual after the cancellation. For example, if there are 6 bright and 5 dark fringes at any instant of time then 5 fringes of one polarity of phases cancel 5 fringes of the other polarity and only 1/11 of the total ac signal remains. As the number of fringes is decreased by better-matching of the wavefronts then the ac beat component collected by the anode increases.

An optical superheterodyne system would be designed to match both signal and local oscillator wavefronts. Atmospheric turbulence or transmitter-receiver angular alignment errors can easily produce appreciable tilting between the signal and local oscillator wavefronts. In addition telescopes used for collecting optics can introduce an angular magnification. We have attempted to solve the mismatched wavefront problem in the optics. Experimental results have shown some sign of success.

The experiments have shown that the reduced angular sensitivity in this system is not only a function of the overlap areas and angular mismatch but also depends upon the shape of the wavefronts being mixed. Thus mixing a plane wave with a spherical wave as compared to mixing either two plane waves or two identical spherical waves produces a different result.

The experiments compared the mixing with spherical waves as opposed to mixing with plane waves. The results of the experiments are shown in Figure 6. The optical design that is most demanding on the pointing accuracy requirements uses plane wavefronts in the mixing process. The fringing obtained under this optical arrangement is shown in Figures 6a and 6b. In photograph 6a the

162

local oscillator and received signal are collinear. In 6b there is a 70-μrad angle between the local oscillator signal and the received signal. The alternate light and dark bands of fringes represent areas where the local oscillator and received signal shift 180° in phase. Thus, the signal in the light band tends to cancel the signal in the dark band. In the misaligned case where there are many more light and dark bands, this cancellation is almost complete so that the mixing process is very inefficient. In fact, the efficiency drops to zero when there are equal light and dark areas and rises to a local small maximum when there is an excess of one kind or the other. Consequently small angular disturbances can produce a 100-percent modulation on the heterodyne signal. Jitter in the servo or optical signal angle of arrival fluctuations caused by atmospheric turbulence will thus produce a noise modulation of the signal. In the plane wave case of Figure 6a and 6b a 1.5-μrad change varies the mixing efficiency from a maximum to zero.

In Figure 6, c and d, spherical waves were used in the heterodyning process. A simplified analysis of the spherical wave mixing shows that although the mixing efficiency at perfect alignment cannot have as large a value as the plane wave case, the efficiency does not go through large oscillations as the angular misalignment is changed. In fact for the case shown in Figure 6d an additional 1.5-μrad misalignment produces only a 2-percent change in the mixing efficiency.

The results of the simplified analysis are shown in Figure 7, where the mixing efficiency is shown as a function of the angular misalignment for the same two cases shown in the photographs. This analysis was performed for a one-dimensional cut through the center of the mixing area perpendicular to the fringes. In the plane wave case the violent oscillations of the efficiency are not shown in order to simplify the drawing. In the spherical case it can be seen that only very minor oscillations occur. Thus the spherical case is less sensitive to misalignment.

The detection of FM modulated light by an optical superheterodyne receiver was performed in an experiment. The significance of this experiment is that it is the first unambiguous demonstration that modulation processes and receiver techniques for FM, which are commonplace at radio frequencies, are directly applicable at optical frequencies.

The experimental setup is shown in Figure 8. The transmitter consists of a single-frequency gas laser operating at 6328 Å. The output of this laser passes through a Sylvania S2ϕ phase modulator. This modulator was excited by 530-kHz sinusoidal wave.

The receiver consists of a photomultiplier upon which was incident the output of the transmitter and a laser local oscillator signal generated by a second single frequency gas laser operating at 6328 Å. The output from the photomultiplier is at a frequency equal to the difference between the laser local oscillator and the transmitter. The output of the i.f. amplifier passes to a discriminator that detects the received signal and supplies an error signal for the AFC loop that controls the local oscillator laser frequency.

The AFC loop for the local oscillator was constructed from the AFC components of an AN/SPS-10 radar. This high-gain loop locked the receiver to the transmitter to within a frequency excursion of about 10 kHz. The bandwidth of the discriminator was about 3.5 MHz.

A spectrum analyzer was connected directly to the output of the i.f. amplifier to permit examination of the translated spectrum of the transmitter output. Photographs of the spectrum analyzer display are shown in Figure 9. Figure 9a shows the unmodulated carrier. Examination of this figure gives a qualitative idea of the frequency jitter and noise on the unmodulated carrier. Figure 9b shows the frequency spectrum for sinusoidal modulation at 530 kHz at a modulation index of 1.8. At this modulation index the first sidebands are maximum and the carrier is slightly smaller than the sidebands.

At this modulation index, the second sideband components are also becoming significant. Figure 9c shows the transmitted spectrum for a modulation index of 2.4 where the carrier goes to zero and the first, second, and third sidebands are visible.

To a large extent these spectra precisely duplicate the spectra one would obtain with a conventional radio frequency system excited with appropriate sine waves. The only difference between these results and those obtained with the rf signal is the presence of a considerable amount of noise on the carrier. This noise takes the form of random frequency and amplitude variations. From the analysis of a particular case it seems reasonable to expect that satisfactory systems can be constructed in spite of a noisy carrier under proper conditions of modulation index and carrier noise. This conclusion is intuitively apparent from inspection of photographs in Figure 9 on the basis of the relative width of the spectral lines compared to the spacing between the lines.

The 530-kHz output from the discriminator is shown in Figure 10. Here the relative amount of noise arising from the carrier noise can be judged directly.

The optical FM receiver is somewhat more complex than the AM receiver. However, optical amplitude modulation systems operating in the atmosphere are subject to rapid fading. The frequency spectrum of the fading may at times contain significant components up to 500 Hz. Also, some lasers have amplitude noise components whose frequency spectrum extends up to several hundred kilohertz. By proper receiver design it is possible to handle these amplitude fluctuations; indeed, these circuitry complications appear simpler than the optics of an FM receiver.

Temporal variations in the average index of refraction along the path between the transmitter and the receiver will cause variations in the phase of the received signal. Hence, these index of refraction variations will produce an incidental phase or frequency modulation of the received signal. These index variations arise from variations in temperature, pressure, and water content of the atmosphere. Taking into account the functional relationship between the optical index of refraction and these state variables it is possible to extrapolate the index of refraction data collected at microwave frequencies. This extrapolation indicates that the phase excursion should be very slow, i.e., on the order of a few hertz, which can easily be tracked by a simple AFC loop. Heavy limiting prior to the discriminator will subdue the amplitude scintillations which will be present on the received signal. Thus the optical heterodyne FM receiver seems intrinsically capable of handling atmospheric fluctuations. The comparative complexity of the optics and laser local oscillator may be justified when the other characteristics of heterodyne detection are desired.

REFERENCE

1. Biernson, G.; and Lucy, R. F.: Requirements of a Coherent Laser Pulse Doppler Radar. Proc. IEEE, vol. 51, Jan. 1963, pp. 202-213.

TABLE I

COHERENT LASER SYSTEM DATA (HOMODYNE OPERATION)

Radiated Power	5×10^{-4} W
Radiated Beamwidth (5%)	5×10^{-4} rad
Average* Received Signal Power	3.2×10^{-6} W
Average* Signal Power at Photomixer	1.3×10^{-6} W
Local Oscillator Power	1.8×10^{-6} W
Peak Local Oscillator Signal-to-Noise	42 dB
Average* Beat Frequency Signal-to-Noise	38 dB
Heterodyne Efficiency**	-10 dB
Retroreflector Target at 914 m (3000 ft)	

---

* Average value signal fluctuating because of atmospheric propagation effects.

** Ratio of average heterodyne signal level to maximum theoretical beat signal level corresponding to measure values of average received signal and local oscillator signal.
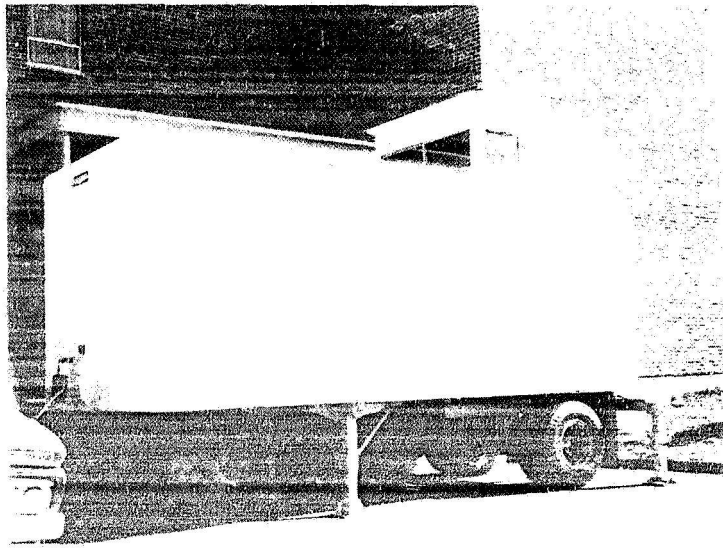
FIGURE 1. OPTICAL SUPERHETERODYNE RECEIVER VAN
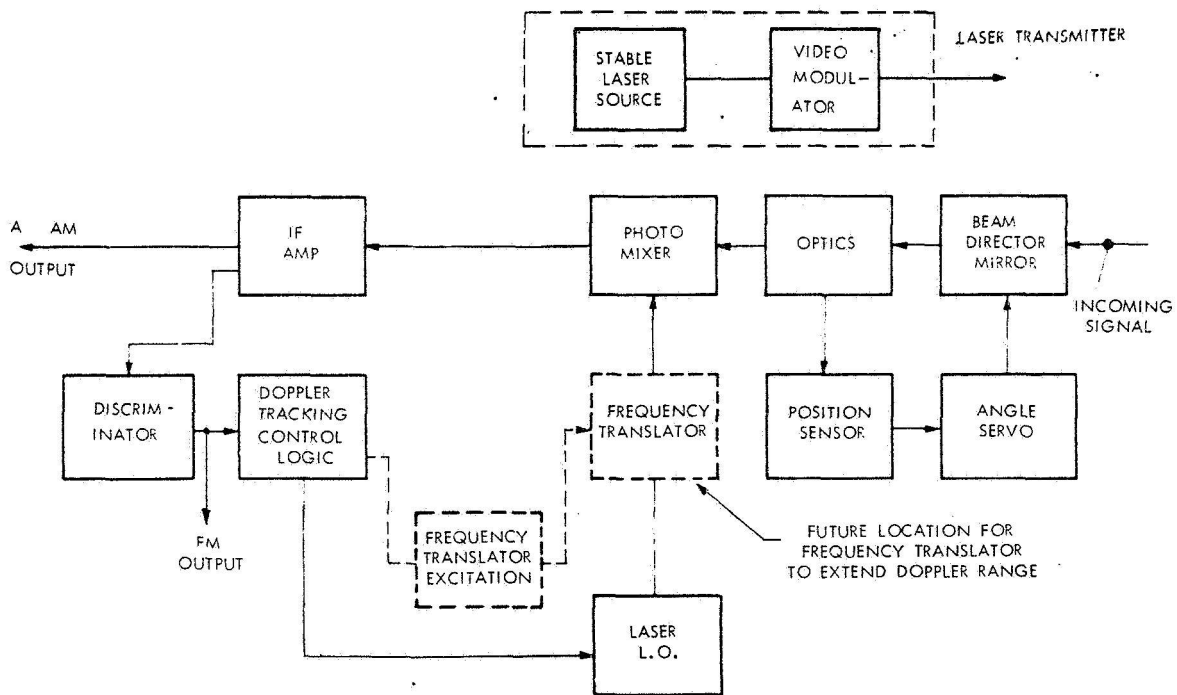
FIGURE 2. OPTICAL SUPERHETERODYNE RECEIVER

168
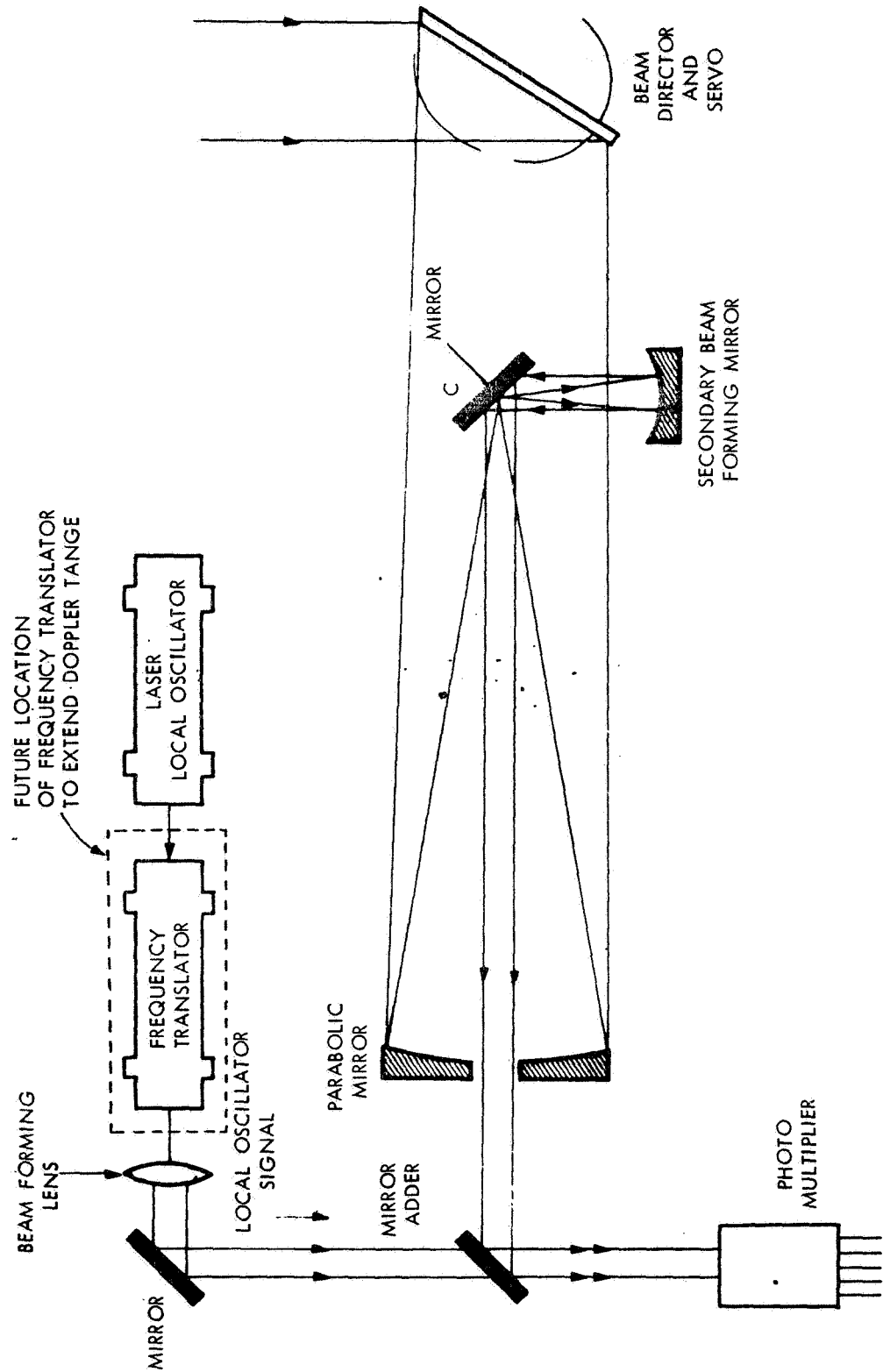
FIGURE 3. OPTICAL LAYOUT OF LASER SYSTEM

169
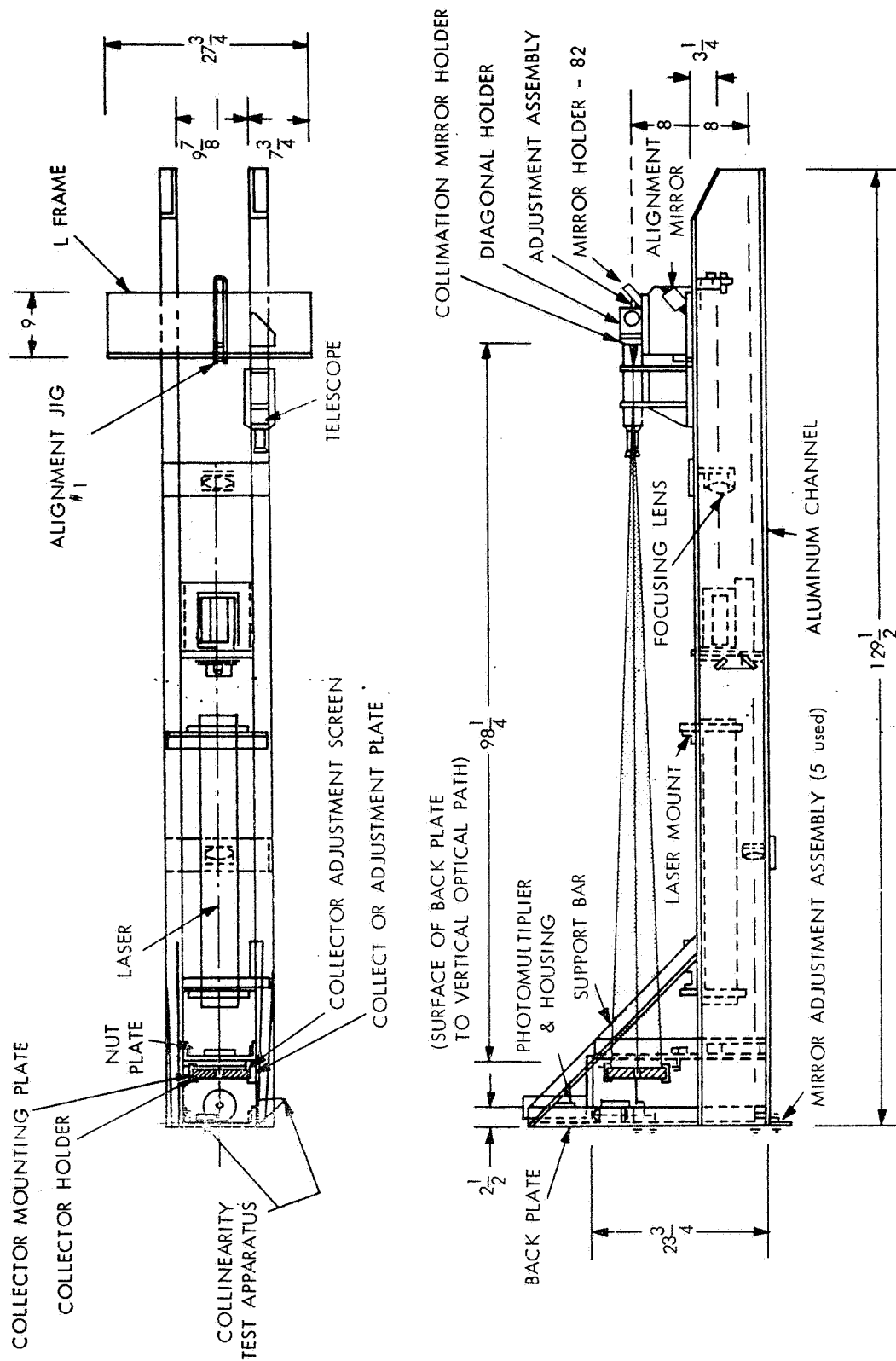
FIGURE 4. RECEIVER OPTICS PHYSICAL DESIGN

170

HETERODYNE
SIGNAL

MAXIMUM
LIGHT

LIGHT
INTENSITY

TIME SCALE 1 MS/DIVISION
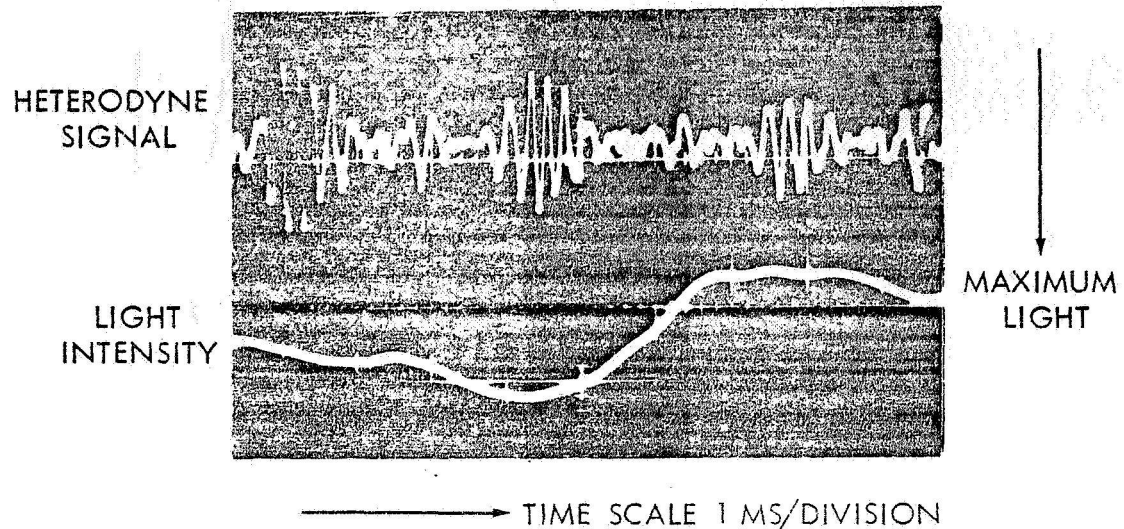
FIGURE 5. OSCILLOGRAM OF RETURN SIGNAL

(a)

TWO PLANE WAVES
COLLIMATED

(b)

TWO PLANE WAVES
70 MICRO RADIANS TILT

(c)

TWO SPHERICAL WAVES
400 CM RADIUS OF CURVATURE
1600 CM RADIUS OF CURVATURE
(COLLINEAR)

(d)

TWO SPHERICAL WAVES
400 CM RADIUS OF CURVATURE
1600 CM RADIUS OF CURVATURE
70 MICRO RADIUS TILT
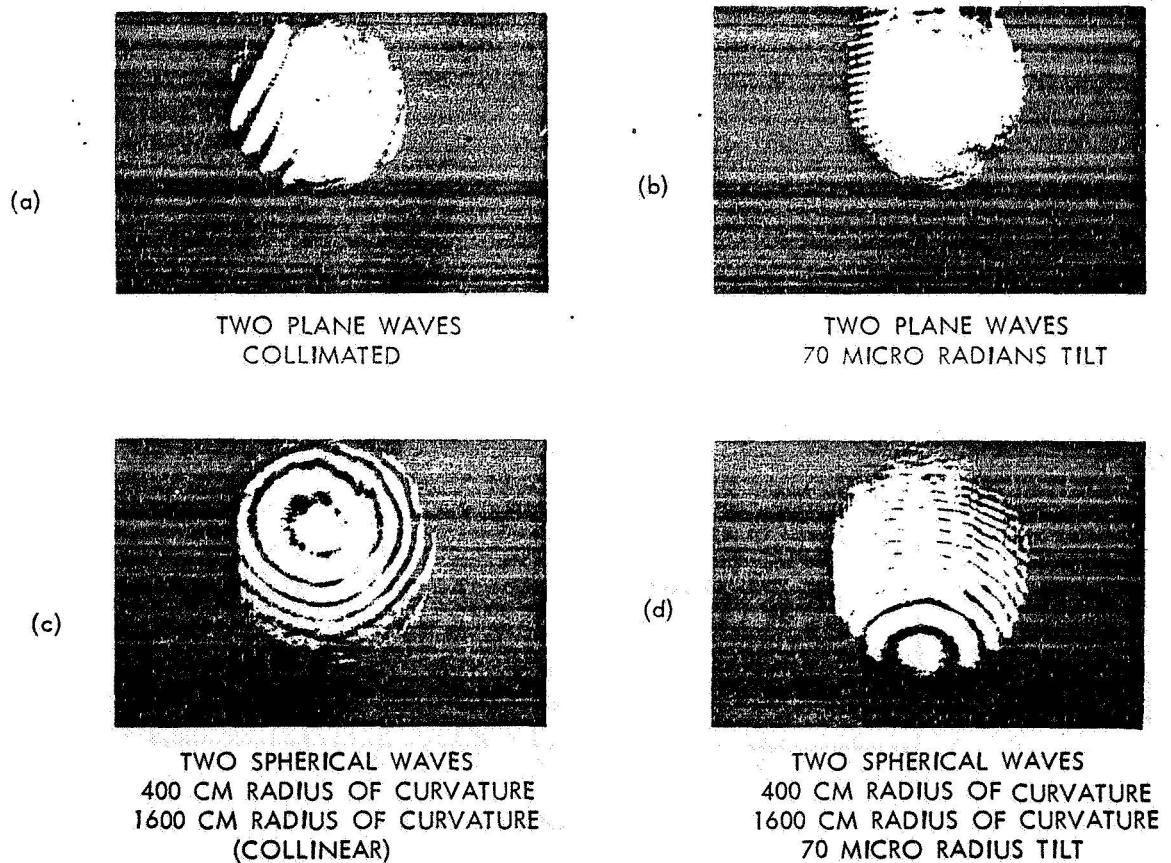
FIGURE 6. RESULTS OF EXPERIMENTS COMPARING MIXING OF
SPHERICAL WAVES TO MIXING OF PLANE WAVES
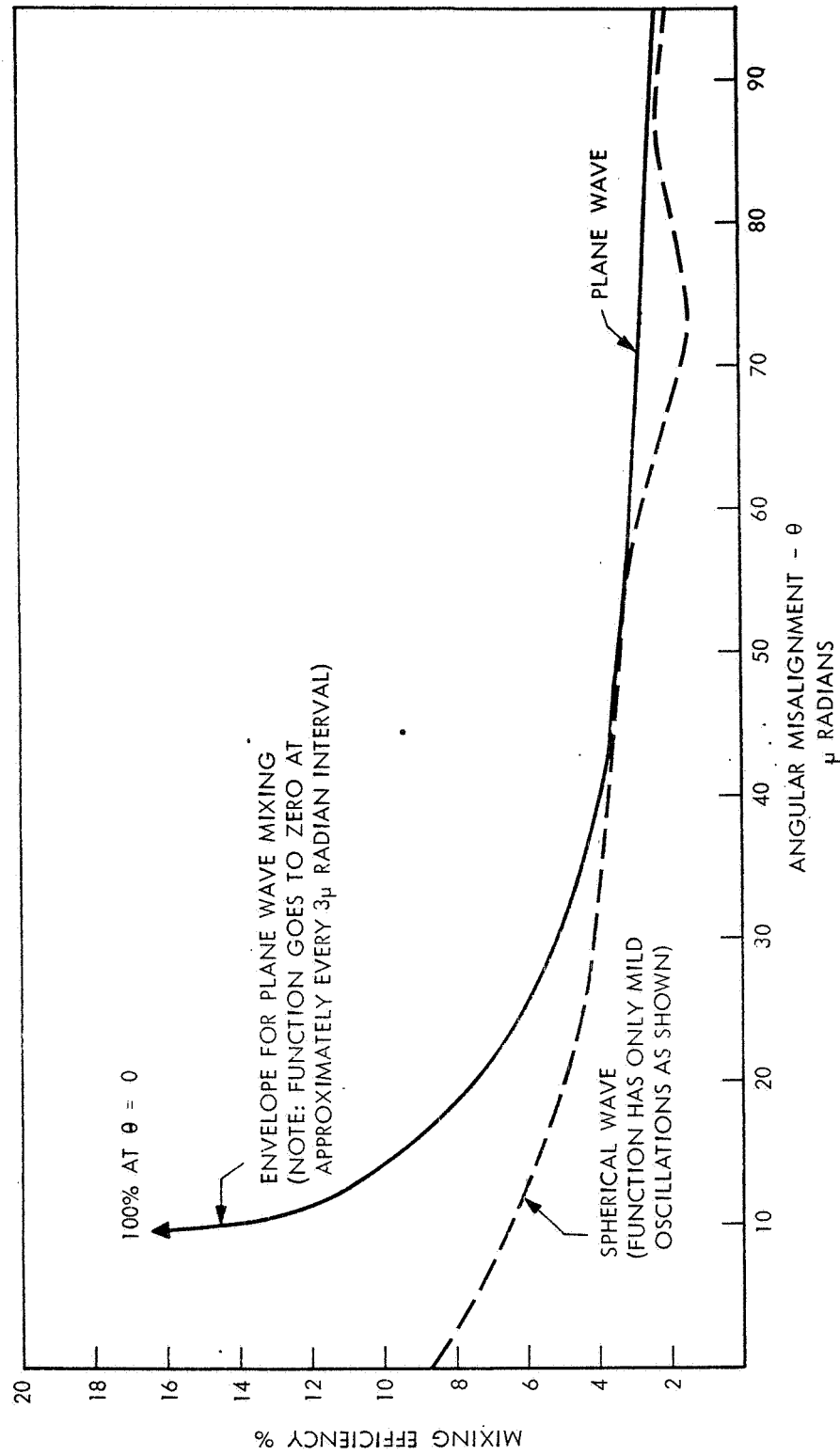
FIGURE 7. MIXING EFFICIENCY VS ANGULAR MISALIGNMENT
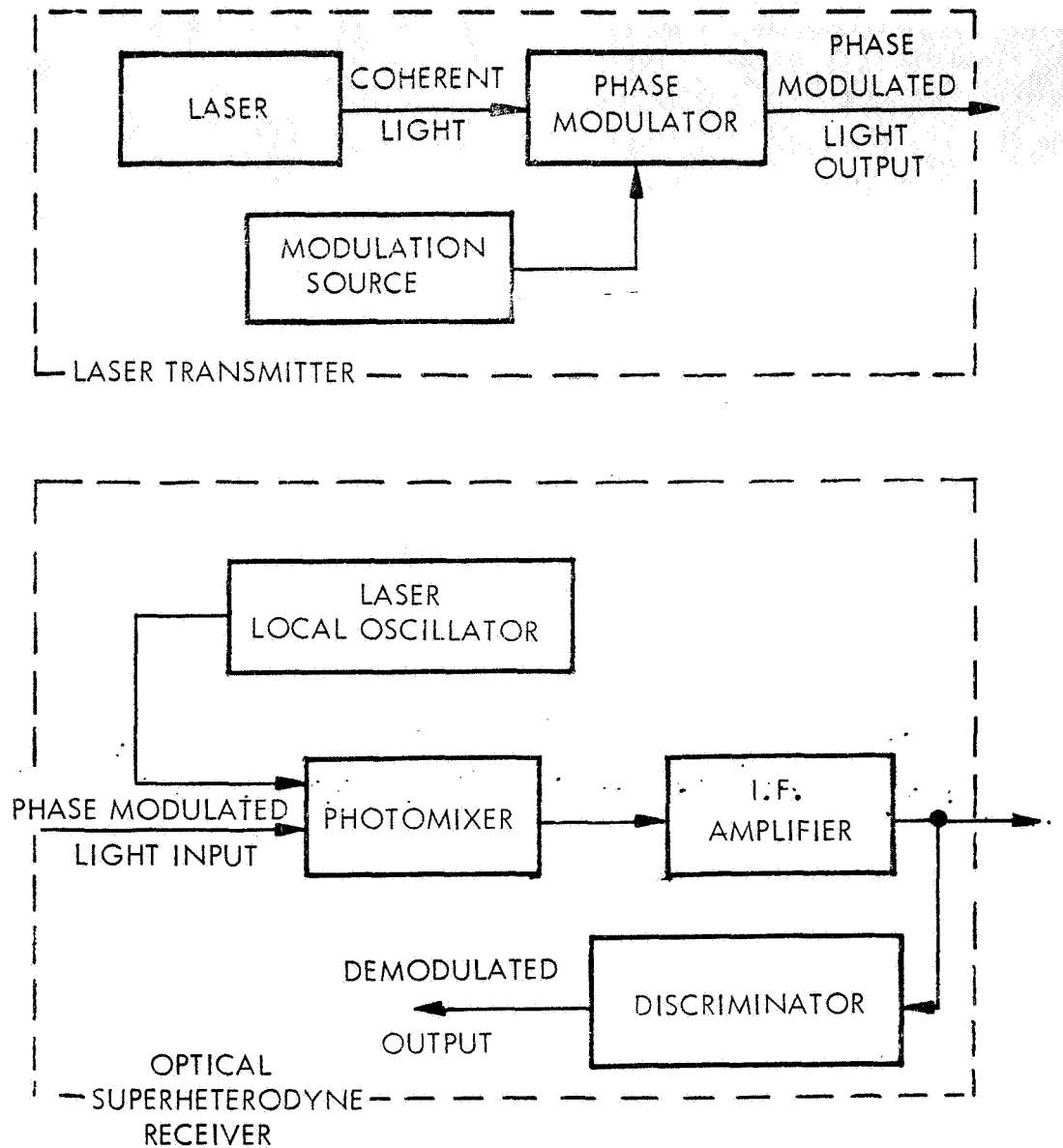
FIGURE 8. FM EXPERIMENT BLOCK DIAGRAM
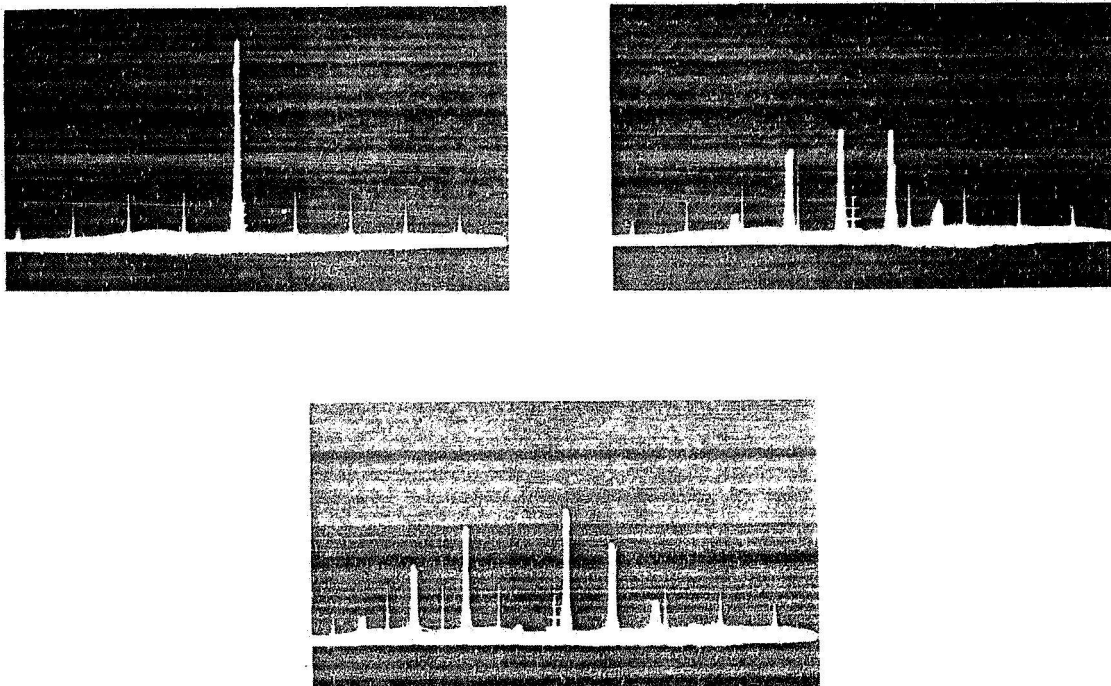
FIGURE 9. FM SPECTRA OF RECEIVED SIGNAL FOR DIFFERENT
MODULATION INDEXES
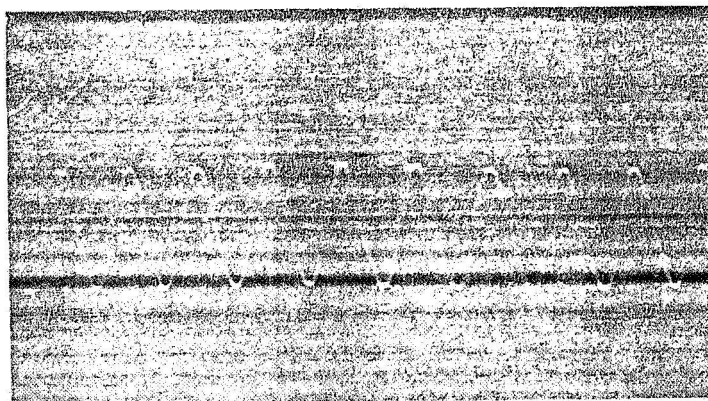
FIGURE 10. DEMODULATED SIGNAL OUTPUT OF DISCRIMINATOR

174

STABLE LASER SOURCE

J. T. LaTourrette
TRG Incorporated

For deep-space laser communications, a laser source with the highest possible spectral brightness is required. Such a laser must be a high-power single-mode laser with constant power output and constant oscillation frequency. Constant, high single-mode power can be achieved by employing an optimally designed laser resonator and a stable power source. The subject of the present paper is the stabilization of the laser oscillation frequency as applied to an He-Ne 6328-Å laser. This work has been supported by the Marshall Space Flight Center under contract monitored by Dr. J. Randall.

It is difficult to achieve passive stability in a laser resonator better than about one part in 10^8. To achieve a stability of one part in 10^{11} or better, it is necessary to actively stabilize the resonator length to maintain an oscillation frequency that is constant with respect to the best available frequency standard, the center of the laser fluorescent line.

One method of stabilizing a laser is to frequency modulate the laser and monitor the modulation of the power output. However, it is necessary to frequency modulate the laser over a fair fraction of the total laser linewidth to detect sensitively an error in the average laser oscillation frequency. This required modulation of the laser frequency limits severely the usefulness of the method.

The present stabilization method consists of modulating the laser medium gain and monitoring a small frequency modulation that results from the dispersion of the laser medium. The method can be applied to any laser medium that has an "inhomogeneously broadened" line and thus exhibits a "Lamb dip" in the power output at line center as shown in Figure 1. Media that have a Lamb dip also have a mode pushing effect which depends on the gain of the laser medium. As a result, modulation of the gain will frequency modulate the laser frequency by an amount that, near line center, is proportional to the difference between the oscillation frequency and line center. This induced frequency modulation is thus an excellent discriminant for correcting the oscillation frequency to line center. A typical discriminant is compared with the single-mode power output in Figure 2.

The induced FM can be detected very sensitively by using optical heterodyne detection to translate the optical frequency spectrum of the modulated laser output down to a convenient radio frequency where a standard rf discriminator can be employed. A second "slave" laser was used as a local oscillator to accomplish this frequency translation by optical heterodyne detection. The experimental arrangement is illustrated in Figure 3. Voltage control of the laser length is accomplished by mounting the reflectors in the laser resonators on piezoelectric transducers. A constant i.f. is maintained with a standard AFC feedback loop. The frequency of the master laser is then stabilized with respect to line center by applying gain modulation (at a frequency that is above the AFC control bandwidth), detecting the induced FM at the discriminator output with a phase sensitive detector, and feeding back the error voltage onto the piezoelectric transducers to produce a null error voltage. It should be emphasized that the induced frequency modulation vanishes at the "null point" that very precisely defines line center. Thus, when the laser is stabilized there is no modulation of the laser frequency. The only modulation of the laser is amplitude modulation, i.e., modulation of the laser power.

It should be noted that the involvement of a second laser in this stabilization method is not a useless complication. In general, it would be desirable to operate the stable "master laser" under low power conditions to achieve stable operating conditions and long-term stability of the reference frequency. The slave laser, which has inherently the same stability as the master laser and which can be displaced by any convenient offset frequency from line center, can be much more powerful and be used as the transmitter laser.

In the stabilization of 3.39-μ lasers, it was possible to modulate the gain by modulating the laser input power as shown in Figure 3. Such power modulation of the 6328-Å laser did not produce a useful discriminant; a direct frequency modulation caused by modulating the plasma was much larger than the desired induced modulation. Therefore it was necessary to apply another method of modulation that would not directly modulate the plasma. Longitudinal optical pumping using a 3.39-μ laser, as illustrated in Figure 4, was tried and produced a symmetrical error signal that is satisfactory for frequency stabilization. This method has been used in a breadboard arrangement to successfully stabilize the 6328-Å He-Ne laser. We are presently constructing two stable laser systems to monitor the stability that can be achieved by a direct comparison of the two output frequencies.

The present stabilization method provides superb control of the laser frequency with respect to line center. The system noise level corresponds to only a few hertz of error, and both long and short-term stability with respect

176

to line center of better than a part in 10^{11} has been demonstrated. However, it is recognized that the fluorescent line at 6328Å is 10^9 Hz broad. A specification of line center to a few hertz corresponds to a minute fraction of the total linewidth. Furthermore, the energy levels of neon atoms in a plasma are subjected to various perturbations that can easily shift the line center. As a result, the line center frequency can probably be shifted, for example, by varying the gas density or the plasma power level over a frequency range which is much larger than the implied residual error between the laser oscillation frequency and line center. An important next step is the investigation of these shifts, which incidentally would be common to any stabilization method.

$\frac{c}{2l} = Hz$
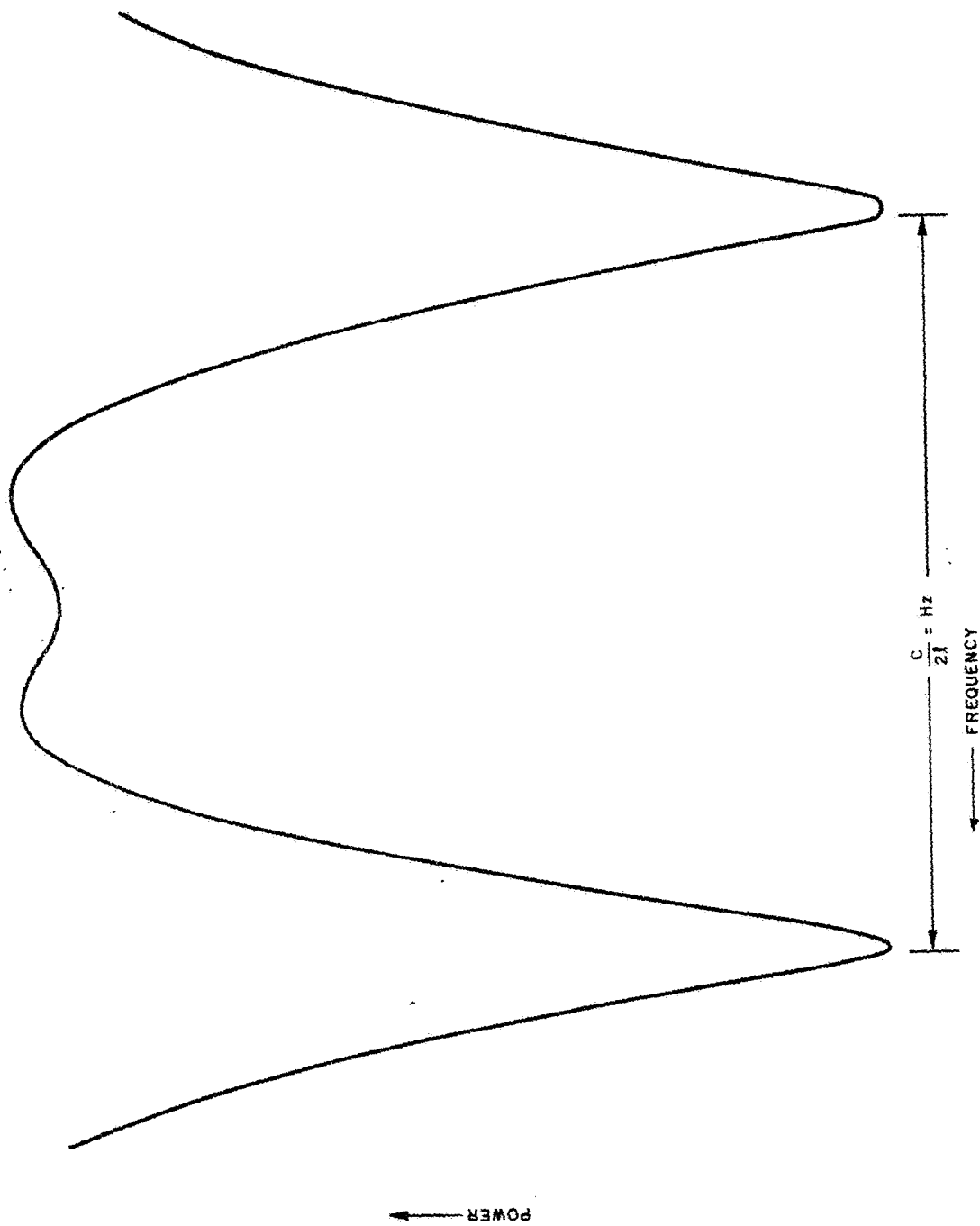
FREQUENCY

POWER

FIGURE 1. OUTPUT POWER OF SINGLE MODE 6328Å LASER VS OSCILLATION FREQUENCY
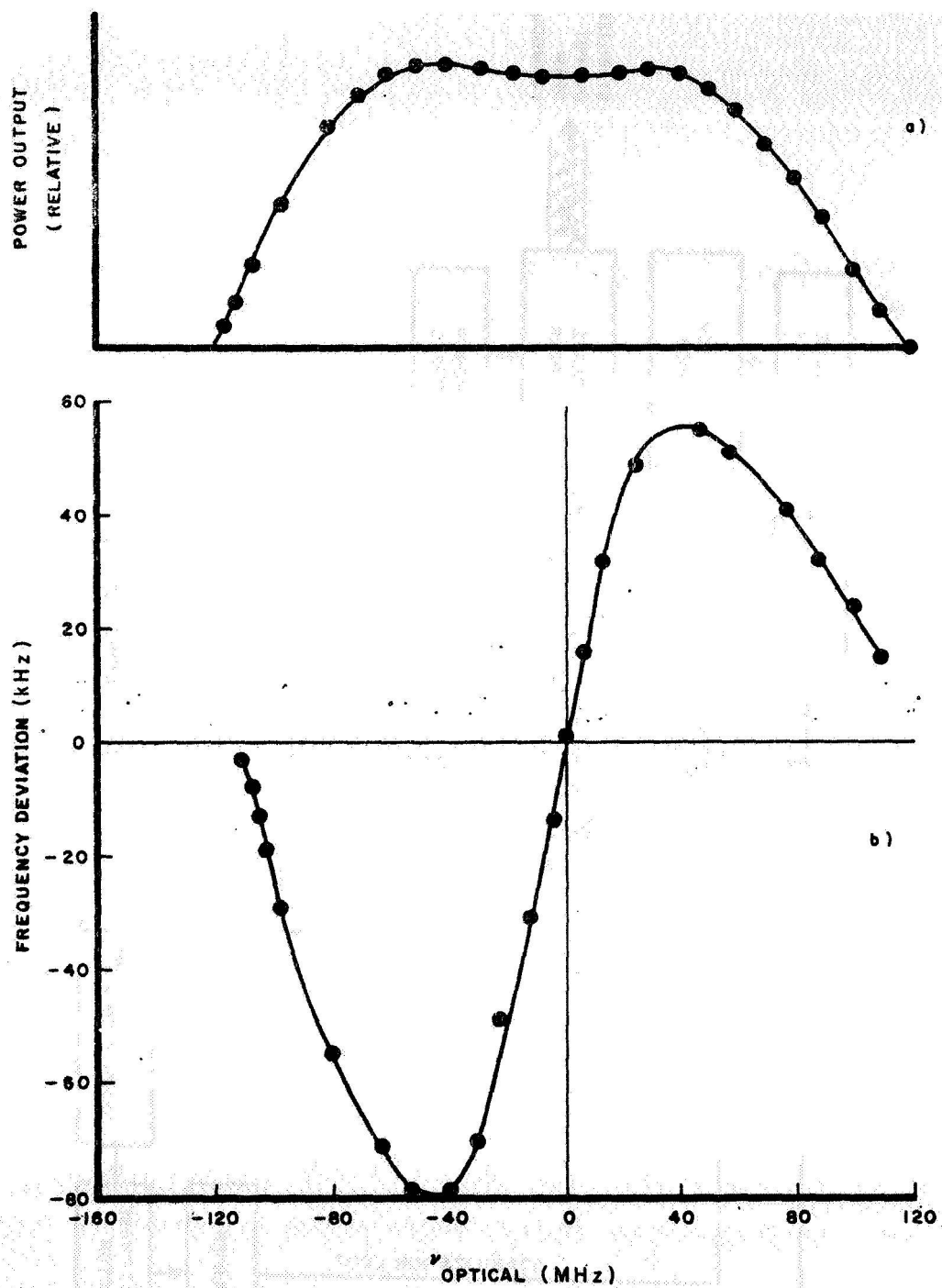
FIGURE 2. SINGLE MODE POWER OUTPUT AND FREQUENCY
MODULATION INDUCED BY GAIN MODULATION
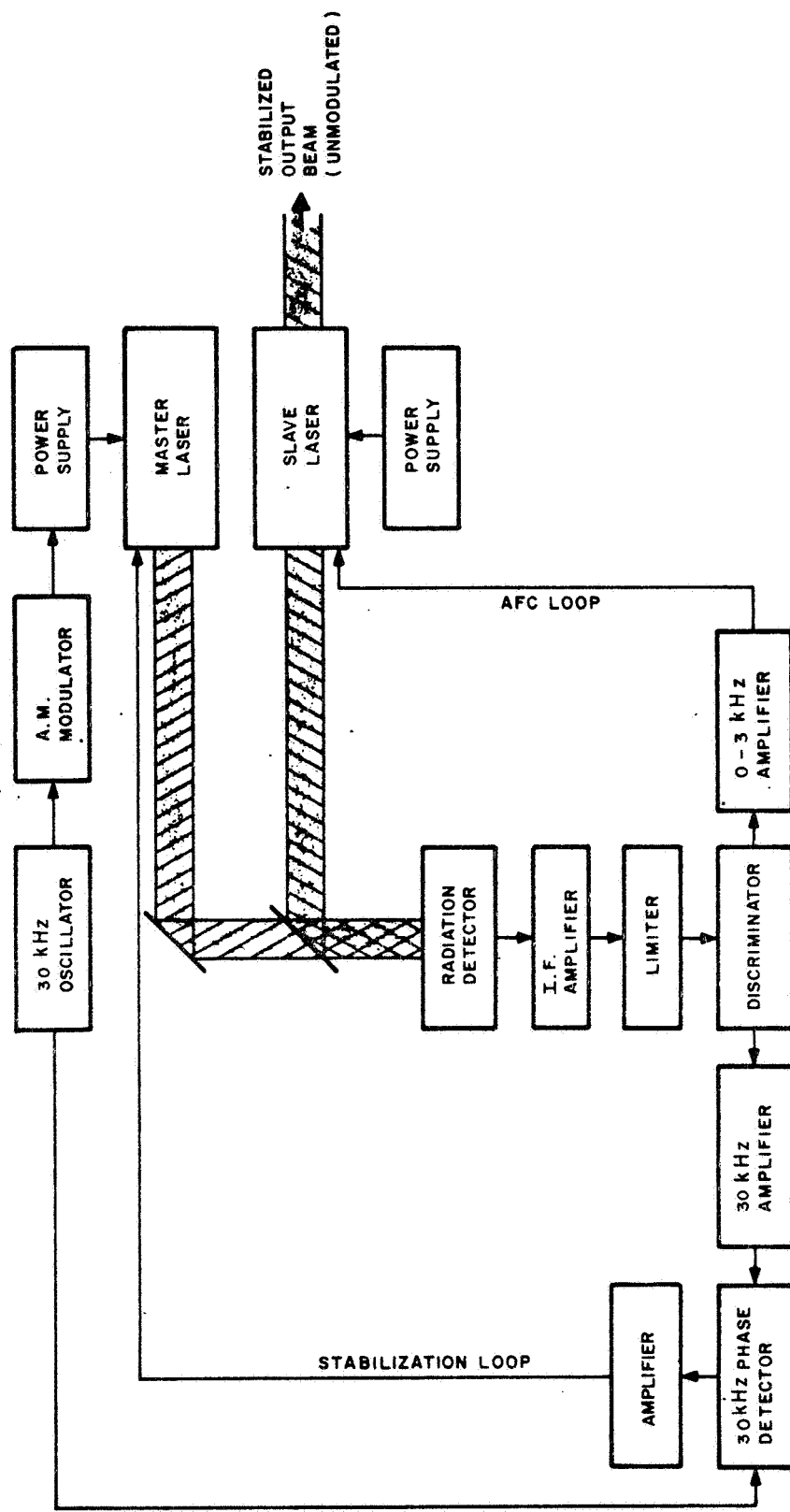
FIGURE 3. EXPERIMENTAL ARRANGEMENT USED TO STABILIZE 3.39μ LASER
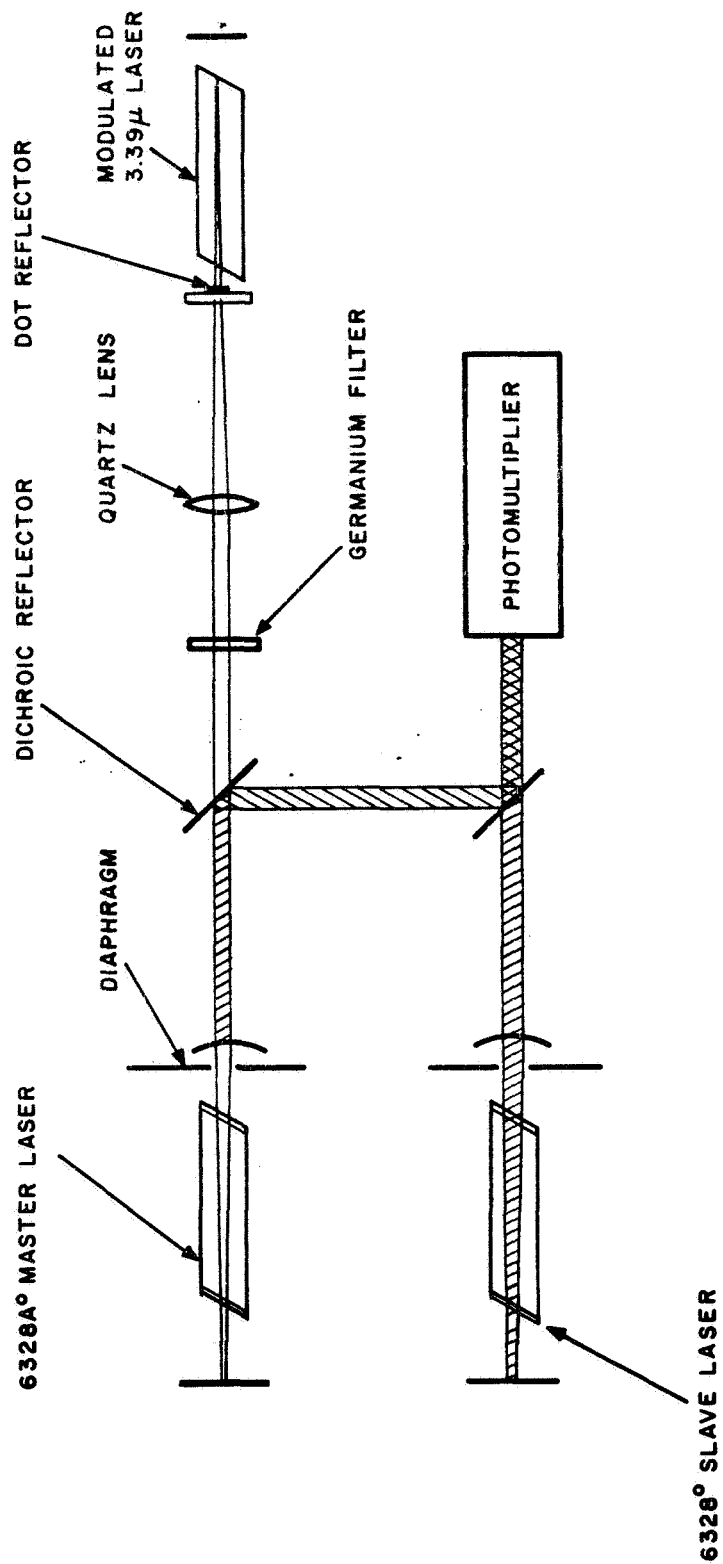
FIGURE 4. GAIN MODULATION OF 6328Å LASER BY LONGITUDINAL OPTICAL PUMPING WITH 3.39μ LASER

ADVANCED STUDY ON OPTICAL COMMUNICATIONS
FROM DEEP SPACE

C. W. Chapoton
J. W. White
Westinghouse Electric Corporation

Since September 30, 1964, the Surface Division of the Westinghouse
Defense and Space Center in Baltimore, Md., has been performing a study on
optical communications from deep space. This work has been sponsored by
the NASA Manned Spacecraft Center in Houston, Tex., under contract NAS
9-3650. The purpose of this paper is to highlight the significant study results.

The communications requirements for manned deep-space missions were
derived with the objective of evaluating modulation techniques for deep-space
communications. Three modulation techniques shown to be promising in a
previous NASA contract were considered. Communications systems concepts
were synthesized using these modulation techniques, and their parameters were
derived. Finally, a comparative evaluation between systems using each modu-
lation technique was made.

The constraints under which the study was performed are shown in
Figure 1. Three links were considered:

1. a direct optical link from the earth's surface to a manned deep-space
vehicle (MDSV) at a range of 80 450 000 km (5×10^7 mi.);

2. a relay link using microwaves from the earth's surface to a syn-
chronous satellite and an optical link from the satellite to the MDSV;

3. a direct optical link from the earth's surface to a low-altitude
manned space station of the Apollo Extended Mission type.

Both up and down links were considered. Three modulations were considered
for each link, as shown in Figure 1:

1. pulse position modulation,

2. pulse code modulation using polarized light,

3. coherent reception with frequency shift keying.

Data transmission requirements were analyzed for these links and are summarized in Figure 2. Command and voice data will be sent over the up links. A low data rate, high quality command channel is required to deliver 1000 bits per second with less than one error per million bits. Digital voice transmissions at a rate of about 30 000 bits per second with less than one error per thousand bits are required. The down links are dominated by the requirement for transmission of real-time, commercial quality television. This video will require a rate of about 50 megabits per second with an error rate of less than one error per thousand bits. Telemetry and voice channels are provided in the down link with the same requirements as on the command and voice channels for the up link.

Concepts were synthesized for the various elements of optical system for each link and each modulation technique. Consider first the PPM transmitter shown in Figure 3 for use on an Apollo Extended Mission vehicle. Video is not considered here because hardware considerations indicate that the high switching rates and extreme synchronization requirements cannot be maintained for high data rate PPM systems.

Command data, after coding to decrease the error rate, is time multiplexed with telemetry data and the synchronization word. Data interlacing is used so that one bit is taken from each data source for every two frames in the output message. Studies have shown that one synchronization frame for every 39 data frames is adequate to maintain system operation. These multiplexed data are grouped into words that time the generation of the output pulse train according to the information content. The resulting pulse train modulates a GaAs diode laser for transmission. The diode laser is chosen for this near-earth satellite application because the beamwidth requirements are not stringent, power requirements are low, and efficiencies are high. The beam is shaped, and output lenses control the pointing of the beam.

Formation of the pulse train is as before, when the PPM transmitter for communication to the MDSV is located in a synchronous relay satellite as shown in Figure 4. However, the diode laser is not used because of the beamwidth and power requirements. In this case, a Q-switched, sun-pumped laser

184

is postulated. Solar energy is collected and optically coupled into the laser. Cooling must be provided for the collector, optics, and laser. Output lenses form an optical system for beam shaping and steering.

A PPM receiver for use on the MDSV is shown in Figure 5. Cassegrainian optics are used because of the size and weight advantage. The signal from the optical telescope is filtered to reduce the background noise and is detected in a photomultiplier tube. The resulting electrical signals are integrated to form pulses from the individually detected quantum of energy. This integrator is dumped at a rate corresponding to the PPM slot rate. Sequential comparison is used to determine the location of the signal pulse in the word group time frame. A parallel circuit detects the synchronization signal and updates the receiver clock. At the end of a frame, the 8-bit word is transferred into a 320-bit storage register during the dead time. The first 8 bits transferred are always related to the synchronization word, and the last 312 bits are information. After 320 bits have been transferred, the bits associated with the synchronization word are ignored, and the 312 information bits are transferred in parallel into a word store. They are read out in a continuous manner until the 320-bit register is full, at which time the cycle is repeated. Format conversion from 8-bit characters transmitted 39/40 of the time to a continuous bit stream is accomplished by reading the 8 bits corresponding to the synchronization frame into a 320-bit register, and then following this with 312 information bits. At that time, the last 312 bits are gated in parallel into a read register, and then read out of this register at 1/2 (312/320) the received bit rate.

The PCM/PL transmitter on the MDSV is shown in Figure 6. The video data are quantized and coded into a PCM signal. This signal is time multiplexed with the command and telemetry data and the synchronization signal. The resultant pulse train is applied to an electro-optical modulator that performs binary switching of the polarization of the sun-pumped laser. The output optics then form and steer the beam.

The earth-based receiver for this link is shown in Figure 7. Cassegrainian optics are used again because of their size and weight advantages. The light from the optical system is filtered to reduce the background noise and passed through a quarter wave plate. This plate converts the circularly polarized input light (with direction of rotation depending upon the character being sent) to orthogonal linearly polarized light. Orthogonal polarizations are separated in a Wollaston prism, individually detected, and converted to an active binary signal. Quantum counting is then performed and the resultant pulses shaped. The output pulse train is demultiplexed and distributed to the appropriate data user.

The coherent transmitter for the FSK system is shown in Figure 8. Input data are again time multiplexed. In this case, they are used to modulate a unimodal gas laser. Only the gas laser has sufficient spectra purity to permit coherent detection. The output beam is then shaped and steered by the output optics.

The coherent receiver, shown in Figure 9, also uses Cassegrainian optics to collect the transmitted beam. The received energy is heterodyned with the local oscillator on the semisilvered mirror and detected by a photo-detector. The photodetector output is processed by a conventional rf receiver and demultiplexed. Decoding and D/A conversion is identical to the other receivers.

In this study, comparison between the above systems and, hence, between modulation techniques has been made on the basis of transmitter power requirements. This measure is particularly significant because it is proportional to spacecraft system weight, and it also provides an indication of the feasibility of obtaining a laser source. Actual weight comparisons, which form the final selection criterion, cannot be made until preliminary system designs have been generated. These designs are beyond the scope of the present study.

To determine transmitter power requirements the power model shown in Figure 10 was used. Choice of a receiver location, an operating wavelength, receiver aperture area, and beamwidth determines the input background noise on the receiver optics. Choosing the optical filter bandwidth determines the noise power into the receiver, which can be expressed as a noise photon rate. In PCM/PL we are interested in knowing the number of noise photons that must be overcome at each decision that is obtained by knowing the data rate. For coherent systems, the noise photons per unit bandwidth, which are obtained from the signal bandwidth since coherent reception rejects noise outside the signal band, are of interest. In PPM systems, the number of noise photons per time slot in which the signal may be is of interest.

The appropriate input noise figure is used in conjunction with statistical detection requirements curves. These curves relate the required signal photons for a given error rate to the input noise photons. The input signal requirements are then used to solve the above process in reverse to find the signal photons onto the receiver optics. The optical communications range equation then defines the required transmitter power.

The heart of this power model is the relationship of the signal photon requirements, noise photons, and error rate. Statistical analyses have been

186

performed to relate signal, noise, and error rate for quantum counting detection. A typical result is shown in Figure 11 for PCM/PL and an error rate of one per thousand bits. Figures 12 and 13 show the similar relations for coherent FSK and PPM. These curves plot the average number of photoelectrons (related to the signal photons by the photosurface emissivity) per decision as a function of the average number of noise photoelectrons that are present for that decision to insure a specified error rate. The abscissa shows only the value of background noise. As this noise becomes smaller, the required signal photoelectrons approach a constant value. This number of photoelectrons represents the quantum limit of the receiver. It is the number of photoelectrons that must be received to have a recognizable signal. For the example in Figure 11, the quantum limit is about seven photoelectrons per decision.

As the background noise increases, the effect of quantum noise decreases and finally becomes negligible. For high background situations the required signal photoelectrons becomes proportional to the background noise photoelectrons per decision.

The following figures* show how the minimal required power varies as a function of data rate for the MDSV to earth link and the three modulation techniques. Figure 14 shows the requirements using pulse code modulation with polarized light (PCM/PL). It can be seen from these curves that increasing the operating wavelength significantly decreases the power requirements. Powers are on the order of two orders of magnitude less for 4μ than $0.6\ \mu$. This shows the effect of the lower noise backgrounds at the longer wavelengths. At high data rates the curves become quantum limited. The number of noise photons per second is so low that system operation is limited by the uncertainties in the signal photons themselves. At lower data rates the noise background determines the required number of photons. This is somewhat similar to the case in microwave communications of increasing the signal bandwidth until it matches the noise bandwidth. Recall that the noise bandwidth is set by the optical filter bandwidth. This is a constant for the data rates considered. For a particular wavelength, when the system operation reaches the quantum limit,

---

* Transmit and receive beamwidths = 10 μ rad; quantum efficiency = 50 percent; optics efficiency = 70 percent; optical filter bandwidth = 0.1 percent λ; aperture area = 10^4 cm in space, 10^5 cm on earth; range = 1.5 x 10^8 km in all curves.

the required signal power should be independent of receiver beamwidth (although reaching this limit is a function of receiver beamwidth).

Because the coherent system limits the noise background much more efficiently than the optical filters (the noise bandwidth is effectively the signal bandwidth), the coherent systems were found to be quantum limited in all cases. This is illuminated in Figure 15. The quantum limit of 10 photons per cycle implies that the required received signal, and hence transmitter power, will vary linearly with data rate. The curves are dependent upon wavelength since the energy per photon is different for different wavelengths. This is an inverse relation between power and wavelength for the lower power requirements at the lower wavelengths. Again, as with PCM operation, power requirements for the MORL link are negligibly small.

The power requirements for pulse position modulation are shown in Figure 16. Although PPM is not considered for video transmission, the down link powers were calculated for the lower data rates to illustrate the performance of a PPM system with limited data handling capability. Since the same alphabet level ($\alpha = 8$) and pulse width (50 nsec) were used for all data rates, the power required curves vary linearly with data rate. These curves again show the advantages of going to longer wavelengths for system operation. Power requirements are significantly different as the wavelength increases. The power requirements for the data rates where PPM is applicable are not significantly different from those systems using PCM or coherent modulation.

Figure 17 summarizes the transmitted power requirements for the various deep space links and data rates of interest. In the 50-megabit per second data rate, corresponding to the transmission of real-time television from the MDSV, PCM/PL offers a small power advantage over coherent FSK modulation. Although not a system requirement, the same advantages are noted if the high data rate is to be sent over the up link to the MDSV.

In the up links, where a data rate of 30 kilobits per second is required, the power requirements are about two orders of magnitude less than for the high data rate down links. No difference is noted for the earth-based and synchronous satellite transmitter since the MDSV receiver is the same in either case and sees the same background noise power.

Comparison between modulations is somewhat more clear cut for the up links. Both PCM/PL and coherent FSK require powers in the order of 0.25 W. However, PPM for this low data rate requires a power in the order of 5 mW.

If the requirement for real-time television on the down links is removed, the data rate will be 30 kilobits per second, and the power requirements are summarized in the figure. Again, PPM offers an advantage of from one to two orders of magnitude in transmitted power over the other two modulation types.

An initial comparison between links can also be made using the figure. In the high data rate down link, the direct optical link to the earth's surface requires the lowest power. This result is seemingly contradictory since the daylight sky background that the earth receiver must see is much more intense than the planetary background seen by the synchronous satellite. However, much larger optical apertures are possible on the earth. Operating within the projected bounds of feasibility, the increased aperture size more than offsets the increased background noise power. Although power and weight on the MDSV required by the communications package is extremely critical, some consideration must be given to the other terminal of the system. If earth-based receivers are used, the problems of occultation and cloud cover must be overcome by using a number of receiving stations distributed over the globe. These additional stations require a broad-band ground-based data network as well as a central command and control facility to choose the proper receiving station and channel the data appropriately. An alternative is to use a communications satellite network. If this network exists and can be used, it is attractive; if it is not, satellite relays are equivalent.

Thus, the choice between earth or satellite terminals depends on a tradeoff between the larger number of stations on the earth and the difficulties of achieving long-term reliable satellite relays. The earth-based stations also imply a larger number of switchovers and, hence, possible loss of data. The increased complexity of the handover and tracking problems for earth stations may be offset by the capability of having more complex systems on the ground than in space.

Communications with the MORL appear to be no particular problem, from a power viewpoint, using any of the three modulation techniques. For beamwidths below 100 microradians, the power requirements are on the order of microwatts for the high data rates. Broadening the beam by orders of magnitude would put the powers into the watt range. PPM again has an advantage at the lower data rates.

A word of caution should be injected into the interpretation of these results. The heart of the power model used to generate these results is in the quantum counting detection requirements curves. These curves are highly

nonlinear. Thus, the power results are very sensitive to assumptions of system parameters and system requirements. An exhaustive search for the "optimum" set of system parameters is beyond the scope of this contract.

Background noise is a critical system parameter. The above evaluation indicates that the region around a wavelength of four microns is optimum. However, the very narrow low noise lines in the sun's spectrum offer possible noise improvements. Because of the nonlinearity of the power model, it is impossible to tell from examination of the Fraunhofer lines which would yield minimum transmitted power requirements. The optimum wavelength may well be different for different modulation techniques.

Finally, the true measure of cost or penalty function for a given modulation technique is spacecraft weight. Because of the variability of laser materials, pumping requirements, efficiencies, and power supplies, weight is not linearly related to output power for all modulation techniques. System designs must be generated and optimized with respect to spacecraft weight for a spectrum of system requirements. In this way, the optimum choices of modulation technique and system design can be developed as a function of system requirement. Furthermore, the up and down links should utilize the same modulation technique to minimize spacecraft complexity. Thus the power advantage gained by PPM at low data rates may be negated if two different techniques are required for transmit and receive in the MDSV.

3 LINKS

MDSV

SATELLITE

3 MODULATIONS

- PPM
- PCM / PL
- COHERENT FSK
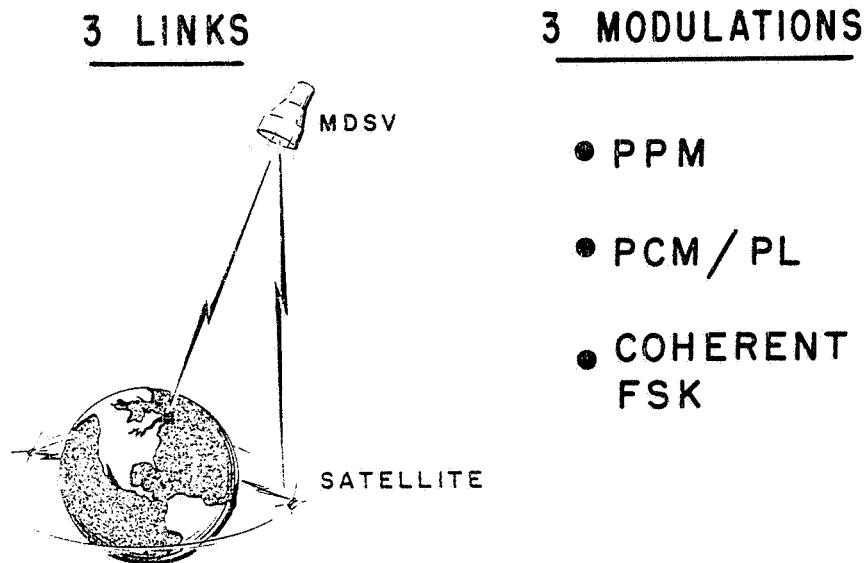
FIGURE 1. CONSTRAINTS

	DATA RATE BITS/SEC	ERROR RATE ERRORS/BIT

UP LINKS

COMMAND _____ 1,000 _____ 10^{-6}

VOICE _____ 30,000 _____ 10^{-3}

DOWN LINKS

VIDEO _____ 5×10^{7} _____ 10^{-3}

TELEMETRY _____ 1,000 _____ 10^{-6}

VOICE _____ 30,000 _____ 10^{-3}

FIGURE 2. DATA REQUIREMENTS
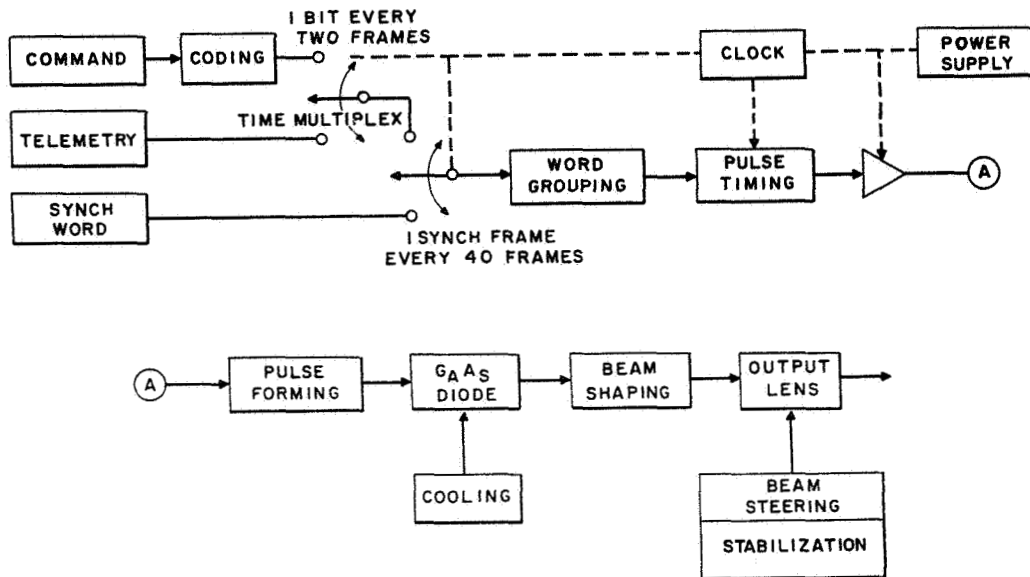
FIGURE 3. MORL PPM TRANSMITTER
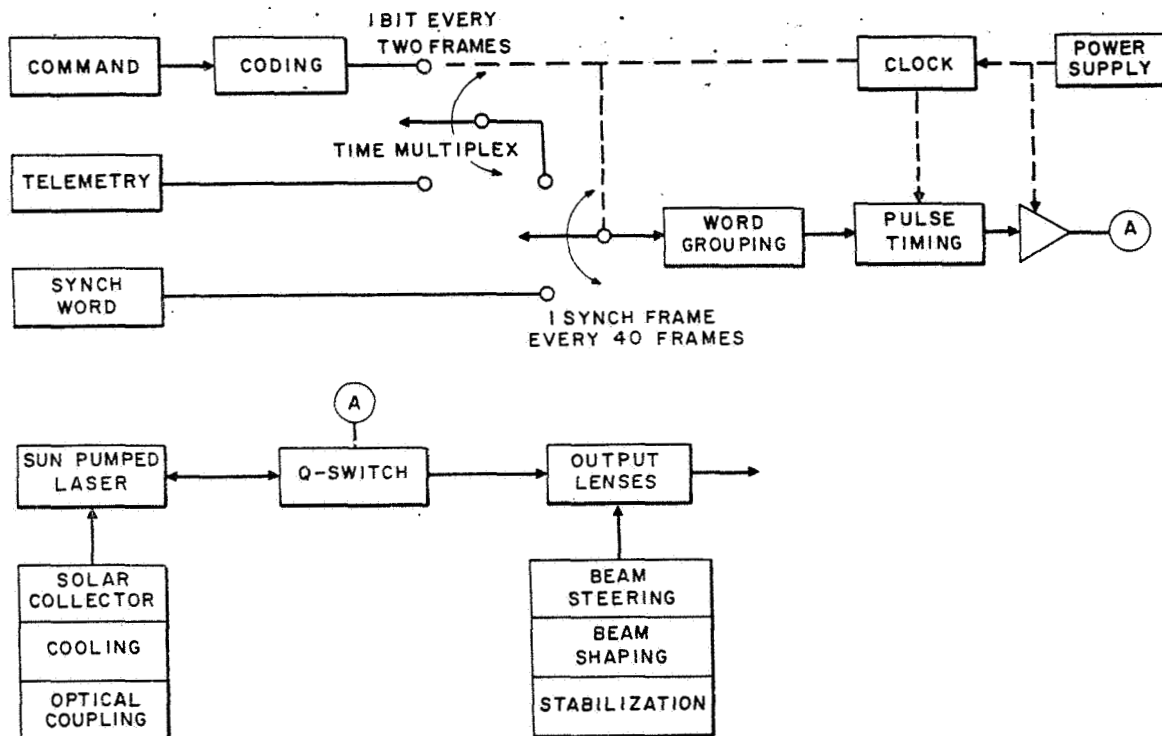
FIGURE 4. SYNCH SATT TO MDSV PPM

192
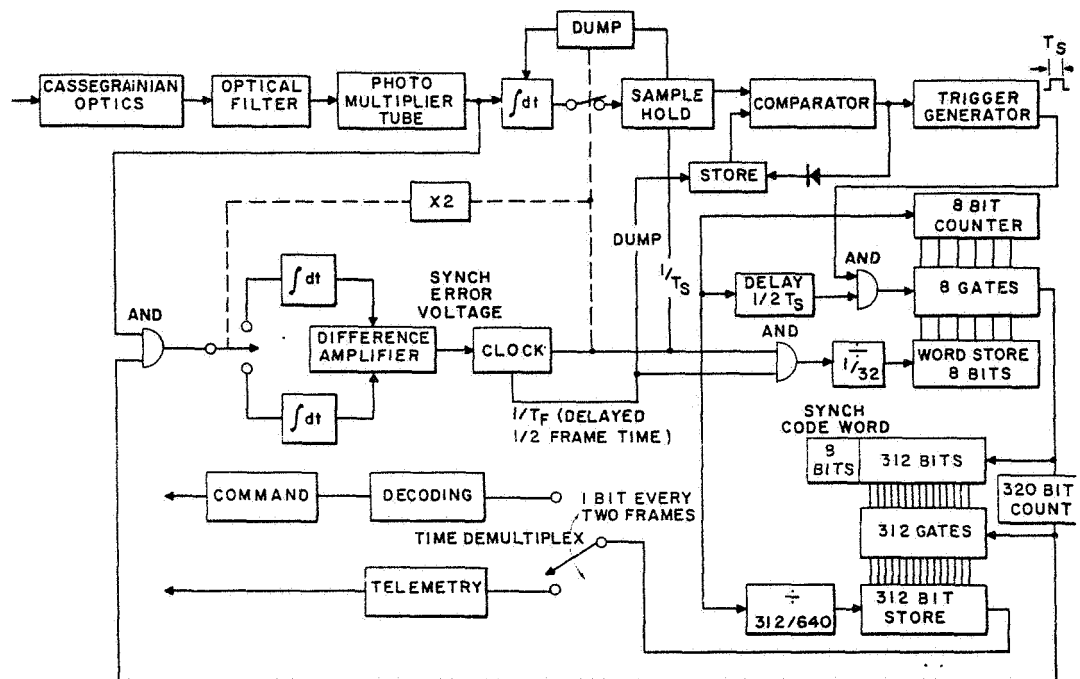
FIGURE 5. MDSV PPM RECEIVER
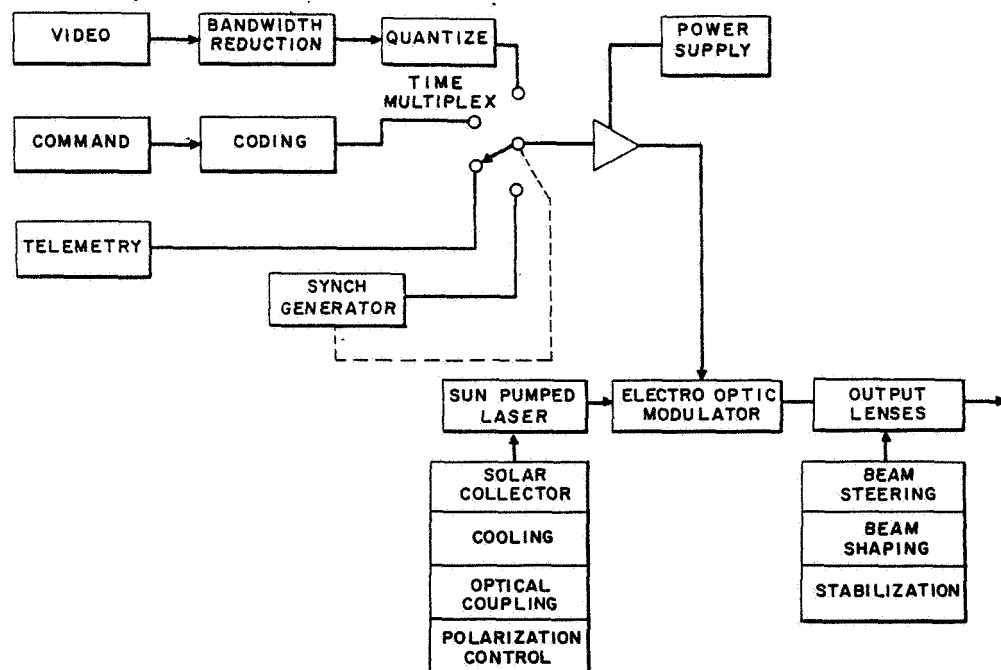
FIGURE 6. MDSV TRANSMITTER PCM/PL

. 193
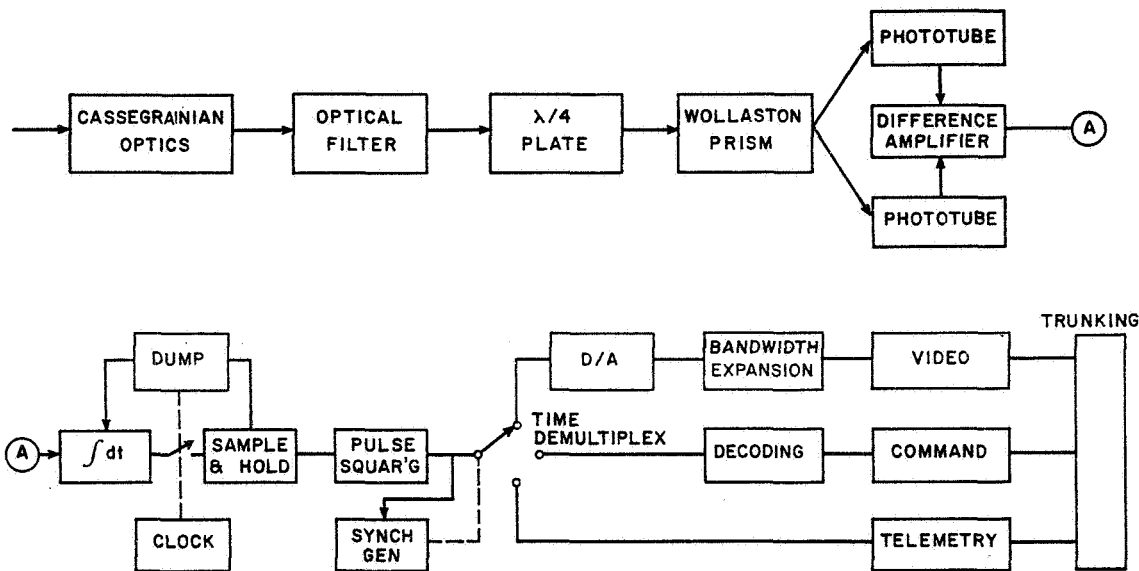
FIGURE 7. EARTH RECEIVER PCM/PL
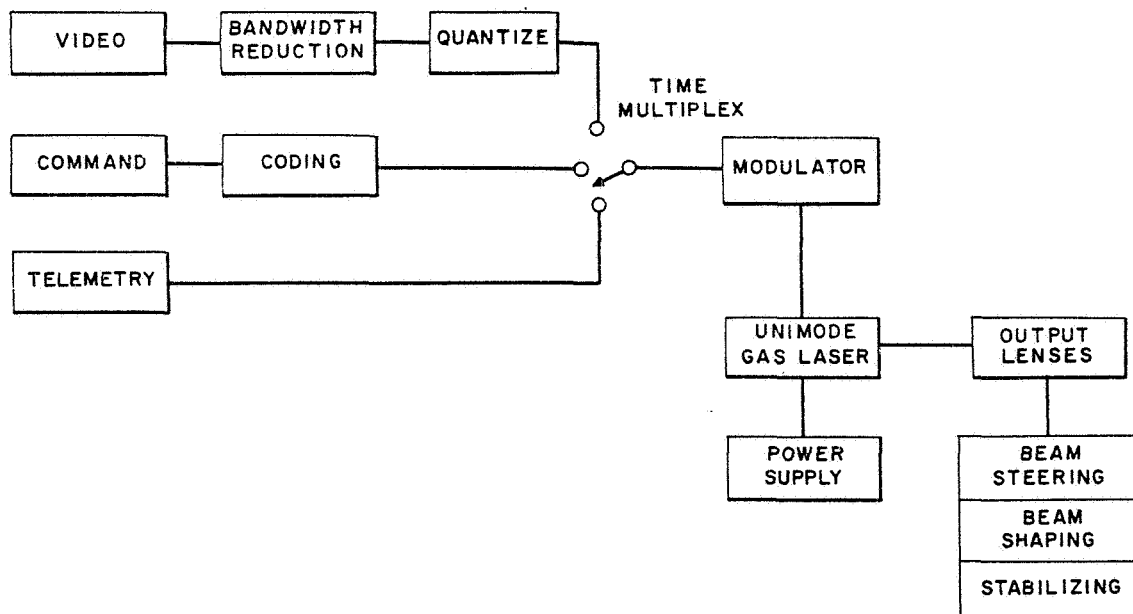
FIGURE 8. COHERENT TRANSMITTER

194
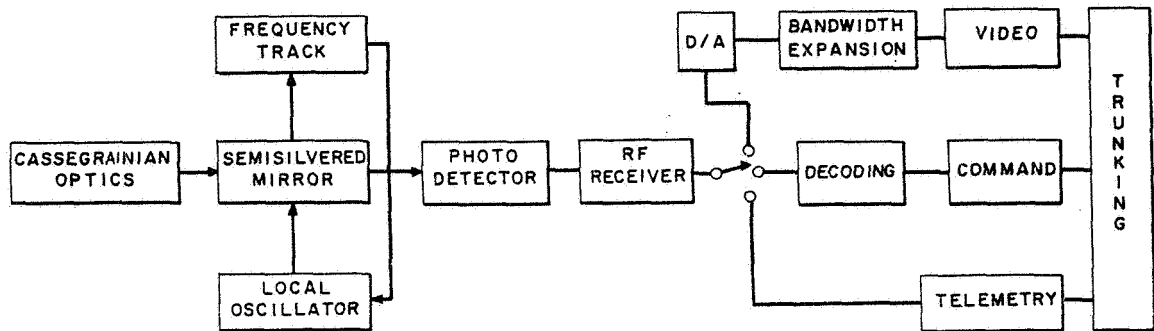
FIGURE 9. COHERENT RECEIVER
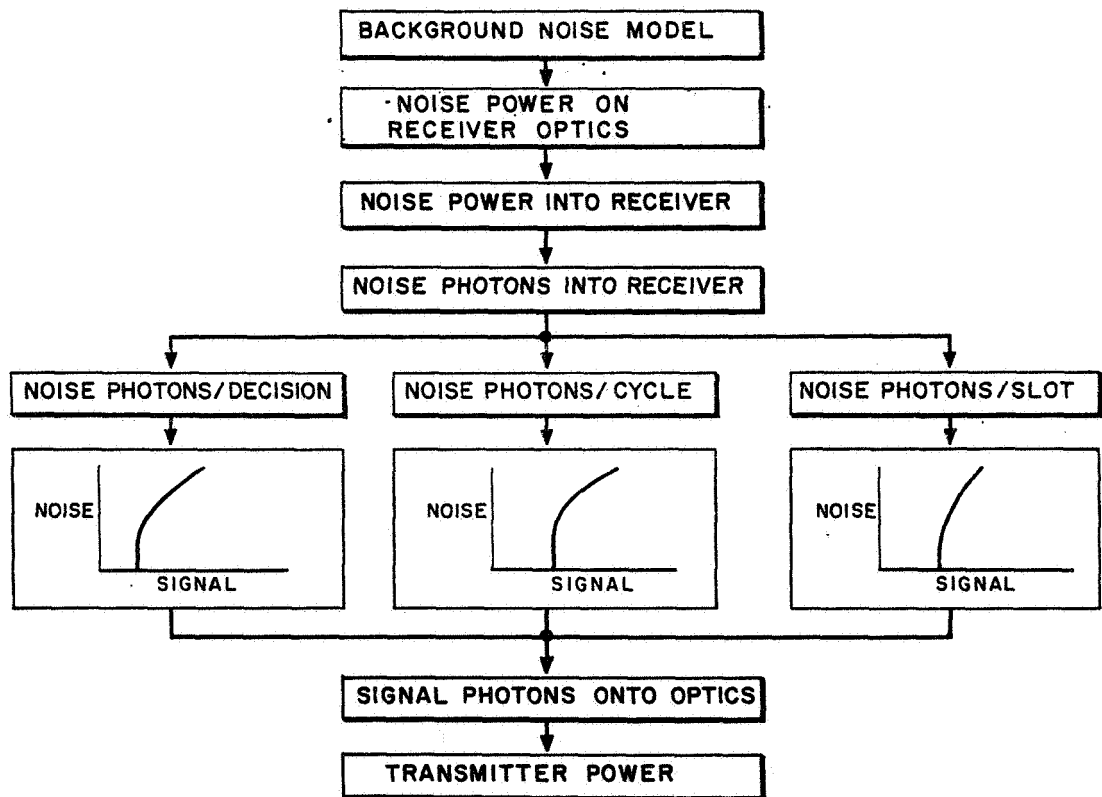
FIGURE 10. POWER MODEL
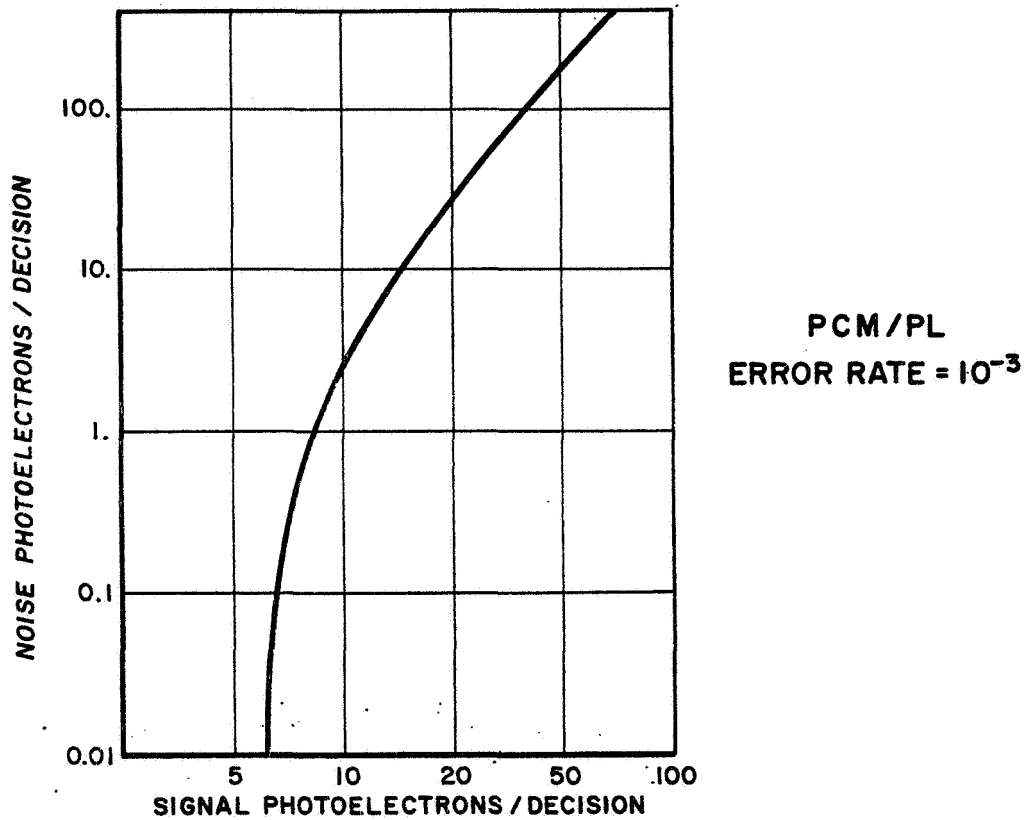
FIGURE 11. DETECTION REQUIREMENTS
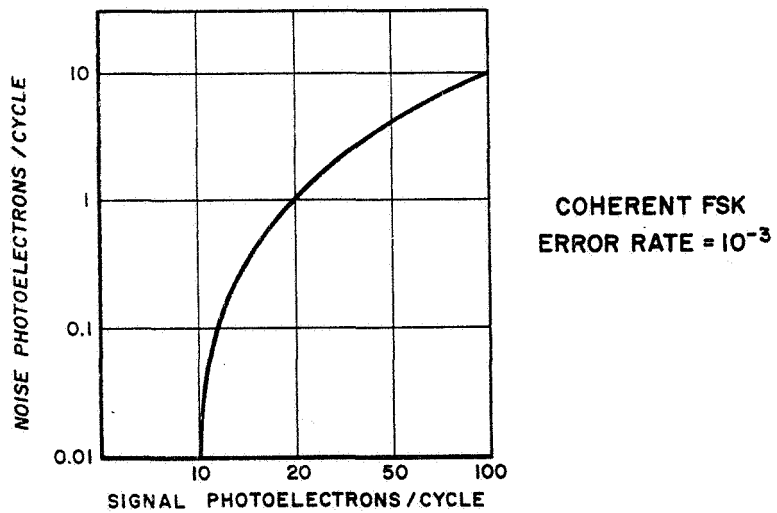
FIGURE 12. DETECTION REQUIREMENTS

196

PPM
ERROR RATE = 10^{-3}
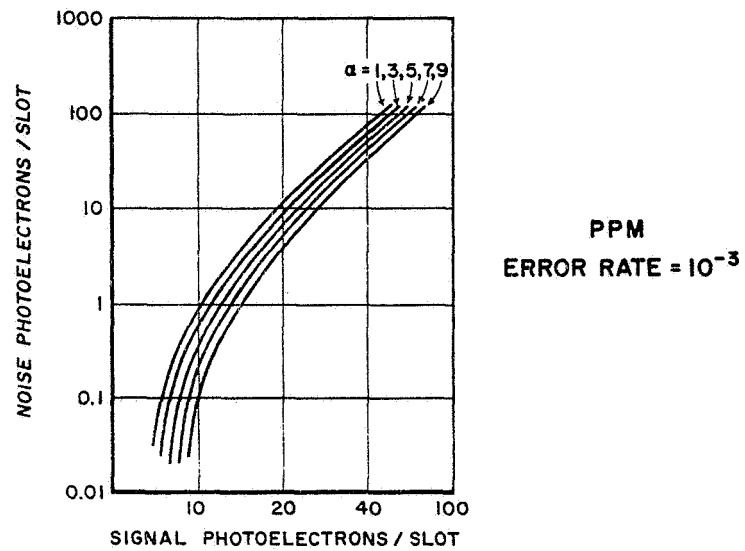
FIGURE 13. DETECTION REQUIREMENTS

PCM/PL
EARTH RECEIVER
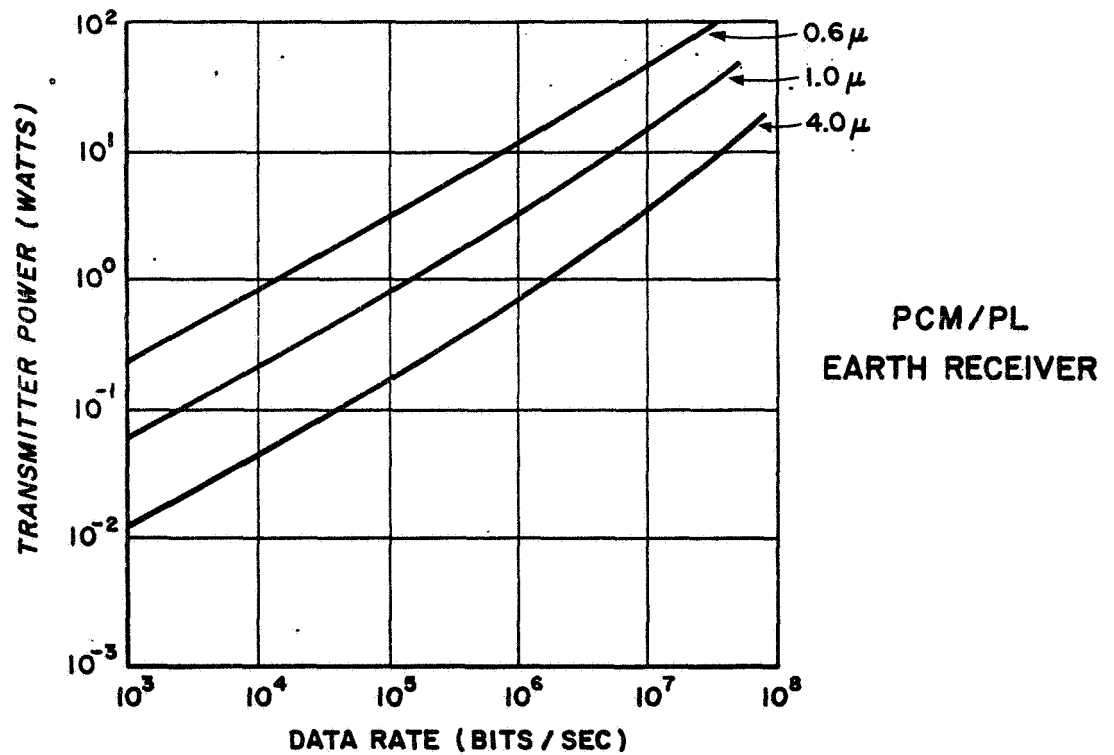
FIGURE 14. MDSV TX POWER
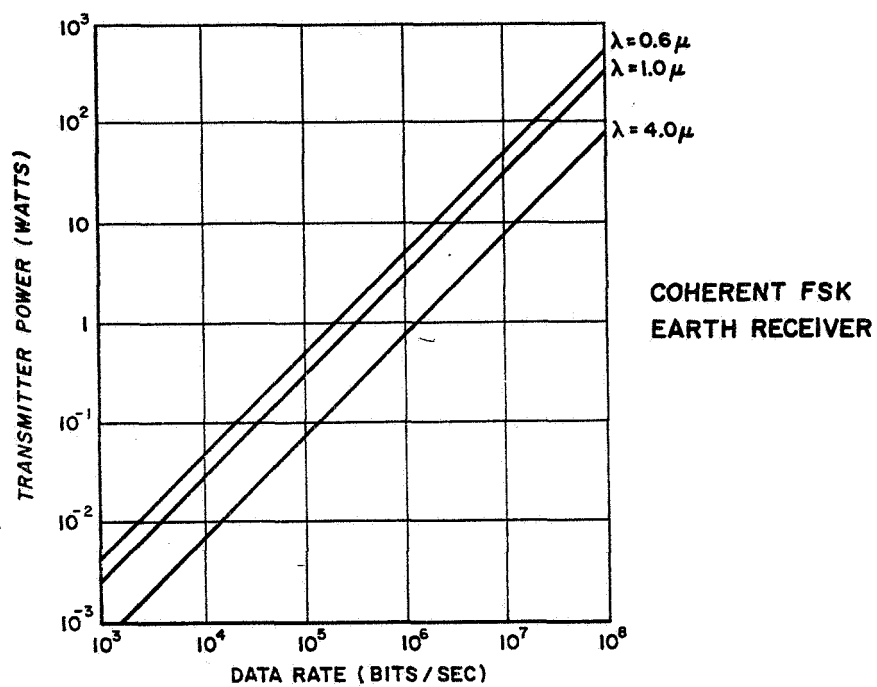
FIGURE 15. MDSV TX POWER
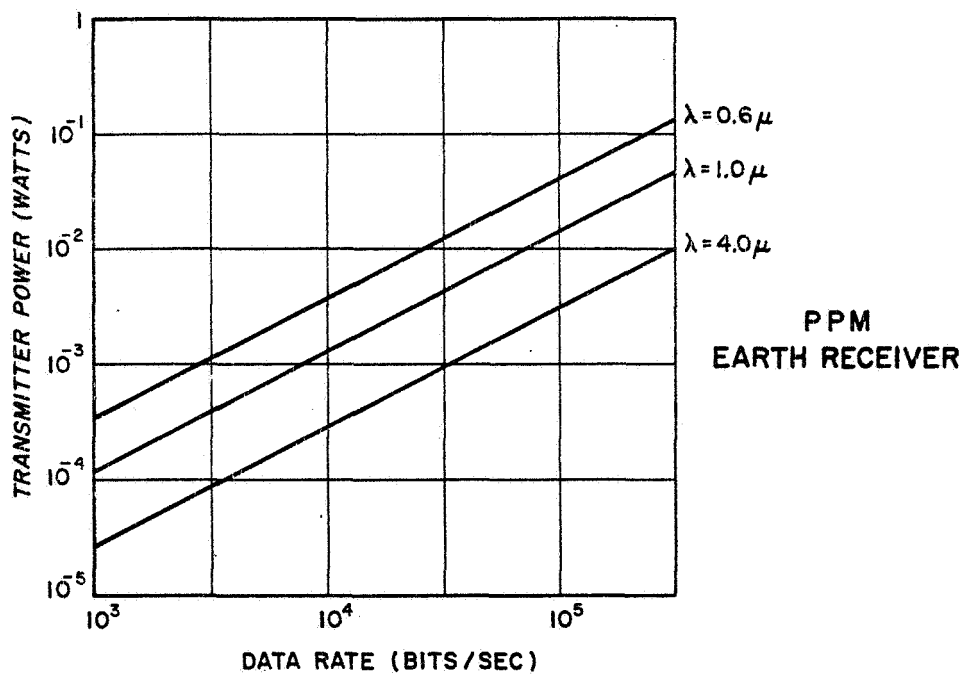
FIGURE 16. MDSV TX POWER

198

DATA RATE	MODULATION	EARTH TRANSMITTER / MDSV RECEIVER	MDSV TRANSMITTER / EARTH RECEIVER	SATELLITE TRANSMITTER / MDSV RECEIVER	MDSV TRANSMITTER / SATELLITE RECEIVER
30 KILO BITS/SEC	PPM	5.4×10^{-3}	1×10^{-3}	5.4×10^{-3}	4.0×10^{-2}
	PCM / PL	2.5×10^{-1}	7.1×10^{-2}	2.5×10^{-1}	3.2×10^{-1}
	COHERENT FSK	2.3×10^{-1}	2.3×10^{-2}	2.3×10^{-1}	2.3×10^{-1}
50 MEGA BITS/SEC	PCM / PL	80	11	80	65
	COHERENT FSK	340	34	340	340

FIGURE 17. TRANSMIT POWERS

199

OPTICAL WAVEGUIDE DESIGN

Donald W. Wilmot
E. Ronald Schineller
Wheeler Laboratories, Inc.

The subject of waveguides and waveguide modes is traditionally a microwave topic. However, there is currently some activity in this area within the optical field. This activity may be partly caused by the fact that these modes are very interesting from a theoretical point of view. A practical motivation for work in this area is the possibility of developing high-performance, waveguide-type, optical components, analogous to those used at microwave frequencies [1,2]. These components require waveguides that operate in a single-mode, or at least in a controlled mode condition. Such components are intended for application in future laser communication and tracking systems.

Waveguide components have several advantages over conventional optical components, particularly for use in high-performance laser systems. One of the most significant advantages is that the component performance characteristics, such as frequency response in the case of a filter or power split in a directional coupler, are independent of the angle of the incident light. The reception pattern at the input determines the amount of power received by the system for a particular angle of incidence; the rest of the system, if it is operating in a single mode, receives this light with a constant, predetermined field configuration regardless of the angle of incidence. Another potential advantage is the future possibility of very compact, rigid, optical structures similar to the printed circuits currently used in electronics.

There are a number of possible waveguide configurations, including metallic and dielectric structures of various geometries. At Wheeler Laboratories, work has been directed toward the development of large-sized, dielectric waveguide of the form shown in Figure 1. It is possible to restrict propagation to a single mode in such large, multi-wavelength structures by establishing a very weak interface between the core and cladding materials, i.e., the core dielectric has only a slightly higher index of refraction than the cladding [3]. The large size is desired to facilitate fabrication of components and increase the power handling capability of the guide. The term "large" is relative because a 100 wavelength guide is only about 60 μ or 0.0024 in. wide.

The analysis of a typical waveguide structure will now be outlined to illustrate the analytical and experimental approach used in the development of optical waveguides and components. The specific structure chosen for this illustration is the bisected dielectric-slab waveguide. The analysis is interesting for its own sake because it demonstrates that, although such a waveguide at optical frequencies may exhibit many of the characteristics of similar structures operated at microwave frequencies, it may also exhibit remarkably different characteristics under particular operating conditions.

For this analysis the technique of transverse resonance is employed. Basically, this involves setting up a transverse equivalent circuit for the structure and solving for the resonance of this circuit. The resonance equation obtained in this manner is the eigenvalue equation for the propagation constants of the modes on the structure. The eigenvalue equation contains the complete solution for the modes of the structure since the propagation constants are related to the guide wavelength, cut-off conditions, field configurations, etc. A cross section of the bisected-slab configuration is shown in Figure 2(a). In this figure, propagation is in the Z-direction, into the page. In the transverse equivalent circuit of Figure 2(b), the core and cladding dielectrics are represented by transmission lines of impedance Z_1 and Z_2, respectively, where the impedances are defined as the conventional wave impedances and are related to the transverse propagation constants of the waveguide. The impedance of the bisecting plane is, in general, complex. The transverse resonance procedure involves selecting a reference plane within the circuit and then solving for the impedance seen looking to the left of this plane, Z_a, and the impedance looking to the right, Z_b. The resonance equation is then obtained by setting the sum, $Z_a + Z_b$, equal to zero. The resulting equation is usually transcendental and often complex. This equation is the same as the characteristic equation that would be obtained by a boundary value solution of the problem.

For the transmission line formulation, it is convenient to define the reflection coefficient as it is seen by an observer looking toward the wall. In this notation the reflection coefficient of a perfect conductor is -1 at all angles of incidence for both polarizations. For real metals at optical frequencies the situation is more complicated and, therefore, the analysis will be restricted to high reflectivity metals. In this case the reflection coefficient is nominally equal to -1 at all angles for perpendicular polarization (this corresponds to TE modes). However, for parallel polarization (corresponding to TM modes) the reflection coefficient varies from about -1 at normal incidence to about +1 at grazing incidence, going through a pseudo-Brewster angle at around 70° to 80°.

202

The above discussion indicates that the reflection coefficient of a real metal for TE modes is nominally the same as for a perfect conductor. Therefore, the metal impedance to be used in the transverse equivalent circuit is nominally that of a perfect conductor and the modes are only slightly perturbed by the finite metal conductivity. For TM modes, however, we have three situations. For modes with a propagation angle near normal incidence the perfect conductor approximation is again valid. For arbitrary propagation angles the situation is complicated and the problem must be solved with grazing propagation angles, and this is the situation for large-sized, weak-interface guides, the reflection coefficient is nominally +1. It is well known that the reflection coefficient of +1 corresponds to a magnetic wall or open circuit. Therefore, by substituting the impedance of an open circuit for the metal impedance, Z_m, the TM propagation constants of the large-sized bisected waveguide may be obtained. The resultant fields are shown in Figure 5. Note that for this case only odd-numbered modes occur for both polarizations and, more important, the TM-0 mode (the dominant one with the perfect conductor bisection) does not exist on such a waveguide at optical frequencies.

The conclusion of this brief analysis is that the TE modes on a metal-bisected waveguide at optical frequencies are similar to those observed on microwave structures, while the TM modes for certain operating conditions may differ considerably from their microwave counterparts. In fact, in the limit of large-sized, weak-interface guides, the odd-numbered TM modes, expected on the basis of perfect conductor assumptions, are nonexistent. Instead even-numbered TM modes, normally associated with a perfect magnetic wall, are found.

The theoretical results have been confirmed using an experimental waveguide that has previously been discussed in the literature [3]. Figure 6 shows a photograph of the developmental model. The waveguide consists of two glass plates suspended in a container of chlorobenzene. The liquid between the plates acts as the waveguide core. During a previous study of unbisected waveguides, both glass plates served as cladding [3]. In the present experiments one of the plates serves as the cladding, while the other plate is a front surface aluminum mirror that is the bisecting wall. The waveguide was illuminated at one end with a He-Ne gas laser as shown in Figure 7. A magnified image of the other end was projected by a microscope and then probed by a small aperture mounted on a photo-multiplier tube.

Several measurements were performed with this arrangement. The most conclusive agreement with theory is shown by the aperture distributions of Figures 8 and 9. The difference in index of refraction between the core and

cladding materials was adjusted by temperature regulation. With the input radiation polarized to excite TE modes only, the angle of incidence was varied. It was found that the only modes that could be propagated were the TE-1 and TE-3; the measured aperture distributions of these modes are shown in Figure 8. The polarization of the laser beam was then rotated 90° so that the TM modes could be excited. In this case, only the TM-1 and TM-3 modes of Figure 9 were observed. A comparison of the measured field distributions (Figs. 8 and 9) with the predicted distributions for a typical metal bisector (Fig. 5) indicates agreement with the theory. It should be noted that the even TM modes, including the TM-0 mode, were not observed.

It was possible by temperature control to slowly vary the difference in index of refraction between the core and the cladding, thereby adjusting the operating point of the guide. In this way, it was observed that new modes were introduced in pairs, i.e., for every TE mode that began to propagate, a TM mode of the same mode number began to propagate at the same operating point. This observation is in agreement with the theory developed for imperfectly conducting bisecting walls. It should be noted that this behavior is quite different from that occurring with a perfectly conducting bisector.

Optical waveguide components have been suggested as a useful alternative to conventional optical components, in some cases providing significant performance advantages. An important goal of the present work is to fabricate such components in a completely solid form suitable for operational use as well as laboratory study. The analysis and design of such components will draw heavily from the wealth of data available in the microwave literature. To illustrate typical design procedures, a bisected dielectric waveguide has been analyzed. In this case a conventional microwave analysis and some simple approximations yield the optical modes of the structure, and indicate that propagation characteristics are generally similar to those observed at microwave frequencies. However, for some operation conditions the TM modal spectrum is significantly altered by the effects of finite metal conductivity. The results have been confirmed experimentally in a laboratory-model waveguide. The analysis employed is typical of the design approach currently employed at Wheeler Laboratories for developing more sophisticated structures such as optical directional couplers and waveguide lasers.

204

REFERENCES

1. Wilmot, D. W.: Macroscopic Single-Mode Waveguide for the Construction of Optical Components. PTGMTT Internatl. Symp. Digest, May 1964, p. 115. (Also Wheeler Labs. Report 1191P; Dec. 13, 1963.)

2. Schineller, E. R.; Wilmot, D. W.; Heinemann, H. M.; and Redlien, H. W.: Development of Macroscopic Waveguide and Waveguide Components for Optical Systems. Wheeler Labs. Report 1247 to NASA; Nov. 28, 1964; NASA Report N65-16252.

3. Kaplan, R. A.: Optical Waveguide of Macroscopic Dimensions in Single-Mode Operation. Proc. IEEE, vol. 51, Aug. 1963, p. 1144. (Also Wheeler Labs. Report 1141P; May 17, 1963.)

4. Collins, R. E.: Field Theory of Guided Waves. McGraw-Hill, 1960.

(a) DIELECTRIC-SLAB
WAVEGUIDE.

(b) DIELECTRIC-ROD
WAVEGUIDE.
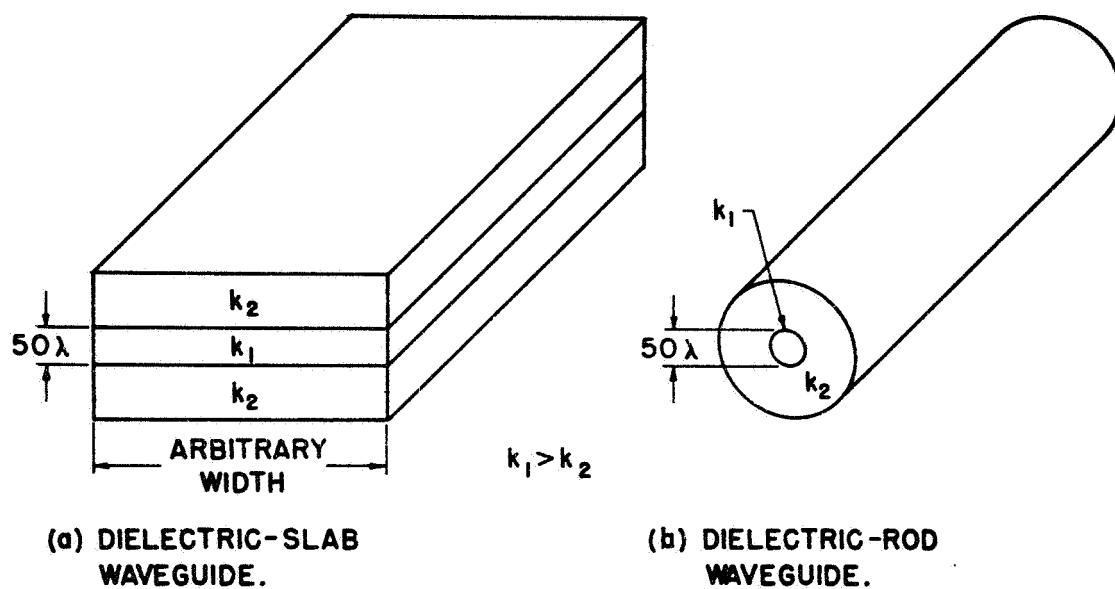
FIGURE 1. DIELECTRIC WAVEGUIDES

(a)

(b)
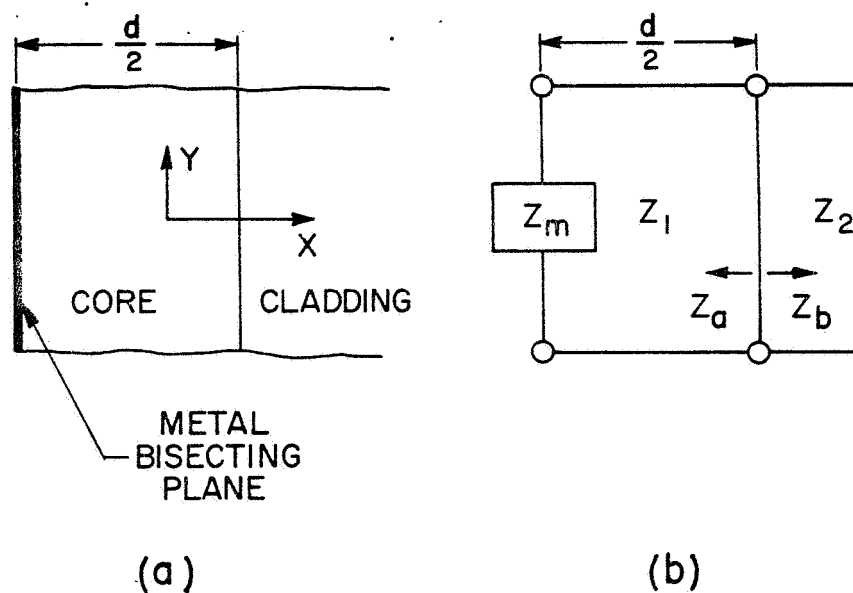
FIGURE 2. TRANSVERSE EQUIVALENT CIRCUIT FOR A BISECTED
DIELECTRIC-SLAB WAVEGUIDE. (a) WAVEGUIDE CROSS
SECTION; (b) TRANSVERSE CIRCUIT. NOTE THAT
PROPAGATION IS INTO THE PAPER
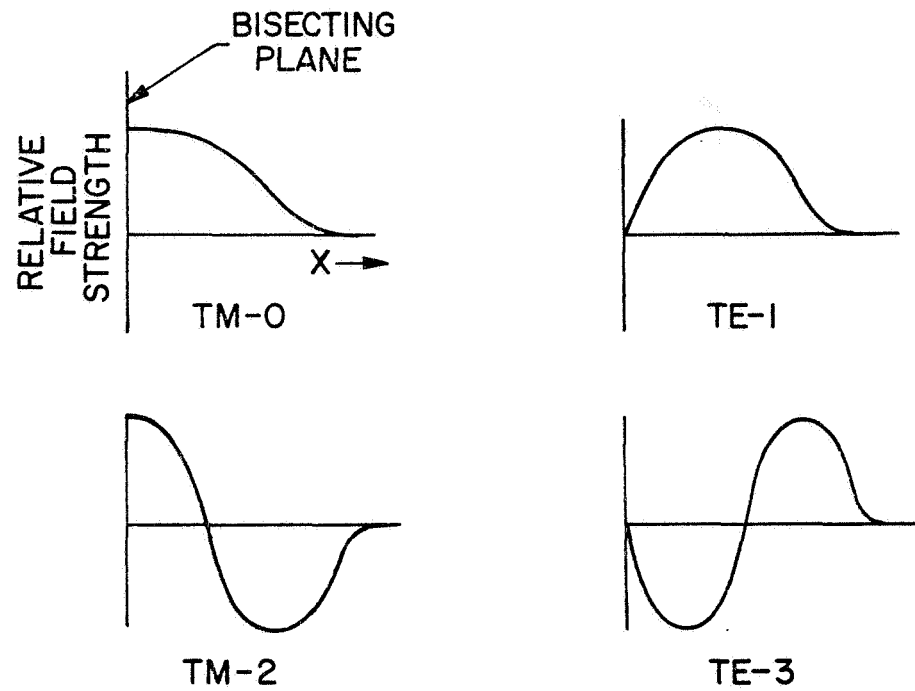
FIGURE 3. TRANSVERSE FIELD DISTRIBUTIONS OF PROPAGATING
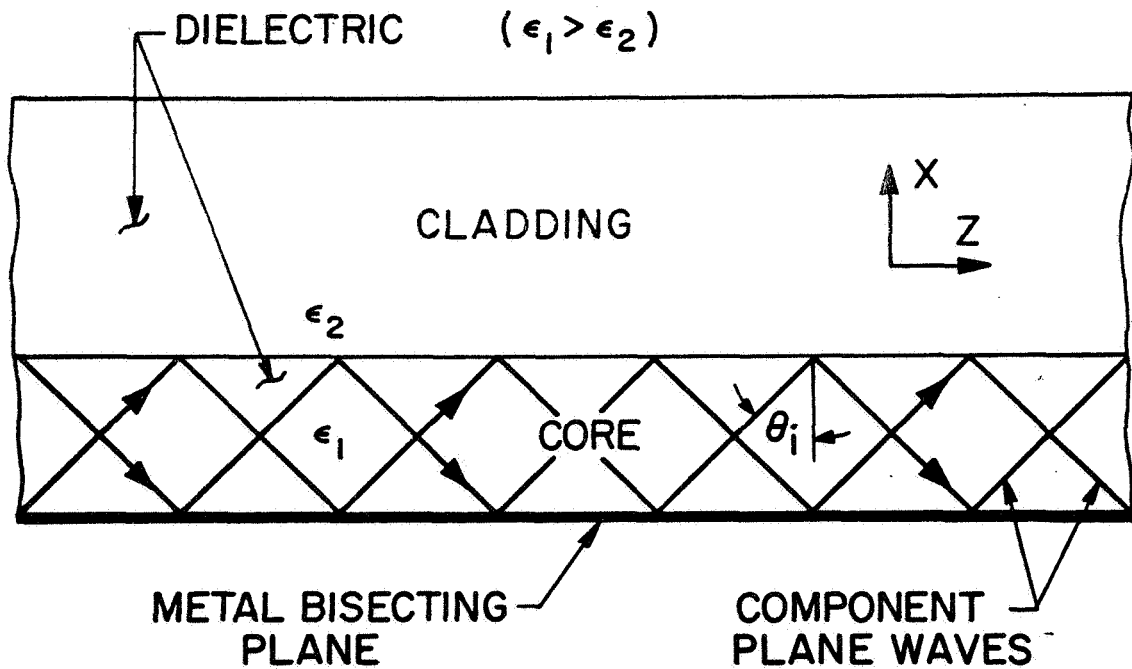MODES ON A DIELECTRIC-SLAB WAVEGUIDE BISECTED
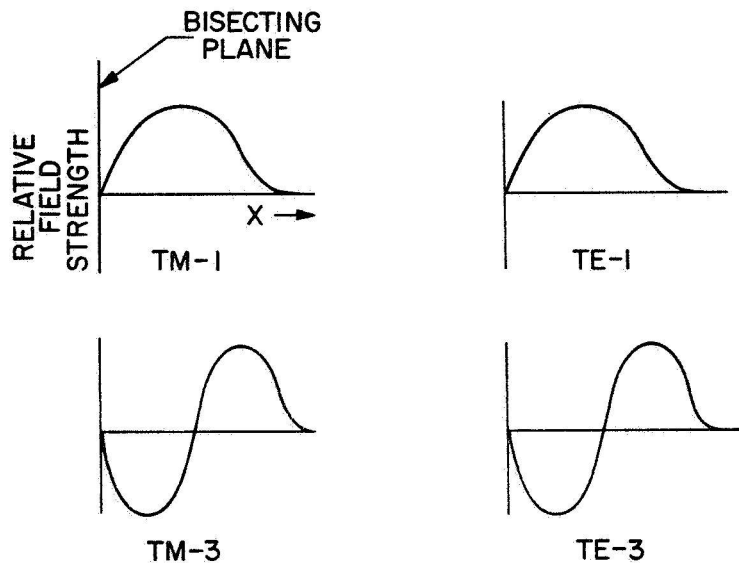BY A PERFECT CONDUCTOR

FIGURE 4. BISECTED DIELECTRIC-SLAB WAVEGUIDE

FIGURE 5. TRANSVERSE FIELD DISTRIBUTIONS OF MODES PROPAGATING
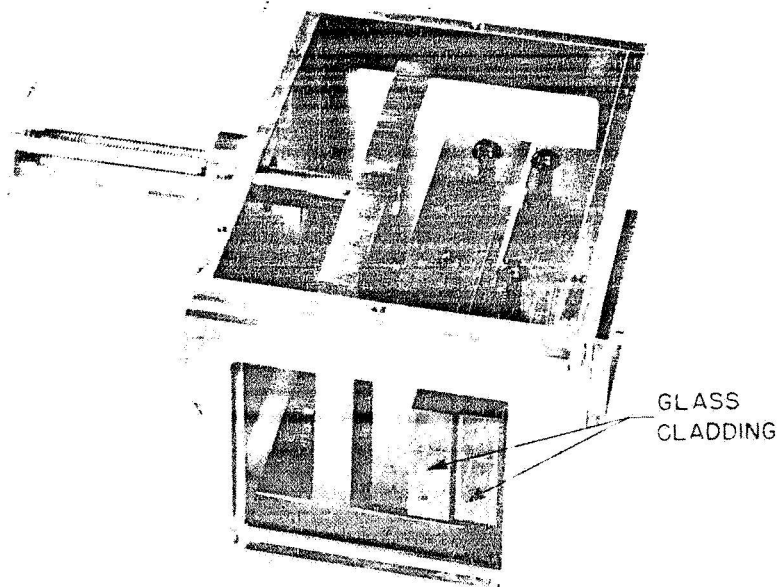NEAR GRAZING INCIDENCE IN A DIELECTRIC-SLAB WAVEGUIDE
BISECTED BY A TYPICAL METAL

FIGURE 6. EXPERIMENTAL WAVEGUIDE, UNBISECTED CONFIGURATION.
THE BISECTED CONFIGURATION IS OBTAINED BY REPLACING ONE
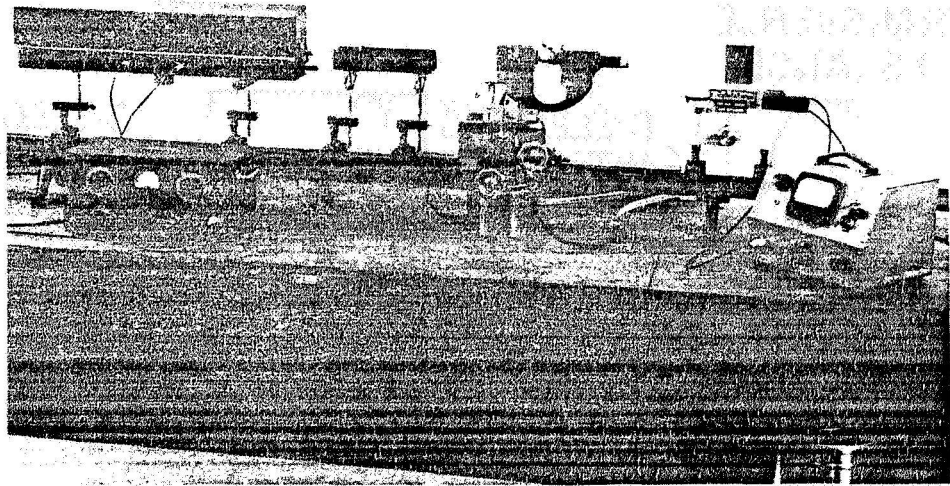OF THE GLASS CLADDING PLATES WITH AN ALUMINIZED GLASS
PLATE

FIGURE 7. EXPERIMENTAL SETUP FOR MEASUREMENT OF
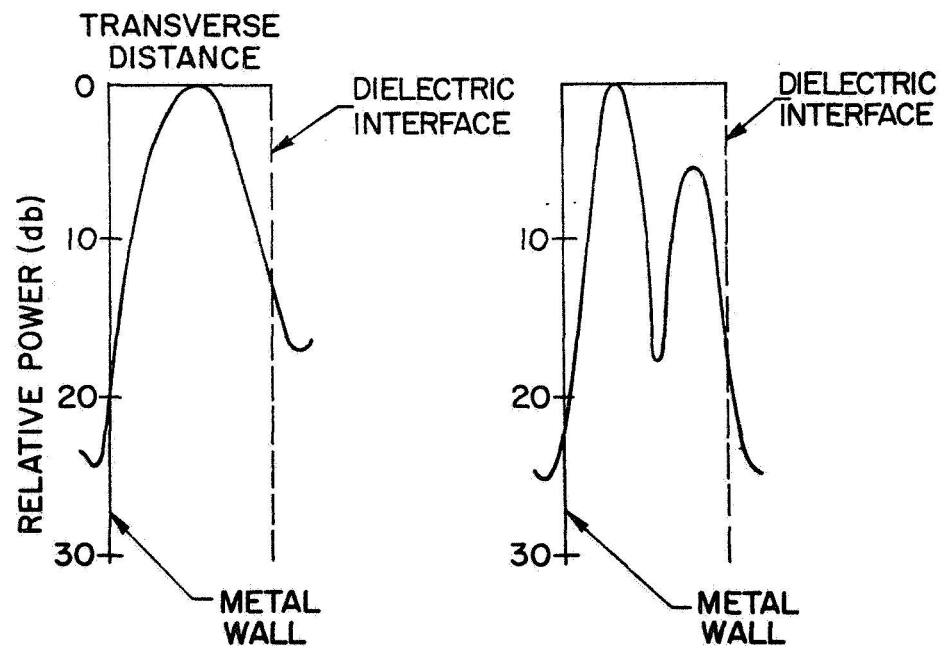WAVEGUIDE APERTURE DISTRIBUTION

FIGURE 8. MEASURED APERTURE DISTRIBUTION OF THE TE MODES IN A
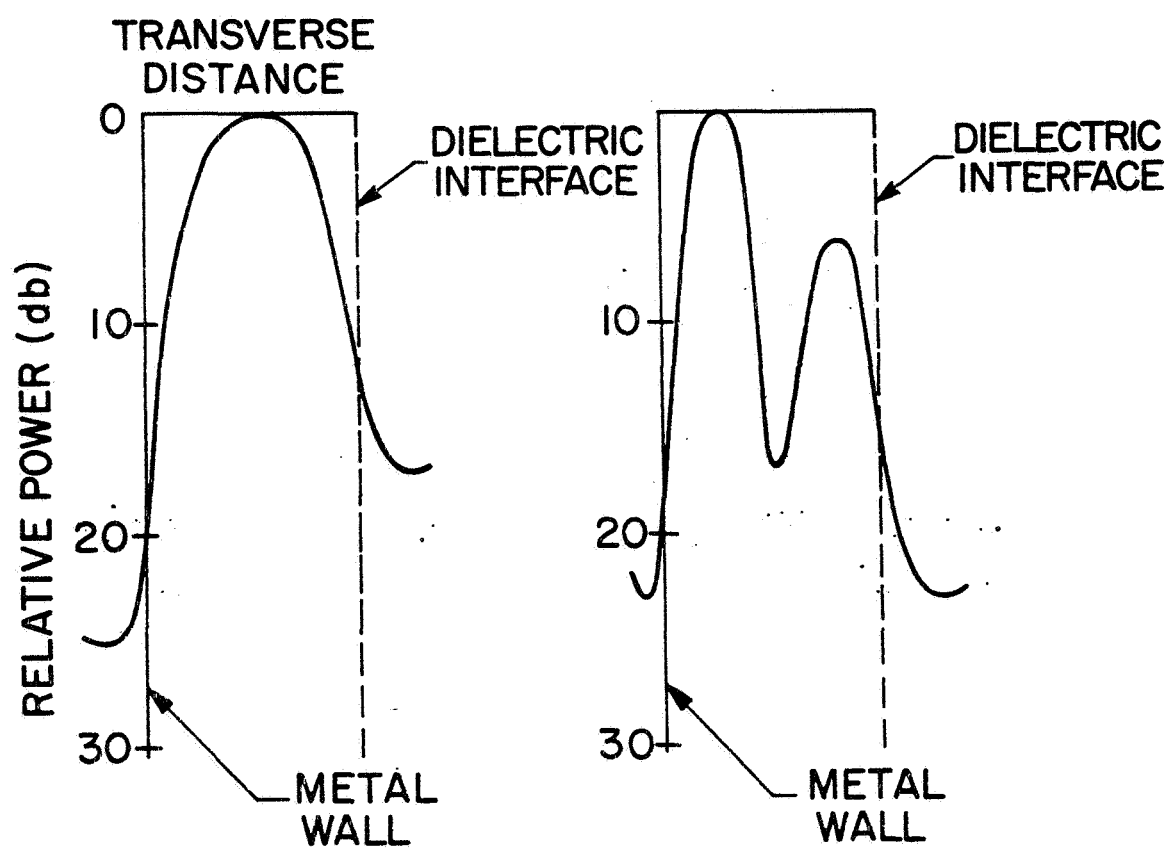BISECTED DIELECTRIC-SLAB WAVEGUIDE AT OPTICAL FREQUENCIES

FIGURE 9. MEASURED APERTURE DISTRIBUTION OF THE TM MODES IN A
BISECTED DIELECTRIC-SLAB WAVEGUIDE AT OPTICAL FREQUENCIES